Optical phase and amplitude modulator and photonic integration for long wave infrared free space optical telecommunications.

Thomas Poletti

PSL
UNIVERSITÉ PARIS

THÈSE DE DOCTORAT
DE L'UNIVERSITÉ PSL

Préparée à l'École Normale Supérieure

Optical phase and amplitude modulator and photonic integration for long wave infrared free space optical telecommunications

Soutenue par
Thomas Poletti
Le 07 mars 2024

École doctorale n°564
Physique en île-de-France

Spécialité
Physique

Composition du jury :

Frédéric GRILLOT Pr. Dr. Telecom Paris, LTCI	*Président* *Examinateur*
Mikhail BELKIN Pr. Dr. Technische Universität München	*Rapporteur*
Sophie BOUCHOULE Dr. C2N	*Rapporteuse*
Daniel DOLFI Dr. Thales research and technology	*Examinateur*
Carlo SIRTORI Pr. Dr. Ecole Normale Supérieure	*Directeur de thèse*
Salvatore PES Dr. III-V Lab	*Co-encadrant*

ENS | PSL

Remerciements

Tout le travail présenté dans ce manuscrit n'aurait pas pu voir le jour sans l'aide et le soutien des nombreuses personnes avec qui j'ai eu la chance de pouvoir collaborer, ou de simplement être entouré. Je souhaite donc naturellement leur adresser un remerciement tout particulier.

En premier lieu, je souhaite remercier les membres de mon Jury. Mes rapporteurs, Mikhail Belkin et Sophie Bouchoule et mes examinateurs Daniel Dolfi et Frédéric Grillot. Merci d'avoir pris le temps d'évaluer ce travail, et de m'avoir fait des retours constructifs le concernant. Merci également à mon directeur de thèse, Carlo Sirtori, pour son soutien et ses conseils avisés sur des sujets tout aussi variés. Merci aussi à Djamal qui m'a expliqué et permis de faire de nombreuses manipes dans votre laboratoire, sans lesquelles cette thèse aurait été bien différente.

Je souhaite également remercier mon équipe directe au III-V Lab, l'équipe MIR. D'abord mon encadrant direct, Salvatore Pes, qui m'a toujours bien conseillé et rassuré, et qui à fait preuve d'une extrême bienveillance à mon égard. Jean-Luc Reverchon, tout aussi bienveillant, et ayant toujours une anecdote à raconter. Merci pour ton soutien indéniable et essentiel quand ce fut difficile. Merci aussi à Virginie dont le travail est un des piliers de cette thèse. Merci aux thésards du groupe avec qui j'ai eu la chance de travailler, Greg et Mathurin, que je devrais appeler docteurs maintenant. J'ai beaucoup apprécié travailler et déconner avec vous, vous chambouler les idées et me les faire chambouler en retour jusqu'à ce que plus aucun d'entre nous n'aie de certitudes.

Je souhaite également adresser un grand merci à Alexandre Delga, qui a été mon encadrant au début de cette thèse et qui ne m'a jamais lâché après son départ. Nos conversations ont toujours été un énorme boost au moral et j'en suis à chaque fois ressorti remotivé et plein d'idées. Ton aide, et surtout ton soutien, ont été essentiels au bon aboutissement de cette thèse et je t'en suis très reconnaissant.

Mes co-bureau successifs, Hajar, Théo et Pierre, merci pour tous les moments passés ensemble, pour tous les échanges et réflexions, pour les manques de réflexion aussi. Merci à Pierre et Théo pour toutes les soirées et journées partagées, le patin à glace sur les lacs gelés, le VTT...

Merci à tous les doctorants et collègues du III-V Lab que j'ai côtoyés, et qui n'ont pas été avares en conseils, blagues, pâtisseries, discussions... Claire, Francois, Frédéric, Sylvain, Yasmine, Sarah, Delphine N., Delphine L., Joan, Catherine, Colin, Muriel, Cosimo, Amin, Ines,

Marco, Nour, Antoine, Emmanuel, Risab, Shirley, Romain.

Merci à Krako qui m'a donné à mesurer des composants qui fonctionnent, ça fait du bien d'enchainer les mesures qui marchent.

Tout ce travail n'aurait pas eu d'aboutissement concret sans la fabrication des composants. Je souhaite remercier tout d'abord les épitaxieurs, Axel, Olivier, Antoine, Jean-Pierre, pour m'avoir fourni les échantillons et les croissances essentielles à ce travail et aux développements technos. Merci à tous les technologues qui ont contribué de manière substantielle à ce travail, Claire, Bouzid, Eva, Michel, Alex, JF, Alex, Jorge, Hervé et tous les autres avec qui j'ai pu échanger. Également aux technologues de TRT, Etienne, Paolo, Julie sans qui il n'y aurait pas eu de composants tout simplement.

Merci aussi à l'équipe de direction et à d'administration du III-V Lab qui m'ont ouvert les portes du labo et les ont laissées ouvertes jusqu'à la finalisation de ce travail. Jean-Pierre, Pascale, Jean-Philipe. Merci à Pascale, Valéria et Fatou pour leur gestion administrative efficace, sans quoi je serais encore perdu dans les fin-fonds de concur.

Enfin, je souhaite remercier mes amis et ma famille pour leur soutien indéniable. Julien, Robin, Mathias, Gael, Marine, Tanguy, Dimo et la team lethal company.

Merci à ma famille aussi pour leur soutien, Rémi, mes parents, mes oncles et tantes, cousins et cousines.

Merci à Ornella de m'avoir soutenu et supporté dans tous les sens du terme.

Résumé

Les communications optiques en espace libre sont devenues un domaine d'intérêt croissant au cours des dernières années, dans lequel les dispositifs optoélectroniques fonctionnant dans la gamme des longueurs d'onde de l'infrarouge lointain (LWIR) pourraient être de sérieux concurrents des longueurs d'onde traditionnelles des télécommunications pour les liaisons atmosphériques. En effet, les grandes longueurs d'onde sont moins affectées par les perturbations atmosphériques. Toutefois, le déploiement des communications en espace libre dans le LWIR est limité par la disponibilité des éléments de base passifs et actifs tels que les modulateurs d'amplitude et de phase rapide et les recombineurs de faisceaux.

Dans ce travail, nous présentons le développement d'un modulateur externe en géométrie guide d'onde, basé sur l'effet Stark inter-sous-bande, fonctionnant à $\lambda = 9$ µm. Cet effet est particulièrement intéressant pour la modulation en raison de sa réponse intrinsèquement rapide, son accordabilité élevée et linéaire en longueur d'onde avec une tension appliquée, et sa faible consommation d'énergie. Nous avons intégré des puits quantiques asymétriques couplés dans un guide d'ondes InGaAs sur InP afin de maximiser l'interaction optique tout en minimisant la capacité électrique du composant. Le résultat est un modulateur polyvalent capable d'effectuer une modulation d'amplitude ou de phase par un choix judicieux de la polarisation et de l'intensité de la modulation RF appliquées. Dans l'optique d'une future intégration monolithique, nous avons conçu et fabriqué des recombineurs de faisceaux passifs en guide d'ondes basés sur des interféromètres multimodes (MMI) ainsi que des détecteurs à cascade quantique (QCD) pour la détection cohérente. Nous présentons leurs performances, et en particulier celles d'un séparateur MMI 2x2 3dB et d'un MMI hybride 90 degrés 2x4, qui sont des éléments essentiels pour les émetteurs-récepteurs intégrés pour communications cohérentes.

Mots clés : Optique intégrée, guide d'onde, modulation optique, télécommunications en espace libre, infrarouge lointain

Abstract

Free-Space Optical (FSO) communications has become a field of growing interest over the past years in which optoelectronic devices operating in the Long Wave Infrared (LWIR) wavelength range could be serious competitors to traditional telecom wavelengths for atmospheric links as they are less impacted by atmospheric perturbations. However, the deployment of LWIR FSO communications is limited by the availability of basic passive and active building blocks such as high-speed modulators and beam combiners among others. In this work, we present an external integrated modulator based on inter-subband Stark effect operating at $\lambda = 9$ µm. This effect is of particular interest for modulation due to its intrinsically fast response, high wavelength tunability under applied bias and low RF power consumption. We embedded asymmetrical coupled quantum wells within a deep ridge InGaAs on InP core waveguide in order to increase the optical interaction and reduce the geometrical capacitance. The result is a versatile modulator able to perform either amplitude or phase modulation by an appropriate choice of applied DC bias and RF modulation. In addition, we designed and fabricated passive waveguide beam combiners based on Multi Mode Interferometer (MMI) and quantum cascade detectors (QCD). We present their performance and in particular 2x2 3dB MMIs splitter as well as 2x4 90 degree Hybrid MMIs which are critical building blocks for integrated transceivers based on complex modulation format and are planned to be integrated with a QCD.

Keywords : Photonic integrated circuit, optical waveguide, optical modulator, free space optical communications, long wave infrared

Contents

Glossary

ACQW *Asymmetrical Coupled Quantum Wells* 82, 84–86, 88, 90, 91, 93, 95, 108, 118, 120, 153

ALD *Atomic Layer Deposition* 35, 110, 140, 153

ASK *Amplitude Shift Keying* 14, 16, 19

AWGN *Additive White Gaussian Noise* 17, 19, 46

BER *Bit Error Rate* 17

BPSK *Binary Phase Shift Keying* 15, 18, 79

CMRR *Common Mode Rejection Ratio* 147–150, 154

EQE *External Quantum Efficiency* 123, 124, 130, 136

FOM *Figure Of Merit* 77–79, 87, 88, 90, 93, 123, 124

FSOC *Free Space Optical Communications* 4, 5, 7, 8, 10, 128, 129, 153

FTIR *Fourier Transform InfraRed interferometer* 31, 35

ICP *Inductively Coupled Plasma* 68, 108, 140

LWIR *Long Wave Infrared - 8 to 12 µm -* 4, 5, 7–11, 16, 29, 34, 45, 48–51, 61, 69, 71, 72, 74–77, 80, 81, 85, 103, 114, 118, 121, 123, 125–129, 144, 153

MBE *Molecular Beam Epitaxy* 85, 108, 142

MMI *Multi Mode Interferometer* 10, 11, 56, 61–66, 68, 69, 71, 72, 95, 99, 102, 103, 107, 129, 146–149, 151, 153, 154

MOCVD *MetalOrganic Chemical Vapour Deposition* 30, 66, 85, 108, 142

MWIR *Mid Wave Infrared - 3 to 6 µm -* 5, 8, 10, 29, 45, 48, 51, 71, 80, 81, 127

MZ *Mach-Zehnder* 99–103, 105, 107

NEP *Noise Equivalent Power* 124, 125, 128, 145, 146

OOK *On-Off Keying* 14, 15, 79

PECVD *Plasma Enhanced Chemical Vapour Deposition* 68, 108, 140

PSK *Phase Shift Keying* 15, 19

QCD *Quantum Cascade Detector* 10, 11, 22, 45, 71, 81, 83, 125, 128–131, 133–138, 140–146, 151, 153, 154

QCL *Quantum Cascade Laser* 10, 11, 22, 29, 37, 45, 48, 49, 52, 71, 75, 81–83, 86, 93, 103, 120, 121, 125, 126, 128, 134, 138, 146, 150, 151, 154

QWIP *Quantum Well Infrared Photodetector* 126–128

RIE *Reactive Ion Etching* 68, 108, 110, 140

SEM *Scanning Electron Microscope* 31–33, 140

SER *Symbol Error Rate* 17

SNR *Signal to Noise Ratio* 17, 137

SWIR *Short Wave Infrared - 1 to 2 µm -* 5, 7–9, 11, 48, 51, 74–77, 79, 80, 120

T2SL *Type II Strained Layer superlattice* 125–127

TMM *Transfer Matrix Method* 27, 36

Chapter 1

General introduction

Objectives

This first introductory chapter aims at presenting the challenges of optical telecommunications through historical and theoretical aspects. In a first part, a brief historical review of the development of telecommunications will be presented, which justifies the predominance of RF in modern wireless telecommunications. This will be followed by a presentation of the challenges and potential advantages of long wave infrared-based free space optical communications that are the main motivations to the development of the components presented on the following chapters of this work.

Contents

1 A quick history of telecommunications

Before the 19th century, and as early as the ancient Greek times, chains of beacons situated on high ground were used to transmit a single binary information. Those were using smoke signals, fires, flags etc... Those beacons, probably constitute the very first organized telecommunication network to transfer information across long distances. Later, this system of beacon chains was reused with more complex alphabets to allow the transmission of more complex messages over longer distances. In particular in the late 1700s, Claude Chappe invented a semaphore telegraph system with a complex alphabet of 92 symbols encoded on the position of three articulated arms on a high pole, which soon was used to transmit messages all over France [1]. In this system, the carrier is the visible light, transmitted from a semaphore to another one through the atmospheric channel. One can say that Chappe's semaphores was the very first free space optical telecommunication system.

Soon after, a new telecommunication system arose with the invention of the electrical telegraph. Democratized by Samuel F.B. Morse and its famous alphabet, and Alfred Vail, it and became commercially used in the United States of America in 1838 [2]. Their system used an electrical current as the carrier and electrical cables as the transmission channel. It soon became a worldwide adopted communication system with the creation of the International Telegraph Union in 1865 to establish standards for international communications. A year later, the first continuous transatlantic communication using a transatlantic electrical cable was established. Those were the early years of electrical communication.

In parallel, with the development of acoustic telegraphy as a way of multiplexing telegraph messages in a single cable, came the invention of the telephone, often attributed to Alexander Graham Bell in the 1870s. Even though the attribution of this invention to Bell is a subject of controversy [3], his contribution to the commercial use of them is indisputable as he created the very first telecom company (the Bell Telephone Company, which then became the American Telephone and Telegraph Company). Bell also is attributed to the invention of modern free space optical telecommunications with his "photophone". Even though this invention never had the same success as the telephone and didn't reach commercial applications, it demonstrated the key principles of free space optical telecommunications and enlighten some of its limitations.

From the 20th century to the 21st century, enormous technological progress lead to the wide and diversified telecommunication technologies used nowadays. The early 20th centuries show the rise of radio transmissions, thanks to the work of Guglielmo Marconi, which used the work of many other physicists to perfect his radio transmitter and receiver, pushing what initially was a laboratory demonstration object, to an actual telecommunication device. Marconi's radio development was followed by a clear renew of interest to free space optical communications, using at their beginning kilohertz to a few megahertz radio waves. From his work, constant technological progress was made, pushing the generation of radio waves up to the GHz frequency range in the second part of the 20th century. Radio frequency communications has since coexisted together with telephone and telegraph communications, until the digital revolution and the birth of the internet era put an end to the latter at the end of the 20th century.

The progress made in semiconductor technologies, in particular the invention of the transistor in 1947, developed to replace electromechanical relays, was the starting point for the development of modern digital communications. This digitalization of communications greatly increased the capacity of the already existing telecommunication network cables. This era, referred to as the semiconductor era, was marked by a quick development of integrated electronic circuits, which soon were found in every telecommunication system. These were the years of the increased development of digital TV and cellular broadcasting services, and satellite microwave telecommunication systems.

At the same time, between the 1960s and 1970s, a new interest arose for optical communications through guided and unguided media. Those interests came from two main breakthroughs : the development of the laser in 1959 by Theodore Maiman followed 7 years later by the first demonstration of an optical transmission through a glass fibre by Charles K. Kao and Georges A. Hockham in the UK [4]. Since this pioneering work, tremendous progress was made in the fabrication of silica fibres, until they reached optical losses much below 1 dB/km approximately in the 1970s, and even down to 0.2 dB/km in the 1980s, with the development of the first single-mode optical fibre. This progress made optical fibres a much more interesting alternative for long range communications than coaxial cables, which were defining at that time the highest standards. The following years were marked by the standardization of optical fibres, the invention of the optical fibre amplifier (such as erbium doped fibre amplifier and Raman amplifiers) and the wavelength division multiplexing, which further pushed the capacity of a single optical fibre to Terabits per second over distances of kilometres. This marked the clear renew for optical telecommunication systems, and optical fibres, became the foundation for local (LAN), metropolitan (MAN) and wide (WAN) area networks. Intercontinental subsea telecommunications links highly rely on optical fibres too, which have been elected as technology of choice for the Internet. Nowadays, there is a growing interest toward exporting optical communications, out of the fibre channel, making use of the free space to transfer information.

Currently, telecommunications systems are using a wide diversity of technologies that is schematically presented in Figure 1.1 covering the electromagnetic spectrum from the Radio Frequency (RF) domain up to the infrared and visible optical domains.

The interested reader willing to deepen the chronicles of telecommunications development from 1850s to nowadays can find extensive information in [4], which served as a basis to this brief historical summary.

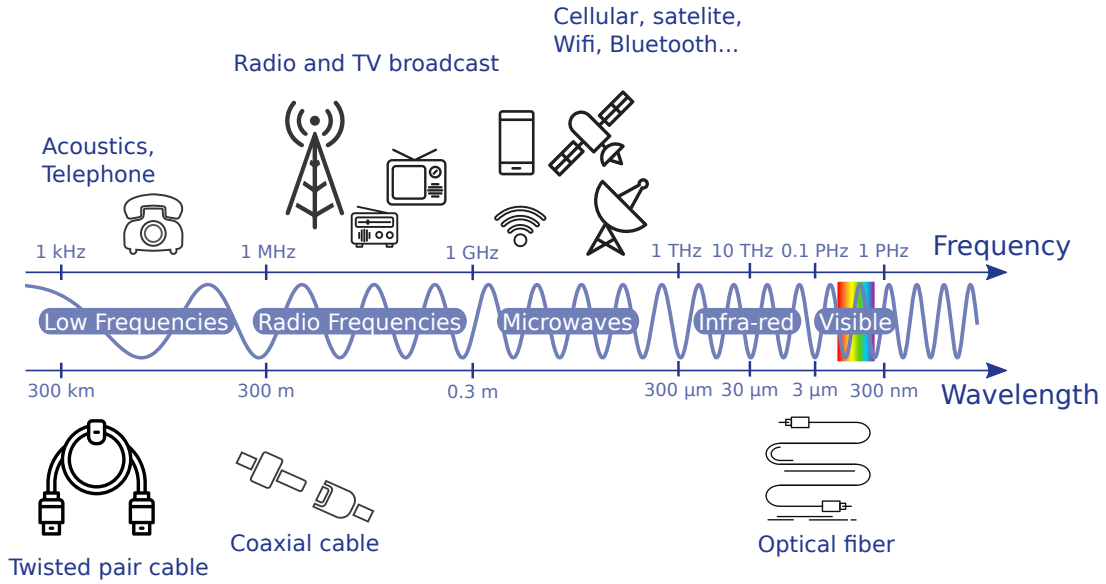

Figure 1.1: Electromagnetic spectrum and principal frequency bands exploited for telecommunications. Wireless communications are on top, wired communications at the bottom. Logos are distributed under a free licence agreement from Vecteezy.com

2 Free space optical communications

In the first part of this introductory chapter we have presented a brief overview of the historical development of telecommunications, leading to the actual modern and diversified panorama. In the following, we focus on wireless communications and particularly, on the development of *Free Space Optical Communications* (FSOC). We will present the reasons driving their technological development, and the practical limitations on the current FSOC technology mainly established at the telecom wavelengths around 1.55 µm, which oriented us toward the *Long Wave Infrared - 8 to 12 µm -* (LWIR) spectral band.

In the past decade, FSOC have shown a renewed enthusiasm and many works dedicated to the development of those telecommunication solutions have resulted to a rapid evolution of this domain. Indeed, the current status of wireless communications, dominated by RF communications, is reaching the saturation of its allocated bandwidth. In RF systems, an allocated bandwidth represents up to 20% of the carrier frequency [5]. The fast-growing demand for higher data rates is therefore not seen as addressable in the years to come, by RF communications only. Solutions must be found, pushing toward the use of optical frequencies [6]. At optical frequencies, an allocated bandwidth of only 1% for a wavelength of 1.55 µm already represents a 2 THz bandwidth, much higher than any RF carrier frequency, revealing the potential of optical communications [7]. FSOC were initially proposed as a solution to the last mile problem, i.e. the connection of the end user to the telecommunication network (optical fibres or coaxial cables), which necessitate the deployment of costly and complex infrastructures for a limited number of users. In fact, it is often in the last mile connection that is lost the most in terms of energy and cost efficiency. It is particularly the case for low population density areas. Other envisioned applications of FSOC have also attracted interest, among them, we can cite : back-haul solu-

tions for cellular or optical fibre systems, network recovery in case of natural disasters, war or terrorism attacks, energy efficient satellite communications [6, 8, 9].

Multiple wavelength windows can be used for such FSOC systems, as presented in Figure 1.2. Three main transmission windows are clearly visible in the infrared domain. It is in the *Short Wave Infrared - 1 to 2 µm -* (SWIR) than most of the effort in developing FSOC has been pursued, due to the already technological maturity of the semiconductor and fibre based technologies. Very recently, a demonstration of a transmission over a distance of 50 km in a turbulent atmosphere has reached the Tbit/s rate using a laser at 1.5 µm, polarization multiplexing and high order coherent modulation formats. This data rate, which is of the same order as data rates transmitted nowadays through commercial optical fibres, has been possible by employing a full adaptive optical system to correct the distorted wavefront of the channel due to the propagation across the turbulent medium [10].

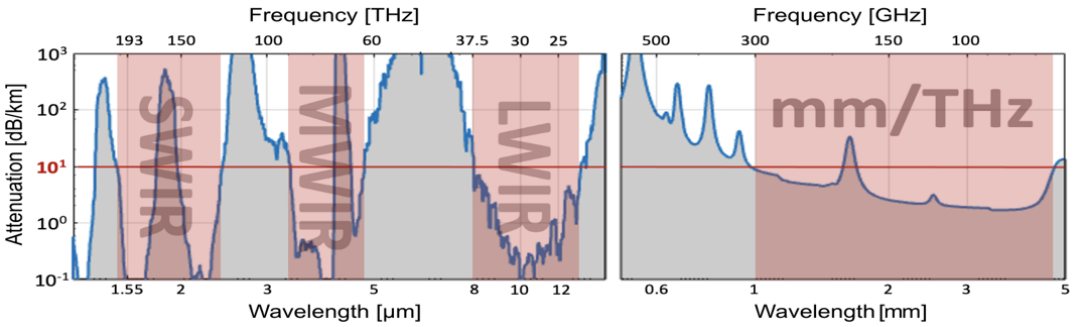

Figure 1.2: Spectral attenuation of an ideal atmosphere on a horizontal plane at sea level. From [11]

However, the practical deployment of FSOC has been facing multiple challenges in their deployment that are still greatly limiting their adoption. Their high sensitivity to weather condition and particles (such as fog, haze, dust, and smog) can greatly impact their performance and even compromise the availability of the telecommunication link [12, 13]. In the following section, we will explain the limitations introduced by the atmosphere on FSOC, that justifies the use of the *Mid Wave Infrared - 3 to 6 µm -* (MWIR) and LWIR spectral band.

2.1 Challenges of FSOC

2.1.1 Transmission through a turbulent atmosphere

The atmospheric channel is essentially a turbulent media characterized by several local inhomogeneities that are linked to temperature variations, gases and particles concentration, densities variations, etc. All these contributions, which chaotically evolve in space and time, lead to local changes of the atmosphere optical index that can be quantified by considering its spatial fluctuations between two positions (r_1 and r_2) at a given instant in time. These can be quantitatively described by the so-called refractive index structure coefficient, $C_n^2 = \langle (n(r_1) - n(r_2))^2 \rangle / |r_1 - r_2|^{2/3}$, which is expressed in $m^{-2/3}$, and is often used as standard metric to quantify the impact of turbulences on the propagation of optical signals through the

atmosphere. Those inhomogeneities can lead to strong deformations of an optical beam, such that a high quality Gaussian output beam from a laser emitter, will arrive completely distorted at the receiver side after its propagation across the turbulent atmosphere, as shown in Figure 1.3. The longer the propagation path, the stronger those effects will be. Typical effects experienced by the propagated beam are beam broadening, beam wandering, scintillation, and attenuation. Each of them is briefly described bellow.

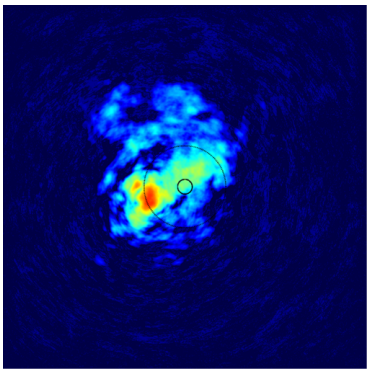

Figure 1.3: A distorted beam after a 10 km propagation through a turbulent atmosphere. The simulation has been performed at 1.55 µm with $C_n^2 = 10^{-14} m^{-2/3}$ and considering a near ground propagation. The inner dark circle represents the original beam size ($1/e^2$) as is is emitted, while the outer circle represents the final size at the receiver for a propagation in a non turbulent atmosphere. Image taken from [12]

Beam broadening : under the influence of turbulences, is a subject that has been widely studied in the literature [12, 14, 15, 16]. During its propagation, a beam (which we assume Gaussian in the following) will progressively broaden due to the combined effects of diffraction and turbulences. The beam broadening in a turbulent medium can be computed under the Rytov approximations, such that it writes as [16, 15] :

$$W(L)^2 = \begin{cases} W_d(L)^2(1 + 1.33\sigma_R^2\Lambda^{5/6}), & \text{if } \sigma_R^2 \leq 0.3 \text{ (low turbulences asymptote)} \\ W_d(L)^2(1 + 1.63\sigma_R^{12/5}\Lambda), & \text{otherwise (high turbulences asymptote) [17]} \end{cases} \tag{1.1}$$

where $\sigma_R^2 = 1.21 C_n^2 k_0^{7/6} L^{11/6}$ is the Rytov variance, $\Lambda = 2L/(k_0 W_d(L)^2)$ depends of the wave vector k_0 and the diffraction broadened beam $W_d(L)$ after a propagation distance L.

As can be seen on Figure 1.4a, the broadening under turbulent conditions is stronger at shorter wavelengths. In the presented example one can see that under moderate turbulence, for $C_n^2 = 10^{-14}\ m^{-2/3}$, the broadening is increased by 6% (with respect to the diffraction induced broadening) at 1.55 µm while it is only increased by 3% at 9.1 µm for a beam propagated across 10 km. The difference is even more significant for high turbulences, at $C_n^2 = 10^{-15}\ m^{-2/3}$ for example, where it represents a nearly 70% increase at 1.55 µm while it is less than 40% at 9.1 µm.

Alternatively, one might want to consider the spatial coherence radius after propagation through a turbulent atmosphere, which is of particular importance for coherent communication

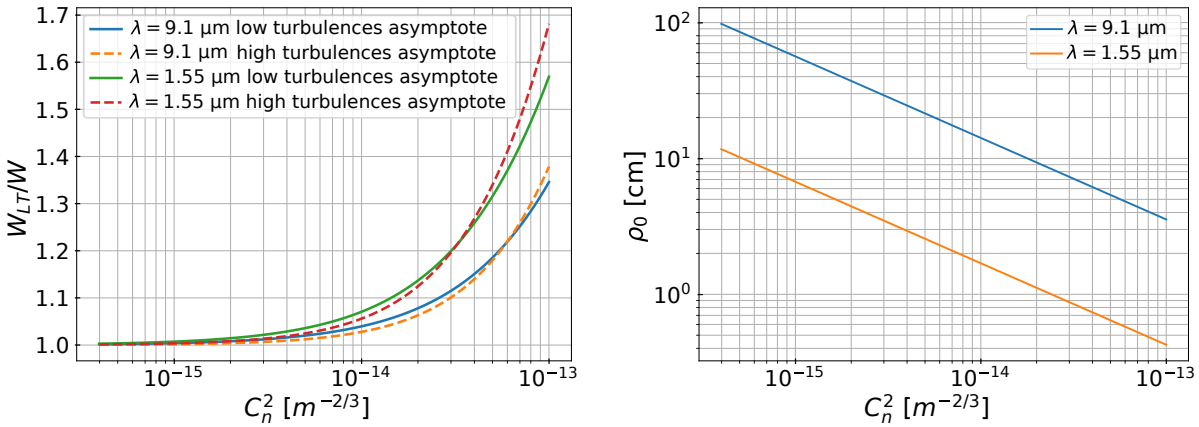

(a) (b)

Figure 1.4: a) Normalised broadening of a Gaussian beam with 0.25 mrad divergence after propagation over 10 km, as calculated by Rytov equations. b) Spatial coherence radius of the same beam after propagation over the same distance with constant turbulences (C_n^2 constant with the position, not depending on z).

systems. The transverse coherence length ρ_0 after propagating over a distance L can be expressed as [12, 15] (with λ the wavelength) :

$$\rho_0 = 0.088 \left[\int_0^L \left(1 - \frac{z}{L}\right) C_n^2(z) dz \right]^{-3/5} \lambda^{6/5} \tag{1.2}$$

The above model is valid only when ρ_0 is much bigger (respectively much smaller) than the inner (respectively, outer) scale of the turbulence. Under strong turbulences, ρ_0 can become smaller than the beam waist. In that case, the divergence angle would not evolve as λ/W_0 but rather as λ/ρ_0, thus resulting in a net $\lambda^{-1/5}$ dependence. This would translate in a slight advantage for LWIR based FSOC with respect to SWIR based ones.

Beam wandering : can be interpreted as the standard deviation of the beam barycentre ρ_c. As stated in [12], there is no general expression of it, but in the case of intermediate turbulences, it writes as :

$$\langle \rho_c^2 \rangle^{0.5} = \frac{0.26 \lambda L}{\rho_0^{5/6} W^{1/6}} \tag{1.3}$$

where W is the beam waist at the emitter. Considering Equation 1.2, $\langle \rho_c^2 \rangle^{0.5}$ appears roughly independent of the wavelength.

Scintillation : is the intensity fluctuation of the received beam. The Rytov variance σ_R^2, introduced in the previous paragraph (beam broadening), quantifies this scintillation effect as the normalized intensity variance and its expression is valid in the weak regime of turbulence (i.e., for $\sigma_R^2 < 0.3$). Its expression is roughly inversely proportional to the wavelength ($\lambda^{-7/6}$). Under strong turbulence, i.e. beyond the validity limit of Rytov approximation ($\sigma_R^2 > 0.3$),

saturation effects appear. Since these effects are stronger for shorter wavelengths, LWIR based FSOC might also have an advantage in comparison to the shorter wavelength.

It can also be shown that the frequency of scintillation evolve as $\lambda^{-6/5}$ [12]. The bandwidth of adaptative optics systems would therefore roughly evolve as the inverse of the wavelength, resulting in great advantage for LWIR with respect to SWIR which also requires fewer actuators due to a larger spatial coherence for longer wavelengths.

2.2 Absorption and scattering

The different particles in suspension in the atmosphere might have a great impact on the diffusion and absorption of a light beam. Many models can be used to describe scattering by particles, the model of Mie scattering by spherical particles is one of those, which provides physical insight of the phenomena involved. In this paragraph, we mainly focus on the scattering by water droplets and clouds, as explained in [12]. The extinction coefficient due to the presence of those aerosols is highly dependent on the droplet's mean size (which are treated as homogeneous spheres). When the typical radius of those is much lower than the optical wavelength (Rayleigh limit), the extinction coefficient grows quickly with increasing particles size over wavelength ratio. On the other hand, when the wavelength is much smaller than the droplet size, the scattering effect reaches a stationary maximum and is relatively independent of the wavelength (this is the geometrical limit).

In [12], Delga et al. reported the expected attenuation of different hydrometeors (a volume distribution of spherical particles made of water droplets) on a laser beam propagating through the atmosphere as a function of the wavelength. Those are presented in Figure 1.5. One can clearly see a non-negligible advantage for the LWIR wavelengths, where the attenuation from different hydrometeors are 40% to 90% lower than in the SWIR. It is interesting to note that there is no substantial advantage for the MWIR wavelengths in comparison to the SWIR regarding this aspect. This argument again suggests a higher potential for LWIR based FSOC.

2.3 Alignment constraint

Contrarily to the RF wireless communications, which have low directivity, the alignment constraints of a laser based FSOC system are much higher. With a typical collimated laser beam with 0.25 mrad divergence, a slight 1 mrad (0,06°) misalignment will result in missing the target by approximately 10 m after a 10 km long propagation. Vibrations of the emitter and receiver (to a lesser extent) must therefore be highly limited, or they would otherwise greatly impact the availability of the FSOC link. For short propagation distances, the point-to-pint alignment may not be so critical on the FSOC link performance, and might be sufficiently ensured by using a laser beam with a wider divergence angle at the emitter side, and dedicated optics to collect the signal at the receiver side. On the other hand, when it comes to long-range propagation, dynamic tracking system must be employed [18]. It particularly is required in the case of coherent systems, where deformations of the phase front introduced by atmospheric turbulences have to be corrected using multiple apertures or adaptative optic systems, but these constraints would

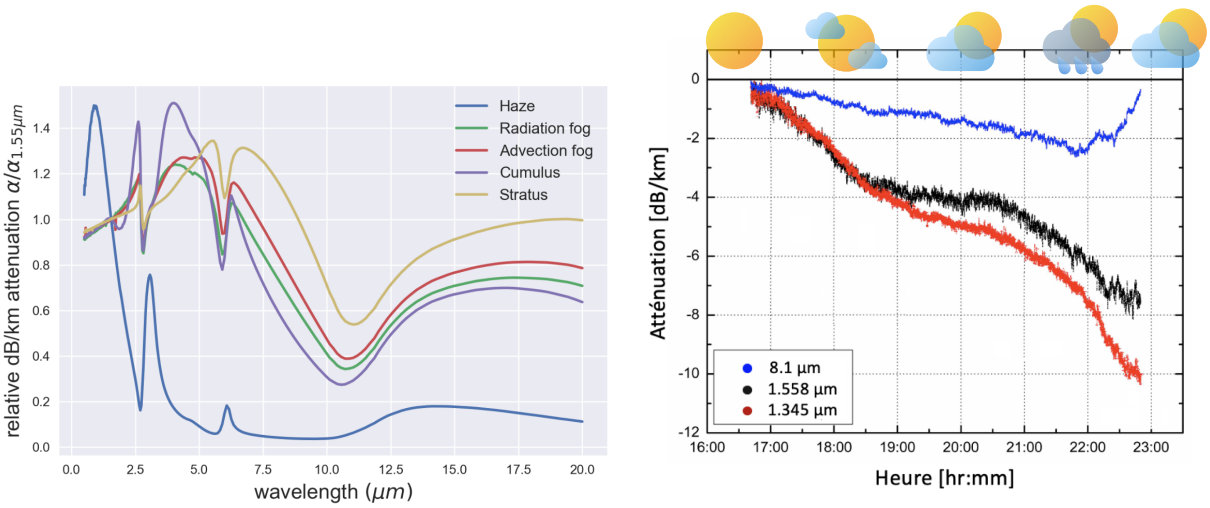

(a) (b)

Figure 1.5: a) Relative attenuation of different types of hydrometeors with respect to $\lambda = 1.55$ µm. obtained from Mie scattering simulations (from [12]). b) Experimental attenuation through the atmosphere of different wavelength during a change of weather and light rain at 22h00. The improvement at 8.1 µm after the rain is attributed to a "washout" effect of the atmospheric pollutants and dust caused by the rain (from [13])

again be relaxed for LWIR wavelengths in comparison to SWIR, as previously explained.

3 Objectives of this work

We have discussed the advantages of LWIR-based optical communications in the previous paragraphs, which motivate the work carried out in this thesis. In particular, in this work we focused on the development of the main photonic building blocks for a LWIR based photonic integrated circuits, FSOC transceiver. Indeed, the low maturity of integrated photonic components working in this peculiar spectral band, until now, has been one of the main limitations to the development of LWIR based FSOC. Additionally, these limitations are not only related to the lack of discrete and telecom grade optoelectronic components, but also to the limitation of characterization equipments and procedures, which represent a great challenge that further limits their wide adoption. The very recent progress made on *Quantum Cascade Laser* (QCL) and *Quantum Cascade Detector* (QCD) brought a new interest to the LWIR spectral band [12, 19]. Yet QCLs are hardly the only product to have reached commercial maturity in this spectral band, even though some QCDs are commercialized in the MWIR band. There also exist many commercial detectors, such as MCT detectors, but those are not very adapted to high-speed telecommunications, as will be discussed in chapter 5. The development of passive components and their integration with QCL sources in the LWIR spectral range has attracted renewed interest [20, 21, 22], while other components such as external modulator, optical amplifier, polarization rotators and isolator have yet not been reported.

The work pursued in this thesis is part of a European H2020 project, the cFLOW project[1], whose aim is to develop a fully integrated platform for FSOC in the LWIR spectral band, composed by an emitter and a receiver photonic integrated circuits. The main goal is to demonstrate coherent communications at a wavelength of 9.1 µm with data-rates above 20 Gbit/s over a 5 km distance at first. The emitter is composed of a QCL, a phase modulator and a semiconductor optical amplifier heterogeneously integrated in a common platform, while the receiver is composed of a QCL, a semiconductor optical pre-amplifier, a passive beam combiner and a quantum cascade detector that will be monolithically integrated on the same chip. A schematic of such integrated emitter and receiver is shown, as an example of a possible integration, in Figure 1.6. In this work, we focus on the design, fabrication and characterization of the modulator, the passive beam combiner and the detector.

In a second chapter, we will present a theoretical background of laser based optical telecommunications, together with the materials and quantum well optical properties, and the framework of guided optics used in the thesis. In particular, the dielectric constant in the LWIR domain of relevant materials used in this work, and the experimental methods employed to retrieve them, will be discussed.

The third chapter will be about the theory and design of Multi Mode Interferometers (MMIs), which will be key building blocks employed as beam splitters and combiners for the development of the heterodyne coherent receiver, and the modulators in a Mach-Zehnder configuration. We will present their design procedure and fabrication, before detailing the experimental performance obtained using a dedicated characterization setup developed in the framework of this

[1] https://cflow-project.eu/

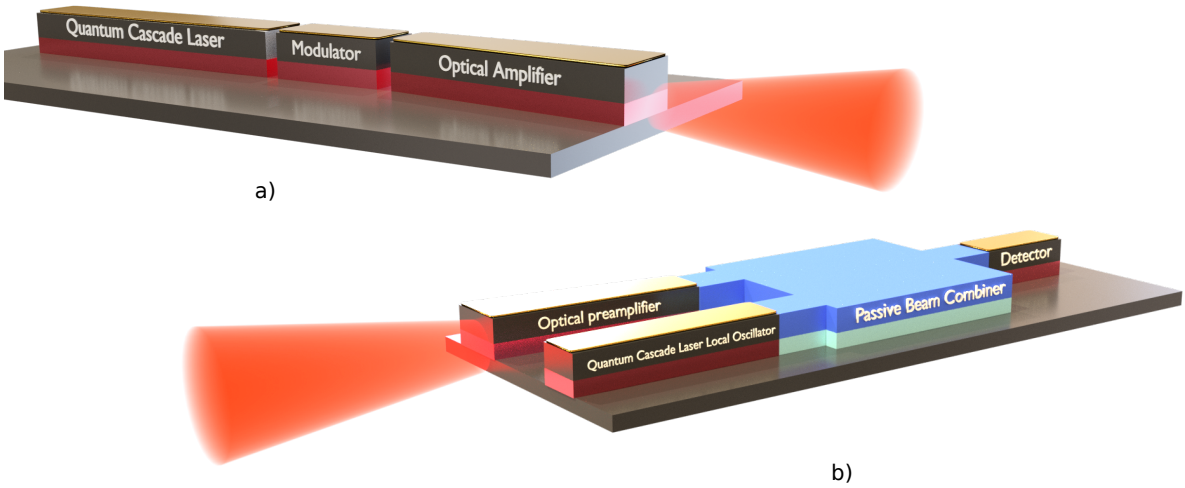

Figure 1.6: a) Artistic view of a possible integration approach for a) coherent emitter PIC integrating a QCL, modulator and a semiconductor optical amplifier. b) The heterodyne coherent receiver PIC, with optical amplifier, local oscillator QCL, QCD and beam combiner.

work. A more general discussion of available waveguide geometries together with the achieved performance in terms of optical losses in a photonic integrated platform will be provided, as well as solutions to model and limit them.

Following the whole theoretical and experimental background introduced in the previous two chapters, the fourth chapter will focus on the modulator development, the most challenging component designed during this thesis. Before providing a detailed description of its design, we will present a theoretical description of the main possible physical effects that can be used for optical modulation, and a state-of-the-art of optical modulation performance achieved in the SWIR and the LWIR optical ranges. The integration strategy followed, and its implications on the fabrication process will then be discussed, before presenting the electro-optical characterization of the fabricated components. We will in particular show a demonstration of an electrically driven waveguide optical phase and amplitude modulator in the LWIR.

In the final chapter, the QCD for the receiver, fabricated and characterized during this work, will be presented after having introduced the theoretical background about their design. On a second part, the design and measured performances of a 90° hybrid MMI will be presented, as well as the perspectives which these developments open toward a fully integrated I/Q coherent receiver.

Chapter 2

Theoretical foundations of optical telecommunications and semiconductor optical properties

Objectives

In this chapter, we introduce some basis of laser-based optical telecommunications. Information encoding on a monochromatic light beam is discussed and the main modulation formats are described. One of the main limitations for data transmission is represented by the additive white Gaussian noise. In this chapter, its impact on the channel capacity is briefly discussed and the theoretical bit error rate achievable on the main coherent modulation formats of interest for this work are also compared. In the second part of the chapter, the optical properties of the semiconductor compounds and dielectric materials relevant for optical communications in the Long Wave InfraRed (LWIR) window are presented. Experimental measurements performed on bulk materials and multi-quantum wells systems are compared with theoretical models, to retrieve the optical parameters of interest. These have been subsequently employed to design the devices presented in the following chapters, and based on the optical waveguide framework, extensively used throughout this thesis.

Contents

1 Optical telecommunications

In this first part, we will discuss the basis of the transmission of information encoded on optical signals. Most of the concepts here presented can also be found in [23]. For this purpose, we consider a general optical telecommunication system composed by a transmitter (on one side), which sends the optical signals through a propagating medium (the transmission channel), and a receiver (on the other side). In a general case, the transmission can be bidirectional, with transmitter and receiver modules present at both ends of the telecommunication link. On the emitter side, the generation of the light beam is generally made by a coherent source, for example a semiconductor-based laser. The information can thus be encoded onto the light beam either by direct modulation of the laser emission (for instance, by directly modulating the current of an electrically driven semiconductor laser), or by using an external optical modulator, which modulates the continuous-wave (CW) output of the laser injected through it. In this thesis, we focus on externally modulated laser, as the direct modulation of a laser produces a slight change of its wavelength which can be detrimental for phase-based modulation formats. The modulated signal can eventually be amplified and sent through the transmission channel (optical fibres, semiconductor waveguides, free space, etc...).

At the other end of the transmission channel, the optically modulated light beam reaches the receiver module, where it can be re-amplified before being detected. It is then decoded by either direct detection on a photodiode in the case of amplitude modulated signal, or by a coherent receiver, in the case of phase based modulation format.

1.1 Modulation formats, encoding information on light

As seen before, an optical telecommunication system uses light as a carrier. In modern laser-based telecommunications, the light is a monochromatic electric field E. Four degrees of freedom can in principle be used to encode information:

$$\vec{E} = E_0 cos(\omega t + \phi)\vec{u}_p$$

- The amplitude E_0.
- The carrier wavelength λ or frequency $\omega = 2\pi c/\lambda$ with c the vacuum velocity of light. This is the "colour" of the light
- The phase ϕ.
- The polarization, this is the orientation of the electromagnetic field $\vec{u}_p$. We can distinguish Transverse Electric (TE) or Transverse Magnetic (TM) orthogonal linear polarizations states.

Contrarily to the radio-frequency domain, fast switching of the wavelength of a laser is generally not convenient and actually quite difficult to achieve. The same is also true for the polarization state of the light. Therefore, these two degrees of freedom are generally reserved for multiplexing purposes.

Amplitude modulation, on the other hand, has been the main way of encoding information on a light beam and is often refereed as *Amplitude Shift Keying* (ASK) modulation. The most classical and natural way to encode information is to switch the optical carrier between two states: ON and OFF. This can be achieved by different means and it does not necessarily imply switching the optical signal on and off, but rather between two discrete levels. This modulation format is called *On-Off Keying* (OOK), where the modulation is performed by simply changing the signal amplitude between the two levels, one of which is set to zero. In this case, the two states (On and Off) are then defining two symbols of 1 bit each, as represented in Figure 2.1. The data transmission speed, which is called the symbol rate or baud rate, and measured in symbols per second, is in that particular case equal to the modulation frequency, as one bit per symbol is used. The amplitude modulated signal is a sinusoidal wave of varying step amplitude that oscillates at the carrier frequency (in practice several orders of magnitude greater than the modulation frequency). The constellation diagram, which is a visual representation of the modulated signal symbol states in the complex plane, is presented on the right side of Figure 2.1. It presents the "0" symbol at the origin and the "1" symbol on the unitary circle and real axis intersection (the amplitude is normalised). In the presence of noise sources in the telecommunication system, either on the phase or on the amplitude of the modulated signal, the position of the symbols in the constellation diagram will be less clearly defined. This results in a "cloud" of points around the theoretical positions, which represents the dispersion of the decoded bits, as shown in Figure 2.1b. From that, it can be easily understood that the more spaced the symbols on the constellation diagram, the more robust the modulation format is against additive noise. In the following part, we will introduce the different modulation formats used in lasers-based optical telecommunication systems and will discuss their impact on the link capacity.

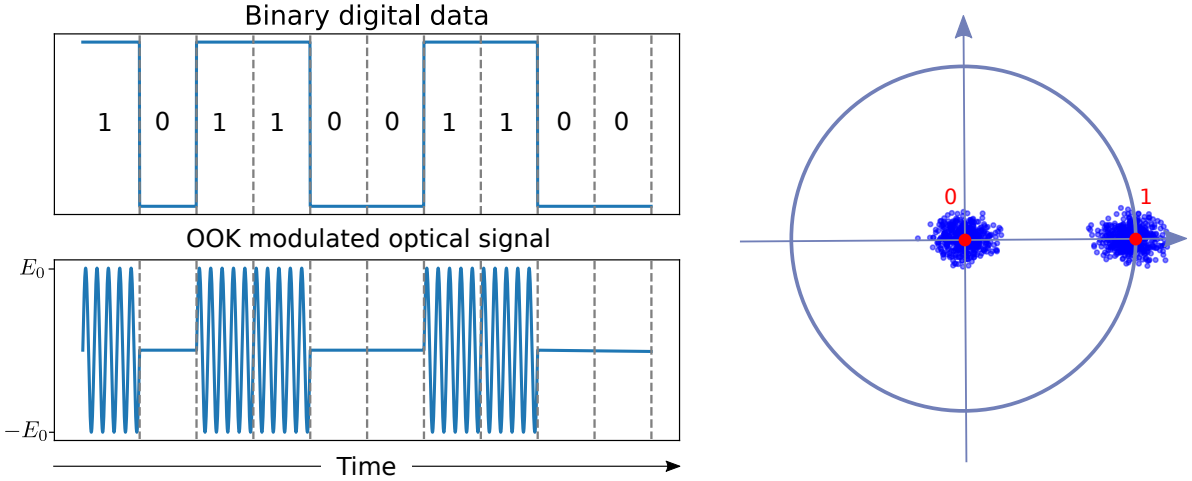

Figure 2.1: Left : Binary digital data to be encoded on the optical carrier and resulting OOK encoded signal. Right : Constellation diagram of an ideal OOK modulation format. Amplitude and phase noises result in received stated that form a "cloud" around the ideal symbol position.

The second type of modulation consists in encoding the information on phase shifts, this

way of encoding is refereed as *Phase Shift Keying* (PSK). The equivalent two symbols in phase modulation format to OOK is the *Binary Phase Shift Keying* (BPSK) in which a π phase shift is used to encode for either a "0" or "1" bit. Such a modulation is represented in Figure 2.2. As can be seen on its constellation diagram, the euclidean distance between both symbols is twice as much as it is in the OOK modulation format. Therefore, a much more robust communication, regarding noises, is to be expected with that modulation format. On the other hand, PSK modulation format require being able to measure the phase of the received modulated signal to decode the information. That cannot be done with the use of a single photodiode and requires the use of interferometry with a local oscillator laser and balanced photodiodes, as represented in Figure 2.4. Coherent communication links also requires the use of laser with very thin linewidth to work properly [24].

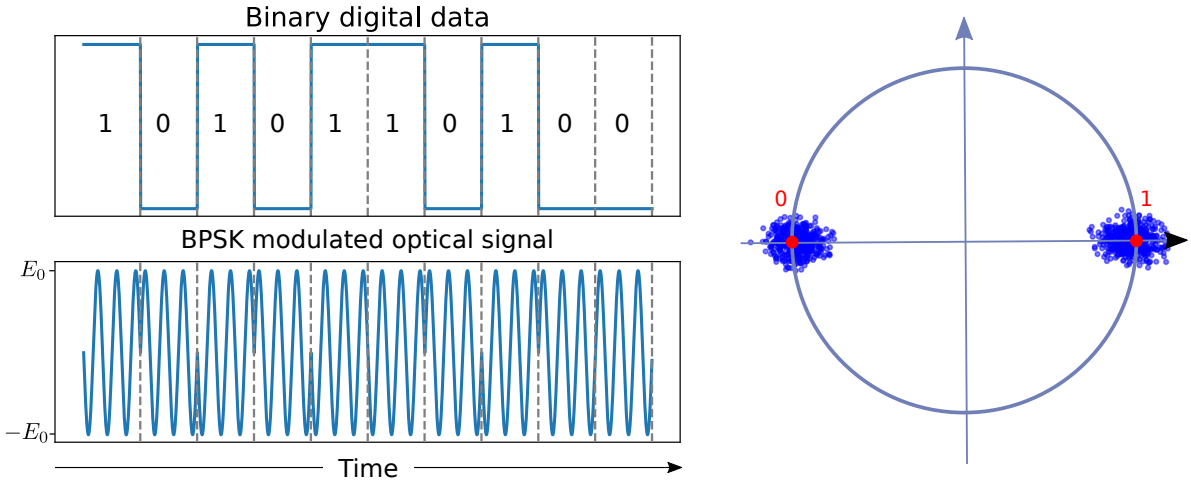

Figure 2.2: Left : Binary digital data to be encoded on the optical signal and resulting encoded BPSK signal. Right : Constellation diagram of an ideal BPSK modulation format. Amplitude and phase noises result in received stated that form a "cloud" around the ideal symbol position.

When the noise is not a limiting factor in the telecommunication link, one can use more advanced modulation format with multi-level encoding to increase the number of bits per symbol. Thus, transmitting at a higher bit-rate for a same baud rate or modulation frequency. With 4 symbols, two bits per symbol are transmitted, hence doubling the bit rate by only changing the modulation format. This can be done with either four phase amplitude levels (PAM4 or 4ASK), four phase levels (QPSK) or two phase and two amplitude levels (2ASK-2PSK). Then each power of two symbols (16, 32, 64 etc...) can be addressed by multiple quadrature amplitude phase modulation (MQAM) formats. Those are modulation formats where the symbols on the constellation diagram are arranged in a square lattice, thus an optimised euclidean distance between each symbol, which implies a higher robustness to noise. Hexagonal MQAM modulations formats are also an even better solution, regarding their higher robustness to noise, than square MQAM (as the inter-symbol euclidean distance is higher). However their practical implementation has been limited due to their inherent difficult compatibility with binary data system as the number of symbol in the constellation is, strictly speaking, not a power of two [25]. Moreover,

hexagonal MQAM requires complex modulator design [26] even though recent results tend to demonstrate the possibility of using, nowadays mature, I/Q modulators to generate them but at the cost of a more complex electrical driving [27]. An example of square 16QAM is presented on the right of Figure 2.3.

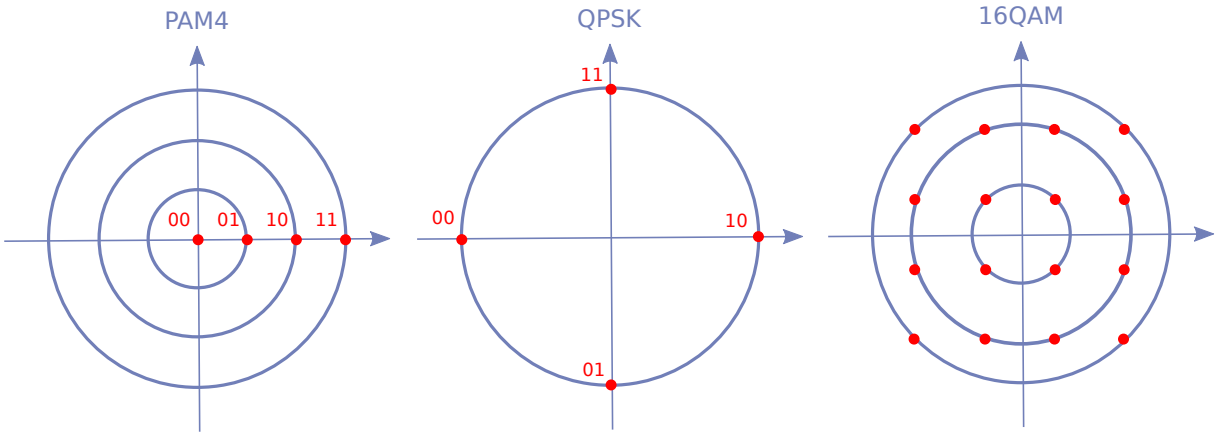

Figure 2.3: Examples of constellation diagrams of advance modulation format. The first two have 2 bits per symbol while the right one has 4.

Then wavelength division multiplexing, polarisation multiplexing or spatial mode division multiplexing can be used to increase furthermore the capacity of an optical telecommunication link. Now we have grasped the importance of the consideration of noise and the impact it might have on different modulation formats.

As we will see in the next part, coherent modulation formats, potentially combining both phase and amplitude modulation such as square MQAM, are more robust than simply ASK in the presence of noise sources. That is the main reason for our interest in them for a free-space LWIR telecommunication link. The most versatile and nowadays most developed implementation of such coherent transceivers is presented on Figure 2.4. The external modulation of the laser is performed in two parallel Mach-Zehnder interferometers in push-pull mode. The top Mach-Zehnder encodes the in phase (I) modulation part while the bottom one, to which a $\pi/2$ phase shift is added, encodes for the in quadrature (Q) part. Their combination provides access to the whole square MQAM constellation. On the receiver side, a local oscillator laser (LO) is generally used as a phase reference to decode the phase modulated signal, and a 90° hybrid photo-mixer used with balanced photodiodes to decode the signal.

The next part focuses on the capacity of an optical telecommunication link with different coherent modulation formats accessible by those typical I/Q modulators, as the main goal of this thesis is toward coherent free-space telecommunications.

1.2 Channel capacity and BER

In the above, we have said that the further the distance between symbols in the constellation diagram of a modulation format, the more robust to noise the communication will be. The ultimate limitation of this, error-free communications, is given by the Shannon-Hartley theorem.

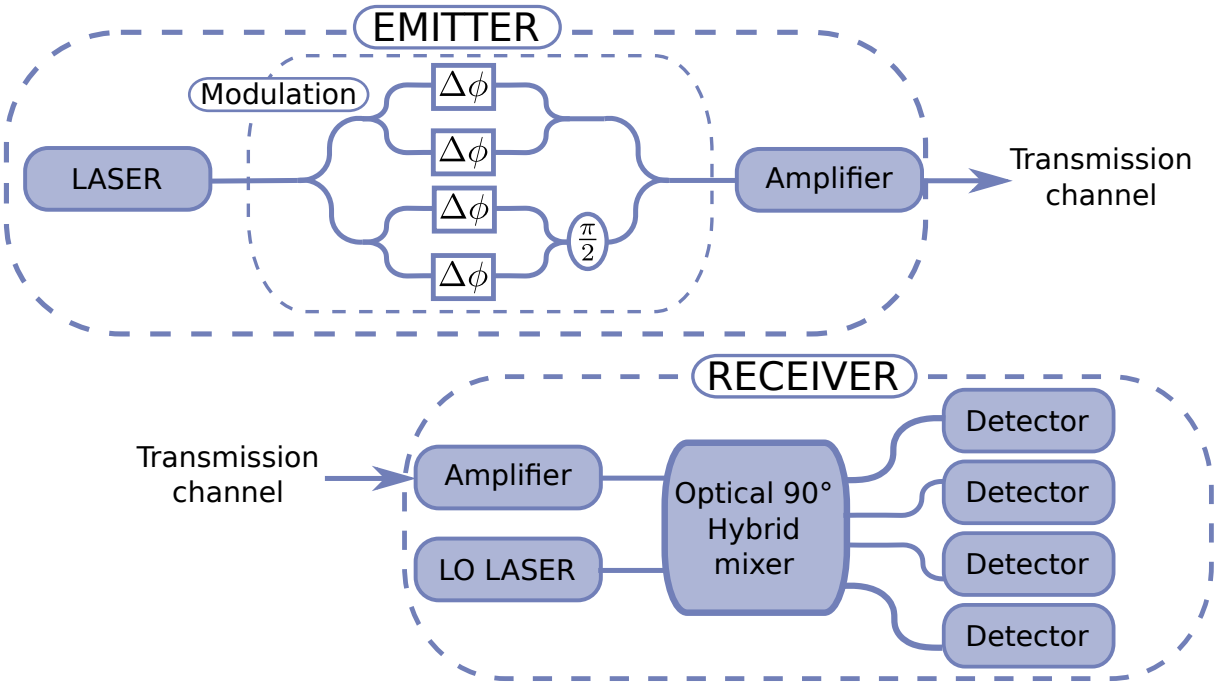

Figure 2.4: Scheme of a coherent emitter-receiver optical communication link. The emitter is composed of a laser, a modulation part often based on 4 phase modulators in two disctinc waveguide Mach-Zehnder interferometers and an amplifier. The receiver is generally formed of an amplifier, a local oscillator (LO) laser, a 90° hybrid optical mixer and 4 balanced photodiodes for the demodulation.

This theorem states that the ultimate capacity of a noisy channel (with an *Additive White Gaussian Noise* (AWGN)) depends both on the bandwidth B of the channel and the signal-to-noise ratio per symbol SNR_s of the receiver signal as [28] :

$$\mathcal{C} = B \log_2 (1 + SNR_s) \tag{2.1}$$

Therefore, increasing the capacity of a telecommunication link can be made either by increasing the system bandwidth or by increasing its *Signal to Noise Ratio* (SNR) per symbol. The noise sources should also be minimised if possible. They are mainly four types of noise sources limiting the SNR of a coherent receiver that are discussed in [29, 30] : the beating AWGN from the laser LO and amplifier, the photodetector shot and thermal noise and the channel noise. In general, the limiting noise source will be the beating AWGN noise. Such noise will create a dispersion of the received demodulated signal state around their ideal value, as shown by the "clouds" in Figure 2.1 and Figure 2.2 constellation diagrams. The lower the signal-to-noise ratio, the bigger the clouds will be, to an extent where some detected bits will potentially be wrongly detected as another. The probability of a wrongly detected bit is given by the so-called *Bit Error Rate* (BER) and it symbols equivalent, the *Symbol Error Rate* (SER). There exist multiple analytical formulas approaching the ultimate limit of AWGN noise limited BER for the different coherent modulation format [23, 31, 32]. We hereby recall the derivation of that of BPSK modulation format to give the ideas behind it.

BPSK BER : In BPSK modulated signal, one detected signal y can have two discrete values $x = \pm\sqrt{E_s} \propto E_0$ (where E_s is the symbol energy) to which is superimposed an additive white Gaussian noise of variance σ^2, characterizing the link noise, $n = \mathcal{N}(0, \sigma^2)$.

The probability $P(y)$ to receive a bit of energy value y is shown in Figure 2.5. The decision threshold between a y value interpreted as a "1" or a "0" bit is defined by the vertical axis $y = 0$. For positive values $y > 0$ a bit "1" will be interpreted, while for $y < 0$ it will be a bit "0". The probability of a symbol interpretation error P_s is thus defined by the sum :

$$P_s = P(y < 0|x = E_s) + P(y > 0|x = -E_s) \tag{2.2}$$

Under the assumption of an equally probable "1" and "0" emitted bit, the above equation reduces to the following, and the integral terms are represented as shaded area on Figure 2.5 :

$$P_s = 0.5\int_{0}^{+\infty} \frac{1}{\sqrt{2\pi}\sigma} e^{-\frac{(x+\sqrt{E_s})^2}{2\sigma^2}} dx + 0.5\int_{-\infty}^{0} \frac{1}{\sqrt{2\pi}\sigma} e^{-\frac{(x-\sqrt{E_s})^2}{2\sigma^2}} dx \tag{2.3}$$

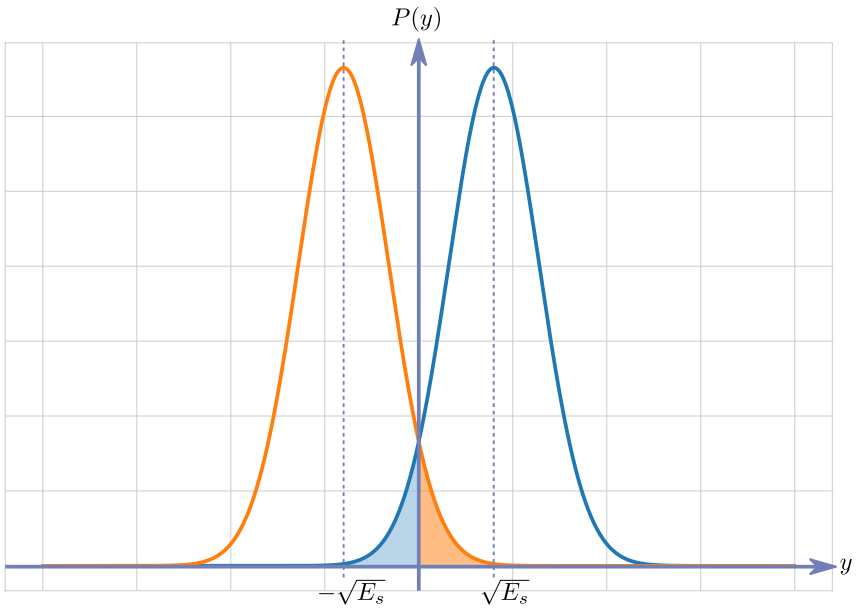

Figure 2.5: Power density probability function of a received signal with AWGN.

It can easily be shown that both the orange and blue terms in Equation 2.3 are equal, and that their values are defined in terms of the $\mathcal{Q}$ function :

$$P_s = \mathcal{Q}(\frac{\sqrt{E_s}}{\sigma}) \tag{2.4}$$

Since the distance between two symbols in the constellation diagram is $2\sqrt{Es}$ for BPSK modulation format, the signal-to-noise ratio per symbol (that is equal to the signal ratio per bit in that case) is equal to $SNR_s = E_s/2\sigma^2$. Therefore, for BPSK modulation format, the bit

error rate writes in AWGN limited channel writes as :

$$BER = \mathcal{Q}(\sqrt{2SNR_b}) \tag{2.5}$$

BER of other coherent modulation format : Similarly to the above derivation, other semi-analytical formulas can be derived for other kind of modulation formats and are found in various books [32, 31]. Those are presented in Figure 2.6.

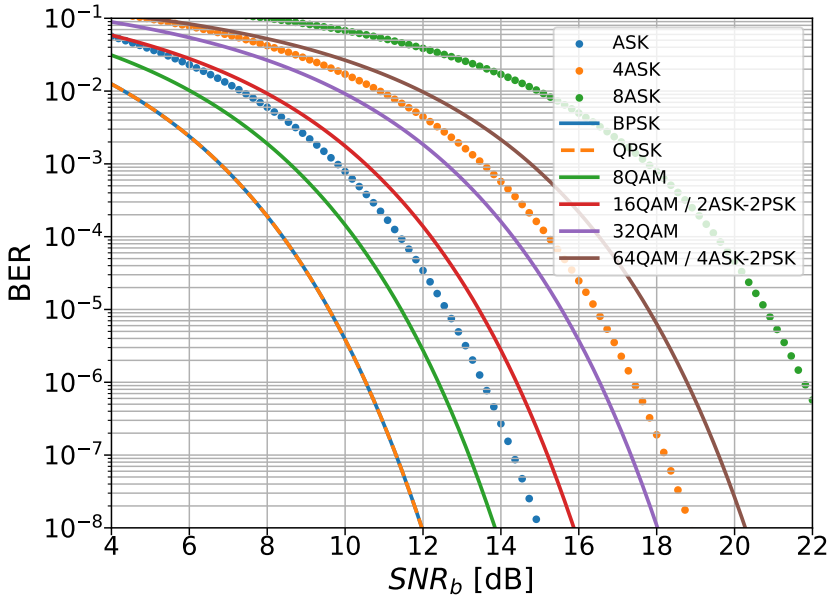

Figure 2.6: BER versus SNR per bit for different coherent modulation format [33, 23].

One can see that at a given signal-to-noise ratio per bit, the lower order modulation format (the ones having less bit per symbol) will produce fewer errors (except for QPSK/BPSK), and even more for a partly in phase modulation format (PSK). Moreover, at a given modulation order, the multiple QAM format outperforms their PSK counterpart, and themselves their ASK counterpart, as is visible in the comparison between (8PSK and 8QAM). That is due to the higher distance between symbols in their constellation diagram, leading to a higher robustness to noise. Those considerations made the mQAM very popular high order modulation format at telecom wavelength (1.3, 1.55 µm). Then after detection, some forward error correction code can be used as well as digital signal processing to increase the data rate of a system but at the cost of added latency. Those are discussed for example in [23] and will not be discussed in this thesis.

Now that we have discussed information encoding on a light beam, one has to introduce the way this encoding is performed in practice. To that end, we exclusively consider photonic integrated circuits as they are the main building blocks of modern laser-based telecommunication systems. The next part will therefore focus on the optical properties of semiconductors and dielectrics and their usage in optical waveguides for photonics circuits.

2 Optical properties of semiconductors

In the present section, we focus on the formalism of optical waveguide and semiconductor theory. We will start by presenting how waves propagates in a medium together with the optical properties of semiconductor materials before diving in more details into quantum well optical properties and waveguide optics. This section is based on the book on semiconductor properties from Yu and Cardona and the course on nano-photonics from Novotny [34, 35].

2.1 Optical wave propagation in homogeneous media

2.1.1 Material susceptibility

When a light beam impinges on the intersection between two different materials (independently of the nature of those materials) it will undergo different transformations. Part of it can be transmitted in the other material or reflected at the interface. Some will have been absorbed or scattered by different mechanisms in the incident material before reaching the interface, and will be absorbed and scattered in the other material too. The interactions and transformations undergone by an optical beam propagating in a homogeneous medium can be well described in terms of the spectral response of the media. We therefore will use the harmonic description of the optical electrical field, which will greatly simplify the notations without loss in generality. Indeed, any optical electrical field $\mathbf{E}(\mathbf{r},t)$, as it is a real and measurable quantity, can be described by a continuous sum of monochromatic plane waves under Fourier formalism :

$$\hat{\mathbf{E}}(\mathbf{r},\omega) = \frac{1}{2\pi}\int_{-\infty}^{+\infty} \mathbf{E}(\mathbf{r},t)e^{j\omega t}dt \tag{2.6a}$$

$$\mathbf{E}(\mathbf{r},t) = \int_{-\infty}^{+\infty} \hat{\mathbf{E}}(\mathbf{r},\omega)e^{-j\omega t}d\omega \tag{2.6b}$$

In the above equations, $\mathbf{r}$ is the position vector, ω the optical pulsation of the electrical field. An incident electrical field $\hat{\mathbf{E}}(\mathbf{r},\omega)$ on a media will induce a local response[1] from the media which is macroscopically described by the induced polarization field $\mathbf{P}$. In the case we consider, a linear homogeneous material, the induced polarization writes :

$$\hat{\mathbf{P}}(\mathbf{r},t) = \varepsilon_0\chi(\omega)\hat{\mathbf{E}}(\mathbf{r},\omega) \tag{2.7}$$

χ is the macroscopic electric susceptibility tensor describing the linear response of the material. In all generality, it is a 3 $\times$3 matrix, but in the practical cases in this thesis which are homogeneous materials, this tensor is composed of 3 diagonal terms which are equals for isotropic materials. The electrical displacement vector then writes as :

$$\hat{\mathbf{D}}(\omega) = \varepsilon_0\left(\mathbb{1} + \chi(\omega)\right)\hat{\mathbf{E}}(\omega) \tag{2.8}$$

The term $\mathbb{1} + \chi(\omega)$ is commonly refereed to, as the effective dielectric tensor of the material ε_r,

[1] We assume only a local response of the media as non local dispersion is negligible in the application we are interested in [34]

and completely defines the linear macroscopic optical response of the material.

Similarly, a magnetic susceptibility tensor can be defined to model the response of the material to an external magnetic field, but at optical frequencies it is close to zero for natural materials. Therefore, we will neglect it in the following. The magnetic field is then linked to the magnetic induction field by the following relation :

$$\hat{\mathbf{B}}(\omega) = \mu_0 \hat{\mathbf{H}}(\omega) \tag{2.9}$$

where μ_0 is the vacuum permeability. Therefore, from the knowledge of the relative permittivity of a material, any light beam propagation in the media can be modelled as will be presented in the next paragraph.

2.1.2 Maxwell equations and wave propagation

The classical field description based on Maxwell's equation is the starting point to describe optical wave propagation in an arbitrary media. In the spectral representation of the electrical field, they write as follows :

$$\boldsymbol{\nabla} \times \hat{\mathbf{E}}(\mathbf{r}, \omega) = j\omega \hat{\mathbf{B}}(\mathbf{r}, \omega) \tag{2.10a}$$

$$\boldsymbol{\nabla} \times \hat{\mathbf{H}}(\mathbf{r}, \omega) = -j\omega \hat{\mathbf{D}}(\mathbf{r}, \omega) + \hat{\mathbf{J}}(\mathbf{r}, \omega) \tag{2.10b}$$

$$\boldsymbol{\nabla} \cdot \hat{\mathbf{D}}(\mathbf{r}, \omega) = \hat{\rho}(\mathbf{r}, \omega) \tag{2.10c}$$

$$\boldsymbol{\nabla} \cdot \hat{\mathbf{B}}(\mathbf{r}, \omega) = 0 \tag{2.10d}$$

$$\tag{2.10e}$$

The combination of both equations Equation 2.10a and Equation 2.10b leads to the wave equation, also called the Helmholtz equation, that describe the propagation of waves in an arbitrary homogeneous media :

$$\boldsymbol{\nabla}^2 \hat{\mathbf{E}}(\mathbf{r}, \omega) - \boldsymbol{\nabla}\left(\boldsymbol{\nabla} \cdot \hat{\mathbf{E}}\right)(\mathbf{r}, \omega) + \frac{\omega^2}{c^2} \hat{\mathbf{D}}(\mathbf{r}, \omega) = 0 \tag{2.11}$$

where c is the vacuum speed of light. General solutions of this equation are found in the form of harmonic plane wave. Every component ($\hat{\mathbf{E}}$, $\hat{\mathbf{D}}$, $\hat{\mathbf{B}}$, $\hat{\mathbf{H}}$) of the optical field will then be written as :

$$\hat{\mathbf{U}}(\mathbf{r}, \omega) = \hat{\mathbf{U}}_\mathbf{0} e^{j(\omega t - \mathbf{k}\cdot\mathbf{r})} \tag{2.12}$$

with $\hat{\mathbf{U}}_\mathbf{0}$ the complex amplitude of the optical field component and $\mathbf{k}$ its wave vector. When looking for the solutions of the waves propagating in a media, $\mathbf{k}$ is the eigenvalue of the solution to the Helmholtz equation that we are looking for and $\hat{\mathbf{U}}_\mathbf{0}$ its corresponding eigenvector. In a given material of permittivity ε_r this wave vector will always verify that $|\mathbf{k}|^2 = 2\pi\varepsilon_r/\lambda$. The value of the projection of the wave vector along the $\vec{z}$ axis, k_z, will characterize the propagation along that axis. Its real value will define the phase velocity of the propagating wave along $\vec{z}$ and its imaginary value, its linear attenuation. In any homogeneous media, causality implies that the real and imaginary part of the relative dielectric constant (ergo the wavevector norm) are

linked to each other by the so called Kramers-Kronig relations [36]:

$$\varepsilon'_r(\omega) - 1 = \frac{2}{\pi}\mathcal{P}\int_0^{+\infty} \frac{\omega'\varepsilon''_r(\omega')}{\omega'^2 - \omega^2} d\omega' \tag{2.13a}$$

$$\varepsilon''_r(\omega) = -\frac{2\omega}{\pi}\mathcal{P}\int_0^{+\infty} \frac{\varepsilon'_r(\omega')}{\omega'^2 - \omega^2} d\omega' \tag{2.13b}$$

where ε' and ε'' are respectively the real and imaginary part of the relative dielectric constant and $\mathcal{P}$ refers to the Cauchy principal value.

2.1.3 Birefringent material and induced anisotropy

In the above, we only treated the propagation in isotropic material where the dielectric tensor is diagonal with one eigenvalue of multiplicity 3. This allows the treatment of most of the materials, and particularly III-V centrosymmetric materials and amorphous dielectrics used in this thesis. But when structured into thin sub-wavelength layers, a material can present an anisotropic macroscopic effective dielectric constant. It is the case for quantum well structures which are at the core of the QCL and QCD devices that will be used in this work. These quantum well structures present an uniaxial anisotropy with one component of the permittivity tensor different from the other two (as will be seen further in this chapter) :

$$\varepsilon_r = \begin{pmatrix} \varepsilon_o & 0 & 0 \\ 0 & \varepsilon_o & 0 \\ 0 & 0 & \varepsilon_e \end{pmatrix} \tag{2.14}$$

In that case, the Helmholtz equation has two non-trivial eigenvalues for k which are solutions to the following equation [37] :

$$\left[k_0^2\varepsilon_o - |\mathbf{k}|^2\right]\left[k_0^2\varepsilon_e - (k_x^2 + k_y^2 + \frac{\varepsilon_e}{\varepsilon_o}k_z^2)\right] = 0 \tag{2.15}$$

where $k_0 = 2\pi/\lambda$. The first solutions to Equation 2.15 are the wavevectors whose norm squared is a sphere of radius $k_0^2\varepsilon_o$ (for both real and imaginary value). The second solutions are wavevectors whose norm squared is an ellipsoid of radius $k_0^2\varepsilon_o$ in the $(\vec{x}, \vec{y})$ plan and $k_0^2\varepsilon_e$ along the $\vec{z}$ axis. Any wave propagating along the $\vec{z}$ axis will then only be sensitive to ε_o and its electrical field be in the plane $(\vec{x}, \vec{y})$ thus called the TE polarised wave. Any other incident angle will split the wave into two polarization states that are either sensitive to the ε_o for the ordinary wave or to an effective dielectric permittivity in between ε_o and ε_e, which depends on the incident angle. Only a wave propagating along the $\vec{z}$ axis will "effectively see" the same dielectric constant for both TE and TM polarization, ergo the name "uniaxial" media. There exist all kinds of anisotropic media such as biaxial crystals, and it is even possible to progressively transition from one to another by applying, for example, a pressure along one axis. Abundant literature exists in this domain and the interested reader can refer to the following references [38, 39].

2.2 Optical waveguides

2.2.1 Reflection at a planar interface

In all the above, we presented the fundamentals equations describing the propagation of an optical wave in a single homogeneous media. When a beam impinges on the interface between two different materials, those are not sufficient to fully describe what happens, and continuity relations are needed. Those can be derived from Maxwell equations themselves and are given in all generality as [40] :

$$\hat{\mathbf{E}}_{\mathbf{t1}} - \hat{\mathbf{E}}_{\mathbf{t2}} = 0 \tag{2.16a}$$

$$\hat{\mathbf{B}}_{\mathbf{t1}} - \hat{\mathbf{B}}_{\mathbf{t2}} = 0 \tag{2.16b}$$

$$\hat{\mathbf{D}}_{\mathbf{n1}} - \hat{\mathbf{D}}_{\mathbf{n2}} = \rho_s \mathbf{n_{12}} \tag{2.16c}$$

$$\mathbf{n_{12}} \wedge (\hat{\mathbf{B}}_{\mathbf{t2}} - \hat{\mathbf{B}}_{\mathbf{t1}}) = \mu_0 \mathbf{j_s} \tag{2.16d}$$

$$\tag{2.16e}$$

The subscript "t_i" and "n_i" respectively means tangent to the interface and normal to the interface between the mediums i and j and in the media i. The vector $\mathbf{n_{12}}$ is the vector normal to the interface between media 1 and media 2 and oriented toward media 2. ρ_s and $\mathbf{j_s}$ are respectively the surface density of charges and surface current vector. In practice, $\mathbf{j_s}$ is null for all real material having a finite conductivity. The planar geometry of the interface considered in the above, as well as the different notations introduced, are presented in Figure 2.7 for both polarization states of the incident wave.

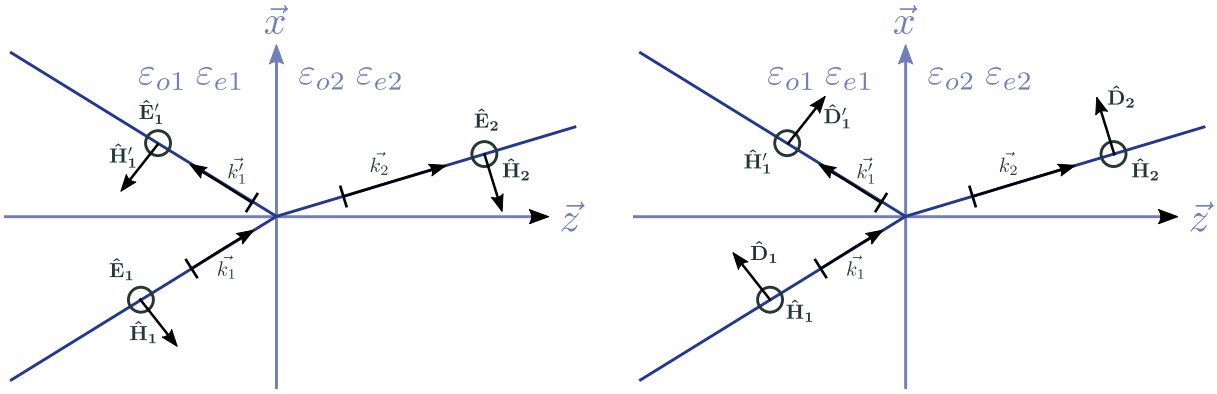

Figure 2.7: Vectorial configuration of the electromagnetic field (a) for a TE polarization, (b) for a TM polarization. The materials are in all generality uniaxial materials whose optical axis is along the $\vec{z}$ axis.

From Maxwell's equations Equation 2.10 and the continuity relations Equation 2.16 one can express the complex amplitude reflection coefficient at the interface between the media 1 and 2 for both TE and TM polarization (the notations and vectorial configuration of the fields are

presented in Figure 2.7).

$$r_{TE} = \frac{k_{z1} - k_{z2}}{k_{z1} + k_{z2}} \tag{2.17}$$

$$t_{TE} = \frac{2k_{z1}}{k_{z1} + k_{z2}} \tag{2.18}$$

$$r_{TM} = \frac{k_{z1}\varepsilon_{o2} - k_{z2}\varepsilon_{o1}}{k_{z1}\varepsilon_{o2} + k_{z2}\varepsilon_{o1}} \tag{2.19}$$

$$t_{TM} = \frac{2k_{z1}\varepsilon_{o2}}{k_{z1}\varepsilon_{o2} + k_{z2}\varepsilon_{o1}} \tag{2.20}$$

where k_{zi} is the z component of the wave vector $\mathbf{k_i}$, and is solution to the left-hand side of Equation 2.15 for the TE polarized wave ($\hat{\mathbf{E}}$ parallel to the interface) or to the right-hand side of Equation 2.15 for the TM polarized wave ($\hat{\mathbf{H}}$ parallel to the interface). From Equation 2.20 it can be seen that there exist, for a TM polarization, an angle of incidence ensuring total transmission of the incident wave that is solution to $k_{z1} = \varepsilon_{o1}/\varepsilon_{o2}k_{z2}$. This specific angle of incidence is called the Brewster angle. Similarly, it is possible to have no transmission at all and a fully reflected wave at a given angle for both TE and TM waves, provided that the dielectric constant of the incident media be greater than the one of the transmission media.

2.2.2 The planar multi-layer structure

In the above, we have discussed the problem of reflection at a single interface between two homogeneous media. Real structured materials, whether it is coatings, filters, waveguides or resonant cavities, are composed of many layers of different materials. It is then important to be able to calculate the reflection and transmission properties of such a structure. To that end, we will extend the above considerations to an arbitrary number of materials, and we consider a 3 layer system as a start with the central layer of thickness d_j. The reflection and transmission coefficients of such a system (from media i to media k, refer to Figure 2.8) can be calculated from the knowledge of the above single interface reflection and transmission coefficients (Equation 2.17 to Equation 2.20) as :

$$r_{ik} = \frac{\hat{E}_i^-}{\hat{E}_i^+} = \frac{r_{ij} + r_{jk}e^{2jk_{zj}d_j}}{1 + r_{ij}r_{jk}e^{2jk_{zj}d_j}} \quad t_{ik} = \frac{\hat{E}_k^+}{\hat{E}_i^+} = \frac{t_{ij}t_{jk}e^{jk_{zj}d_j}}{1 + r_{ij}r_{jk}e^{2jk_{zj}d_j}} \tag{2.21}$$

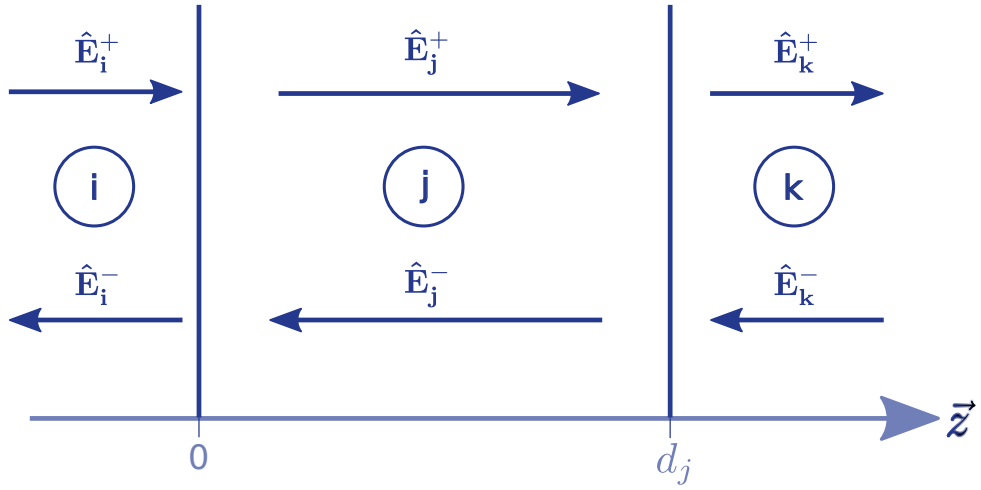

Figure 2.8: Notations used for the calculation of the reflection and transmission coefficient of a three layer planar structure. The amplitude of the electric field is used in the definition of the reflection and transmission coefficients.

In the above, the complex amplitudes $\hat{E}_i^+$ and $\hat{E}_i^-$ are the amplitudes of the propagating and contra-propagating waves in media i. They are scalar values that have to be multiplied to the unitary polarization vector to retrieve $\hat{\mathbf{E}}_\mathbf{i}^+$ and $\hat{\mathbf{E}}_\mathbf{i}^-$. From Equation 2.21 it is possible to calculate analytically the reflection and transmission coefficient of an arbitrary stack of homogeneous mediums by calculating the coefficients of the last three layers, then replacing the last two layers with an interface having the the previously calculated reflection and transmission coefficients, and repeating the process up to the first interface.

2.2.3 Planar optical waveguide mode solver

We have presented the equations driving the propagation of an optical beam in a multilayer structured planar material, and we have noted that propagation in a homogeneous media in a given direction is possible if and only if the component of the wave-vector in the direction of propagation has a non-null real part. In a multilayer planar structure as we consider here, we will call the direction of propagation the parallel direction and the in plane wave-vector amplitude real value $k_{/\!/}$.

Following the discussion about the solutions of the Helmholtz equation and the continuity relations Equation 2.15 Equation 2.16, a wave propagating in a given layer of relative permittivity ε_r (that we consider real and constant with respect to λ in the following discussion for simplicity but without loss of generality) will necessarily have a $k_{/\!/} \leq k_0\sqrt{\varepsilon_r}$. If that is not the case, the non parallel component of the wave vector k_z will necessarily have a pure imaginary value, therefore meaning a propagation along the parallel direction only without propagation in the other direction. The line $\hbar\omega = \hbar c/\sqrt{\epsilon_r}k_{/\!/}$ will then separate the domain of existence of a propagating solution to the Helmholtz equation in the parallel direction. Below that line, no propagation is possible in the media of relative permittivity ϵ_r alone. Above that line there is a continuum of solution of propagating wave-vector.

Defining a structure formed of a high dielectric constant media sandwiched between two

lower dielectric constant mediums gives the possibility to guide light in the central layer. The solutions for guided modes to the Helmholtz equation in that case are to be found in between the two light lines formed by the highest dielectric constant media and the highest dielectric constant of the two outermost media. Indeed, above the latest line (in red on Figure 2.9), a solution to the Helmholtz equation will propagate in at least one of the outer media, it is therefore not a fully guided mode. In the region below the light lines of all media, a hypothetical solution to the Helmholtz solution will not be a propagating wave in any of the media constituting the structure. Nevertheless, such solutions can exist, an example of which is surface plasmons polaritons, but those soluions are not the topic of this thesis.

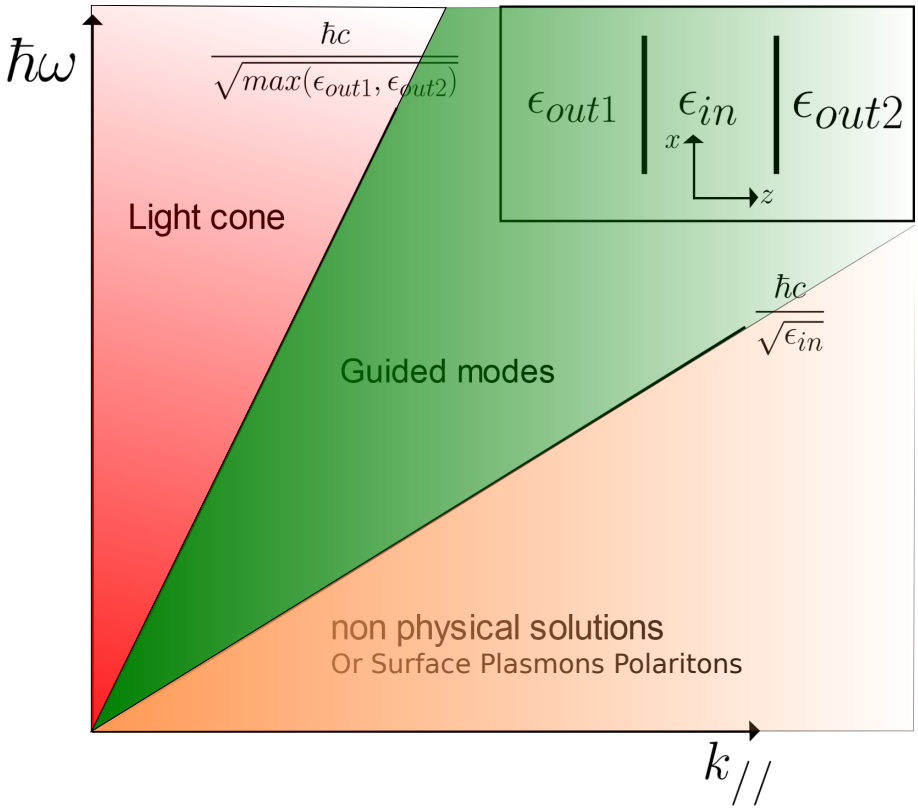

Figure 2.9: Light cone of a simple three layer planar waveguide.

How to find optical modes ? Having identified the regions of the light cone supporting optical guided modes in a planar structure, one has to be able to effectively calculate their propagation constant $k_{//}$ which completely defines them as they are eigenvalues of the Helmholtz equation and equal in every media constituting the structure. To that end, we consider the structure represented in Figure 2.8. A guided mode must satisfy the following conditions :

- **Total internal reflection** : no power must leak outside the waveguide.
- **Phase matching** : after one round trip in the guiding region, the propagating wave must constructively interfere with itself.

The above two conditions respectively imply that (we consider the fields amplitude to be taken on the right side of the interface z=0 and neglect any material absorption without loss of generality)

:

$$\hat{E}_j^+ = r_{ji}\hat{E}_j^- = r_{ji}r_{jk}e^{2jk_{zj}d_j}E_j^+ \Rightarrow \hat{E}_j^+\left(1 + r_{ij}r_{jk}e^{2jk_{zj}d_j}\right) = 0 \tag{2.22}$$

where k_{zj} is the transversal component of the wave vector in material j and solution to the Helmholtz equation, Equation 2.15. Solution to the above equation are values of k_{zj} that yield to the divergence of the Fresnel reflection and transmission coefficient Equation 2.21 of the structure. This has been demonstrated above in the case of a simple three-layer structure but is the case of a waveguide structure composed of an arbitrary number of layesr two, as discussed in the calculation of the reflection coefficient of any structure in subsubsection 2.2.2. The home-made optical mode solver in planar geometry used throughout this thesis relies on the calculation of the Fresnel coefficients of a given structure to find it's supported guided modes by looking at the divergence of them, and further optimise the structure afterwards.

Mode field distribution : Once an optical mode propagation constant $k_{/\!/}$ is found using the method described above (thus k_z can be calculated in every layer composing the structure using Equation 2.15), one has to calculate the field distribution and contributions to the optical losses, to optimise the waveguide structure. To that end, the *Transfer Matrix Method* (TMM) is used. This method is used in a wide range of physical domains which allows the calculation of wave functions decomposed in the form of a propagative and contra-propagative plane waves and therefore particularly adapted to the calculation of optical modes in a waveguide.

$$\hat{E}_j(z) = \hat{E}_j^+ e^{-jk_{zj}z} + \hat{E}_j^- e^{jk_{zj}z} \tag{2.23}$$

Let us consider again the fields represented in Figure 2.8. In a homogeneous layer, the amplitude of both waves on the left side are linked to the amplitude of the waves on the right side by a propagation matrix as (in layer j for instance) :

$$\begin{pmatrix} \hat{E}_j^+(0) \\ \hat{E}_j^-(0) \end{pmatrix} = \begin{pmatrix} e^{jk_{zj}d_j} & 0 \\ 0 & e^{-jk_{zj}d_j} \end{pmatrix} \begin{pmatrix} \hat{E}_j^+(d_j) \\ \hat{E}_j^-(d_j) \end{pmatrix} \tag{2.24}$$

Then passing from one side of an interface to the other, a transfer matrix is used, such as for the interface between media i and j, with r_{ij} and t_{ij} the amplitude reflection coefficients from Equation 2.17 to Equation 2.20 :

$$\begin{pmatrix} \hat{E}_i^+(0) \\ \hat{E}_i^-(0) \end{pmatrix} = \begin{pmatrix} \frac{1}{t_{ij}} & \frac{r_{ij}}{t_{ij}} \\ \frac{r_{ij}}{t_{ij}} & \frac{1}{t_{ij}} \end{pmatrix} \begin{pmatrix} \hat{E}_j^+(0) \\ \hat{E}_j^-(0) \end{pmatrix} \tag{2.25}$$

Using fixed boundary conditions with an arbitrarily chosen value of the amplitude of the propagative wave and no contra-propagative wave in the last layer (as there can't be a reflected wave from infinity), one can successively iterate the matrix products presented in Equation 2.25 and Equation 2.24 to calculate the field amplitude on both sides of each interface composing the structure. Anywhere in the structure, the field distribution can then be calculated using Equation 2.23

Optical absorption decomposition : In the above paragraph, we have seen how it is possible to calculate the field distribution in a waveguide structure from the knowledge of the mode propagation constant $k_{//}$. The optimisation of a given waveguide, whether it is an active photodiode, modulator or passive waveguide relies on the ability to identify the different sources of losses in the waveguide. Such a decomposition is possible from the field distribution, and detailed discussion are available in [41, 42] whose main results are recalled below. We consider an optical mode whose propagation constant is $k_{//} = \beta + j\alpha/2$. Each material i composing the waveguide has dielectric constants $\varepsilon = \varepsilon_0(\varepsilon' + \varepsilon'')$. In the general case of a 2D cross section of a waveguide $\mathcal{A}$, one can show that the linear power attenuation of the optical mode can be calculated from the field distribution as [42] :

$$\alpha = \frac{\omega\varepsilon_0 \iint_{\mathcal{A}} \epsilon'' \left|\hat{\mathbf{E}}\right|^2 d\mathcal{A}}{\iint_{\mathcal{A}} \mathrm{Re}\left(\hat{\mathbf{E}} \times \hat{\mathbf{H}}^*\right) \cdot \vec{n}\, d\mathcal{A}} \tag{2.26}$$

where $\vec{n}$ is the vector normal to the waveguide cross-section $\mathcal{A}$ in the direction of propagation (parallel to $k_{//}$), and ω the photon pulsation. The integral on the cross-section $\mathcal{A}$ has to be performed numerically on a large enough window to approach the correct value it should have over the whole space $\mathbb{R}^2$. In the case of TE polarised waves, Equation 2.26 greatly simplifies to the following formula :

$$\alpha = \sum_i \Gamma_i^{TE} \varepsilon_i'' \quad \text{with} \quad \Gamma_i^{TE} = \frac{k_0^2}{\beta} \frac{\iint_{\mathcal{A}_i} \left|\hat{\mathbf{E}}\right|^2 d\mathcal{A}_i}{\iint_{\mathcal{A}} \left|\hat{\mathbf{E}}\right|^2 d\mathcal{A}} \tag{2.27}$$

The summation over i is performed over all layers composing the waveguide and the integral over $\mathcal{A}_i$ is performed on the cross-section of this layer (i) only. This formula is often used in its weak guiding approximation both for TE and TM polarization in the literature. While it is mostly justified in low loss weakly guiding structure, this approximation can lead to important error in the calculation of the TM polarization absorption coefficient as discussed in [43]. The correct formulation that has been used throughout this thesis for the TM polarized wave is the direct decomposition of Equation 2.26 applied to uniaxial material whose optical axis is along the vertical axis (the growth axis) $\vec{z}$:

$$\alpha = \sum_i \Gamma_i^{TMpar} \varepsilon_{oi}'' + \sum_i \Gamma_i^{TMz} \varepsilon_{ei}'' \tag{2.28}$$

$$\text{with} \quad \Gamma_i^{TMpar} = \frac{k_0^2}{\beta} \frac{\iint_{\mathcal{A}_i} \left|\hat{\mathbf{E}}_{\mathbf{par}}\right|^2 d\mathcal{A}_i}{\iint_{\mathcal{A}} \mathrm{Re}\left(\hat{\mathbf{E}} \times \hat{\mathbf{H}}^*\right) \cdot \vec{n}\, d\mathcal{A}} \quad \text{and} \quad \Gamma_i^{TMz} = \frac{k_0^2}{\beta} \frac{\iint_{\mathcal{A}_i} \left|\hat{\mathbf{E}}_{\mathbf{z}}\right|^2 d\mathcal{A}_i}{\iint_{\mathcal{A}} \mathrm{Re}\left(\hat{\mathbf{E}} \times \hat{\mathbf{H}}^*\right) \cdot \vec{n}\, d\mathcal{A}}$$

where "par" refers to the part of the field which is not along the z axis and is thus sensitive to the ordinary part of the dielectric constant ε_{oi} of the media i. Equation 2.28 allows the decomposition of the losses induced by each individual media composing the waveguide as well

as each absorption mechanism (phonon absorption, free carrier absorption, etc...).

2.3 Optical properties of materials

The above development of semiconductor waveguide clearly states the importance of the knowledge of material's dielectric constant. While the literature is quite furnished for wavelength in the short wave infrared domain (wavelength between 1 and 2.5 µm) [44, 45], specific data in the MWIR and LWIR domain is still lacking and especially for doped semiconductors.

Many methods exist to measure the dielectric constant of a material depending on its nature and the spectral band of interest. Indeed, we have stated in the above that causality implies that the absorption and refraction properties of a material (i.e the imaginary and real part of the dielectric constant) are linked to each other through the Kramers-Kronig relations Equation 2.13. For low absorptive materials (far from any resonances), it is convenient to use techniques that rely mostly on the measurement of the real part of the dielectric constant.

One commonly used technique in that case, that gives very accurate results, is the measurement of the deviation angle of a beam passing through a prism made of the material to be measured. Despite its precision, this method requires the processing into a prism of the material, which is not convenient to all deposition techniques apart from the bulk growth of semiconductor crystal. Another method commonly used, known as the *m-lines* method, consists in measuring the reflectance spectrum of a planar waveguide structure deposited on a substrate using optical coupling through a prism pressed onto it [46]. Whenever the absorption of a material rises, either by increased free carrier absorption while increasing the doping level, or closer to an optical resonance such as the gap of a semiconductor, measurement of the reflected or transmitted light becomes more complicated and thinner films are required to limit the impact of absorption. One very popular method for the characterization of thin film dielectric constant is the ellipsometry technique [47]. This method relies on the measurement of the change in polarization angle of a beam reflected on the thin film. The elliptically polarised reflected beam gave the name to the method.

All the above method are not easily implemented in the LWIR domain. Indeed, ellipsometry while well available for short wave infrared wavelengths is very less for the LWIR wavelengths and the m-lines technique only provides the real part of the optical index and not the complex dielectric constant which is not very adapted to doped semiconductor materials. In the following parts, we will discuss measurement of dielectric constant in the LWIR domain of doped semiconductor and thin film dielectrics.

2.3.1 Fabry Perot measurement of III-V Semiconductors

Both active and passive waveguide components that are developed throughout this thesis are planned to be combined with QCL on the InP technological platform. To ensure the best compatibility and integrability with them, the semiconductors classically used for those devices will be explored here. Dielectric constants of InGaAs, InAlAs latticed matched on InP substrate, that are the material components of the active structure quantum wells, as well as InP which will

constitute the cladding of our waveguides, have been measured using the Fabry-Perot reflectivity technique developed in the team. This method, as well as the results presented here, is explained in detail in [48, 11] and we hereby recall the general principles and results.

A Fabry-Perot cavity is a device formed of two reflective interfaces producing optical interference patterns with respect to the angle of incidence θ at a constant wavelength, and with respect to the wavelength at a constant angle of incidence Figure 2.10. The examples shown in Figure 2.10 graphs are the reflectance of a 100 µm thick cavity at λ=9.1 µm for the top graph and 3 µm thick at an angle of incidence of 30° for the bottom graph. The cavity used in those examples is a single layer slab of relative dielectric constant presented in the legend.

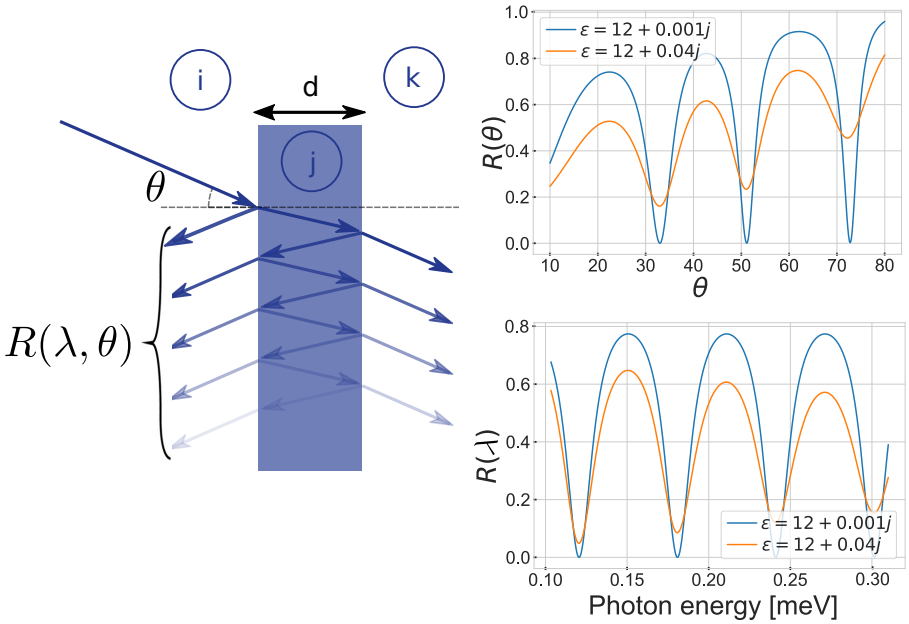

Figure 2.10: A typical Fabry-Perot cavity composed of one layer of arbitrary material. An incident beam will be reflected at both interfaces, leading to interference patterns with respect to the angle of incidence θ at a fixed wavelength and also with respect to the wavelength at a fixed angle, as shown in the example inset reflectance curves.

One can clearly see the successive ups and downs of the total reflectance, they are directly linked to the optical path in the cavity and thus mostly provide information on the real part of the dielectric constant of the material. On the other hand, both the width of the peaks and the contrast of the curves are directly linked to the imaginary part of the dielectric constant, ergo the absorption of the material. This technique therefore gives access to the complex dielectric constant, provided that the thickness of the cavity is well known. Indeed, the reflectance is given by the expression square modulus $|r_{ik}|^2$ from Equation 2.21 where $k_{zj}^2 = k_0^2 \left(sin^2\theta - \varepsilon\right)$ directly depends on the wavelength, the incident angle and the material relative dielectric constant.

In this work we present the measurement and result of InP films with different doping concentration, grown by *MetalOrganic Chemical Vapour Deposition* (MOCVD) on InP substrate with a thin 300 nm undoped InGaAs buffer. Those are then metallised with 200 nm thick sputtered gold and bonded by thermocompression [49] on an identically metallised silicon substrate.

Doping (cm^{-3})	Thickness (nm)		
nid	4807	4533	4047
1e17	4995	4493	3973
1e18	4891	4314	3275

Table 2.1: Thickness of the different steps of InP Fabry-Perot cavity samples.

The InP substrate is then chemically removed in an HCl:H_2O (3:1 in volume) solution and the InGaAs buffer acting as an etch stop is removed in H_3PO_4:H_20_2:H_2O (3:1:10). Successive lithography step and wet chemical etching in H_2SO_4:H_20_2:H_2O (3:1:1) are then performed to define 3 steps used as three different Fabry-Perot cavities. Three samples are then cleaved through the steps and their thicknesses are measured using a *Scanning Electron Microscope* (SEM) on the trench, their dimensions are reported in Table 2.1.

Reflectivity spectrum of each step of each of the samples is then recorded using a commercial *Fourier Transform InfraRed interferometer* (FTIR) (Vertex 70 from Bruker) at 6 different angles of incidence (between 10° and 70°), both for TE polarized and TM polarized light. This results in a set of 36 different measurement conditions for each differently doped material (12 per step). A careful calibration of the FTIR "background" spectrum is performed before each sample measurement to account for slight change of condition (chamber temperature, CO_2 or H_2O vapour concentration when changing the sample in the chambre, etc...). Those calibration are performed on a "perfect" gold mirror fabricated at the same time as the samples on a silicon substrate.

To extract the complex dielectric constant from all those measurements, a dielectric constant model is used to account for the main contribution at the wavelengths of interest (between 4 and 12 µm in this work). The identified contributions to the relative dielectric constant for InP samples in this wavelength, window with respect to the photon energy or frequency ω, are all represented by Kramers-Kronig compatible models :

$$\varepsilon_r(\omega) = \varepsilon_\infty \frac{\omega_{LO}^2 - \omega^2 + j\gamma_{LO}\omega}{\omega_{TO}^2 - \omega^2 + j\gamma_{TO}\omega} - \frac{\omega_{FCA}^2}{\omega^2 + j\gamma_{FCA}\omega} \tag{2.29}$$

- The first term ϵ_∞ accounts for the contributions that are far from the measurement window and appears as a constant, real term.

- The blue term models the interaction with longitudinal (LO) and transversal (TO) optical phonons through damped oscillators in the factorised form [50]. ω_{LO}, ω_{TO}, γ_{LO}, γ_{TO} are the LO and TO phonon resonance energies and damping.

- The brown term models the free carrier absorption for doped samples through a Drude contribution. ω_{FCA} is the plasma energy depending on the dopant concentration and γ_{FCA} the damping.

The contribution from the gap, often modelled as a damped oscillator, is neglected for the InP samples as the gap energies lies well below the measurement window (at wavelength around

920 nm) [51]. In the undoped sample, contribution from free carriers are neglected and only the 4 parameters from the phonon contribution are fitted. The Lydane-Sachs-Teller relation is then used to calculate $\epsilon_\infty \omega_{LO}^2 = 12.37\omega_{TO}^2$ [50]. The obtained values are then used in the fit of the doped components, and only the 3 parameters for the free carrier absorption and the step thickness are fitted on them (within a ±5% margin around the SEM measured one for the latter, to account for thickness uncertainty).

All the measurement sets, comprising the measurements of all three steps of a sample at both TE and TM polarization and 6 different angles of incidence (thus 32 spectrum), are globally fitted using the parametrized function Equation 2.29. The cost function minimised in the fitting process is [48].

$$MSE = \sqrt{\sum_{j}^{N} \sum_{\lambda} \left(R_j^{th}(\lambda, \alpha) - R_j^{exp}(\lambda) \right)^2} \tag{2.30}$$

Where the summation over j is done over all 32 spectrum of a measurement set, R^{th} is the theoretical reflectance of the sample which depends on the cavity thickness and the fitting parameters (represented by the vector α), and R^{exp} is the measured reflectivity spectrum. An example of measured and fitted spectrum at an angle of incidence of 33° is presented in Figure 2.11 for two different doping levels. The resulting parameters fitted on all measurements are presented in Table 2.2.

Sample	ϵ_∞	ω_{FCA} (meV)	γ_{FCA} (meV)	
InP nid	10.14	-	-	
InP n:1e17	10.14	**60.65**	**0.01**	
InP n:1e18	10.14	**193.80**	**9.28**	
	ω_{LO} (meV)	γ_{LO} (meV)	ω_{TO} (meV)	$\gamma_{TO}(meV)$
InP nid	**48.4**	**0.67**	**43.82**	**0.47**
InP n:1e17	48.40	0.67	43.82	0.47
InP n:1e18	48.40	0.67	43.82	0.47

Table 2.2: Fitted parameters to model the InP dielectric constant. Bold values are the fitted values on the samples. Plain text values are not fitted but used in the model.

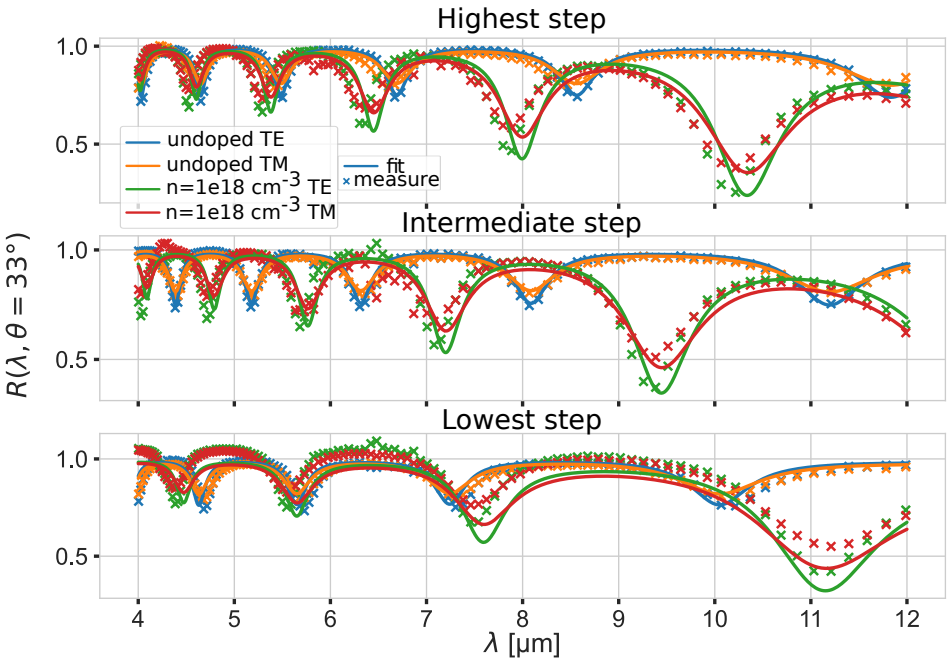

Figure 2.11: Measured and fitted reflectivities at an angle of 33° of InP samples. Not all the data is presented.

The corresponding dielectric constant of the measured InP samples are presented in Figure 2.12. An estimation of the fitting error of the dielectric constant is presented as the shaded area around the curves and relies on error propagation using the Jacobian matrix of the dielectric function and the fitting covariance matrix. Detailed discussion of those uncertainties can be found in [48]. The resulting dielectric constant follows nicely the values reported in the litterature [52, 53] with a seemingly constant offset over the whole spectrum. Adachi's model is as expected, not matching with any other as it models near gap interactions only, and doesn't take into account phonons interactions [51]. The offset between our model and Bi or Petit models can be explained by the uncertainty on the InP film thickness that we estimate to be around 5% of the total thickness. Indeed, the sample is several centimetres long and the step thickness, measured on the cleaved trench using SEM, while the measurement is performed in the middle of the sample (see [48]). A sample thickness inhomogeneity of the epi-layer, and an inhomogeneous etching due to the wet etching recipe used, could have led to the discrepancy between our model and the ones reported in the literature. Moreover, constraint effect might appear due to the thermocompression bonding process that can affect the phonon resonance frequencies and damping. As seen in Figure 2.12, the change in the relative permittivity between a non intentionally doped, and an n:1e17 cm^{-3} doped InP is relatively low. This indicates that phonons are the main source of losses in those cavities up to at least an n:1e17 cm^{-3} doping. Above that doping, free carrier absorption becomes predominant, and the optical constant becomes driven by the Drude term of Equation 2.29.

Similar measurements have been performed in the team on doped InGaAs and AlInAs sam-

ples using the same method developed for that purpose. The resulting dielectric constant models and the method are described in details in [48]. It is those models that have been used to design the components presented in that thesis, for InGaAs and AlInAs materials. On the other hand, due to the discrepancy between our model and the ones reported in the literature, the optical model from Bi et al. [52] was used for InP, with an additional Drude term for the free carrier absorption calculated from carrier lifetime measurement reported in [54].

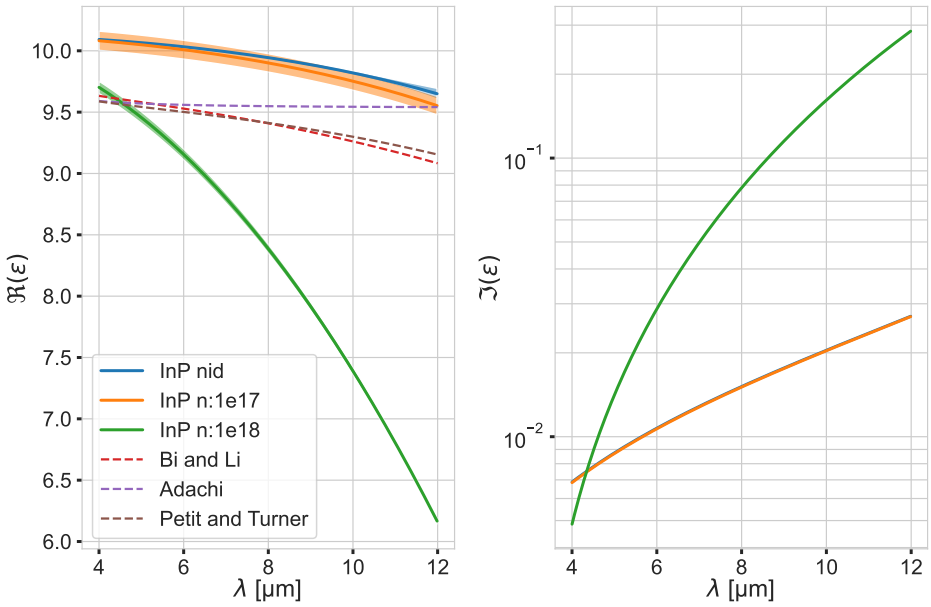

Figure 2.12: Complex dielectric constant of InP fitted on Fabry-Perot reflectivity spectrum. The models for undoped InP from the literature, are extracted from [52, 53, 51]. The shaded region represents the fitting uncertainty.

2.3.2 Multipass absorption measurement of dielectric thin film

The passivation of the side of an optically active waveguide plays an important role in the device performance. To that end, dielectrics presenting low absorption losses in the optical frequency window are essential. Similarly to the above semiconductors, very few dielectric constant data are available in the LWIR window for those materials. Those dielectrics are deposited in very thin layers of less than a micro meter in our clean-room facility. Thus, the above used Fabry-Perot method is not adapted to characterize their dielectric constant as the free spectral range (the spacing between two lows in the spectrum) would be too large to ensure a good quality of the fit. Moreover, we are mostly interested in the absorption of these materials rather than their optical index, as they will be used in thin layers on the sides of our active waveguides. A multipass absorption measurement is in that case a better solution to characterize the material absorption. It relies on the measurement of the transmission spectrum of the sample of interest placed in a tunable cavity. The dimensions of that cavity allow adapting the number of passes of the optical beam through the sample to better address its optical absorption, Figure 2.13.

A thin film of dielectric, whose complex permittivity is to be measured, is deposited on a

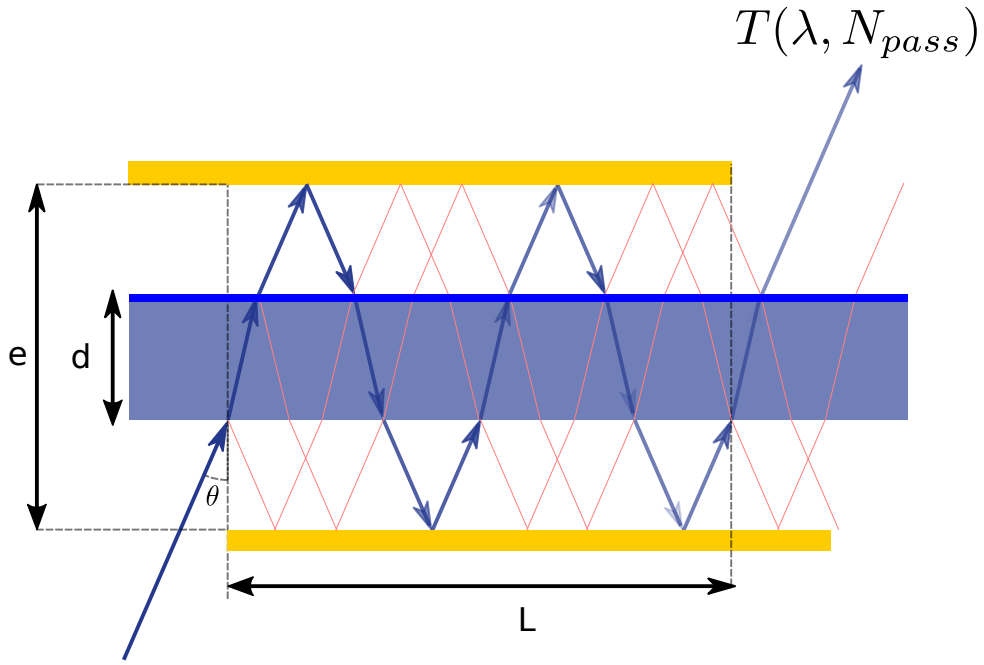

Figure 2.13: Multipass configuration measurement. The multipass cavity is formed by two parallel mirrors, their spacing e (and the sample thickness d) and the length of the cavity defines the pass number N_{pass}. The total transmission is the measured quantity. In light pink are represented some parasitic beams from specular reflection at the interfaces.

polished substrate (in our case an undoped GaAs substrate). The number of passes through the cavity is defined by the cavity width and length, e and L, as well as the substrate thickness and optical index d and n_{sub}. Moreover, an incident angle of 73°, the Brewster angle at the wavelength of 9 µm, is chosen to limit parasitic specular reflections at the interfaces air-sample. Under the assumption of negligible reflections, a defined number of passes is chosen, and a transmission spectrum measured using the same FTIR Bruker Vertex 70. The devices to be fabricated in this thesis will present high topography with high aspect ratio, and a deposition technique ensuring high uniformity over all surfaces no matter their orientation is required to passivate the side of the waveguides as well as the planar surfaces. Only an *Atomic Layer Deposition* (ALD) deposition chamber was available in the clean room that met these requirements. We measured two different dielectrics, Alumina and Hafnia deposited by ALD in plasma enhanced mode, that appeared to be good candidates from the literature [55, 56]. For both materials, two deposition temperatures were tested which seemed to have a great impact on the material effective permittivity, as will be presented. Each of them were measured for different pass number in order to optimise the fitting procedure robustness. Samples and measurement conditions are presented in Table 2.3.

Sample	Material	Deposition temperature (C°)	thickness (nm)	Substrate	N_{pass}
1	HfO_2	100	100	GaAs 500 µm	3,5,9
2	HfO_2	250	100	GaAs 500 µm	3,5,9
3	Al_2O_3	100	100	GaAs 500 µm	3,5,9
4	Al_2O_3	200	210	GaAs 350 µm	3,5,9

Table 2.3: Thin film oxide deposited by ALD and measurement conditions for dielectric constant characterization.

The dielectric constant model used for all samples is a sum of Brendel oscillators. Brendel oscillators is a phenomenological model that has been used for decades to model the non Lorentzian broadening observed in the infrared response of amorphous materials whose "disorder", in opposiion to crystalline structures, causes a "random" shift of the resonant Lorentzian transition according to a Gaussian distribution. The dielectric function is parametrised as follows [57, 58] :

$$\varepsilon_r = \varepsilon_\infty + \sum_i \frac{j\sqrt{\pi}\omega_{pi}^2}{2\sqrt{2}\alpha_i\sigma_i}\left(w(z_{ai}) + w(z_{bi})\right) \tag{2.31}$$

with :

$$\alpha_i = \sqrt{\omega^2 + j\gamma_i\omega} \tag{2.32a}$$

$$Z_{ai} = \frac{\alpha_i - \omega_{0i}}{\sqrt{2}\sigma_i} \quad Z_{bi} = \frac{\alpha_i + \omega_{0i}}{\sqrt{2}\sigma_i} \tag{2.32b}$$

In the above equation, ω_{pi}, γ_i, ω_{0i} respectively are the oscillator strength (expressed in terms of energy and often refereed to, as plasma energy, by analogy with Drude-Lorentz optical models), broadening and resonance energy of the "i-th" Lorentzian contribution, σ_i its Gaussian broadening, ω the photon energy and w the Faddeeva function. Two methods are found in the literature to fit such a model to a measured spectrum. The first is to use as much Brendel oscillators as needed to best fit the measured data, but this procedure seemed to lack a physical sense. The second method that we chose, is based on the fact that every Brendel oscillator should have a physical origin (for example the vibration of a chemical bond, a phonon etc...), and based on that (and the visible absorption peaks in the spectrum) a fixed number of Brendel oscillators is chosen to fit the measurement. This method gives mores sense to the obtained dielectric constant even though the Brendel oscillator model is stricto sensu not a physically valid model, in that it doesn't satisfy causality principle and lacks Hermeticity. Nevertheless, it is a simple model with a few parameters for a relatively robust fit, and some extensions to this model has been reported to make it verify the causality and Hermeticity principles, known as Gauss-Lorentz oscillators [59, 60].

The fitting procedure is the same as the one used in the previous part (global fit of all measurement conditions of one sample) except that the MSE from Equation 2.30 is based on the transmission T calculated using the TMM described in subsubsection 2.2.3. The $N = 3$ globally fitted spectrums per sample, are three spectrums recorded for a cavity tuned to have 3, 5 or 9 passes through the material. Some of the resulting fits and measures are presented in Figure 2.14.

Four Brendel oscillators have been used to fit the HfO_2 sample deposited at 100 C° and two for the other three samples to account for all the absorption peaks in the transmission spectrum. Their respective parameters are presented in Table 2.4 and the corresponding dielectric constant is plotted in Figure 2.15. The fitting error as calculated by mean of the Jacobian matrix and presented in the previous part has not been used for those measurements, instead we estimate the quality of the obtained dielectric constant with the dispersion of the obtained ones fitted on individual sample and measurement conditions (thus three individual fit per global one). Indeed, the fitting error propagation by means of the Jacobian matrix only accounts for discrepancies between the model used and the fitted measurements, supposing the measurement conditions uncertainties to be of second order impact. In the present case, this is obviously not the case, as visible on the dispersion represented by the shaded area on Figure 2.15. The uncertainties mostly comes from the measurement setup, through the cavity thickness, length and parallelism as well as the sample positioning. From those results, it appears that the method used together with the measurement doesn't give accurate dielectric constants except for the hafnia sample deposited at $250C^{\text{deg}}$. This could be partly attributed to the low dielectric constant of the dielectric thin film which would cause non-negligible reflection at the interface (air-oxide), thus perturbing the measurement (and adding more uncertainties there again). Nevertheless, general trends can be extracted from those measurements together with the spectrums from Figure 2.14. At equivalent pass number and film thickness, the hafnia deposited at 250°C appears to be much less absorbing than the alumina films at the wavelength of interest (9 µm). This is coherent with an abortion resonance close to 10.5 µin the alumina films while it is further, close to 13 µm in the hafnia 250°C film. Models reported in the literature also show less absorption at this wavelength in hafnia than in alumina even though we can't really conclude on that part, from only the fitted dielectric constant. More recent results using mid-infrared ellipsometry following our work has been reported also placing hafnia film as less absorptive than alumina [61].

Sample	ε_∞	ω_{p1}	ω_{01}	γ_1	σ_1	ω_{p2}	ω_{02}	γ_2	σ_2
1 (HfO_2 250 C°)	3.909	0.289	1.999	1.697	1.234	0.084	0.085	0.004	0.004
3 (Al_2O_3 100 C°)	2.259	0.027	0.684	0.001	0.109	0.112	0.083	0.003	0.016
4 (Al_2O_3 250 C°)	1.201	0.032	0.559	0.001	0.141	0.079	0.089	0.002	0.011
2 (HfO_2 100 C°)	1.224	0.025	0.188	0.001	0.016	0.055	0.056	0.015	0.020
	-	ω_{p3}	ω_{03}	γ_3	σ_3	ω_{p4}	ω_{04}	γ_4	σ_4
	-	0.027	0.402	0.001	0.033	0.234	2.759	1.485	1.293

Table 2.4: Fit parameters of the different dielectric constant model of alumina and hafnia. Values are given in eV except ε_∞ which has no unit.

2.4 Quantum wells

For now, we have discussed the optical properties of bulk materials only, but active optical components based on the QCL technologies rely on the use of confined electronic states in

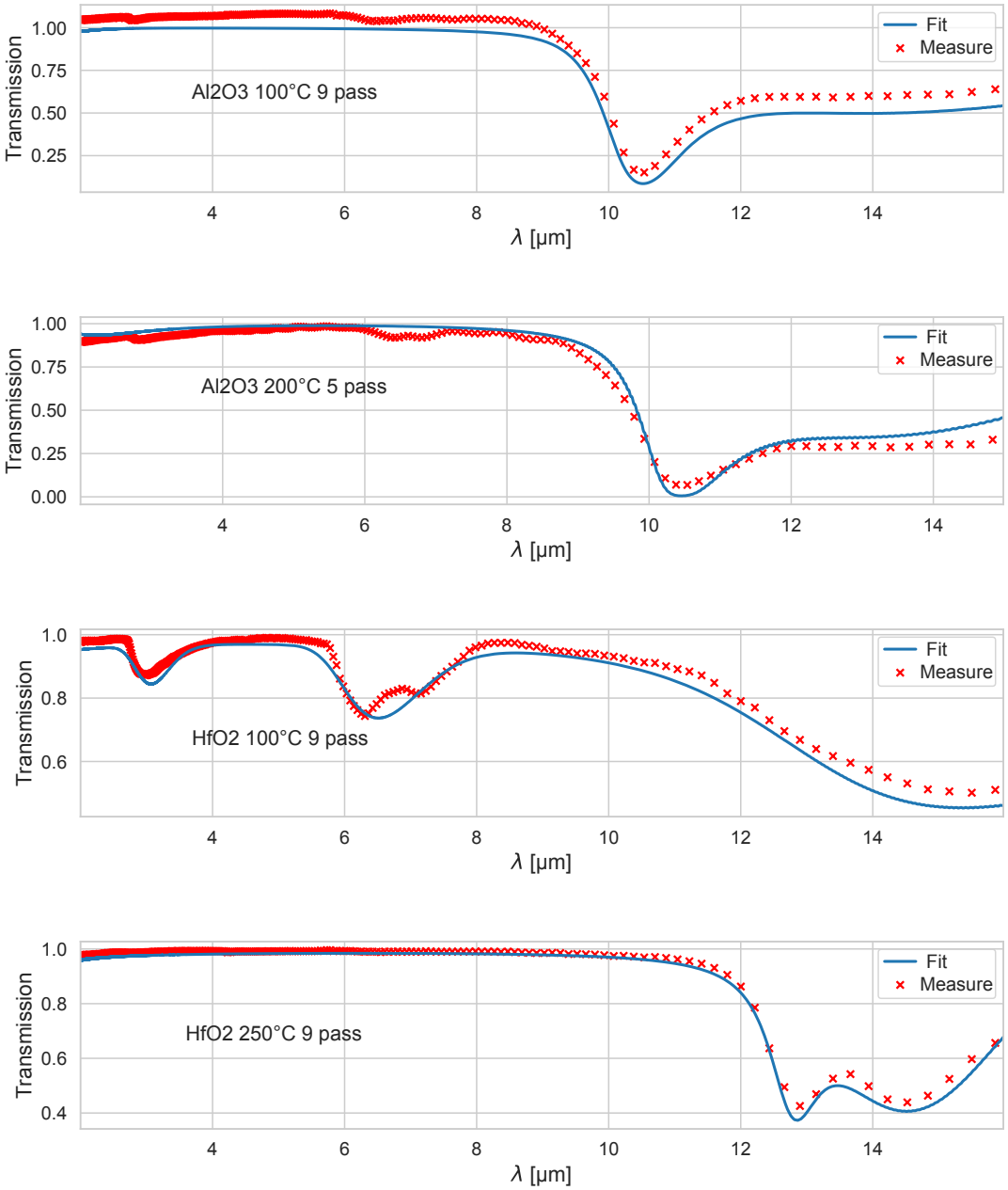

Figure 2.14: Measured and fitted multipass transmission spectrums of different samples. Not all the data is plotted.

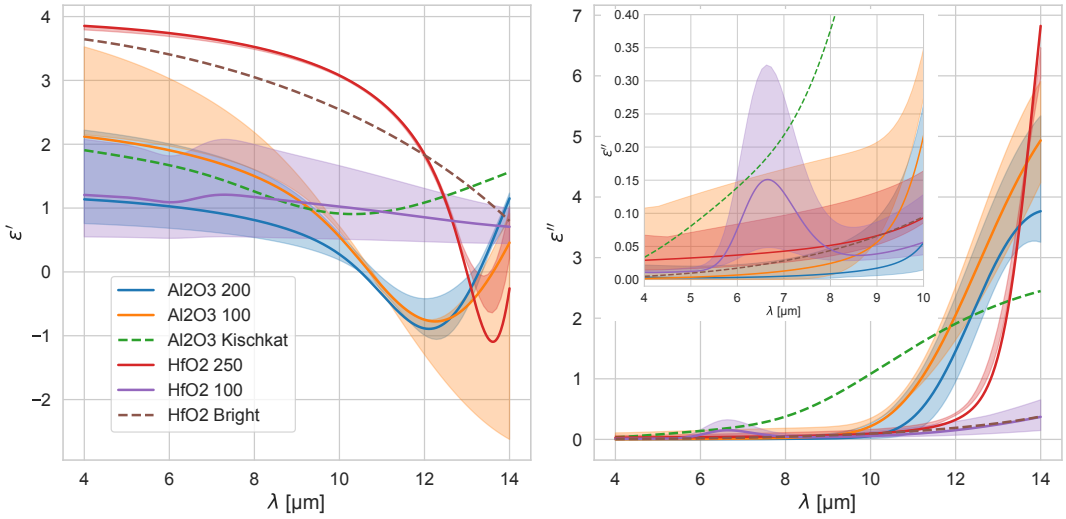

Figure 2.15: Resulting relative dielectric constant of the measured oxides thin films. Kischkat Alumina model is from [55] and Bright Hafnia model from [56]. The dielectric constant is of the form $\varepsilon' + k\varepsilon''$. The shaded area are the dispersion experienced when the fit is performed individually on all measurement rather than globally on all measurement from one sample.

quantum wells (and most active modern optical components two). It is therefore important to understand the physics behind quantum wells and their induced optical properties. That is the main objective of the following part. For detailed description of semiconductor band structure which we will not discuss here, one can refer to [34, 62].

2.4.1 Confined electronic states in quantum wells

In a crystalline material such as semiconductors, electrons are evolving at their scale (the angström) in a seemingly infinite periodic structure formed by successive repetition of the same lattice. These lattices are themselves constituted by ions, which can be considered fixed under Born-Oppenheimer approximation. The behaviour of electrons in those crystalline materials is well described as waves and governed by the analogous wave equation in the electronic domain, which is the Schrödinger equation :

$$j\hbar\frac{\partial\Psi(\mathbf{r},t)}{\partial t} = \mathcal{H}(\mathbf{r},t)\Psi(\mathbf{r},t) \tag{2.33}$$

In that equation, $\mathcal{H}(\mathbf{r},t)$ is the Hamiltonian of an electron evolving in the periodic structure (with $\mathbf{r}$ its position vector) and $\Psi(\mathbf{r},t)$ its associated wave function. Similarly to the resolution of the Helmholtz equation, Equation 2.15, we are interested in the stationary solutions of Equation 2.33. Those solutions are by definition found in the form :

$$E\Psi(\mathbf{r}) = \mathcal{H}(\mathbf{r})\Psi(\mathbf{r}) \tag{2.34}$$

where E is the eigenvalue of the eigenvector $\Psi(\mathbf{r})$ solution to Equation 2.33. E is the energy of the electron described by the wavefunction Ψ. In a bulk semiconductor, this energy depends on

the local potential energy $V_{sc}(\mathbf{r})$ and the electron kinetic energy. The Hamiltonian describing the crystal then writes as :

$$\mathbf{H}_{sc} = \frac{\mathbf{p}^2}{2m_0} + V_{sc}(\mathbf{r}) \tag{2.35}$$

with m_0 the vacuum free electron mass and $\mathbf{p}$ its momentum. A system of solutions $|n, \mathbf{k}\rangle$ to Equation 2.35 was given by Bloch [63] in the form :

$$\Psi_{n,\mathbf{k}}(\mathbf{r}) = \frac{1}{\sqrt{V}} e^{j\mathbf{k}\cdot\mathbf{r}} u_{n,\mathbf{k}}(\mathbf{r}) \tag{2.36}$$

Where V is the volume of the crystal used to normalise the wavefunction and $u_{n,\mathbf{k}}(\mathbf{r})$ is a periodic function having the same period as the crystal (thus as V_{sc}). The Bloch system $(E_n,|n, \mathbf{k}\rangle)$ is a basis of solutions to Equation 2.35 with $\mathbf{H_{sc}}$.

Heterostructure :
When alternating different layers of semiconductors in a heterostructure, one ends up with a varying supplementary potential $V_{het}(z)$ (z being the growth axis) which varies at scales which are the thicknesses of each layer, the nanometre scale. This scale being much larger than the scale at which the crystal potential, V_{sc}^i, in each layer i varies (the angstrom), it is possible to develop the solutions to the Hamiltonian describing the whole system $\mathcal{H}_{het}(\mathbf{r}) = \frac{\mathbf{p}^2}{2m_0} + \sum_i V_{sc}^i(\mathbf{r})$ with the envelope approximation [64]:

$$\Psi_{n,\mathbf{k}}^{het}(\mathbf{r}) = \xi_n(\mathbf{r}) u_{n,\mathbf{k}=\mathbf{0}}(\mathbf{r}) \tag{2.37}$$

where $\xi_n(\mathbf{r})$ is the envelope function modulated by the periodic function introduced by Bloch at the bottom of the conduction band, $\mathbf{k} = 0$. When reintroducing Equation 2.37 into $\mathcal{H}_{het}$ it is then possible to decompose the total Hamiltonian into two independent terms as :

$$\mathcal{H}_{het}(\mathbf{r}) = \mathcal{H}_{het}^z(z) + \mathcal{H}_{het}^\perp(\mathbf{r}_\perp) \tag{2.38}$$

where $\mathbf{r}_\perp$ is the direction orthogonal to the growth axis (z) and :

$$\mathcal{H}_{het}^z(z) = -\frac{\hbar^2}{2}\frac{\partial}{\partial z}\left(\frac{1}{m^*(E_{n,\mathbf{k}_\perp=0}, z)}\frac{\partial}{\partial z}\right) + V_{het}(z) \tag{2.39a}$$

$$\mathcal{H}_{het}^\perp(\mathbf{r}_\perp) = -\frac{\hbar^2}{2m^*(E_{n,\mathbf{k}_\perp}, z)}\nabla_\perp^2 \tag{2.39b}$$

In those form, the crystal potentials V_{sc}^i have been included in an effective mass m^*. The solutions to the above equation are found in the form of a plane wave in the $\mathbf{r}_\perp$ direction, and a wavefunction $\phi_n(z)$ in the growth direction which directly depends on the heterostructure potential $V_{het}(z)$

$$\xi_{n,\mathbf{k}}(\mathbf{r}) = \phi_n(z) e^{j\mathbf{k}_\perp\cdot\mathbf{r}_\perp} \tag{2.40}$$

The energy of the electron in the state $|n, \mathbf{k}\rangle$ is then :

$$E_{n,\mathbf{k}} \approx E_n + \frac{\hbar^2 k_\perp^2}{2m^*(E_n)} \tag{2.41}$$

where we approximated the state effective mass as parabolic and equal to the effective mass at the bottom of the band $m^*(E_n, \mathbf{k}_\perp) \approx m^*(E_n)$. The simplest heterostructure is perhaps the quantum well, which is made of a smaller gap materials in-between two larger gap materials. Such a structure and the corresponding levels is presented in Figure 2.16 for an InGaAs (SC_2) quantum well with AlInAs (SC_1) barrier (lattice matchd to InP).

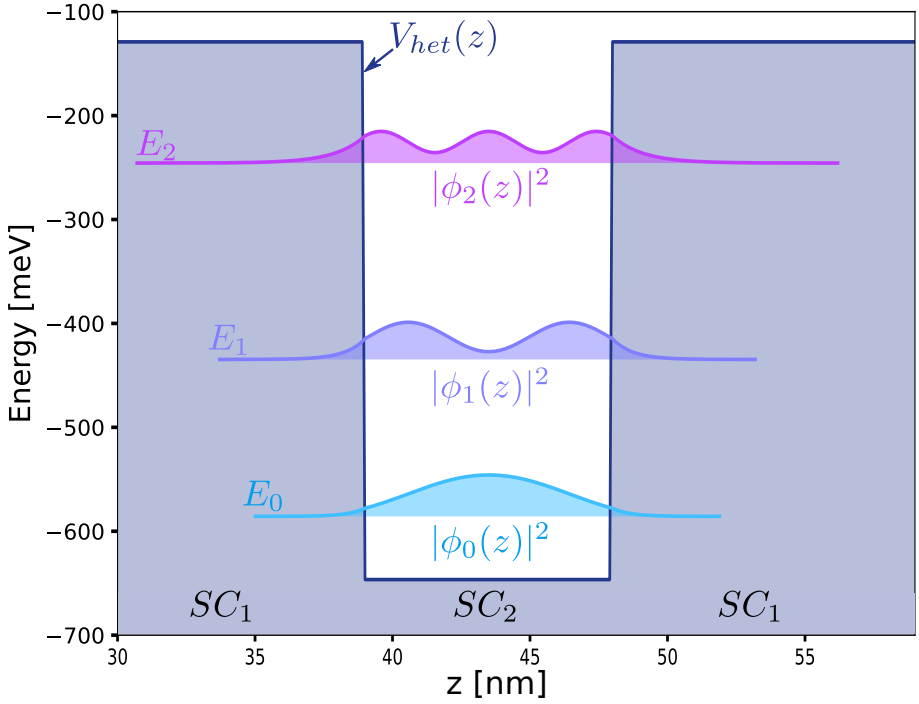

Figure 2.16: A quantum well and its corresponding energy levels and wavefunctions of the eigenstates $|n, \mathbf{k}\rangle$. The heterostructure potential $V_{het}(z)$ is presented as the dark blue line. The parabolic in plane dispersion is not represented.

The simple resolution presented above is convenient to treat an ideal problem where no transport occurs and no imperfection in the materials are present. Those can be treated as added contributions to the one dimensional Hamiltonian $\mathcal{H}^z_{het}(z)$ if they are expected to have a non-negligible impact on the confined levels $|n, \mathbf{k}\rangle$. This is the case of an applied potential $V_{app}(z) = qFz$ (with q the elementary charge and F the applied electric field) on the structure and the resulting charge displacement potential $V_{poisson}(z)$. The other contributions having a negligible impact on the wave functions but not on the electronic populations, can be treated as perturbation to the one dimensional Hamiltonian. They are interactions with phonons, alloy disorder, interface roughness, etc [65, 66, 67, 68]. The classical treatment of those is explained in great details in [68] as well as some additional considerations on tunnel interactions. The complete resolution of band structure and electronic population in a given heterostructure is carried out using a rate equation model [69], and is summarized in Figure 2.17.

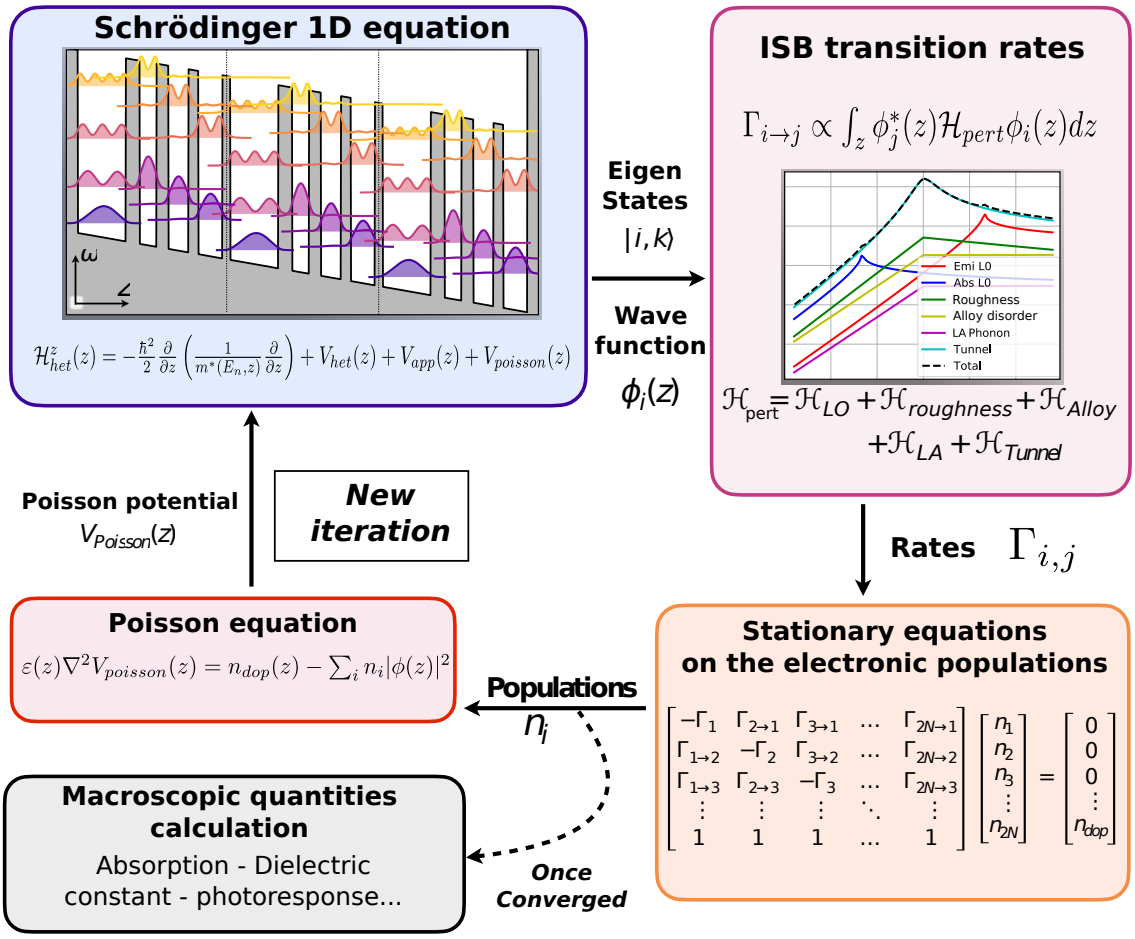

Figure 2.17: Calculation steps of a complex heterostructure. Adapted from [68].

2.4.2 Optical properties of quantum wells

From Equation 2.39, we see that electrons behave differently in the z direction where they occupy discrete state of energies, with respect to the $(\vec{x}, \vec{y}) \equiv \perp$ plane, where they behave as free electrons. In the optical domain, these different behaviours lead to the modelling of quantum wells as uniaxial media whose optical axis is the growth direction $\vec{z}$. The in-plane contribution, ordinary relative permittivity ε_o (see Equation 2.14) is therefore modelled as a free carrier absorption permittivity using a Drude model at the optical frequency ω :

$$\varepsilon_o = \varepsilon_{BKG} - \frac{\omega_p^2}{\omega^2 + j\gamma\omega} \quad \text{with} \quad \omega_p^2 = \frac{q^2 n_{2D}}{\varepsilon_0 m^* L_{eff}} \tag{2.42}$$

where ε_{BKG} is the background dielectric constant of the material constituting the quantum wells, q the electron elementary charge, ω_p the free carrier plasma frequency and γ the associated damping. The background dielectric consant accounts for all the optical contribution of the material to the dielectric constant in the absence of the quantum well effect and doping. The effective length L_{eff} over which is applied the dielectric constant is defined by the micro-current spatial distribution between the first optical transition in the quantum well. It is, in general, greater than the physical length of the quantum well by about 20 to 40 percent [70, 71, 72]. n_{2D} is the two dimensional carrier density, m^* the effective mass of the free electrons and ε_0 the vacuum permittivity.

In the other direction, the extraordinary contribution to the dielectric constant of the quantum well is calculated as the sum over all optical transitions between level i and j and integrated over energies E as [73] :

$$\varepsilon_e = \varepsilon_{BKG} + \sum_{i,j \ i\neq j} \int_E \frac{\omega_{pij}^2 \rho_{2D}(E) \left[f_{FD}(E_i)(1 - f_{FD}(E_j)) - f_{FD}(E_j)(1 - f_{FD}(E_i)) \right]}{(\omega_{ij} + E(1 - m_i/m_j))^2 - \omega^2 - j\Gamma\omega} dE \tag{2.43}$$

where ω_{ij} is the energy difference between both levels, $\omega_{pij} = \sqrt{q^2/(\varepsilon_0 m^* L_{ij})}$ the plasma frequency of the transition with L_{ij} the effective length of the transition (the micro-current spatial distribution), f_{FD} the Fermi-Dirac distribution and ρ_{2D} the two-dimensional electronic density of states [74, 73], Γ is the transition linewidth and m_i, m_j the effective masses of each energy level i and j at the bottom of the subband to take into account non-parallel subbands. In essence, we consider each ISB transition as an inhomogeneous broadened lorentzian to account for effective mass non-parabolicity. This non parabolicity of the effective masses is taken as its simplest form : a linearized variation with energy, $m_i^*(E) = m_0^* + \alpha\omega_i(k = 0)$ as it is found to be sufficient to model non parabolicity effects for usual doping [68], with m_0^* the effective mass at the bottom of the conduction band, $\omega_i(k = 0)$ the energy of the subband i at its bottom and the α parameter is found in the literature (for example [75]) or fitted on calibration measurements. In this formula m_i, m_j and ω_{pij} are calculated prior to the integration and treated as independent of E in the integral.

If parallel subbands were considered, the contribution to the dielectric constant would be a

sum of Lorentz oscillators of the form (with $\omega_{pij}^2 = q^2\Delta n_{2Dij}/(\varepsilon_0 m^* L_{ij})$):

$$\varepsilon_e = \varepsilon_{BKG} + \sum_{i,j \ \ i\neq j} \frac{-\omega_{pij}^2}{\omega_{ij}^2 - \omega^2 - j\Gamma\omega}$$

It would be tempting, considering Equation 2.28, to say that the absorption in a quantum well of length L_{QW} is directly proportional to $\mathrm{Im}\{\varepsilon_e(\omega)\}L_{QW}$, but that would be an error. Indeed, the thickness of a quantum well is very small compared to the optical infrared wavelength such that the field in the quantum well is constant. Therefore, the amplitude of the field in the quantum well is imposed by the contrast between the dielectric constant of the quantum well and its direct environment (the barriers of the contacts), as imposed by the continuity equation of the electric displacement D_z (Equation 2.16). Since the dielectric constant of the barrier does not change much with the wavelength of the incoming light (contrarily to the one of the quantum well), it results that the absorption spectrum $\alpha(\omega)$ is more conveniently expressed as :

$$\alpha(\omega) \propto \frac{\mathrm{Im}\{\varepsilon_e\}}{|\varepsilon_e|^2} |\varepsilon_b E_b|^2 L_{QW}$$

with ε_b and E_b the transversal component of the dielectric constant and electric field in the barrier. After some algebra, it comes that :

$$\alpha(\omega) \propto \mathrm{Im}\left\{\frac{-1}{\varepsilon_e}\right\} \approx \frac{\omega_p^2 \Gamma\omega}{\left(\omega_{ij}^2 + \epsilon_{BKG}\omega_{pij}^2 - \omega^2\right)^2 + (\Gamma\omega)^2} \tag{2.44}$$

In the case where only one transition exists (or is predominant), the approximation of the above equation leads to an absorption spectrum which is a Lorentzian function but shifted at a greater energy $\tilde{\omega}_{ISB} = \sqrt{\omega_{ij}^2 + \epsilon_{BKG}\omega_{pij}^2}$ (to simplify, we consider the background permittivity to be real, as the intersubband transition will be the dominant non-real term). This shift in energy comes from the enhancement of the electric field at higher photon energy than the intersubband transition energy due to the reduction of its dielectric constant. This is the effect of in phase electrons oscillations with the incident electric field in the quantum well and is often dubbed plasma-shift [76].

2.4.3 Non ideal interfaces

In the above, we described perfect square shaped quantum wells. In reality, there is a continuous transition between one material and the other over a few atom layers, resulting in smooth quantum well edges [77]. For the system of material we use, $In_{0.53}Ga_{0.47}As$ and $Al_{0.48}In_{0.52}As$, this transition is modelled as a sigmoidal transition between the two ternary materials constituting the well and barrier (lattice matched to InP). There is at the interface between both materials, a quaternary material $Al_xIn_yGa_{1-x-y}As$ where the aluminium concentration x follows a sigmoidal distribution of parameter σ representing the typical inter-diffusion distance (details in [68, 78],). The sigmoid is used as a simple, one-parameter effective function for the transition, without deeper physical reason.

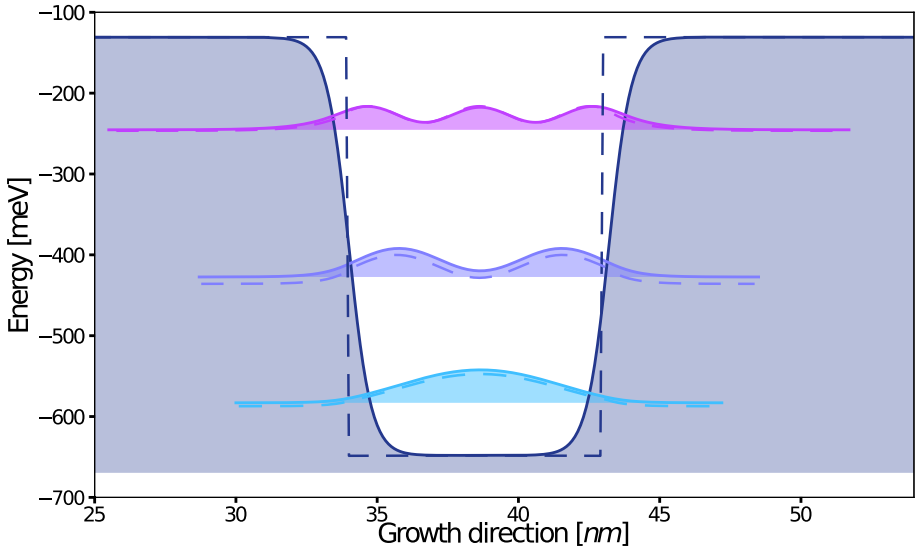

Figure 2.18: Confined electronic states in a 90 angstrom InGaAs quantum well (with AlInAs barrier) for a 4 angstrom sigmoid parameter σ. The dotted lines are the results of a perfect square quantum well.

The Figure 2.18 presents a simulation of an 9 nm InGaAs quantum well with AlInAs barrier for an inter-diffusion length $\sigma = 4$Å. One can see that the effect of this inter-diffusion tends to enlarge the well at the top and reduce its width at the bottom. This increases the energy level of the confined states, with a higher impact on the levels situated halfway to the bottom. This results in a blue shift of the inter-subband transition energy by several percents. The thinner the well and the barrier, the more impact the inter-diffusion might have on the resulting energy levels. It is therefore particularly important to have a good idea of what will be this inter-diffusion prior to the design of a complex structure such as QCD or QCL.

2.4.4 Material parameters calibration

From the above considerations, it becomes clear that reliable material parameters for the simulation of quantum well based devices are of great importance. To that end, test structures composed of quantum wells whose inter-subband transitions cover the all MWIR and LWIR wavelength domain are realised for different doping concentrations. Multipass absorption measurement (as described in subsubsection 2.3.2) are then used to calibrate material parameters that will be used for the active device design. The effective mass dispersion α will distort the spectral absorption and tends to red-shift it. The inter-diffusion length described by the sigmoid parameter σ will itself tend to blue-shift the transitions. The energy depth of a quantum well called the bandoffset, the offset between the bottoms of the conduction bands of both wells and barrier, will also have an important impact on the confined states energy levels. Those band-offset are fixed for ternary alloys and a bowing parameter is used to model the gap (thus the band offset) transition with material composition change caused by the inter-diffusion.

Prior to every design of an active structure, all those parameters have to be calibrated. As the material parameters (band offset bowing and effective mass dispersion α) are not expected

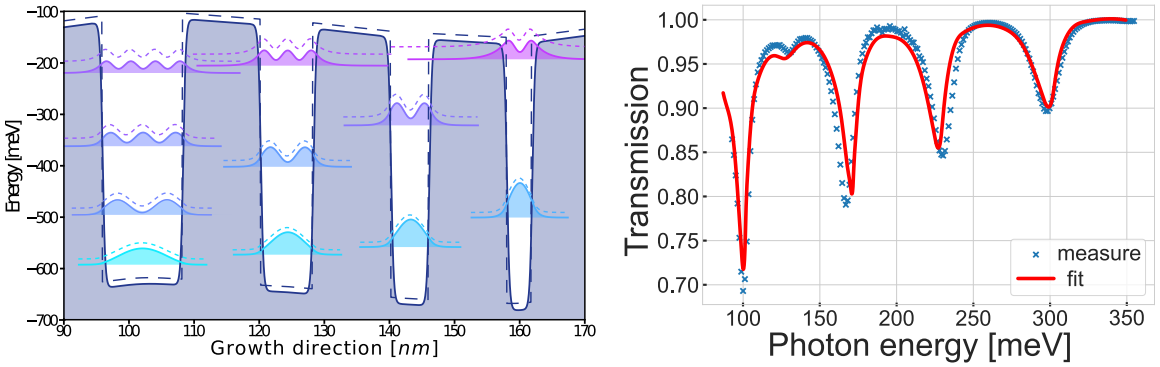

Figure 2.19: Example of a calibration sample with 4 different quantum well widths and its fitted and measured multipass absorption spectrum. The dotted lines are the levels of the ideal vertical interface quantum wells.

to vary much as mostly dependent on the material used, the inter-diffusion parameter σ is itself expected to vary in time as it depends mostly on the growth chamber used and its current state. A sharp change of σ could be a symptom of a problem of the growth chamber.

3 Conclusion on the theoretical aspects

In the first part of this chapter, we introduced the optical modulation of a monochromatic light beam to transmit information. Multiple modulation types in phase and amplitude have been introduced, and several high-order coherent modulation formats discussed. The capacity of an AWGN channel has been presented, and we have seen the equal importance of having a high bandwidth and a good signal-to-noise ratio, which is the equivalent of the so-called gain / bandwidth product of transistors. The bit error rate of various modulation formats have been presented and the importance of a well paved constellation diagram has been shown.

In the second part of this chapter, we have exposed all the theory used to design the active and passive optical components that will be presented in the following chapters of this thesis. The optical properties of the materials used throughout this work have been presented and their measurement and limitation exposed. Material structuration in quantum wells and their impact on the optical effective permittivity has been presented, as well as the main limit to the practical fabrication of those.

In the following chapter, we will focus on design aspects of firstly passive components. Subsequently, the application of the above theory to the design of active waveguide phase modulators will be presented before discussing the performances of a waveguide quantum cascade detector. Except for the laser, all buildings blocks necessary to form an integrated coherent receiver will be presented by the end of this thesis.

Chapter 3

Beam routing and passive building blocks

Objectives

The main achievement of photonics circuits is the ability to route the light beam where it is needed and to form complex optical functions only with the help of passive and active building blocks. In this chapter, we review the main waveguide technologies available and focus on the ones adapted to QCL in the LWIR wavelength domain. The different losses in a photonic circuit and ways to limit them will be presented. Finally, a focus will be given on design rules of passive beam splitter, which are the main-used building block of photonics circuits, followed by a discussion of the performances of a designed 3dB MMI splitter.

Contents

1 Optical waveguide technologies

1.1 Waveguide materials

The materials used in a waveguide strongly impact its optical performances. They define their confining strength and, most of all, their transmission properties. Historically, the advantages of the silicon-on-insulator waveguide platform (i.e. their high maturity and readily available fabrication facilities) have pushed researchers to investigate the use of this platform for higher wavelengths. However, SiO_2 becomes strongly absorbent for wavelengths greater than 3µm due to multiple atomic bond resonances (Si-O-Si, Si-OH, Si-O), making it not usable in the LWIR spectral band. On the other hand, compatibles materials that are silicon and germanium have absorption losses below 1 dB/cm in the MWIR and LWIR bands [44]. In the LWIR wavelengths, germanium-based waveguides appear to be more adapted, nevertheless, as its phonon absorption bands are further to the LWIR wavelengths (Ge multi-phonon absorption are found from 16 to 100 µm while crystalline silicon are between 6 and 25 µm wavelength) [79, 80, 81]. As said, the main advantage of Ge/Si materials are the high maturity of their fabrication process, which can be subcontracted to a commercial foundry.

Another alternative to silicon and germanium semiconductor alloys are III-V semiconductors. Those are made of different alloy composition of elements from the III and V columns of the periodic table of elements. Their composition, which can be widely tuned, determines the absorption of the gap electronic transition and phonon (possibly multi-phonon) absorption. It is particularly interesting that in III-V semiconductors, gap transition energies are usually in the SWIR while their phonon absorption lies in the upper bound of the LWIR and more [34], making them suitable materials for MWIR and LWIR photonics. Typical losses reached by III-V semiconductor waveguides are on the order of 5 dB/cm at 9 µm.

Finally, a last alternative could be chalcogenide glasses. Those materials contain at least one chalcogen element, sulphur (S), selenium (Se) or tellurium (Te). Typically, ZnSe which is widely employed for bulk optics in the MWIR wavelength, is a chalcogenide glass. In particular selenium and tellurium based glasses cover a broad wavelength range over and beyond the LWIR [82]. Extremely low optical losses have been demonstrated in the LWIR, with losses below 0.3 dB/cm in As_2Se_3 glass. On the other hand, many of those material present strong non-linearities and birefringence that can be a limiting factor for their integration in photonics circuits [20, 81] in the case we are interested in, but can advantageously be used for specific applications such as supercontinuum generation, four wave mixing or parametric amplification [83]. On the other hand, their fabrication process requires dedicated equipments.

A brief review of optical losses in waveguides from different platform is presented in Figure 3.1, adapted from [81]. In the present thesis, our choice of technological platform went to the III-V material platform, as all the processing and material growth equipment was readily available in the laboratory. This choice was further reinforced for its compatibility with the available QCL laser in the prospect of their integration with the designed components. In particular, the InGaAs on InP platform was retained.

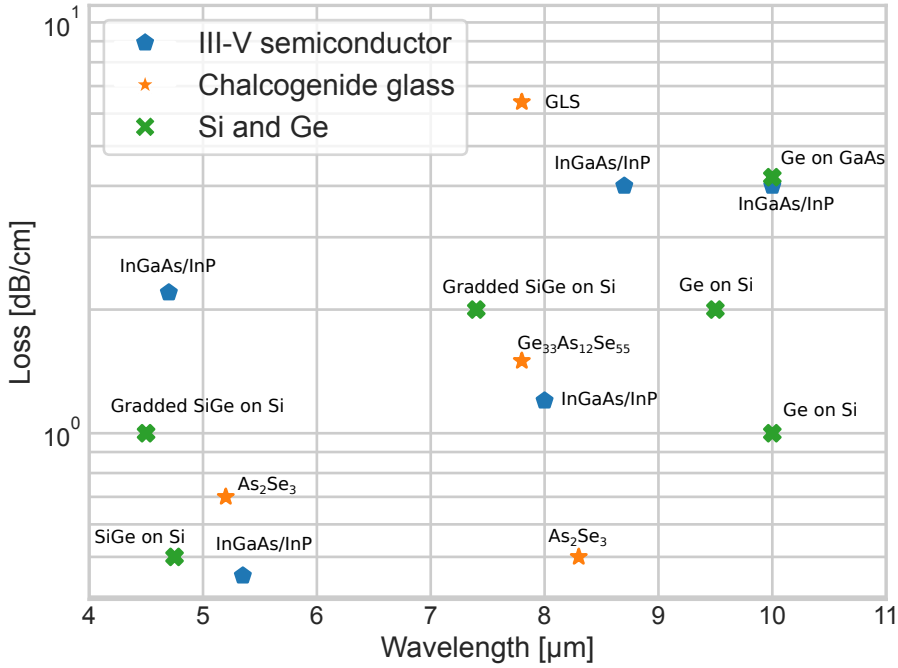

Figure 3.1: Reported waveguide optical losses in the literature. References used : [81, 84, 85, 20, 86, 87, 88, 89, 90, 91, 92, 93]

1.2 Waveguide geometries

In the previous chapter, we have explained the importance of the knowledge of the optical properties of materials in the design of optical waveguides. Their resolution in a planar structure has been presented which can be the starting point of the resolution in more complex 2D cross-section waveguide geometry, using various methods, such as the effective index method [94, 95], variational methods [96, 97], Marcatili's method [98, 99] or others [100]. Many forms of waveguides have been introduced and used in integrated photonics circuits that each have their advantages and drawbacks in terms of fabrication and performances, the main ones are presented in Figure 3.2.

Buried waveguides are formed of a "high" optical index core material embedded in a lower index material. Depending on the optical index contrast of the materials used, it can have a high confinement, or a low confinement. In the LWIR domain they are mostly made by laser inscription in chalcogenide glass [101], or through epitaxial regrowth for buried QCL waveguide structure [102], where their thermal properties are advantageous. Optical injection through lenses is facilitated in such waveguide structures in comparison to ridge waveguides, as the optical mode is likely to be larger (see also section 2). These structure can easily be made polarization independent using a symmetrical waveguide core, which can be a great advantage for polarization multiplexing.

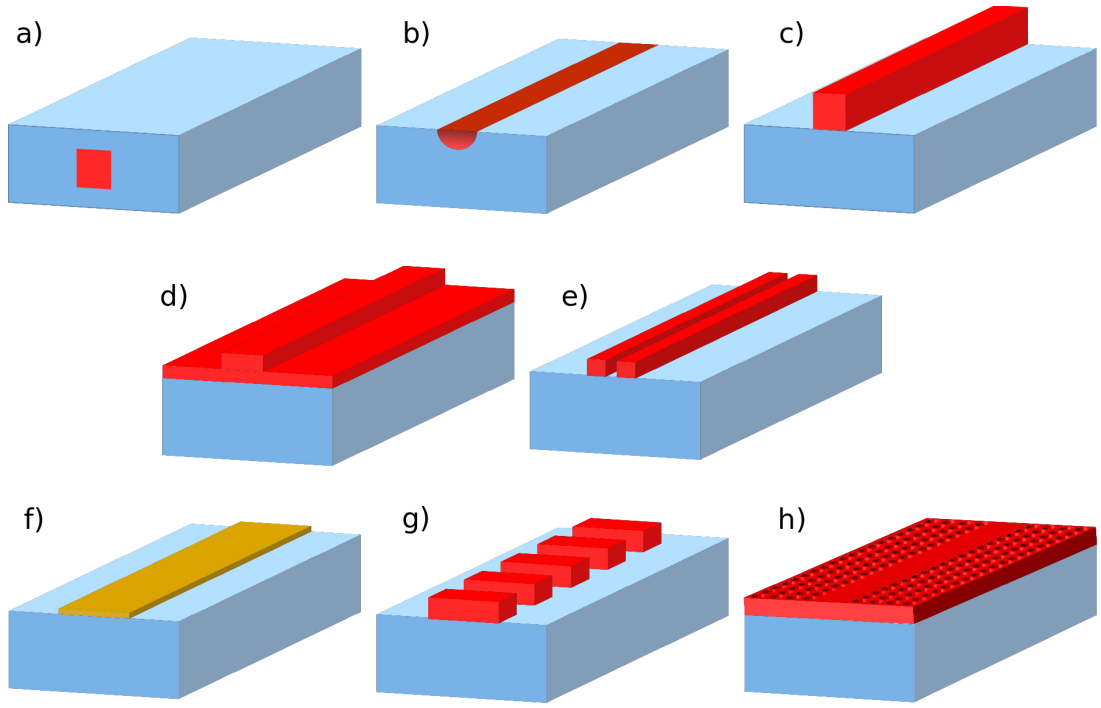

Figure 3.2: a) Buried, b) diffused, c) ridge, d) rib, e) slot, f) plasmonic, g) sub wavelength grating waveguide and h) photonic crystal waveguide. The high index material is represented in red, the low index material in blue.

Diffused channel waveguide are fabricated by diffusive ion exchange, local ion implantation or laser writing [103, 104, 105]. The optical index profile presents a smooth transition with an overall small optical index contrast. Therefore, the integration density with those waveguides is small, as any bend must be very large to limit radiation losses. There are mostly used in lithium niobate to form active devices for telecoms wavelength application. In the LWIR domain there is, to the best of my knowledge, no report of diffused channel waveguides.

Ridge and rib waveguides are probably the most currently used waveguide geometries in LWIR photonic circuits. They are formed by locally etching the waveguide core (and top cladding) to define the waveguide structure. The optical index contrast and the optical confinement can be very high, especially for ridge waveguides. Whenever the sidewall roughness induced losses are important it can be convenient to use the rib waveguide geometry, but their lower confinement (in comparison to the ridge waveguide) makes them less adapted to bent waveguide and thus lowers the integration density. A combination of both waveguide types can be useful, but comes at the cost of a more complex fabrication process [106, 20].

Slot waveguides are formed of two high index strip waveguides separated by a sub-wavelength gap. The light, polarized perpendicularly to the gap (quasi TE polarization), undergoes a high optical index discontinuity resulting in an amplification of the field in the gap region. Whenever the decay length of the electric field becomes comparable to the gap dimension, the field doesn't have time to decay in between both strips, and propagation becomes possible [107]. The very

high confinement obtained with those waveguides makes for very compact and high-performance devices in the telecom wavelength when used in combination with an active material [108, 109]. In the LWIR domain, where most laser are TM polarized, their use is limited and no report in the literature have been found of devices using slot waveguides yet.

Plasmonic waveguides are formed by a metallic layer (or any high electron density layer) whose interaction with the optical electric field leads to a local field propagation at the surface of the layer. They are relatively easy to fabricate and give a very high sub-wavelength confinement, making those waveguides suited to compact and sensitive applications, such as spectrometry in the LWIR spectral band [110]. But this does come at the cost of high propagation losses, and therefore plasmonic waveguides are limited to short propagation lengths. Moreover, those waveguides have very low tolerance to bending, and thus complex photonics circuits using plasmonic waveguides are yet difficult to realize [111].

Sub-wavelength waveguides are waveguides formed of a periodic repetition of high and low index material in a grating like form (see Figure 3.2). The width and height of the high index material is typically the same as a ridge waveguide. The thickness of each plot and their spacing is sub wavelength, such that the grating period is smaller than half the wavelength in the medium to avoid the opening of a photonic bandgap. The choice of the grating duty cycle allows access to a wide choice of waveguide core effective refractive index while considerably lowering the optical losses, providing a new degree of freedom to the designer [112]. They have been proposed as athermal, low dispersion waveguides in the SWIR [113], as candidates for bio-chemistry or gas sensing in the MWIR and LWIR domains [114, 115, 116]. Their fabrication process is slightly more complicated than the ridge waveguide geometry due to the potential high aspect ratio etching required. A well mastered fabrication process is therefore an important prerequisite. Nevertheless, they are potential significant competitors for future LWIR photonics integrated circuits.

Photonic crystal waveguides are formed of periodic variation of the refractive index, for example by etching holes in a planar waveguide structure. The periodicity of those leads to the formation of photonics bands, similarly to electronic bands in semiconductors. Waveguides formed in a photonic crystal can have very sharp and low-loss bends, providing a way for extremely high density photonic circuits [117]. Similarly to sub-wavelength grating waveguides, the designer, through the choice of the lattice parameter and filling factor, has access to a wide range of waveguide effective core index, together with a potentially low dispersion [118]. Their fabrication can, on the other hand, be very challenging as it requires high aspect ratio etching, the high index layer having a thickness similar to the ridge waveguide thickness. Very few experimental demonstrations in the LWIR domain have been found, but some simulation shows the potential of such waveguides [119, 120].

Throughout this thesis, essentially the ridge waveguide geometry will be used due to the relatively low technological maturity of the InGaAs/InP LWIR photonic platform. Moreover, the

compatibility requirement between the developed photonic components with the already developed QCL mostly impose that choice, as it would otherwise require much further development of mode converter and other specific building blocks which is not the focus of this thesis. The next part of this chapter will focus on the optical losses in photonic circuits and further justify the importance of compatible waveguide geometry with the QCL.

2 Optical losses in a system and how to limit them

2.1 Transition losses and coupling losses

Light injection into a waveguide can be quite challenging depending on its dimension and optical confinement. In this paragraph, we present the different injection techniques adapted to ridge waveguides. As the injection into a waveguide is closely linked to the transition losses between two waveguides with a different cross-section, we present at the end of this part the taper transition implemented in our designs.

End fire coupling : consists in focussing a laser beam directly on the waveguide front facet using a lens, (Figure 3.3a). In that case, the maximal coupling efficiency can be high, provided that the incident light electric field distribution matches the one from the optical waveguide mode to be excited. The coupling efficiency can be estimated by the following expression [121, 122] :

$$\eta = \frac{\left|\iint E_m^* \cdot E_{in} dxdy\right|^2}{\iint |E_m|^2 dxdy \iint |E_{in}|^2 dxdy} \tag{3.1}$$

where $E_m(x, y)$ is the optical mode field distribution in the waveguide and $E_{in}(x, y)$ the focused beam field distribution. Note that this expression doesn't consider the Fresnel reflection at the input facet, which can represent a 30% losses in InGaAs/InP waveguides. Ideally, an anti-reflection coating would be needed. In practice, the small dimensions of the waveguide do not allow a very effective injection by this technique, which is mostly limited by the diffraction limited focused spot [123]. Different methods can be used to overcome those limitations, such as enlarging the optical mode of the waveguide through inverse buried taper structure [122] for example.

Direct butt coupling : is quite similar to the end-fire coupling except that the laser beam and the laser waveguide itself is placed in close proximity to the waveguide facet (Figure 3.3b). The coupling efficiency in that case is estimated by the same Equation 3.1 and facet reflectivity calculation. To reach an efficient injection by this technique, sub-micro-metric positioning of the laser with respect to the waveguide facet is required. A particular care in the optical mode geometry through the waveguides geometries must be taken to maximize the overlap integral of the fields. That technique requires additional assembly steps, that can be challenging and costly, and are more adapted to the assembly of a final product than to a laboratory characterization setup.

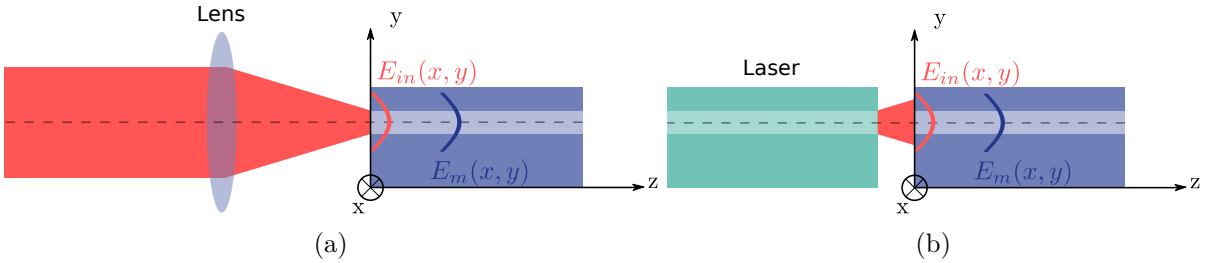

Figure 3.3: a) End fire coupling, a laser beam is focused into the waveguide. b) Butt coupling, the laser is placed as close as possible to the waveguide facet.

Prism coupling. The above two coupling methods make use of direct injection of the laser beam into the waveguide front facet. Both of these can be particularly difficult if the waveguide is strongly confining and/or is of small dimensions. This is the case of plasmonic and slot waveguides, for example. Those need other coupling techniques allowing to inject the laser beam from a side of the guide itself. The prism coupling method is one of them (Figure 3.4a). It consists in closely matching the phase velocity of the propagating mode β_m to the one from the incident wave. This is done through the use of a prism, whose optical index n_p is greater than that of the waveguide core, placed in close proximity to the waveguide. When the incident angle on the prism produces a total internal reflection into the prism at the angle θ_p, a local plane wave propagating along the $\vec{z}$ direction is formed with a propagation constant $\beta_p = n_p k_0 cos(\theta_p)$. If the angle of incidence is chosen such as $\beta_p \approx \beta_m$, and the distance d is sufficiently small, evanescent coupling between the propagating mode into the waveguide and the local plane wave in the prism will occur, and thus, power injected in the waveguide mode. The same method can be used to extract power from the waveguide [123].

Grating coupling is another, nowadays widely used method, of phase matching between an incident laser beam and an optical mode (Figure 3.4b). A periodic corrugated waveguide section (by local etching of the cladding, for example) of period Λ, diffracts the incident light beam in preferential directions resulting from constructive interferences. Those are caused by a shift of the wavevector axial component by an integer number q of $\frac{2\pi}{\Lambda}q$. The phase matching condition is met if $k_0 n_{ext} cos(\theta) + q\frac{2\pi}{\Lambda} = \beta_m$, q is called the grating diffraction order. The coupling efficiencies with gratings can be very high but requires a carefully designed grating and waveguide associated to precise knowledge of the waveguide effective index. The fabrication induced variability can also have a great impact on those [124].

The deep ridge waveguide structure used throughout this thesis and the requirement of being able to characterize the designed devices for a broad wavelength spectrum made the use of phase matching injection techniques (prism or grating coupling) impossible. Therefore, for all designed waveguide components, characterization was foreseen to use end fire coupling in the waveguide front facet, and the integration, to use butt coupling with the laser waveguide. The dimensions of the waveguides designed in this work were therefore matched to the ones of the available laser.

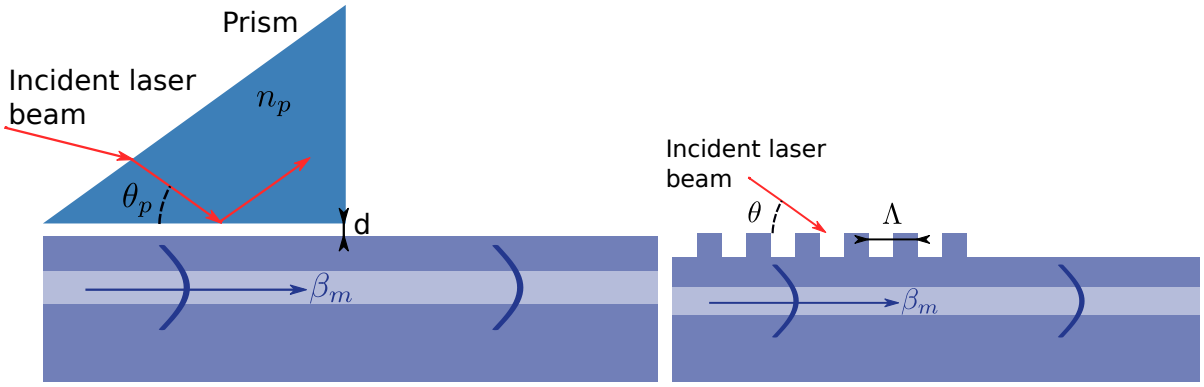

(a) (b)

Figure 3.4: a) Coupling using a prism. b) Using an engraved grating coupler.

On chip transition and tapers can be a high source of optical losses on photonics circuits. Indeed, complex photonic circuits embedding different active and passive functions are likely to use waveguides with different cross-sections. Throughout this thesis, we varied the width of waveguide sections for different reasons exposed in the next chapter. The interconnection between those sections must ensure a smooth transition to limit the transition losses due to impedance mismatch. Those can easily be understood through Equation 3.1. A mode mismatch necessarily leads to optical losses. Moreover, a short transition between waveguides having a different cross-section will reduce the propagation losses, and this is highly important when the waveguide structure as relatively high material absorption as is the case in this work (see chapter 4). Many works have been dedicated to the finding of the best transition, i.e. taper parametrization [125, 126, 127, 128, 129]. It appears, to the best of our knowledge, that the shortest adiabatic taper having the best performances might be obtained using a simple rule design introduced by Milton et al. [130], as reported in [131] for a waveguide technology close to the one we use.

In their method, the local angle $\theta(z)$ of the taper transition is designed to be lower than the projection of the ray angle of the local lowest order mode, $\theta_p(z)$, to avoid perturbation of the phase front leading to mode conversion [130] (see Figure 3.5). Now following analytical developments of waveguide propagation constant for a strongly confined mode, one can show that this condition implies that :

$$\theta(z) = \alpha \frac{(\nu+1)\lambda}{2n_c W(z)} \tag{3.2}$$

where n_c is the waveguide core index, ν the optical mode index, α a user-defined parameter, which a positive real number lower or equal to one, and $W(z)$ the local waveguide width. Expressing the coupled variation of the local width and the local angle θ one can show that the taper parametrization with the above explained criterion follows the expression, where W_0 is the input taper width :

$$W^2(z) = W_0^2 + 2\alpha \frac{(\nu+1)\lambda_0}{n_c} z \tag{3.3}$$

Moreover, in their development, Burns and Milton showed that with those taper design, the

expected transition losses would be on the order of $1/16\alpha$. The bigger the α factor, the bigger the taper transition losses, but the shorter the taper and thus the material absorption through the transition. As it is of great importance in our case (as will be explained in chapter 4) to keep the components as short as possible, we used an $\alpha = 1$ value in all our designs. In their work, Fu at al. [131] showed that this value could even reach $\alpha = 1.5$ without quantitatively increasing the losses. An example of an implemented taper transition is presented in Figure 3.5b).

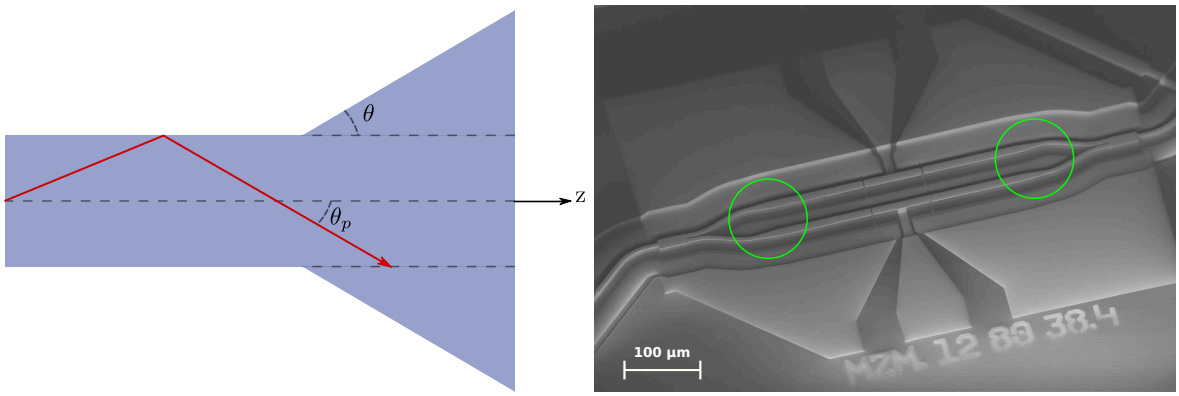

(a) (b)

Figure 3.5: a) Schematic representation and notation in the design of a taper. b) Implementation of those taper in a Mach-Zehnder modulator structure (green circle) fabricated in the present work.

2.2 Interface roughness

When processing a waveguide using any etching technique, in particular dry etching techniques, the roughness of the used mask will be transposed on the sidewall of the waveguide leading to sidewall roughness Figure 3.6.

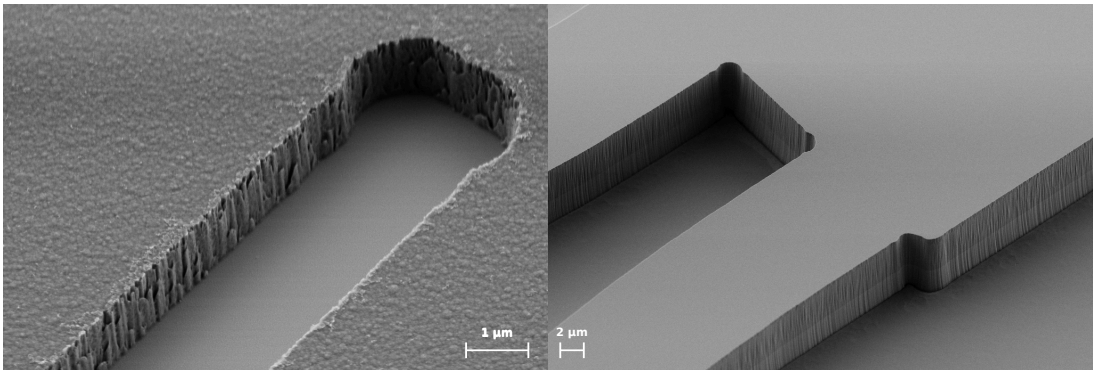

Figure 3.6: SEM picture of a SiN hard mask (left) used in the etching of waveguide structures by ICP-RIE dry etching (right). The sidewall roughness of the hard mask has visibly been transferred to the waveguide.

Many descriptions of the impact of this sidewall roughness have been reported in the literature and first theoretical description presented in [40], then simplified by [132, 133] and after

used by many authors to describe the impact of sidewall roughness in their waveguide technology [134, 135, 136]. Those theoretical descriptions rely mostly on the knowledge of the spectral density function of the surface roughness, which is hardly accessible to the designer and the experimentalist. This one is therefore mostly assumed to have an exponential autocorrelation function described by its coherence length L_c and roughness rms σ. The absorption losses α due to the interface roughness can then be estimated by [133] :

$$\alpha = \varphi^2(d)(n_c^2 - n_{cl}^2)\frac{k_0^3}{4\pi n_c}\int_0^{\pi} \tilde{R}(\beta - n_{cl}k_0 cos(\theta))d\theta \tag{3.4}$$

where $\varphi(d)$ it the modal field amplitude at the interface, n_c the waveguide core index and n_{cl} the claddings index. $\tilde{R}$ is the power spectrum function describing the surface roughness of the waveguide and is linked to the exponential autocorrelation function through the Fourier transform ($\Omega = \beta - n_{cl}k_0 cos(\theta)$) :

$$\tilde{R}(\Omega) = \frac{1}{2\pi}\int_{-\infty}^{+\infty} R(u)exp(i\Omega u)du \quad \text{with} \quad R(u) = \sigma^2 exp\left(-\frac{|u|}{L_c}\right) \tag{3.5}$$

In the derivation of the above equations, one considered a planar waveguide with random variation of its width to account for the sidewall roughness, and an optical electric field parallel to the interface core-cladding [133]. The resolution of the above equation can be reduced to a similar form, which we find to be more physically insightful [20, 132] (Eq.20 for the later ref.), particularly as it shows the wavelength dependency (where a planar waveguide model is used, the interfaces being perpendicular to the $\vec{x}$ axis, and long coherence length approximation used) :

$$\alpha = \frac{\sigma^2 4\pi^2 k_\perp}{\lambda^2 \beta}\frac{E_s^2}{\int E^2 dx}\Delta n^2 \tag{3.6}$$

In that equation, β and $k_\perp$ are the propagation constant and transversal wave-vector in the waveguide core of the fundamental mode. We recall here that a planar waveguide with interfaces transversal to the $\vec{x}$ axis is considered here, which is sufficient in most practical cases. The ratio $\frac{E_s^2}{\int E^2 dx}$ is the normalized modal field amplitude at the rough interface and Δn is the optical index contrast between the waveguide core and the lateral cladding.

Equation 3.6 teaches us that the losses induces by the interface roughness are directly proportional to the square roughness rms σ^2 as expected but also, in first order approximation (meaning by that, that the electric field overlap with the rough interface be unchanged), inversely proportional to the free space wavelength. In all generality, the wavelength dependence of those losses would be more complex as the confinement of a given waveguide structure will decrease with an increasing wavelength thus leading to more field overlapping with the rough interface and potentially over compensating the $1/\sigma^2$ term. An estimation of those losses for a very similar waveguide structure used throughout this thesis is still given in [20] and losses on the order of 5 dB/cm (partly attributed to the sidewall roughness) are presented. Those are expected to be negligible in our waveguide structure as the waveguide doping would be the main contribution to the absorption (as will be presented in the next chapter). Only the passive MMI

waveguide structure (which still are processed on doped InP substrate) could have comparable losses. Therefore, sidewall roughness losses will be neglected in all the hereafter presented design as :

1) Strongly confined mode will be used in most design of undoped waveguides

2) Whenever a more weakly confining waveguide will be used, the main sources of losses will be from material absorption and/or radiation in bent waveguides.

3) A special care will be put on the development of a "smooth" sidewall etching recipe.

2.3 Bent waveguide losses

When routing a beam in photonic integrated circuits, bent waveguide sections are essential. In a bent section, the optical mode profile changes and the field is compressed on the outer part of the bent waveguide, and a fraction of the power leaks outside the waveguide Figure 3.7. It is therefore important to well design those waveguides to limit those losses as much as possible. Different approach exists to describe those waveguides and limit their losses making use of conformal mapping [137], match bend method [138], slight misalignment [139] or a variational approach [140].

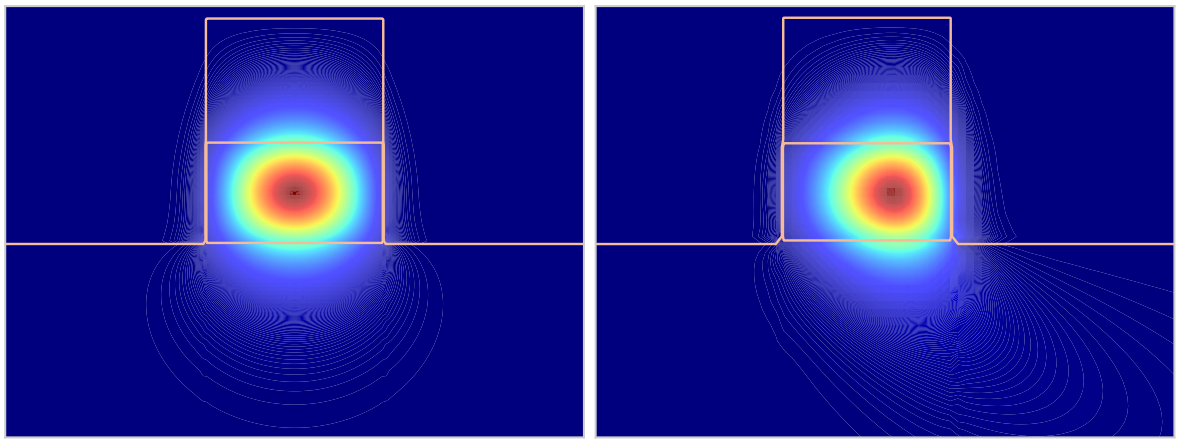

(a) (b)

Figure 3.7: Poynting vector in the direction of propagation for a) a straight waveguide, b) a bent waveguide with radius 50 µm. The waveguide is a deep ridge waveguide with 3 µm InP cladding and 2.5 InGaAs core simulated at a 9.1 µm wavelength.

The sources of losses in such bent section are mainly :

- Radiation losses outside the bent section. They evolve roughly as $C_1 e^{C_2 R}$ [141] with C_1, C_2 two constant mostly independent of the bent radius R ($C_2 < 0$).

- Material absorption, as in the case of straight waveguide

- Transition losses when passing from a straight to a bent waveguide section or between two different bent sections.

- Interface roughness. The field being pushed outside the waveguide, bent sections are more sensitive to interface roughness.

To cope with the above sources of losses, different type of bent sections have been introduced in the literature, which are now widely used. A detailed comparison of those can be found in [106] from which we recall the main conclusions below.

Arc-circle : is the most natural one. It consists of a section of constant curvature bent waveguide. With such a parametrized bend, the linear propagation losses are constant at any curvilinear abscissa, but a potentially strong discontinuity occurs at both extremities of the bend thus potentially strong transition losses.

Hyperbolic cosine : is a close alternative to the arc-circle bend, as at any curvilinear abscissa their curvature is below or equals that of the arc circle. The advantage being a reduced (by a factor 2) curvature at the extremities and a continuous transition to the arc-circle curvature. This allows the reduction of the transition losses at both extremities while also reducing the local curvature radius throughout the bent section, thus trading radiation losses for distributed transition losses, which has shown to be advantageous in low-loss waveguides [106].

Sine bends : have a null curvature at the extremities, thus no transition losses there. Their local curvature evolves gradually toward a maximum curvature, which is more than twice the arc-circle curvature. There again, constant radiation losses and extremities transition losses are traded for distributed transition and radiation losses. As their local curvature reaches twice the one from the above two bends, their losses become advantageous only for "large" bend radius in comparison to the other parametrize bends.

Clothoid bends : also does not show a curvature discontinuity at its extremities, while its curvature evolves linearly with the curvilinear abscissa to a maximum approximately 1.9 times the arc-circle curvature. Their expected losses have been shown to be always lower than those of the sine-bend except for "very small" bend radius where hyperbolic-cosine bend, anyway, have better loss figure [106].

All the above four types of bend parametrization have been explored only in the case of low-loss semiconductor waveguides. When the waveguide material, and especially the core of the waveguide, have a strong absorption (which will be the case in our modulator design as explained in chapter 4), it can be advantageous to use sharp curvature radius to displace the field outside the waveguide core, therefore trading material absorption losses for radiation losses. Moreover, in most practical applications, the optimal path is not made of simple 90° bend but rather more complex forms such as s-bends. In that prospect, we used the semi-analytical approach presented in [142] which we recall below.

The bent path is defined as a polynomial curve of 12 parameters in the $(\vec{x}, \vec{z})$ plane.

$$\mathbf{r}(t) = \begin{cases} x(t) = \sum_{n=0}^{5} a_n t^n \\ y(t) = \sum_{n=0}^{5} b_n t^n \end{cases} \tag{3.7}$$

The arc length s is then defined as the following integral along the path :

$$s(t) = \int_0^t \left| \frac{d\mathbf{r}(t')}{dt'} \right| dt' \tag{3.8}$$

The 12 parameters of Equation 3.7 are solutions to a system of equations defined by the following requirements :

1) The extremities position and slope (or angle) are fixed by imposing the continuity of the waveguide, and it's direction θ.

2) The transition at the extremities of the bent path should be smooth in order to avoid transition losses there.

3) The bend must be smooth enough so that there is negligible contribution from distributed transition losses.

From 1) and 2) we deduce the following set of equations if we denote (x_i,$\dot{x}_i$, $\ddot{x}_i$) the input position, slope, and curvature. Similarly, the f subscript denotes the same values at the output :

$$\begin{cases} x_i = a_0 \\ \dot{x}_i = a_1 \\ \ddot{x}_i = 2a_2 \end{cases} \quad \text{and} \quad \begin{cases} x_f = a_0 + La_1 + L^2a_2 + L^3a_3 + L^4a_4 + L^5a_5 \\ \dot{x}_f = a_1 + 2La_2 + 3L^2a_3 + 4L^3a_4 + 5L^4a_5 \\ \ddot{x}_f = 2a_2 + 6La_3 + 12L^2a_4 + 20L^3a_5 \end{cases} \tag{3.9}$$

There exists an infinite solution to the above system of equations that is defined by the choice of the upper bound of the integration path Equation 3.8, the t parameter, which is called L in the following as it is closely linked to the length of the path. The choice of the value of L maximizing the transmission from one side of the path to the other, gives the 12 parameters and the whole optimised path for arbitrarily positioned input and output, making that path definition extremely versatile. To minimize the losses, we use the following definition of the total absorption, which is then minimized using any numerical method (it is the third requirement), details are found in [142] :

$$I(L) = \int_0^L \alpha(t) \left| \frac{d\mathbf{r}}{dt} \right| dt \tag{3.10}$$

The knowledge of the local absorption coefficient $\alpha(t)$ is then needed for that optimization. To that end, a simulation for various curvature radii of the waveguide structure is performed using a commercially available mode solver (Fimmwave). The waveguide structure is simulated for non-lossy media (we only use the real part of the dielectric permittivity and set its imaginary value to 0). The material absorption losses can then be computed analytically from the modal

field distribution using Equation 2.27 or Equation 2.28 and added to the simulated radiation losses. The result of that procedure for the calculation of $\alpha(t)$ is presented in Figure 3.8 and the local curvature radius is linked to the parameter t via the formula :

$$R(t) = \frac{(\dot{x}^2(t) + \dot{y}^2(t))^{2/3}}{\ddot{x}(t)\dot{y}(t) - \ddot{y}(t)\dot{x}(t)} \tag{3.11}$$

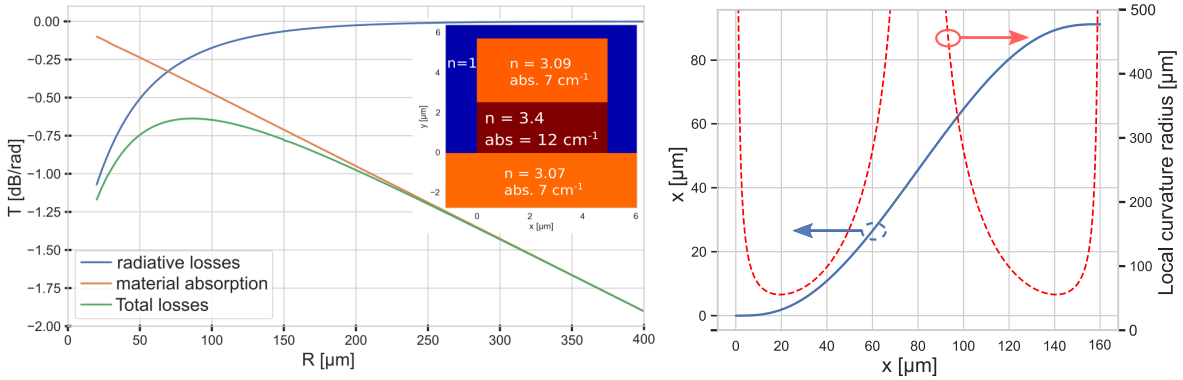

(a) (b)

Figure 3.8: a) Simulation of the transmission, including radiation losses and material absorption losses, for different values of the arc circle bend radius at a wavelength of 9 µm. Core material absorption has been fixed at 12 cm^{-1} and claddings at 7 cm^{-1}. A $\pi/2$ rad angle corresponds to a 90° bend. The insert shows the simulated waveguide cross-section. b) Optimised path (blue curve) between two points for an S-Bend transition with the above losses. The length final value of t, L=144 optimised the transmission.

One can clearly see that for very tight bend radius the losses are dominated by radiation losses, while for large bent radius the opposite occurs. The optimal bent radius is then a trade-off between both, and naturally the optimized path curvature will tend to reach that value. In all our designs, we followed the above explained procedure, choosing the parameter L with an added constraint of minimum local curvature radius along the path greater than 50 µm. This value has been chosen in order to limit the impact of optical index contrast uncertainties (as seen in chapter 2).

Having discussed the sources of losses in passive photonic components, we can discuss the main function of passive building blocks that are beam power splitter. That is the topic of the next section of this chapter.

3 Beam routing and passive optical function.

Passive waveguide components are probably the main constituents of all photonic circuits. They are used to split a light beam into as many as needed secondary beams with arbitrary power splitting and phase relation. They are used for polarization or wavelength multiplexing and demultiplexing. Likewise, they are used as spectral filters. In this part, we focus on the most elementary passive function, which is a power splitter or combiner. This passive function is indeed one of the most important ones, and especially for optical telecommunications in the

LWIR spectral band. As we will discuss in more detail in chapter 5, direct (or also called quadratic detection) at those wavelengths is less performing than field detection. Therefore, integrated beam combiners, such as can be provided by the devices presented below, are essential components for a high performance, possibly heterodyne detection scheme. It is even more essential, not to say mandatory, for coherent detection with higher-order modulation format.

In photonics circuits, beam splitter can be realized by different type of waveguide construction. The first and foremost being the "Y" junction where one feeding waveguide is split in two, forming a symmetrical "Y" shape, Figure 3.9a). The symmetrical fundamental mode of the feeding waveguide is projected onto the even super-mode in the multimode section and a 50/50 splitting is realized. On the other hand, when used as a beam combiner, the fundamental mode from both branches are projected onto both the even and odd super-mode (the ratio depends on the phase difference of both input modes) and only the even super-mode is transmitted while the odd one is radiated or reflected.

The second method, also widely used, is the directional coupler represented in Figure 3.9b). It is made of two waveguide sections sufficiently close to each other for evanescent coupling between both optical mode to happen. A Rabi oscillation will therefore occur throughout the propagation, such that the right choice of the length of the coupler will lead to any chosen splitting ratio. Those devices are particularly sensitive to the separation between both waveguides, which require a well mastered fabrication process. One way to limit the impact of this might be to break the component symmetry, for instance using a wider waveguide on one branch, which will greatly relax the precision requirement on the optimal length for the chosen splitting ratio.

The last method is the use of MMI which has become a reference component for their fabrication tolerance and high spectral bandwidth. The control of the phase relation between the output has also been a great advantage to their wide adoption, especially as 90° hybrid splitter. Those are extensively described in the following paragraphs, as they are our choice of component for beam splitting and 90° hybrid splitter.

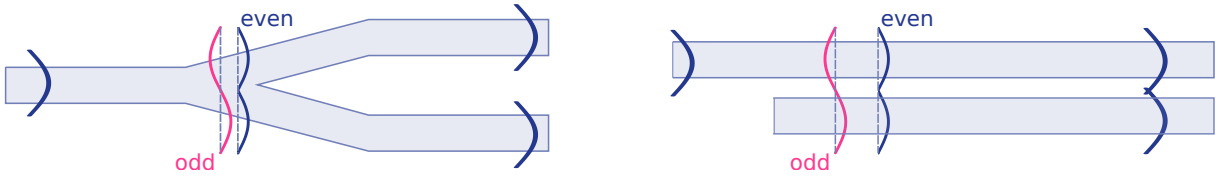

(a) (b)

Figure 3.9: a) Principle of the "Y" Junction and, b) the directional coupler

3.1 Multi mode interferometer

As previously explained, MMI are one of the main and most robust building blocks when it comes to beam splitting. Their work principle relies on the projection of an optical mode from a feeding waveguide, onto a set of new optical modes in a larger waveguide. The phase velocity relations between each of the new modes will lead, throughout their propagation, to an interference pattern similar to the Talbot carpet [143]. With a judicious position of the input

waveguides and output waveguides, one can have a wide spectrum of functionalities with such devices, making them very versatile in their design. In the following we present the theory behind MMI and its application to a 3dB splitter, the main building block required for integrated Mach-Zehnder interferometer (those will be discussed in the next chapter as a way to characterize the phase shift introduced by modulators).

3.1.1 Theory behind MMIs

The theory behind the MMI has been extensively developed in the years 1990s by Bess, Bachmann and Soldano team [144, 145, 146, 147]. They presented an extensive theoretical description of the work principle of MMI, their bandwidth, and robustness to fabrication induced imperfection. In this part, we recall the main aspects of those developments based on the above references.

An MMI is composed of ideally mono-mode input waveguides injecting an optical mode into another (highly) multimode waveguide section. The notations and representation of such waveguide MMI is represented in Figure 3.10. For simplification, we consider a planar step index waveguide made of non-absorbing isotropic media, the dielectric constant is thus real and the square of the optical index. The core material has an optical index n_c (shaded area in Figure 3.10) and the claddings and index n_r. The calculation of those indexes can be made by use of the actual 3D multimode waveguide and the effective index method, for example [148, 149]. Following the modal propagation analysis [150], one can express the propagation constant β_ν of each mode of the multimode section as :

$$\beta_\nu \approx k_0 n_c - \frac{(\nu+1)^2 \pi \lambda_0}{4 n_c W_e^2} \tag{3.12}$$

where k_0 and λ_0 are respectively the free space wave-vector and wavelength. W_e is the effective width of the multimode section, meaning that it is the physical width of the waveguide, to which we add 2 times the field penetration depth of the first order mode outside the waveguide to account for the Goos-Hänchen effect. The propagation constant spacing can then be defined with respect to the first order mode β_0 as :

$$\beta_0 - \beta_\nu \approx \frac{\nu(\nu+2)\pi}{3L_\pi} \quad \text{with} \quad L_\pi = \frac{\pi}{\beta_0 - \beta_1} \approx \frac{4 n_c W_e^2}{3\lambda_0} \tag{3.13}$$

Throughout their propagation, each mode will accumulate a different (but determined by design) phase such that at a given section z, the field distribution will be expressed as the coherent sum of all guided mode Ψ_ν (we assume the coupling with any radiative mode to be negligible) :

$$\Psi(y,z) = \sum_\nu c_\nu \Psi_\nu(y) e^{j\frac{\nu(\nu+2)\pi}{3L_\pi} z} \quad \text{with} \quad c_\nu = \frac{\int \Psi(y,0)\Psi_\nu(y)dy}{\sqrt{\int \Psi_\nu^2(y)dy}} \tag{3.14}$$

A carefully positioned input waveguide defines the coupling coefficients c_ν while their propagation constant produces the interference pattern. One can directly see that at any integer multiple distance of $3L_\pi$ the imaged input field will repeat itself with an eventual π phase shift.

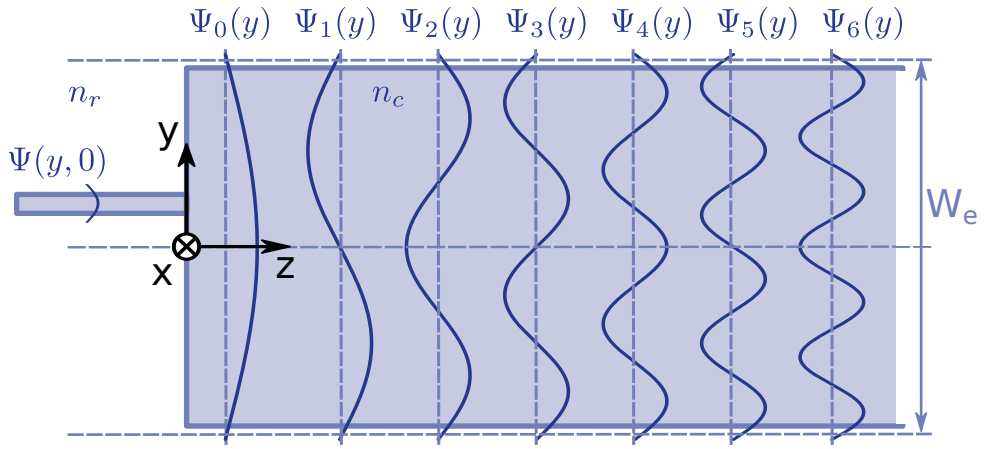

Figure 3.10: Schematic representation of step index waveguide MMI and is first 7 guided mode normalised amplitude Ψ.

In the general case of N arbitrarily positioned input waveguides (meaning not necessarily positioned at the nodes of some mode), the position and phase relations of the N-fold images (N imaged repetition of one input waveguide) at the distance $L = 3L_\pi/N$, can be obtained by Fourier analysis [145]. In that case, the first N-fold images of an input waveguide field are located at :

$$x_q = (2q - N)\frac{W_e}{N} \tag{3.15a}$$

$$\psi_q = q(N - q)\frac{W_e}{N}\pi \tag{3.15b}$$

Those N-fold images of the input waveguides are not necessarily superposed for two different input waveguides, and a careful positioning of the input is required to ensure this superposition. Those are described in detail in [145]. In the case of an even number of input/output N, those must be situated at $y = a + \frac{W(4k-N)}{2N}$ and $y = -a + \frac{W(4k-N+4)}{2N}$ with k an integer between 0 and $N/2 - 1$, and $0 < a < W/N$.

In a 2×N MMI it is also possible to position the input waveguides at $y = \pm\frac{W_e}{6}$ such that the modes Ψ_ν for $\nu = 2, 5, 8, ...$ are not excited. This results in shorter components by a factor of 3, the firs N fold images being at $L = L_\pi/N$. Those components are refereed as **paired interference MMIs**. Similarly for symmetrical excitation, as in the case of the 1×N MMI the length can be further reduced to $L = 3L_\pi/(4N)$ as only the even modes are excited. Those MMIs are refereed to as **symmetric MMIs**.

Bandwidth and robustness to small design variations :

One of the main advantages of MMI as basic building blocks such as 3dB splitter is their relative robustness to design variation potentially introduced during the fabrication process, and their wide bandwidth in comparison to other component such as Y junctions. Those tolerances are especially derived in [144]. Considering the above discussion, the optimal length L of a designed MMI for N-fold images at an optimal wavelength λ_{opt} is given by (in the general case where we assume a strong index contrast such that $W_e \approx W$, the physical width of the multimode section)

:

$$L_{opt} = \frac{4n_r W}{N\lambda_{opt}} \tag{3.16}$$

Therefore, taking the logarithm of the above equation and expressing its differential, one obtains that :

$$\frac{|\delta L|}{L_{opt}} = \frac{|\delta\lambda|}{\lambda_{opt}} = 2\frac{|\delta W|}{W} = \frac{|\delta n_c|}{n_c} \tag{3.17}$$

In [144], Besse et al. derives an analytical formula expressing the excess loss induced by a small variation of the design, by approximating the fields of the input/output waveguides by a Gaussian beam of waist d_0, and considering no crosstalk between the outputs (i.e. well separated waveguide). For a given maximal excess loss $\alpha \equiv -10log_{10}(T)$, they show that this limit is reached by :

$$|\delta L| \leq Z d_0^2 \frac{\pi n_c}{2\lambda_{opt}} \quad \text{with} \quad Z = \left[\frac{4 - 5T^2 + \sqrt{(4-5T^2)^2 - 16T^2(T^2-1)}}{8T^2}\right]^{1/2} \tag{3.18}$$

They therefore obtained, injecting Equation 3.18 into Equation 3.17, that the bandwidth of the MMI with a considered maximal excess loss writes as :

$$2|\delta\lambda| = \frac{\pi N}{4}\left(\frac{d_0}{W}\right)^2 \lambda_{opt} \tag{3.19}$$

The main conclusions to their work are then the followings :

- The larger the input/output number N, the lower the MMI bandwidth
- The fabrication tolerances are independent of the input/output number N
- All other coefficients being equal, the larger the input/output waveguide (waist d_0), the larger the fabrication tolerances and the bandwidth.

In a development stage, one can include multiple variation of length by step $\pm|\delta L|$ for a chosen excess loss α to compensate for fabrication induced variation in width, laser wavelength variation, or optical index uncertainty.

3.1.2 Design of 2×2 MMI 3dB splitter

The above theory behind MMI having being explained, we present here its direct application to the design of 2×2 MMI acting as 3dB splitters. Those are especially useful to form waveguide integrated Mach-Zehnder interferometers, which are the main building blocks of most coherent transceivers. Their main advantage in comparison to the other alternative, being a 1×2 MMI, lies in the potential reflection when used as a beam combiner for a signal and a local oscillator laser, which can cause detrimental perturbation [151]. Indeed, when two beams in phase opposition are injected (thus an odd symmetry injection) in a 2×1 MMI, those interfere destructively at the only output (whose supported mode has an even symmetry), and part of the power is radiated outside the component, but a non-negligible fraction is reflected back to the input waveguides.

This doesn't happen with 2×2 MMI as all the injected power is transmitted to the output waveguides with reduced reflection. Another alternative to deal with reflections would be to use tapered input/output waveguides, but that comes at the cost of longer components and a slightly more complex design while not solving the reflection problem of the 1×2 MMI used as a beam combiner.

The main parameters in designing 2×2 3dB splitter MMI are summarized in Figure 3.11, and the main figures of merit to be optimized are both the imbalance (the splitting ratio between both outputs when injecting only one input) and the overall transmission. Ideally, the phase relations between both outputs with respect to the inputs should be a 180° phase difference. When a phase difference between both inputs $\delta\phi$ is introduced, the output power should evolve as the $cos(\delta\phi)$ at one output while at the other it should evolve as $-cos(\delta\phi)$, thus a phase relation of 180° between both outputs.

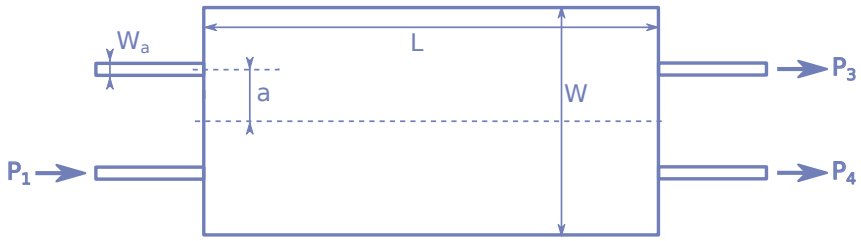

Figure 3.11: Parameters to be optimised in the design of a 2x2 MMI 3dB splitter.

From the above discussions, we already know that the larger the input, the better the transmission and the fabrication tolerances. This conclusion has been made under the assumption that no coupling exists between the input/output waveguides. To ensure that, a numerical simulation using the planar waveguide simulation whose principle has been introduced in chapter 2, of the beat length between two separated waveguides, has been made (We recall that those waveguides are 8 µm wide, have an undoped InGaAs core of 2.5 µm and a top cladding of 4 µm undoped InP). It showed that for a waveguide separation greater than 2 µm, the beat length between the odd and even super-mode exceeds 100 µm, which means a coupling coefficient on the order of 0.01%. This value of 2 µm (thus $a = 5$ µm) waveguide separation as therefore been chosen as the lower bound in the design process, fixing at the same time the lower bound for W, at 18 µm.

For the choice of the optimal width (and length) of the MMI, we took inspiration from the work of Hill et al. [152]. In his paper he studied the imbalance and insertion loss properties of 2×2 MMI defined as (see Figure 3.11 for the notations of the power injected P_1 and extracted P_3, P_4) :

$$\text{Insertion loss} = -10log\left(\frac{P_3 + P_4}{P_1}\right) \tag{3.20}$$

$$\text{Imbalance} = 10log\left(\frac{P_3}{P_4}\right) \tag{3.21}$$

In particular, Hill showed that the optimal width of the access waveguides was on the order of 0.3 times the width of the multimode section to minimize the imbalance (and it was shown to be

true for both paired and general interference MMI). Moreover, he showed that slight deviation from the optimal position of the feeding waveguides could be detrimental to this imbalance, especially in the case of the general interference MMI where only a small region in terms of waveguide position and width is presenting very low imbalances. Those findings are the starting point of our design process. We studied for multiple values of the ratio W_a/W in the proximity of 0.3, the simulated performances of the 2×2 MMI for various waveguide separation (parameter "a") and at the targeted wavelength 9.1 µm both for the general interference case and the paired interference case (access waveguide at W/3 and 2W/3, please refer to page 63). The choice of an optimal design was then made in both case by the determination of the most robust design, in that a small change of the ratio W_a/W or of the waveguide position a should have the lowest impact on the performances, while guaranteeing overall good performances (imbalances below 0.22 dB or 5% and insertion losses below -0.5 dB). A special care is taken on the MMI bandwidth in that process via the study of the impact of small changes of the optimal length on the imbalance. This design process led us to the following two designs, found to be optimal, Figure 3.12 for the general interference 2×2 MMI, and Figure 3.13 for the paired interference one. Their dimensions are presented in Table 3.1.

In both cases, the simulated performances show excess losses below -0.5 dB for a large length tolerance band greater than $\pm 10\mu m$ around its optimum. A similar band ensures imbalances below 0.15 for the general interference design and 0.35 dB for the paired interference design. In terms of spectral bandwidth those design should meet the targeted performance for imbalance (imbalance below 5%) on a spectral band around 0.4 µm wide centred at the targeted 9.1 µm wavelength using the uncertainty relation Equation 3.17. In order to check the validity of the assumption leading to Equation 3.17 and Equation 3.18, we numerically simulated two devices with a length variation of $\pm\delta L = 20\mu m$ (gray shaded area on both Figure 3.12 and Figure 3.13) for a theoretical added excess loss of -1 dB (yellow shaded area on both Figure 3.12 and Figure 3.13). Those two simulations are shown as dotted gray lines on both figures and show that their peak performances are indeed within the constraint represented by the yellow shaded areas in both cases, while the imbalances are not changed to a detrimental extent and are still below 0.4 dB (less than 10 percent). Moreover, it is also interesting to note that the optimized general interference design found with this method has its access waveguide placed near the edges of the multimode section, a finding also reported in [152].

MMI 2×2	W [µm]	L [µm]	a [µm]
General Int.	25.6	494	8.26
Paired Int.	27.8	194	5.18

Table 3.1: Dimensions of the 2×2 MMI 3dB splitter with 8 µm access waveguides.

3.1.3 Fabrication

The fabrication process of those passive components is quite simple. The structure, made of 2.5 µm undoped InGaAs and 4 µm undoped InP, is grown by MOCVD on a 2 inches InP n:1e17cm^{-3}

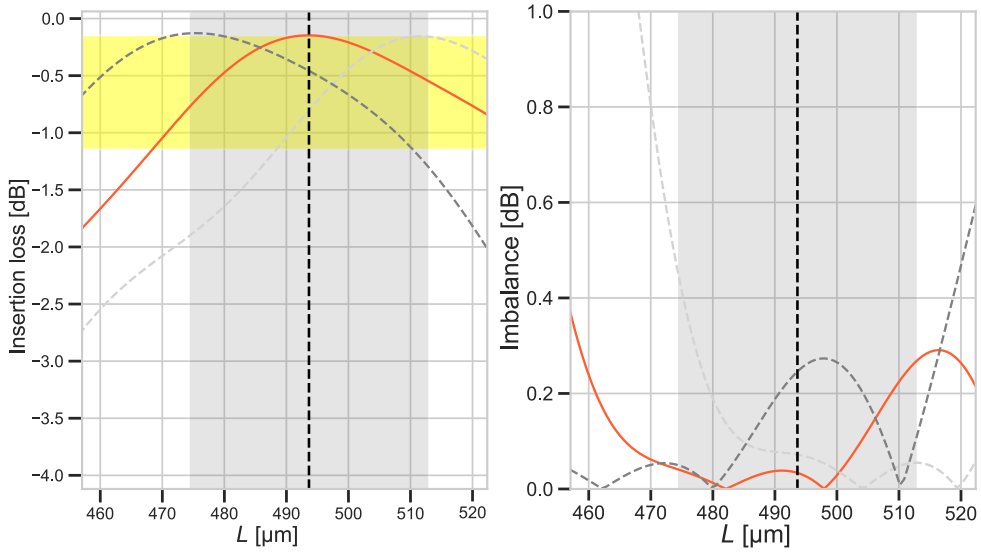

Figure 3.12: General interference 2×2 MMI performances simulated (orange curve). The dark and light gray curves correspond to the performances simulated of the same design with a $\pm\delta L$ length. The dark gray area is the corresponding $2\delta L$ length band around the optimal length, limiting the excess loss to -1dB.

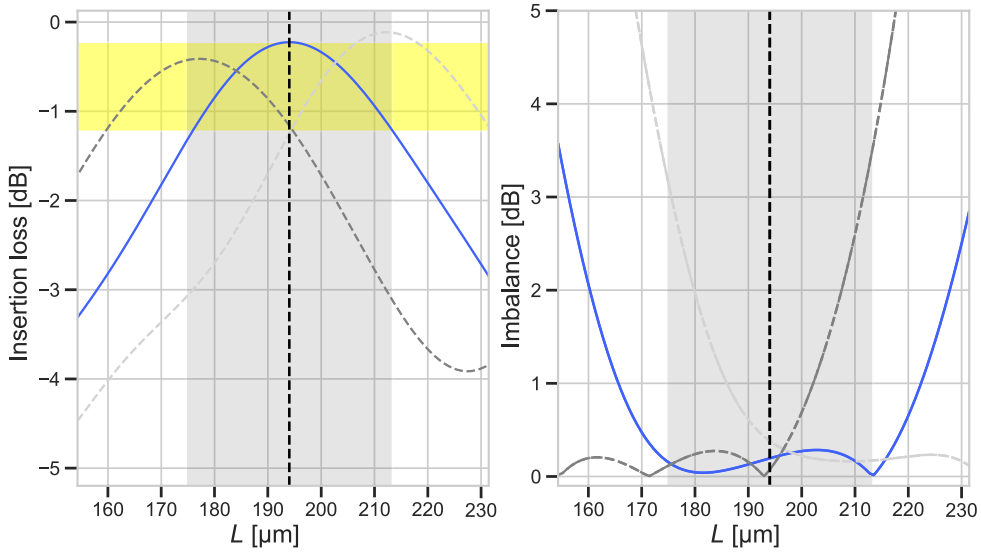

Figure 3.13: Paired interference 2×2 MMI performances simulated (blue curve). The dark and light gray curves correspond to the performances simulated of the same design with a $\pm\delta L$ length.The dark gray area is the corresponding $2\delta L$ length band around the optimal length, limiting the excess loss to -1dB.

substrate. The usage of a doped substrate is required by the used dry etching recipe on our available *Inductively Coupled Plasma* (ICP) chamber. A thick 1.2 µm SiN film is then deposited on the whole sample by *Plasma Enhanced Chemical Vapour Deposition* (PECVD) which is then locally opened with a lithographic step and a fluorinated *Reactive Ion Etching* (RIE) plasma etch to define the MMI. This dielectric film then serves as a hard mask for the ICP-RIE dry etch used to define the MMIs. A Cl_2:CH_4:H_2 18:8:4 sccm recipe is used with the following etching parameters : pressure 2 mTorr, RIE power 100 W, ICP power 1200 W and a fixed carrier temperature of 60°. To allow the temperature of the sample to effectively build up and for the etching to go well, the sample is placed without thermal grease on the carrier. The remaining hard mask is then removed using the same RIE recipe previously used. The resulting 2×2 MMI fabricated are shown in Figure 3.14. In this fabrication process, 8 length variations by step of $0.5\delta L$, ensuring a maximal -1dB loss, are processed around the optimal design. Multiple other optimized designs of 1×2, 2×2 paired and general interference MMIs and 2×4 90° hybrid MMIs with access waveguides 6, 8 or 12 µm wide are processed, as well as a sample composed of straight waveguides in order to be used as references for insertion loss measurements.

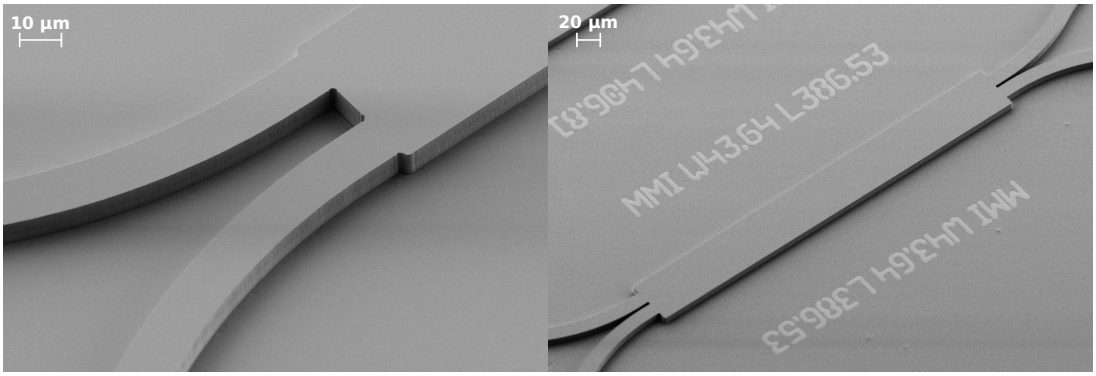

Figure 3.14: SEM picture of two fabricated 2×2 MMI 3dB splitter, general interferences design (Left) and paired interferences design (Right)

Then the wafers were thinned down to 150 µm and every sample (made of 9 different length variations of the same MMI design) was cleaved. A thin film of Y_2O_3 has been deposited on the output waveguides cleaved facet by sputtering, to act as an anti-reflection coating. The 1400 nm thick film partially delaminated from the sample, nevertheless some waveguide seemed to be intact and apt to be optically characterized. An image of the resulting output facet of a sample is presented in Figure 3.15.

Figure 3.15: Optical microscope image of an AR coated output facet of 2×2 MMI samples. Multiple "cracks" on the AR coating are clearly visible and some facet seam to have been damaged in the process.

3.1.4 Performances

In order to characterize the performances of the fabricated 2×2 MMIs, we designed the following characterization setup Figure 3.16. An external cavity quantum cascade laser (ECQCL, a MirCat™) is used as a widely tunable coherent source for the characterizations. It is split ino two different branches using a 50/50 ZnSe beam splitter. One of the beams is then delayed by a piezoelectric delay line with a nano-metric resolution (Thorlabs™NF15AP25 stage). The use of prisms guaranties the auto-alignment of the beams in this delay line throughout its motion. A slightly tilted mirror allows injecting the delayed beam into a different input waveguide of the MMI through an aspherical lens. A 2° tilt is enough to focus the delayed beam 100 µm away from the direct beam, thus addressing the two inputs of the MMI independently. The output of the MMI is then collimated and focussed with a magnification (here roughly 8 times) on a LWIR camera (WinCamD-IR-BB from DataRay), allowing clear distinction of the two output waveguides. The injection and collimation lenses, as well as the component, are placed on micrometric tri-axis stages. A pre-alignment of all beams without the component is performed, then the component is placed and aligned, and the collimation lens translated a distance equal to the length of the component.

The characterization of the imbalances (which we refer as the splitting ratio in the following) follows the procedure hereby explained. The laser beam is injected in only one of the input waveguide of the MMI at a time (we use only one branch of the Mach-Zehnder setup presented in Figure 3.16) and a scan of the wavelength if performed while imaging the output waveguides using a LWIR camera. For each wavelength, a mean background is made of the average of 10 images recorded with the camera integrated shutter. This background is then subtracted from another set of 10 images averaged, recorded without the camera shutter. That way, we limit the impact of any temperature deviation of the camera and average some low frequency sources of noise. The power at one output is then directly proportional to the pixel sum around the waveguide output. We estimate it by the sum of a 15 pixels square around the visible output waveguide. Slight change in dimension and position of this square didn't produce a substantial difference in the results in comparison to the estimated measurement uncertainties. The latter are calculated by repeating the same measurement multiple times (at least 3 times) on the same component, with misaligning and re-aligning it between every measurement. The mean values and deviations are figured respectively as continuous line and shaded area on Figure 3.17.

Phase relations are measured using a similar procedure, except that both beams are injected into the 2 input waveguides of the MMI, and the delay line scanned for all measurement wavelengths. This forms a set of 2 interferograms for each scanned wavelength. Those are cleared from high-frequency noise in the Fourier domain and renormalized between -1 and +1 (as we are only interested in the phase for that measurement, the amplitude would be an unnecessary fitting parameter). The delay is then corrected assuming a linear variation of half a scanned wavelength of the delay between each consecutive extrema in the interferograms (we use the highest throughput interferogram for that). Then the phase relation is globally fitted on both interferograms. The result is presented in Figure 3.17 b) for the best performing 2×2 paired interference MMI.

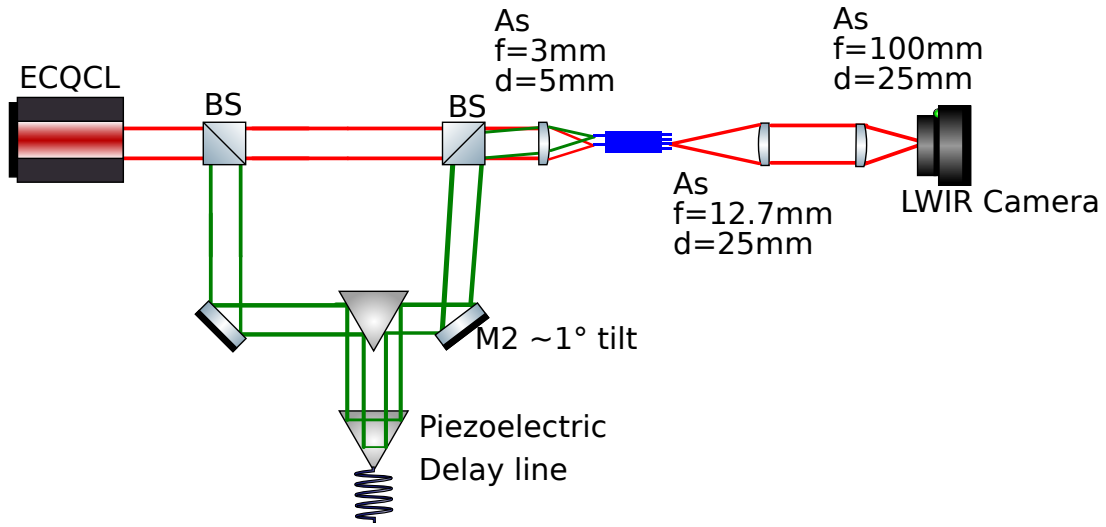

Figure 3.16: Optical setup used for the characterization of the 2×2 MMI splitting ratio and output phase relations. ECQCL : External Cavity Quantum Cascade Laser, BS : Beam Splitter, As : Aspherical lens, M : Mirror.

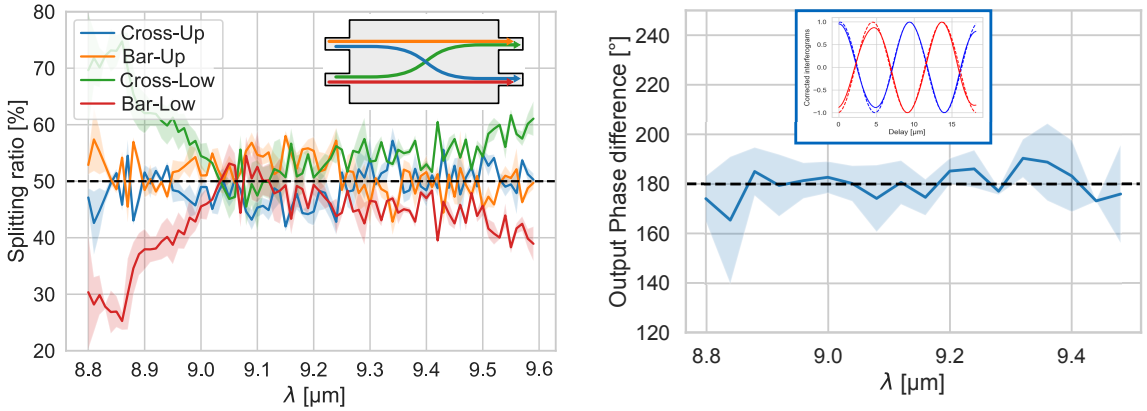

(a) (b)

Figure 3.17: Measured performances of the 2×2 paired interferences MMI of length $L_{opt} + 1/2\delta L$. a) Splitting ratio and b) Phase output relation. The inset shows one of the processed interferogram and fitted phase relation for a wavelength of 9.08 µm.

Its splitting ratio show an ± 8% excursion from the ideal 50% on the 9 to 9.4 µm spectral band and phase errors from the ideal 180° below ±10° on the 8.9 to 9.3 µm band. The uncertainties shown as shaded areas on the figures comes mostly from the laser instabilities due to mode hopping caused by feedback in the cavity, as the input facet are not AR coated. On Figure 3.17a) an asymmetry in the performances can be seen whether the beam is injected in the upper or the lower branch of the MMI. This might come from either an asymmetry on the MMI itself or, most likely, in the output facet of the waveguides themselves, as we have noticed that some of them were damaged or had delaminated AR coating. Those results are comparable to the ones reported in [20] on Y junction and directional couplers. Very little performance reports of MMI devices were found in the literature in the LWIR spectral band (except for [153] where is presented a 1×2 SiGe bases MMI) as they seem to be considered as, to the best of my knowledge, more a mean to an end than a device to effectively optimise and report on at LWIR wavelengths. Some other work has been dedicated in this spectral band, to the development of photonic integrated beam combiners for coherent detection, but using dielectric loaded surface plasmon polariton waveguides (DLSPP) in "Y" junction geometries. Nevertheless, the insertion losses, let alone through the S-bend of a Y junction, are quickly growing with the offset such that it exceeds that expected for MMI beam combiners [154], without considering the injection losses due to mode mismatch with the near Gaussian laser mode. On the other hand, the main advantage of using DLSPP beam combiner lies in the greatly facilitated monolithic integration of QCL, optical pre-amplifier and QCD [155], which is yet the only alternative to butt-joint regrowth of passive waveguide structures.

One might have noticed that no characterization of insertion losses is reported here. During the thinning process of the straight waveguides planned for that measurement, the latter were damaged to an extent where their insertion losses were higher than that of the MMI. Therefore, the optical characterization of the MMI insertion losses could not be presented here. Nevertheless, the phase relation and splitting ratio being close to the theoretical ones, we expect them to be low, close to the theoretical ones, as those devices phase relation, splitting ratio, and transmission are closely connected.

4 Conclusion of the chapter

This chapter has focused on optical waveguide geometries and optical losses in photonic circuits. The choice of ridge waveguide has been justified for integrability of the developed components with an already developed QCL technology. Then different approaches to designing the main photonic passive building blocks (bend optimization, taper, MMI) have been presented which are used in the design of all components presented in this thesis. In particular, we presented the theoretical background behind MMI and used it to design fabrication tolerant, broad band, 3-dB splitters, the main component used in photonic circuits. Indeed, in the MWIR and LWIR spectral band, the direct quadratic detection is less performing than the field detection, and therefore heterodyne detection scheme is likely to be the solution for detection at those wavelengths. For that purpose, integrated beam combiners and beam splitters are essential components, and es-

pecially for coherent telecommunication applications. The ones based on MMIs, presented in this chapter, have shown very promising results for future LWIR photonic integrated circuits, and especially with respect to their robustness to fabrication variations. To the best of our knowledge, the performances reported here of the 2×2 MMI as a beam combiner, are at the state of the art in the LWIR spectral band. But very little report of such component's performance were found in the literature for LWIR operation. In the next chapter we will discuss the implementation of an active function, essential to coherent telecommunication systems, the phase and amplitude modulator.

Chapter 4

Integrated phase and amplitude modulator for FSOC

Objectives

One key component for optical communications is the optical modulator, whose function is to encode the information onto an optical carrier. In this chapter, we focus on the development of an integrated version of the optical modulator operating in the LWIR domain, and more precisely around 9 µm. Firstly, we will present the different physical effects that can be exploited to realize electro-optic modulation, and we will justify our technological choice based on the intersubband Stark shift in asymmetrically coupled quantum wells. Based on this latter approach, two designs of optical modulators in waveguide geometry, optimized for phase modulation, will be detailed and their implementation in a fully integrated emitter platform discussed. Different characterization strategies will be presented, with specifically designed components layouts that have all been fabricated in this thesis. Finally, we will present the measured performances of a modulator, and we will discuss the experimental results.

Contents

1 Optical index modulation in the LWIR range

The first part of this chapter focuses on the different physical effects that can be exploited to produce an electro-optic modulation in the LWIR wavelength range. One can differentiate between two kinds of modulation, as discussed in chapter 2 :

- The amplitude modulation, produced by a variation of the optical mode propagation losses, which is currently referred to as **electro-absorption** modulation.
- The phase modulation, produced by a variation of the optical mode phase velocity, which can also be referred to as **electro-refraction** modulation.

At the end of a waveguide modulator section of total lentgh L, the output optical field E_{out} can be written as :

$$E_{out} = E_{in} exp\left(-\frac{\alpha_{eff}(V)}{2}L\right) exp\left(-j\frac{2\pi}{\lambda}n_{eff}(V)L\right) \tag{4.1}$$

E_{in} being the optical field at the input, α_{eff} is the optical mode power attenuation (expressed in m^{-1}), and n_eff the optical mode effective index. Both α_{eff} and n_{eff} can be modified by changing the applied bias V across the device. The operation of an electro-absorption modulator relies on the amplitude variation introduced through the α_{eff} term, while an electro-refraction modulator acts on the n_{eff} term to modify the phase of the output field.

There are a multitude of physical effects that can be used to induce electro-optical modulation in semiconductors, and especially electro-refraction modulation, which is the one we are particularly interested in (see chapter 2). We will present the ones that are particularly suited for the LWIR spectral band, as we aim to work at a wavelength of 9.1 µm. That clearly excludes all the effects that result from electronic transitions occurring around the energy band gap, as is the case of the Franz-Keldysh effect [156, 157] or the interband quantum confined stark effect [158, 159], two widely used effects in the SWIR band, that are anyway much more efficient for electro-absorption, rather than electro-refraction modulation.

Pockels and Kerr effects : are respectively linear and quadratic effects occurring in some material when exposed to high electrical field (optical of not). The Pockels effect, is an effect present in non-centrosymmetric crystalline materials, as is the case of most III-V semiconductors such as InAs, GaAs or InP [160, 161]. On the other hand, the Kerr effect is present in all crystals, but is generally much weaker than the Pockels effect.

The linear change in refractive index Δn provided by the Pockels effect depends on the particular crystalline orientation and, in the case of Zinc-Blende crystals, is maximized for a wave propagating at an angle of 45° with respect to the (010) and (001) crystalline axes. The resulting optical index variation under an applied quasi-static electric field E_x along the (100) x-direction is then [160] :

$$\Delta n_{\pm} \approx \pm\frac{1}{2}n_0^3\gamma_{41}E_x \tag{4.2}$$

where n_0 is the material refractive index at zero bias (i.e. without the presence of Pockels effect), and γ_{41} the non-zero component of the linear electro-optic effect tensor for the Zinc-Blende

structure. The + sign holds for the $(0\bar{1}1)$ direction and the − one, for the (011) direction. At that point, we can draw two main considerations :

(i) The first one is that for standard epitaxial structures that are grown along the (100) direction, as is the case for those on standard InP substrates, only TE polarized optical fields will be impacted by Pockels effect. That prevents using Pockels effect with TM polarized light produced by QCLs, or it would require the use of polarization rotators that are not available in the LWIR domain (neither bulk nor photonic integrated versions).

(ii) Secondly, the literature is very sparse concerning any reported use of linear electro-optic materials in the LWIR spectral band. Nevertheless, it appears that these effects happen near electronic resonances as described by the model of Hagn [162], which in the SWIR band is the gap electronic transition. Therefore, material candidates having a substantial linear electro-optic effect in the LWIR spectral band would likely have electronic transition in that spectral band two. Moreover, it should also have a symmetry structure allowing TM polarized light modulation. Such materials could be GaSe [163], organic crystals [164] or polymers [165]. Unfortunately, the few interesting materials, especially polymers, often show strong absorption in the LWIR and are not adapted to monolithic integration, which is our ultimate goal. Therefore, Pockels effect is not considered a viable option for LWIR optical modulation in the framework of this work.

Plasma dispersion effect : it is the effect produced by free carrier density modulation. Under illumination, the free carriers in a material oscillate with the optical electric field, creating a self-induced contribution to the electric field as discussed in chapter 2. The plasma dispersion effect can be modelled as an additive Drude contribution to the dielectric constant, which impacts both the real and the imaginary parts of the material refractive index. It is possible to show from that model that the variation of the optical refractive index change, Δn, with the variation of the free carrier concentration, writes as [166]:

$$\Delta n \approx \frac{-e^2\lambda^2}{8\pi^2 c^2 \varepsilon_0 n}\left(\frac{N}{m_e}+\frac{P}{m_h}\right) \tag{4.3}$$

with e the elementary charge of the electron, λ the free space wavelength, c the vacuum velocity of light, ε_0 the vacuum permittivity, N and P the electron and hole doping concentrations respectively, m_e the electrons effective mass and m_h the holes effective mass (taking into account heavy and light holes). On the other hand, the free carrier absorption, which depends on the plasma frequency, writes as [34] :

$$\alpha_{fca}(\omega) = \frac{\omega_p^2 \gamma_c}{n_r c(\omega^2+\gamma_c^2)} \quad \text{with} \quad \omega_p^2 = \frac{N_c e^2}{\epsilon_0 m^*} \tag{4.4}$$

where N_c is the free carrier density, m^* the effective mass, γ_c the free carrier scattering rate (which depends on the carrier mobility), and n_r is the material optical index in the absence of free carrier effects. At high frequencies, both the optical refractive index and absorption tend

to evolve as λ^2. In practice, the dependence of γ_c with the doping modifies this dependence and both effects are slightly more impacted by the wavelength as they evolve more as λ^p with p between 2 and 3 [167].

Modulators using plasma effect in a waveguide geometry can be made of P-N junctions, P-I-N junctions or capacitive junctions. Each of the aforementioned approaches has advantages and drawbacks, that are discussed in [168]. The typical dimension of the modulation of carrier density in the depletion region of a P-N junction or the accumulation layer of a capacity, embedded in an optical waveguide, do not scale with the optical wavelength. On the other hand, the optical mode cross-section itself, scales roughly as the square of the wavelength. Therefore, the overlap of the optical mode with the depletion/accumulation region should evolve approximately as λ^{-1}. In fine, as the plasma effect on the optical index evolves as λ^2, the overall performance of a modulator should scale up roughly proportionally to λ. In comparison to SWIR plasma-effect based modulators, one could expect similar performances in the LWIR domain, as shorter components would be needed, compensating for the larger waveguide dimensions and thus geometrical electrical capacitance.

Inter-subband Stark shift : is an effect occurring in quantum wells and enhanced in asymmetric quantum wells, where the energy of the transition between two (or more) bound electronic states can be tuned by applying an external electric field. It was first proposed by Yuh et al. [169] in the early 1990s to use asymmetrical quantum well structures to control the absorption with an applied bias. The first experimental demonstrations of modulators using this principle came shortly after [170, 171, 172]. The optical transition between two electronic confined states in a system of coupled quantum wells, that leads to a Lorentzian like contribution to the optical index (see chapter 2), is made tunable by an external applied bias, by breaking the symmetry of the quantum wells system. That can be implemented either by using step quantum well as suggested by Yuh et al. and reported by Dupont et al. [169, 172], or in asymmetric coupled quantum wells (sometimes referred to as Electron Transfer Infrared Modulator - ETIM -) [173, 171, 174]. The advantage of that latter approach lies in the versatility introduced by thin barriers between two quantum wells Figure 4.1. The reduced thickness of the barrier has a crucial impact both on the oscillator strength of the inter-subband transition, and on its tunability with the applied bias. Indeed, the Stark shift occurring in such asymmetric-coupled quantum wells is roughly equal to the potential drop between the wave functions barycentres, and linear with the applied bias [174]. When using those structures for an enhanced Stark-shift, as reported in [174], one can benefit from a very strong and widely tunable modulation of the optical index as shown in Figure 4.1b), and without charge transfert (contrarily to the structures using electron transfer [173, 171]). This should allow the full exploitation of the very high intrinsic response time of those unipolar devices without the limitation of carrier transit time.

For such reasons, among all considered effects, the inter-subband Stark shift appeared as the most promising to realize fast and linear long wave-infrared modulators. Another important asset of such an approach is that it directly stems from the Quantum Cascade technology, and therefore provides a consistent material platform for further integration, which it has already

been successfully used with [175]. The deep ridge waveguide geometry selected, as discussed before, should greatly reduce the geometrical electrical capacitance of the device, which was a limiting factor in previous work using that effect [175]. Moreover, and contrarily to the plasma effect seen above, the free carrier absorption with those structures can be very low while conserving a high doping in the quantum wells, as a TM polarization (electric field in the growth direction) is not affected by it (see chapter 2 discussion on quantum well dielectric function).

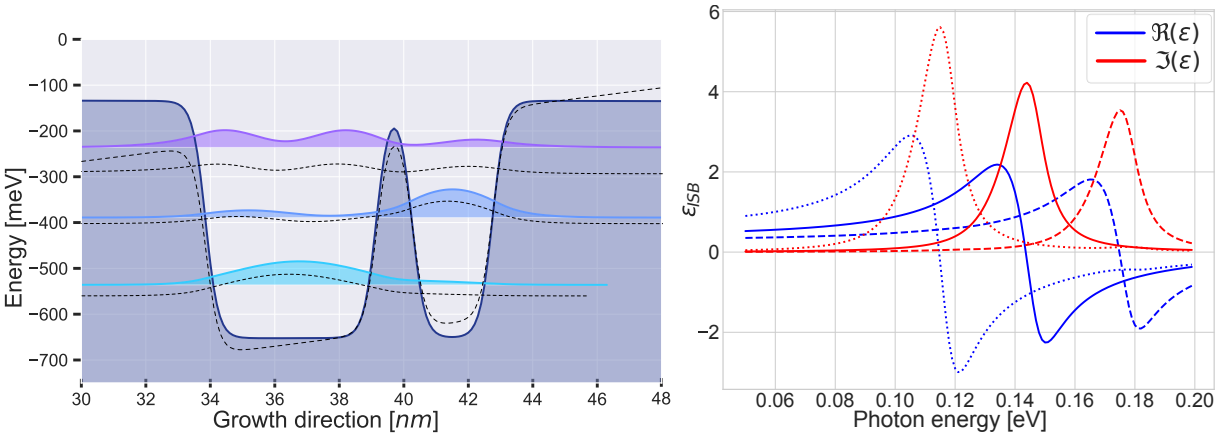

(a) (b)

Figure 4.1: a) Example of asymmetrically coupled quantum wells system. In continuous line : at a zero electric field, in dotted lines : at a 100 kV/cm applied electric field. b) Evolution of the dielectric constant associated to the inter-subband transition (ISB) for different values of the applied electric field. Dotted line : -100 kV/cm, continuous line : 0 kV/cm, dashed line : 100 kV/cm.

Other effects can be exploited to realize optical modulation in the long wave-infrared domain, we can cite phase transition in materials such as vanadium oxide [176], liquid crystal reorientation [177] or carrier density modulation in graphene [178]. Since all those are at an earlier stage of development, and yet hardly compatible with integrated photonic circuits on a chip scale, they will not be further discussed in this thesis.

After having briefly introduced the principal effects that can be used to modulate the optical index of a material in the LWIR spectral band, and before moving forward to the discussion of the integration strategy and the optical design of the waveguide phase modulators using asymmetrical coupled quantum wells, we aim to briefly present the state of the art of optical modulation in the LWIR spectral band, and compare it to the performances obtained in the SWIR range, which currently represent the spectral band of reference for established FSOC.

2 State of the art of optical modulation, SWIR versus LWIR

In order to give an accurate and fair comparison between the existing technologies in the SWIR and the LWIR, and to discuss the implementation of optical modulation in both wavelength domains, we will first introduce the main Figures Of Merit (FOMs) that can be currently found

in the literature. We refer the interested reader to [168, 23] for further details and deeper discussion.

2.1 Figures of merit (FOM)

The modulation efficiency is one of the key FOM to describe the performance of a modulator. Two definitions are currently used in the literature, whether the modulator is based on electro-absorption or electro-refraction effects. In the first case, the variation of the absorption between the "on" and the "off" states normalized by the "on" state absorption (we consider the "on" state to be the one of minimal absorption) is used.

$$\eta_{eff} = \frac{\alpha_{off} - \alpha_{on}}{\alpha_{on}} \tag{4.5}$$

In the case of an electro-refraction modulator, the modulation efficiency is rather defined as the ability of a modulator to produce a specific phase shift for a given bias and length. It is generally expressed as the product between the bias V_π and length L_π necessary to obtain a phase shift equal to π at the applied bias V_π:

$$V_\pi L_\pi = V_\pi \frac{\lambda}{2\Delta n_{eff}(V_\pi)} \tag{4.6}$$

where $\Delta n_{eff}(V_\pi)$ is the optical mode effective index variation at the bias V_π (with respect to a zero-bias or a reference bias).

The optical losses depend on the active region intrinsic optical performance, but also on its implementation in a photonic integrated platform in terms of fabrication quality and device geometry. Concerning the active region, optical losses are directly linked to the absorption coefficient α_{eff} of the optical mode that propagates across the structure, they are due to material absorption in the different materials such as free-carrier absorption or other absorption mechanisms. On the other hand, the fabrication process can introduce scattering losses associated to the sidewall roughness of the waveguide. Access waveguide injection, transitions, and bending sections (that have already been described in chapter 3 are related to the particular geometry of the component, and the architecture of the photonic circuit. All the optical losses can be generally regrouped into a single term indicated as "insertion loss", which is defined as the overall transmission of the modulator when it operates in its "on" state, and is given in dB (one can define an insertion loss for all specific constituent of a complex photonic circuit, i.e. modulator, passive waveguide combiner etc..., or for the whole assembled component, i.e. a Mach-Zehnder modulator for example.) :

$$IL = 10log\left(\frac{P_{out}}{P_{in}}\right) \tag{4.7}$$

The extinction ratio is similar in its definition to the above insertion loss, except that the ratio of the output power between the "on" and the "off" state is used :

$$ER = 10log\left(\frac{P_{on}}{P_{off}}\right) \tag{4.8}$$

It describes the ability of an electro-absorption modulator to produce well-defined intensity levels to encode the information.

The electro-optical bandwidth describes the ability of the modulator to transmit data at a given rate. This bandwidth is influenced by the characteristic dynamic properties of the active region, and by the device geometry as well. One example of the former can be the intrinsic time of the physical effect exploited to perform the optical modulation (for example, the recombination time of minority carriers in a P-N junction). The access time of the electrical signal through the electrical contacts, usually described as a geometrical R-C filter, is mostly linked to the device geometry.

The electro-optical bandwidth of a modulator can also be greatly impacted by impedance mismatch between the co-propagating electrical and optical signals. This effect can be detrimental as the modulator dimension approaches that of the RF wavelength, and specific RF lines must be carefully designed in that case. Travelling wave electrodes are a great way to cope with these co-propagation effects at the cost of an added complexity [23].

We also can cite the impact of photon lifetime in modulators using resonant effects, that could limit the bandwidth.

The energy consumption is the last FOM that we present here. This FOM is estimated by considering the dissipated energy per bit, when used with two levels encoding (OOK or BPSK). In a simplified picture, where the modulator is seen as a capacitor which is charged or discharged when changing the bit, the energy consumption can be written as :

$$E = \frac{1}{4}C(V_{dd})^2 \tag{4.9}$$

where V_{dd} is the supply voltage and the modulator is driven in-between a 0V and V_{dd} bias [179]. In practice this energy has to be measured or be adapted to the actually used modulator technologies and driving circuit.

2.2 State of the art of electro-optical modulators

Until now, the research on electro-optical modulators has been mostly focused on the SWIR wavelengths. The development of high-performance and telecom-grade components in the SWIR domain has been especially motivated by the evolution of optical communications on one hand, driven by the increasingly higher needs for high-speed telecommunications, and the progress of photonic integrated circuits on the other hand, pushed by the increased demand of miniaturization to cope with low fabrication costs and high-energy efficiency. Contrarily to the SWIR,

to the best of our knowledge, there has not been any reported integrated waveguide modulator operating in the LWIR spectral band so far. Therefore, we will present a non-exhaustive state of the art of recently reported performances obtained in the SWIR, that will set the tone, and be the ultimate goal for future LWIR photonic circuits. Detailed review of pre-2015 results can be found in [180] and more recently in [181] for the MWIR spectral band.

2.2.1 SWIR optical modulators

In the SWIR spectral band, most of the electro-optical modulators employed in telecom systems are based on the plasma effect (in PN, PIN, or capacitive junctions) or the quantum confined Stark effect for commercial application. Those are indeed technologically mature, often CMOS compatible, and therefore attract a lot of interest for commercial applications. Devices based on carrier injection (PIN junctions, for example) have been shown to be mostly limited by the minority carrier lifetime across the junction, and their electro-optical bandwidth is thus typically limited to the GHz range without using electrical signal pre-processing [168]. On the other hand, modulators based on the plasma effect are mostly using the depletion of PN junctions, or accumulation (or desertion) effect in capacitive junctions, which are reasonably fast phenomena, compatible with high-speed applications. Indeed, components based on carrier depletion show electro-optical bandwidth from 30 to 60 GHz with $V_\pi L_\pi$ ranging from 1 to 3 V.cm in carrier depletion modulators [182]. Slightly lower frequency bandwidth, from 10 to 40 GHz, have been reported for capacitive junction modulators, but those values have been obtained for a much lower $V_\pi L_\pi \approx 0.05$ V.cm [183, 184, 185].

More recently, modulators based on Pockels effect in lithium-niobate or other electro-optical materials, has shown promising performances when coupled to travelling wave electrodes. Electro-optical bandwidth up to 70 GHz with low insertion losses of 0.2 dB and $V_\pi L_\pi$ around 2 V.cm have been demonstrated [186]. When using plasmonic structures, those performances can be further pushed, up to electro-optical bandwidth above 170 GHz and $V_\pi L_\pi$ as low as 0.45 V.cm, as reported in [187]. In general, the recent trend for compactness and energy efficiency has pushed the scientific community towards the development of plasmonic modulators [180], in order to benefit from the significantly stronger light-matter interaction provided by the plasmonic architecture.

2.2.2 MWIR and LWIR optical modulators

Moving toward higher wavelengths, very few demonstrations of optical modulators in waveguide integrated geometry have been reported so far. Contrarily to the LWIR spectral band, where reports on electro-optic modulators are very scarce, in the MWIR, there has been a growing interest in the past few years, with a rising number of demonstrations concerning modulators based on carrier depletion, injection, quantum confined Stark effect, or Pockels effect in lithium niobate platform.

Electro-absorption modulators based on quantum confined Stark effect have struggled to reach the gigahertz landscape in the LWIR, and even lower bandwidth have been reported for

MWIR based devices employing the same approach [181]. It is worth noticing, however, that a very recent published work has theoretically discussed the possibility to achieve potentially much higher performances, with 60 GHz electro-optical bandwidth for 12 Vpp and insertion losses below 2.5 dB, for SiGe-based modulators operating in the LWIR [188].

Lithium-niobate modulators in the MWIR spectral band are rarely operating at bandwidth exceeding 10 GHz, with driving voltages above 10V and $V_\pi L_\pi$ above 3V.

Several studies have been reported using hybrid plasmonic waveguides in combination with graphene, but in the related works, their operating frequency bandwidth is rarely indicated and the very few reported values are not exceeding 10 MHz, which reveals their early stage of technological maturity [181].

Finally, a few demonstrations of capacitive modulators on the SiGe platform have been reported, that worked both in the LWIR and MWIR domains, but their performance was limited to the GHz range and low extinction ratio (around a dB) for a strong applied bias (around 8V) [189, 190].

A few other reported work in the LWIR optical window also showed promising results in non-integrated non-waveguide geometries, but nevertheless worth mentioning. Making advantage of polariton splitting in a reflective modulator, a modulation contrast between 20% and 30% with a -3dB electro-optical bandwidth around 750 MHz has been reported in [191]. Very recently, a LWIR modulator based on inter-subband Stark effect in asymmetrical coupled quantum wells, has been reported [192, 193]. The authors achieved a frequency cut-off on the order of 5 GHz, with an almost 3 dB modulation depth. The phase modulation, on the other hand, appeared small for the moment and limited to 5° for an applied bias excursion of $7V$. Similarly, a phase modulation of about 60° has been reported using similar meta-surfaces and coupled quantum well structures for a 6 volts bias excursion [194].

3 Integration strategy

Prior to focusing on the design and fabrication of the devices, one has to consider all the constraints due to the particular integration strategy chosen to combine all the components constituting the emitter (QCL, modulator and amplifier), and receiver (QCL, QCD, amplifier, and beam combiner) PICs of an integrated platform. Many integration strategies have been developed throughout the years, consisting in either fabricating all optical active and passive functions on the same wafer, or on discrete ones that are then assembled on a shared submount [195, 196, 197]. We here focus only on the emitter part, as this is the topic of this chapter, the receiver part being discussed in chapter 5.

The first possibility would be the heterogeneous integration, that involves the combination of components based on different material technologies in a common single photonic integrated circuit. This heterogeneous strategy consists for example in fabricating the active devices on the III-V (active) material, while the passive functions across the chip (routing for example) would be realized by using SiGe waveguides, that are compatible with MWIR and LWIR wavelengths [198]. This approach benefits from considerable advances in fabrication maturity of the SiGe

platform, which can reach very low propagation losses in the mid infrared wavelength, compared to other material systems, as discussed in chapter 3. The whole III-V active material can then be reported on the pre-processed Si/SiGe waveguides by molecular bonding [199]. The processing of the active components can be done right after. This method is convenient for the collective fabrication of a large quantity of similar active components, the entire active structure being deposited on all the hosting passive substrate. Despite these advantages, this method is hardly suitable in the case of the integration of a Stark modulator and a QCL on the same platform. Their active region being significantly different, it needs to be grown separately (for an external modulator at least, see [175] for an example of direct modulation with QCL and *Asymmetrical Coupled Quantum Wells* (ACQW)).

Another close solution to this is to grow the active components individually, and then to report them on the processed Si-SiGe hosting substrate with the so-called die-to-wafer bonding technique, before processing them. This strategy allows the integration of different active structures onto the same passive platform [200, 201]. These two methods of heterogeneous integration are illustrated in Figure 4.2.

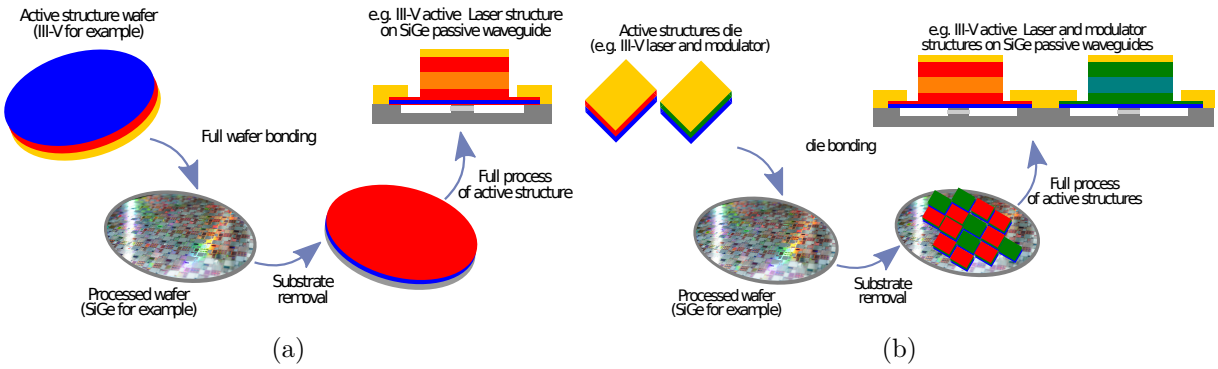

Figure 4.2: Two methods of hetero-integration process. a) Whole wafer bonding and b) die bonding of different active structures.

The second possibility is the homogeneous integration of active and passive components on the InP substrate. In that approach, the active waveguide structure (QCL, modulator and amplifier) can be grown on a passive waveguide structure during the same epitaxial growth. The optical coupling between active and passive waveguides is performed vertically by evanescent coupling and/or by adiabatically tapered sections. Both approaches have advantages and drawbacks, as discussed in [20]. Typical evanescent transitions from the upper to lower waveguide (and vice et versa) need a transition length of about 100 µm or more, this could considerably limit the electro-optical bandwidth of the modulator and the overall footprint, since it would require excessively long components (more than 200 µm long).

Alternatively, the homogeneous integration can be performed by successive localized growth (selective area growth or butt joint regrowth) of active and passive structures. The difficulty of such an approach lies in the diverse contamination from the etching and dielectric deposition steps that can have a detrimental effect on the quality of the epitaxial process, translating into fabrication-related issues and/or poor device performance [202]. Moreover, regrowth of

thin quantum wells, such as the ones employed in the active region of QCLs and QCDs, is challenging and still lacks of technological maturity. Homogeneous integration is schematically presented in Figure 4.3, in the practical case of a laser integrated onto a passive waveguide, with the vertical coupling obtained through the tapered section.

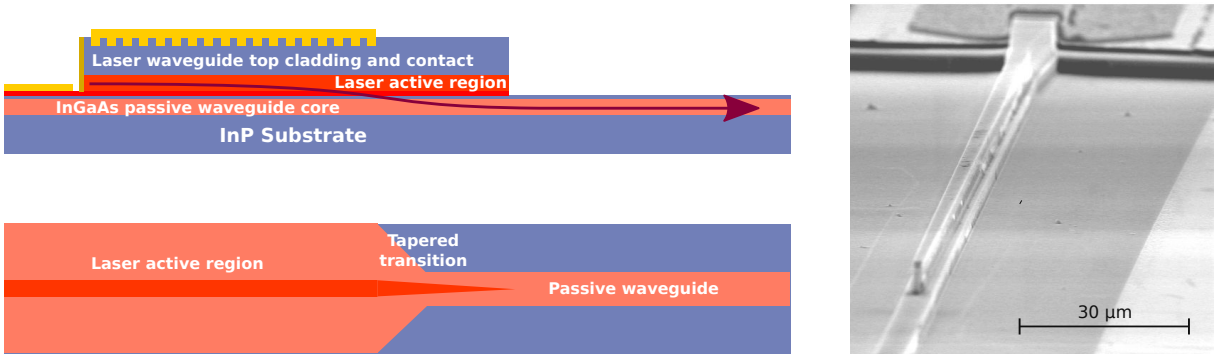

(a) (b)

Figure 4.3: a) Homogeneous integration of a laser and a passive waveguide in the InGaAs/InP platform. b) SEM picture of such a tapered device, taken from [20]

The approach retained in this work has been significantly dictated by the integration constraints defined in the framework of the collaborative European H2020 cFLOW project[1], to which this thesis work was largely associated. The fabrication process of the QCL emitter (which was led by mirSens[2], a partner of the cFLOW consortium) was already set up, so it largely defined the layout and integration approach for the other two components forming the emitter PIC. Therefore, the integration strategy retained was to process all the components individually, cleave them into discrete chips, and then assemble them on a common electrical submount in an epi-down configuration. This integration method, which in the cFLOW project was led by CSEM[3], is also referred to as hybrid integration in the literature.

The emitter design for this first generation of PIC is composed of individually cleaved chips for the QCL, the phase/amplitude modulator, and the optical amplifier, which are assembled in a butt-joint configuration as illustrated in Figure 4.4a. To that end, the processed individual components have different metallic layer thickness for the top gold contact, to be able to compensate for the different height of the components and thus align the three waveguide active regions. Those are then flip-chip bonded on an AlN carrier submount, chosen for its thermal and RF properties, with the electrical access and RF lines. The different gold thicknesses deposited on the active components, allow the formation of different eutectics with the AuSn solder on the submount, making possible to heat the individual chip to different temperature for the bonding while not remelting the other, the highest bonding temperature being used on the first bonded chip.

This method considerably relaxes the constraints on the processing side, the design of all active and possibly passive components can thus be optimized as would be the case for a homoge-

[1]https://cflow-project.eu/
[2]https://mirsense.com/
[3]https://www.csem.ch/

neous integration strategy. On the other hand, the heterogeneous butt-joint approach requires a compatible waveguide design for the vertical alignment of components (z-axis), a well planar top structure, and precise gold thicknesses of their top contacts. A precise horizontal (x and z-axis) positioning of the different chips is also required. A tolerance analysis, performed by CSEM on the alignment, showed that a spacing lower than 5 µm should ensure a coupling efficiency between the individual components greater than 50%. A variation of $\pm 2\mu m$ on the lateral and vertical alignment would produce respectively 10% and 20% more coupling losses, showing the challenges of this integration method.

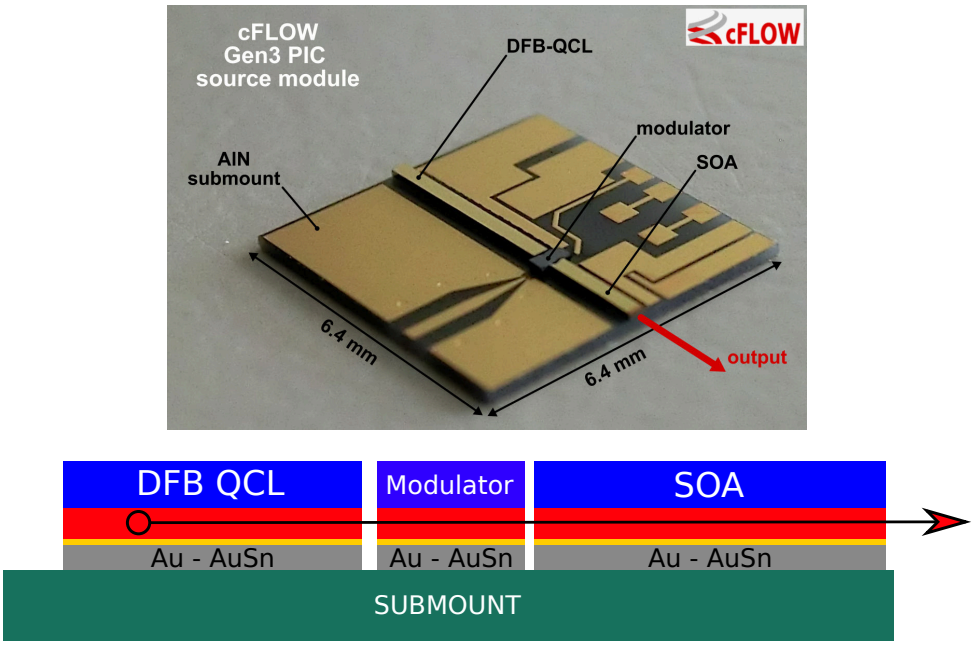

Figure 4.4: cFLOW emitter PIC integration strategy : (top) Epi-down, flip-chip, butt-joint integration onto an AlN submount performed by the CSEM, a partner of the cflow project, with the modulator designed and fabricated in this work. (bottom) Schematic lateral view of the emitter assembly. Credits for the picture go to CSEM.

In the next part, we will discuss some additional constraints induced by this heterogeneous integration scheme, both on the design of components and on their fabrication process.

4 Waveguide Stark phase modulator in the LWIR

At the beginning of this thesis, the ultimate goal was to design modulators showing high performance. For this, an approach based on an active region consisting of a high number of ACQW with a high doping level was initially investigated, which inherently results in a highly absorbing waveguide structure. As we will see later on, this is not an issue for the modulator section itself, since its optimal length is relatively short, and the resulting net absorption through its length is reasonable. On the other hand, a relatively thick and highly absorbing structure also means that "passive waveguide" sections from the same platform used for beam routing and guiding, have intrinsically high absorption losses two, unless low absorption passive waveguide structures are

used. This also set a challenge for the development of the integrated Stark modulator, independently of the chosen layout (whether it is a straight waveguide, a Mach-Zehnder configuration or a more complex photonic circuit such as the one presented in Figure 2.4 emitter), and underline the necessity to use low-loss passive waveguide structures with the high absorption modulator waveguide sections.

Initially, the process flow of the modulator was planned as follows :

- High-performance modulator structures fabricated from a single *Molecular Beam Epitaxy* (MBE)+MOCVD growth.
- Butt joint regrowth of thick undoped passive waveguides from InGaAs/InP (eventually employing iron doped InP).
- Use of semi-insulating substrate (iron doped InP) for enhanced RF compatibility.

That ambitious program supposed that previous development bottlenecks associated to the use of butt-joint regrowth of thick low-loss passive waveguide structures, and the dry etching of structures grown on semi-insulating substrates, to be available and reliable before the design and processing of the waveguide modulators. Unfortunately, those two building-blocks (whose development was not the topic of this thesis work), were still not available before the beginning of the thesis, nor have they in the time-frame of this work. Therefore, trade-offs on the design of components were made to cope with the technological constraints related to having high-losses passive waveguide sections, and to be compatible with the future generations of components based on the two above-mentioned building blocks (butt joint regrowth of passive waveguides and semi-insulating substrate processing).

These trade-offs and design adjustments also resulted in unforeseen difficulties that translated into a considerable accumulation of delay in the fabrication of the components, which also had a severe impact on the final characterization activity of the devices. For these reasons, in this chapter extensive discussion of the characterization results of the modulators and their performance, as is would ideally have been, will not be possible. Despite that, we will still present how we adapted the layout designs in the case of the current lossy waveguide structures, while ensuring that the characterization of components would still be possible with reasonable efforts. We will also discuss how each layout, designed for a precise and dedicated measurement, could be used to extract the full optoelectronic characteristics of the modulators. The task of in-deep and fully characterization of the devices will then hopefully be pursuit by the successors of this work.

4.1 Optical design and expected performance

In this first section, we will present the design of a waveguide modulator operating in electro-refraction mode in the LWIR ($\lambda = 9.1$ µm). The design can be decomposed in two steps. The first one is the design of the modulator active region, that is composed of a repetition of N periods of ACQW, which are placed in the core of an InP/InGaAs/InP waveguide and are illustrated in Figure 4.5a with the hereafter used notations. The optimization of the active

region is performed using the home-made anisotropic planar mode solver and Schrödinger-Poison band structure and electronic transport solver, whose theoretical background has already been discussed in chapter 2. Further informations on the latter can also be found in references [68, 69].

For the preliminary design of the modulator, we used a vertical waveguide structure that is summarized in Table 4.1. As previously mentioned, their top cladding and core layer thickness were matched to the ones of the QCL designed by another partner, to minimize the butt-coupling losses. The optical index of materials used in the simulations are the ones presented in [48] for InGaAs and AlInAs. For gold, we used the data reported by Palik et al. from [44], while for InP we used the model from Bi et al. [52], to which we added an additional Drude contribution calculated from values reported in [54], to account for the doping effect. The inter-subband contribution to the dielectric constant is calculated by the Schrödinger-Poisson solver (see Equation 2.43) and applied to the large quantum well L_{thick} (with a re-normalization of the plasma frequency by a factor L_{eff}/L_{thick} to account for the difference between the well dimension used in optical simulations, and the dipolar moment effective length of the inter-subband transition). The different degrees of freedom used in the design of the ACQW active region are the wells thickness, L_{thick} and L_{thin}, the barrier thickness L_{bar}, the separation between two ACQW periods L_{sep} and the doping concentration n_{2D} in the larger well. Those parameters are schematically indicated in Figure 4.5.

Material	Dop. [cm^{-3}]	Thick. [nm]	Repetition
Au	-	∞	Top contact
InGaAs	2×10^{19}	100	Ohmic contact
InP	1×10^{17}	2700	Top cladding
InP	2×10^{16}	1200	Top cladding
InGaAs	6×10^{16}	2500	Core
ACQW	-		N
InGaAs	6×10^{16}		Core
InP	1×10^{17}	∞	Substrate

	Material	Dop. [cm^{-3}]	Thick. [nm]
ACQW	AlInAs	nid	$L_{sep}/2$
	InGaAs	nid	L_{thin}
	AlInAs	nid	L_{bar}
	InGaAs	$n_{2D}L_{thick}$	L_{thick}
	AlInAs	nid	$L_{sep}/2$

Table 4.1: Vertical structure of the waveguide used in the simulations.

We have therefore a total of six parameters in our design (namely N, L_{sep}, L_{thin}, L_{bar}, L_{thick} , n_{2D}). Some of them might have a second order impact on the device performance and are only adding complexity for the design optimization. The separation between two successive periods, L_{sep}, is there mostly to decouple two adjacent ACQWs, and we chose to fix it to a value of 20 nm, which is largely sufficient to avoid any significant coupling between the different periods. The thickness of the large quantum well will mostly impact the first and third confined energy level position while the thickness of the thin well mostly dictates the position of the second confined energy level. Therefore, we also decided to fix the large well thickness to $L_{thick} = 52$Å. This value ensures that the first energy level is located deep enough, so that the second confined level can stay sufficiently far from the continuum of states, even under a strong applied bias. Moreover, such a choice ensures a highly resistive structure as well. That leaves us with 4

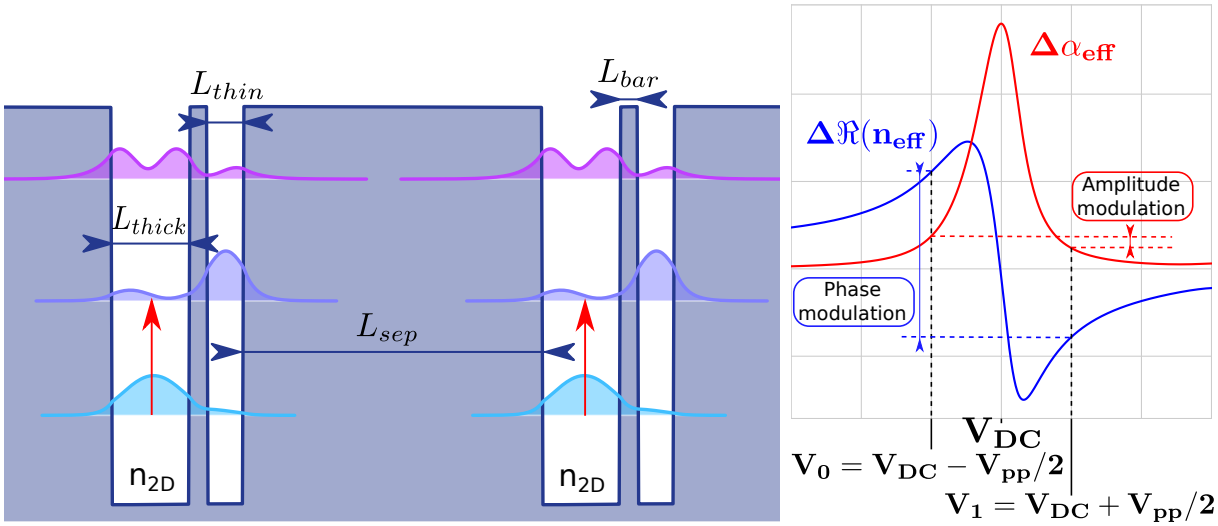

(a) (b)

Figure 4.5: a) Two periods of asymmetrical coupled quantum wells with their geometrical parameters and doping. The optical transition of interest, which takes place between the two first confined states, located in the adjacent wells of the system, is represented by the vertical red arrow. b) Typical Drude-Lorentz contribution to the dielectric constant due to the inter-subband transition in the ACQW, as a function of the applied bias on the structure.

parameters to optimize : N, L_{thin}, L_{bar} and n_{2D}. In our design process, simulations have been automatized to scan the whole phase space and find the parameters values that optimize the modulator performance, within the following boundaries :

- N taking values between 1 and 25 periods
- L_{thin} ranging from 24 to 27 Å, for an inter-subband transition close to the selected target wavelength of 9.1 µm ($E_{ISB} \approx 136$ mev). Its value mostly impacts the energy of the inter-subband transition.
- L_{bar} ranging from 10 to 14 Å. Its value mostly affects the tunability of the inter-subband transition with an applied bias.
- n_{2D} taking values between 1.5×10^{11} and 2×10^{12} cm^{-2}. Its value mostly impacts the real and imaginary index modulation strength.

As our goal is to design of a phase modulator, in principle without any net modulation of the absorption (i.e. of the imaginary part of the effective index), we tried to select the above mentioned values so that the modulation will be performed between biases V_0, and V_1 on both sides of the Lorentzian like absorption peak (which is almost symmetrical). That way the amplitude modulation between the two selected biases will be kept minimal, while at the same time the phase modulation associated to the real part of the effective index variation will be maximal, maximizing the modulator performances as presented in Figure 4.5b.

To quantify the simulated modulator's performance and select an optimal design among all of them, we defined the following FOM, which we maximized for a couple of bias (V_0 and V_1

being defined in Figure 4.5b) through numerical simulations :

$$FOM = f_{RC}\frac{min(T(V_0), T(V_1))}{1 + |T(V_0) - T(V_1)|} \tag{4.10}$$

That FOM (Equation 4.10) is optimized by maximizing the minimal transmission between V_0 and V_1 (maximizing the minimum between the two is maximizing both of them), minimizing the absorption modulation (denominator), and maximizing the electro-optical bandwidth f_{RC}. The latter is inversely related to the modulator length, which is set to obtain a π phase modulation, and defined as :

$$L_\pi = \frac{\lambda}{2|n_{eff}(V_0) - n_{eff}(V_1)|} \tag{4.11}$$

The calculation of the electro-optical bandwidth f_{RC} then comes from the assumption that the N periods of ACQW inserted between the doped contacts are, in first approximation, acting as a capacitor with a high shunt resistance. The frequency cut-off is then calculated by considering the 3dB cut-off of the associated RC low-pass filter, where $R \approx 50\Omega$ is the (perfectly matched) load impedance of the RF line and C the geometrical capacitance of the ACQW structure approximated as follows :

$$f_{RC} = \frac{NL_{per}}{2\pi R L_\pi W \varepsilon_r \varepsilon_0} \text{ where } C = \frac{\epsilon_r \epsilon_0}{NL_{per}} W L_\pi \tag{4.12}$$

where $L_{per} = L_{thin} + L_{thick} + L_{bar} + L_{sep}$ is the ACQW period thickness, W is the ridge waveguide modulator width (we set W=8 µm for the optimization of the design) and ε_r is the relative permittivity of the materials that we use, which we took as constant with a value of $\varepsilon_r = 11.6$ in the RF frequency domain. Furthermore, for all the simulations we consider an inter-subband transition linewidth of 11 meV, non-abrupt interfaces with a sigmoid parameter $\sigma = 2$Å and a non-parabolicity parameter $\alpha = 1.11$ (see chapter 2 for the description of these material parameters). At each iteration, the optimal value of V_0 and V_1 are then retained as the ones maximizing the FOM expressed by Equation 4.10.

Nominal design, (QWASS 01) : The nominal design for the modulator active region is indicated as "QWASS 01". For this first design, we set some constraints on the maximum electric field applied to the modulator, which should be kept below 80 kV/cm in order to limit the risk of damaging it. Moreover, the peak to peak voltage has been constrained to a 3V excursion range, as most commercial electrical drivers are typically limited to that range. From all the simulations with varying doping levels, we retained a doping concentration of $n_{2D} = 1 \times 10^{12}\ cm^{-2}$ as the best compromise between reasonable optical losses and high performance. We stress that this particular doping level is relatively high, and falls at the extreme limit of validity of the model used to perform the simulations. Selecting a higher doping concentration were therefore deemed too much of a risk, since we would have expected severe deviation from the modelled device performance, on one hand, increased optical losses and reduced the device resistivity on the other hand. For lower doping levels, the model shows that the performance sharply decreases : for a doping level that is 50% lower, the FOM declines by 30%. This is mostly due to a reduction

of the f_{RC}, which is directly linked to the doping of the active region. The simulations of the performances for different variations of the parameters at $n_{2D} = 1 \times 10^{12}\ cm^{-2}$ are presented in Figure 4.6.

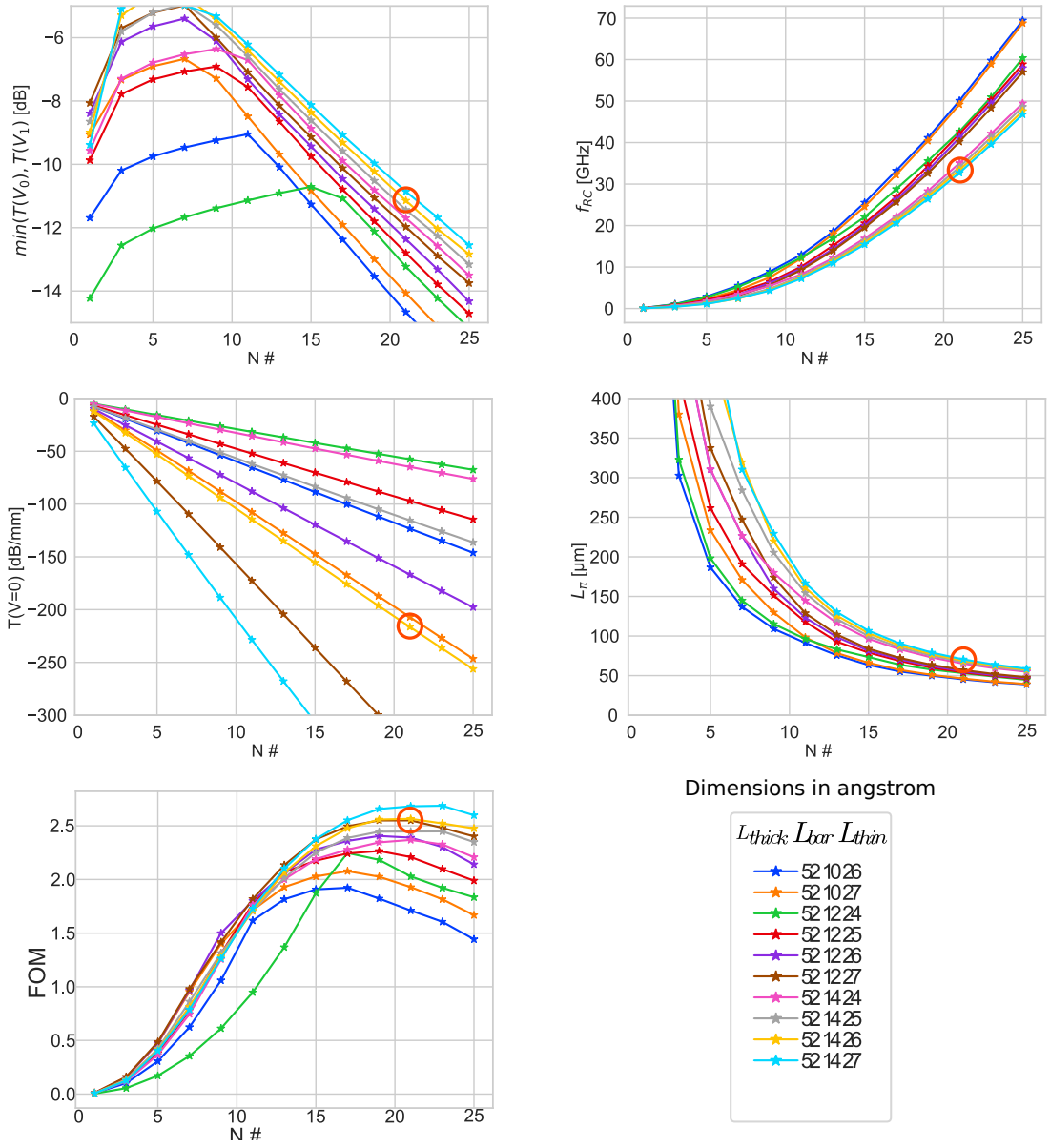

Figure 4.6: Simulated performance of a planar waveguide modulator integrating N periods of ACQW doped at $n_{2D} = 1 \times 10^{12}\ cm^{-2}$ in the middle of the waveguide core, at a wavelength of 9.1 µm. Constraints on the applied electric field below (<80kV/cm) and on the peak-to-peak driving voltage ($V_{pp} < 3V$) have been considered. The retained biasing point V_0 and V_1 values are the ones maximizing the FOM with those constraints and defines the overall performances. The retained design (QWASS 01) is indicated by the red circle. From left to right, and top to bottom : minimal transmission at working bias V_0 or V_1, estimated cut-off bandwidth f_{RC}, Transmission of the modulator section at 0V, Length of the modulator section and FOM (in arbitrary unit).

It is worth noting that, the higher the number of periods, the shorter the necessary length to

reach a π phase shift. Indeed, as the modulation effect can be expressed through the overlap of the optical mode with the ACQW active region (as defined by Equation 2.28), it is possible to show that the effective permittivity of the optical mode evolves, in a first order approximation for a fully TM polarized field, as [41] :

$$\delta\varepsilon_{eff}(V) \approx N\Gamma_p^{TMz}\Delta\varepsilon_z(V) \tag{4.13}$$

where Γ_p^{TM} is the overlap integral of the field with one period of ACQW defined in Equation 2.28, which is assumed to be constant with the bias V, and $\Delta\varepsilon_z(V)$ is the complex dielectric constant of the ACQW in the growth direction at the bias V, which is roughly proportional to the doping of those (see Equation 2.43). We can further show that :

$$L_\pi \approx \frac{\lambda n_0}{N\Gamma_p^{TMz}\Delta\varepsilon_z(V)} \tag{4.14}$$

Here n_0 is the effective optical mode refractive index (real part only) in the absence of inter-subband transition, or equivalently for N=0 ACQW period. This dependence of L_π as $\frac{1}{N}$ also explains the parabolic dependence of f_{RC} as a function of the number of active periods N, as shown in Figure 4.6. The apparent saturation of the FOM (bottom left graph) comes from the limitation imposed by $V_{pp} < 3V$ of the present design. This constraint considerably limit the accessible electric field excursion from the inter-subband transition position with increasing period number N. The transient regime in the first plot explains as, at a low number of periods, one can modulate sufficiently far from the inter-subband peak position (small V_0 and V_1 are corresponding to large electric field, far from the inter-subband transition) to get the best performance, and low absorption modulation. At some point when increasing the number of period N, the accessible electric field excursion decreases, (V_0, V_1 excursion is still limited to 3V, but the corresponding electric field excursion on a ACQW period is smaller). The optimal modulation biases are in that case found at the bound of the limited 3V excursion, thus the linear decrease in the transmission with the number of period. As the corresponding applied electric field on a period is inversely proportional to N, the inter-subband transition tunability within the limit of $V_{pp} = 3V$ is two, and this results in optimum biases found closer to the inter-subband transition. Therefore, a higher absorption with increasing N is found in that limit. This decrease of the transmission is firstly compensated by the sharp increase in the frequency cut-off, and the FOM still continue to rise, until it is no more the case, and it slowly starts to decrease. To give a simplified picture, increasing N is equivalent to shrinking the x-axis values in Figure 4.5 without shrinking the curves, and keeping a voltage excursion V_{pp} of 3V.

Moreover, one can see 3 distinct sets of curves in the f_{RC} graph that correspond to the three different values of the barrier width. This illustrates the reduction of the oscillator strength (ergo the plasma frequency) of the inter-subband transition with an increased barrier thickness, longer components are then needed for a same phase modulation, thus the f_{RC} reduction.

From all the different designs that have been simulated, we selected the one ensuring a good compromise between our requirements on the minimal bandwidth of the components ($f_{RC} >$

$20GHz$) and a reasonable value for the transmission in the modulator section ($T > -12dB$). The simulated performances of the retained design are summarized here :

- $L_{thick} = 52$Å, $L_{thin} = 26$Å, $L_{bar} = 14$Å, $n_{2D} = 1 \times 10^{12} cm^{-2}$ in the large well.
- N = 21 periods
- $f_{3dB} \approx 32$ GHz
- transmission at the operating (optimal) biases, through the modulator section : -11 dB
- $L_\pi \approx 70$ µm
- transmission at 0V : -210 dB/mm

Given the particular configuration of the device, and the relatively short length of the active (modulating) section, the latter has been inserted between two passive waveguide sections, whose role is to ensure the routing of the optical signal towards and from the modulating section, as will be shown in the following parts. As we estimate to be able to cleave chips as short as 300 µm with a good facet quality, a 230 µm long passive waveguide section would have to be added to the modulator waveguide. Ideally, this section should be made of undoped semiconductor layers, in order to limit the optical losses associated with the passive waveguide. However, since no butt-joint regrowth were available at the moment of this work, we decided to use the same vertical structure as the one employed for the active (modulating) section, with its associated optical losses. To palliate for these additional (unwanted) optical losses, we have planned to independently bias the passive waveguide sections with respect to the active waveguide section, in order to deplete them and hence decrease their absorption losses (see Figure 4.5b for a high applied DC voltage V_{DC}, the losses are reduced as the inter-subband transition is detuned regarding the targeted wavelength). Since the overall optical losses are expected to be quite high, an alternative design was made with a lower doping level and a detuned inter-subband transition at zero-bias. This was done to lower the risk of having a non-functioning device due to a shift from the design (especially concerning the doping level, a higher doping could lead to low resistivity and limit the accessible bias range to the device without burning it) or a non-measurable one due to too high absorption, and further relaxing the constraint on $V_{pp} < 3V$.

Alternative design (QWASS 02) : As said, the main objective of this second design is to avoid the need of biasing the otherwise heavily absorbing passive waveguide sections of the QWASS 01 design. To achieve this, the inter-subband resonant transition has to be sufficiently shifted from the target wavelength so that at zero applied bias its absorption in the structure is lowered, and the doping of the layers composing the ACQW reduced, to further limit the inter-subband absorption. We chose for that design a doping of $n_{2D} = 2.6 \times 10^{11}\ cm^{-2}$ in the large 52Å well. The above design process is repeated with the constraints of a maximum applied electric field lower than 80 kV/cm and a transmission greater than -50 dB/mm at 0V (which, for a 300 µm long component, translates into an overall transmission greater than -15 dB).

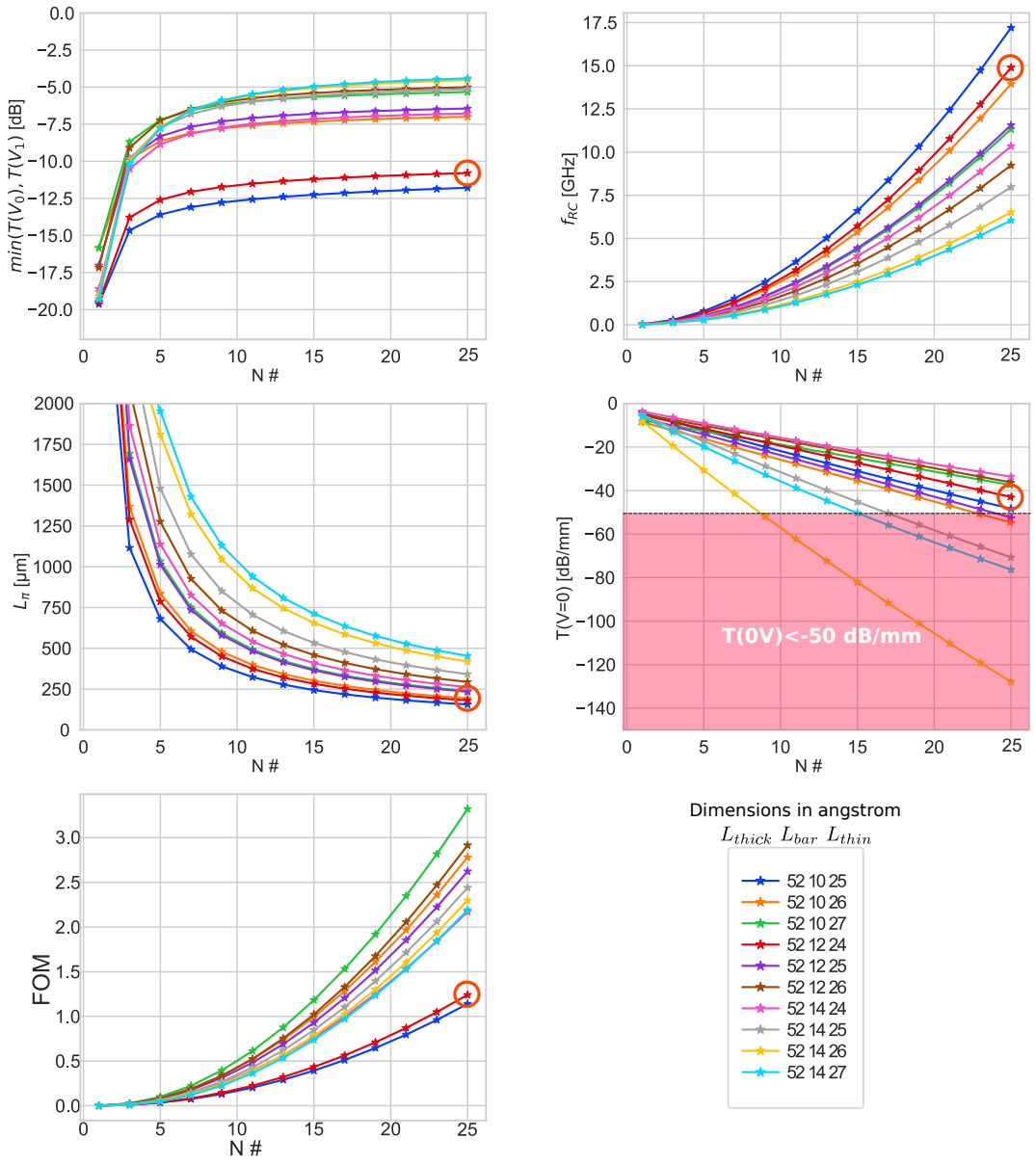

Figure 4.7: Simulated performance of a planar waveguide modulator integrating N periods of ACQW doped at $n_{2D} = 2.6 \times 10^{11}\ cm^{-2}$ in the middle of the waveguide core, at a wavelength of 9.1 µm. Constraints on the applied electric field (<80kV/cm) and on the transmission at zero-bias ($T(0V) > -50dB/mm$) have been applied. The retained biasing point V_0 and V_1 values are the ones maximizing the FOM with those constraints and defines the overall performances. The retained design is circled in red. From left to right, top to bottom : minimal transmission at working bias V_0 or V_1, estimated cut-off bandwidth f_{RC}, Transmission of the modulator section at 0V, Length of the modulator section and FOM (in arbitrary units).

The limitation of $V_{pp} < 3V$ has been relaxed in this design, therefore stronger bias excursion is possible (within the 80kV/cm limit). This implies a FOM driven by the quadratic increase of f_{RC} with N, as the minimal transmission at working bias becomes flat rapidly with increasing N, as shown in Figure 4.7 top left graph. Indeed, the optimum biases for the phase modulation are always accessible within this constraint. In conclusion, we chose a trade-off between a higher cut-off bandwidth f_{RC} and reasonable losses at 0V for this alternative QWASS 02 design :

- $L_{thick} = 52$Å, $L_{thin} = 24$Å, $L_{bar} = 12$Å, $n_{2D} = 2.6 \times 10^{11} cm^{-2}$ in the large well.
- N = 25 periods
- $f_{3dB} \approx 15$ GHz
- transmission at the operating (optimal) biases through the modulator section : -11 dB
- $L_\pi \approx 190$ µm
- transmission at 0V : -41 dB/mm

This concludes the design of the vertical structure that is the active core of our waveguide phase modulator.

2D geometric design of the waveguide : This second step in the design allows defining the lateral structure of the modulator waveguide. In order to choose the optimal width of the waveguide such that it ensures a truly single-mode operation, we injected the simulated optical index of the above designed ACQW into a commercial 2-dimensional mode solver (Fimmwave, FMM mode solver). For that aim, the deep ridge waveguide geometry has been chosen since it maximizes the optical field confinement and facilitates the next step of integration with the QCL source. This design step is therefore essential as it sets the basis for the right choice of the waveguide dimensions. To that end, we simulated the effective index of a ridge waveguide whose vertical structure is the one from Table 4.1 with the QWASS 01 design, as it is the one with the stronger effective index modulation. The result of this simulation is presented in Figure 4.8.

From those simulations, we selected three waveguide width w to be fabricated. The ones with width $w = 6\mu m$ and $w = 8\mu m$ have been selected to ensure single-mode operation independently of the applied bias. The third wider waveguide with $w = 12\mu m$, despite its bi-modal behaviour, can simplify the alignment during the flip-chip integration process, and improve the optical coupling through the modulator if needed. The simulated modulation characteristics of the two designs at $\lambda = 9.1\mu m$ are presented in Figure 4.9, in the case of the 8 µm wide waveguide design.

The resulting optimal biases and performances obtained from the 2D simulations are summarized in Table 4.2. We stress that the computed performances are slightly modified in comparison to the previous planar waveguide simulations, especially in terms of the optical losses that substantially diminished due to the geometrical waveguide dispersion and the effect of lateral confinement.

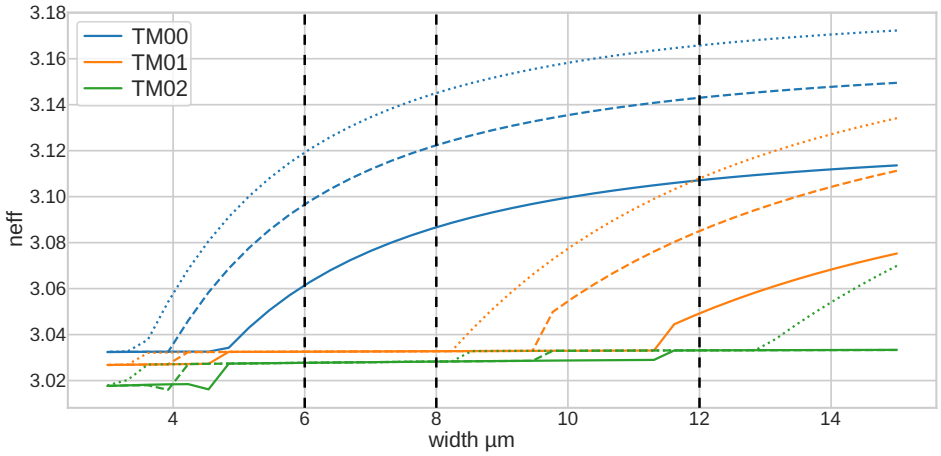

Figure 4.8: Effective index calculation of the first three quasi-TM modes of the ridge waveguide integrating the QWASS 01 structure for three different biases : $V \approx -2V$ producing the lowest effective index (continuous line), $V \approx +2V$ producing the highest effective index (dotted line), and at the resonance $V \approx -1V$ (dashed line).

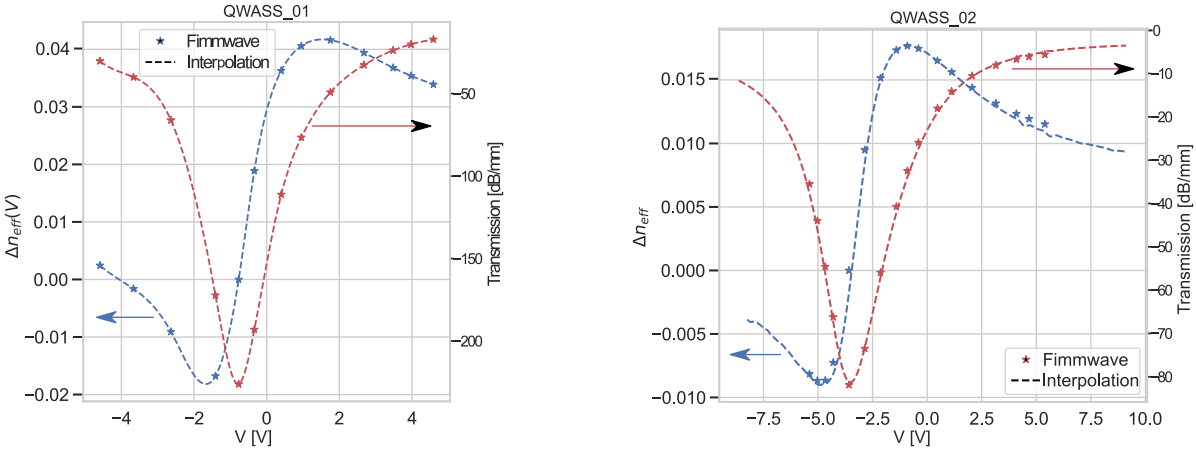

(a) (b)

Figure 4.9: 2D ridge waveguide simulated characteristics in terms of transmission (red) and effective index contrast (blue) as a function of the applied bias, for a w = 8 µm wide waveguide integrating a) the QWASS 01 or b) the QWASS 02 active region

	QWASS_01	QWASS_02
Biases V_0 V_1 [V]	-2.3 and 0.7 V	-5.8 and -0.4
V_π [V]	3	5.4
L_π [µm]	87	195
f_{RC} [GHz]	27	14
$min(T(V_0), T(V_1))$ [dB]	-8	-5

Table 4.2: Summary of the simulated performance of the two designed modulators, obtained from 2D mode simulations, in the case of a waveguide width w = 8µm.

4.1.1 Layouts for the integration of the modulator

The above two optimized designs presented in the previous paragraph are planned to be flip-chip integrated onto an AlN sub-mount with DC and RF electrical contacts. Moreover, as previously explained, to ensure high quality cleaved facets while keeping the components as short as possible (in order to limit the optical losses associated to the passive sections), we selected a total device length equals to 300 µm. Two improved layouts compatible with high-speed operation of the devices have therefore been designed. They are composed of a single straight waveguide (embedding the ACQW) that is separated into two or three electrically isolated sections. The active section will be connected to the G-S-G[4] RF coplanar waveguide on the sub-mount. The other section(s) will be DC biased in order to shift the inter-subband transition away and reduce their absorption, therefore acting as passive waveguide sections. These two layouts are schematically shown in Figure 4.10, with their relevant geometrical dimensions. On the QWASS 01 layout, the central section is the active modulator section that will be driven by the RF signal applied through the G-S-G electrode of the sub-mount, while in the QWASS 02 layout, the active region is the bottom section.

4.2 Layouts for the electro-optical characterization of modulators

Prior to the integration of the modulator layout presented in the previous section, their performances should be measured in order to focus the integration work on the most promising devices. Different layouts have been therefore designed with on-chip electrodes. All layouts presented below have been designed with an active modulator section of width 6, 8 and 12 µm, while the passive sections have 6 µm wide waveguides, providing the shortest MMIs, thus the lowest material absorption losses that are by far the dominant source of losses.

4.2.1 Layouts for absorption measurements

To retrieve the absorption characteristic of the modulator as a function of the applied bias, multiple measurement methods can be employed, each of them requiring dedicated layouts. Those have mostly already been discussed in chapter 2 in the case of the characterization of the dielectric constant of materials.

[4]G-S-G : Ground-Signal-Ground

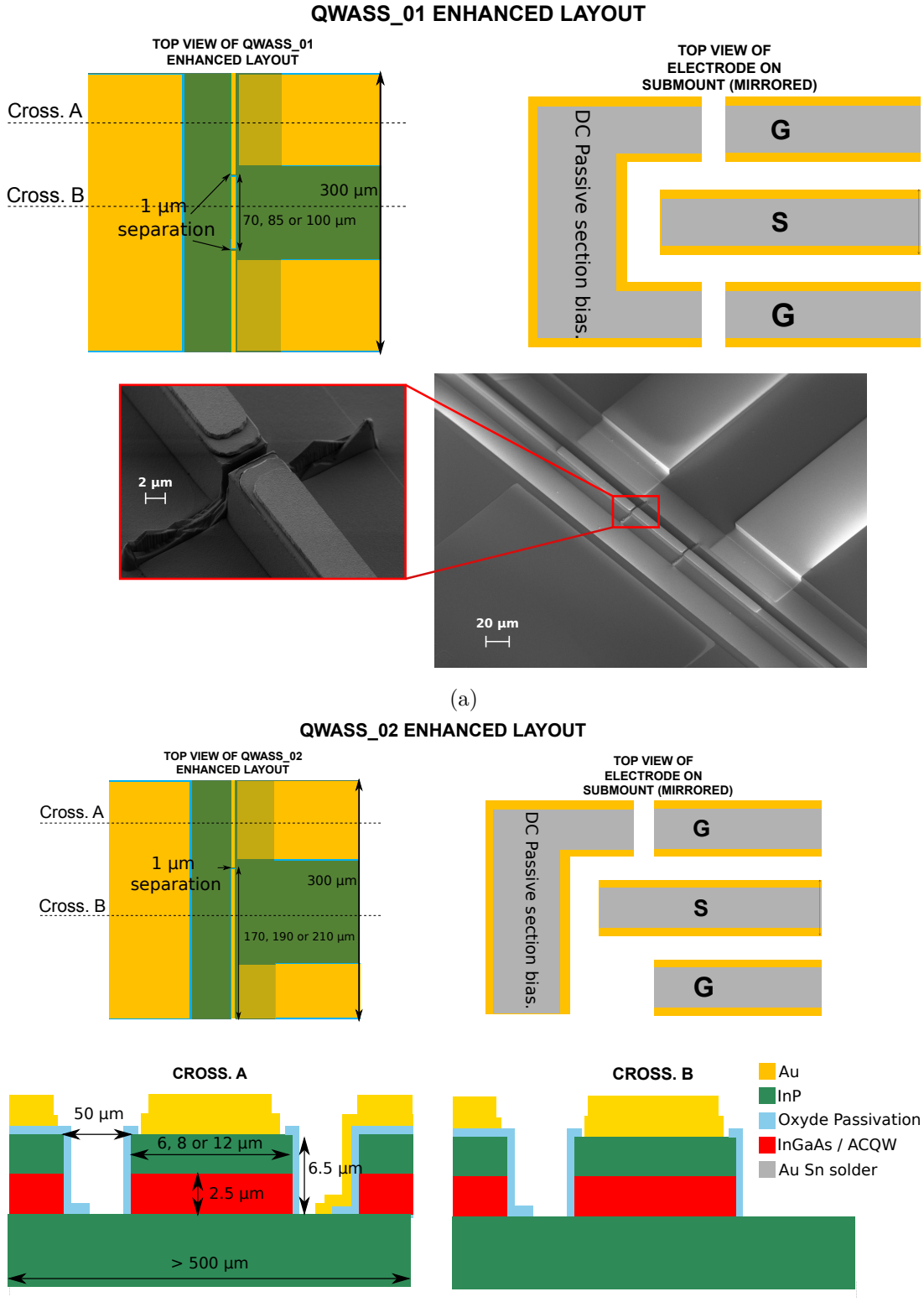

Figure 4.10: Layouts devoted for the flip-chip integration of the modulators onto the AlN RF submount: a) QWASS 01 layout with three sections (one central active section between two passive sections) and b) QWASS 02 layout presenting two waveguide sections (one active and one passive). The corresponding electrodes on the two different submounts are shown, as well as the top view and the (common) cross-sections of the devices. The main dimensions are also indicated. a) Bottom image : a SEM image of a fabricated QWASS01 device during the thesis.

The first method to estimate the absorption losses is based on the measure of the Fabry-Perot transmission spectrum of a waveguide whose length is accurately known [203, 204]. The advantage of this method is that it is non-destructive, but requires good knowledge of the waveguide facet reflectivity, which can be estimated from simulations [204]. The free spectral range of the transmissivity spectrum is inversely proportional to the length of the waveguide, and the contrast is linked to the optical losses. This technique is therefore adapted to relatively short waveguides with rather low losses (around a cm long for losses below 2 dB/cm is possible [20]). This makes this method hardly compatible to the measurement of our device, whose absorption is expected to be high.

The second method, very close to the above-mentioned, is based on the simultaneous measurement of both the reflectivity and transmissivity spectrum of the waveguide [205]. The measurement setup is therefore a bit more complicated, but in return allows measuring slightly more absorbent waveguides (with losses of the order of 5 dB/cm [20] for centimetre long waveguides). The knowledge of the facet reflectivity is there again required.

Finally, the third measurement method is the so-called "cut-back" technique [206]. As the attenuation in a waveguide evolve as :

$$I_L = I_0 e^{-\alpha(V)L} \tag{4.15}$$

where $\alpha(V)$ is the linear absorption coefficient of the modulator waveguide at a bias V, L its propagation length and I_0 the injected power into the waveguide. The cut-back method thus consists in measuring the transmission of waveguides of different length. That can be either the same waveguide, which is successively cleaved shorter and shorter (destructive), or different waveguides processed to have different lengths (non-destructive) [207]. The advantage of this method is that one can adapt the length of the waveguide to the expected absorption in order to get a precise characterization by exploiting the full measurement dynamics offered by the detector at disposal. Moreover, a good estimation of the injected power into the waveguide is readily accessible by this method, and the knowledge of the facet reflectivity is not needed. Since the modulator waveguides are expected to show a high variation of absorption with the applied bias, this is the method that we retained for the characterization of our devices.

With this aim in mind, we designed "S" shaped waveguides in order to displace the output waveguides of 600 µm with respect to their input, in order to benefit from an estimated -60 dB attenuation of the stray light (the light that would not be coupled into the waveguide) impinging on the detector that collects the output signal. The central, straight waveguide section is 450 µm long and is made of a modulator section of variable length L, electrically isolated from the others by the "spacer" (an etched trench between waveguide sections). The other two sections, connected to the "S" bended sections, are biased to decrease their absorption as much as possible. An illustration of such a layout is presented in Figure 4.11a. The overall chip for the characterization setup is planned to have a constant length of around 6.5 mm and width of 1 mm, adapted to a support specifically designed for their characterization. They are composed of 4 different layouts designed for the absorption measurement with two additional straight waveguides for alignment purpose. Two version of such chips are made to accommodate

for the 6 different active section lengths. The theoretical absorption of the central straight section versus the applied bias is presented in Figure 4.11b, for an applied electric field equal to 75 kV/cm (corresponding to $\approx 4.5V$) on the passive sections, decreasing their losses to approximately 10 dB/mm. The losses in the passive sections could be further lowered if a higher bias is applied, but the component might be damaged, and we preferred some safety margin to ensure that the characterization would be possible even in the case of an unwanted shift from the optimal design, the dopant concentration having a $\pm 10\%$ or more uncertainty in during the epitaxy).

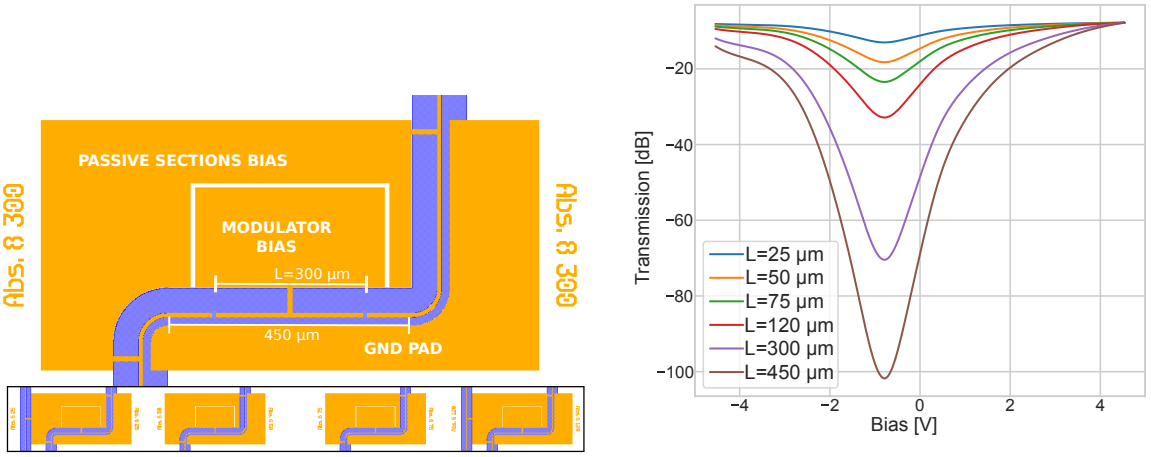

(a) (b)

Figure 4.11: a) Typical layouts designed for the estimation of the absorption characteristics of the modulator. Four different layouts with variable modulator lengths are present on a single characterization dedicated chip, here we show an example with L=300 µm. b) Simulated absorption of the "S" layout (passive waveguides biased at 75 kV.cm) for devices integrating the QWASS 01 active region (the more absorbent) as a function of the bias applied on the central active modulator section for different values of the length L.

The overall absorption characterization is expected to be carried out the following way :

1) The measurement setup is prepared in such a way that the injection and the collection lenses are aligned on the same axis.

2) The chip is then mounted on a manual 3-axis translation stage, and inserted in between the two lenses. The chip is initially aligned on the lens axis by employing the straight waveguide of the chip, to facilitate the procedure. A bias is also applied on the passive section (the straight waveguide for the alignment is made of one section connected to the passive bias pad) to limit as much as possible the absorption and maximize the signal at the detector during the alignment.

3) The chip is then moved to align the input of the first "S" layout with the injection lens using the micro-metric stage, and the collection lens is moved toward the "S" layout output

waveguide (600 µm away). Here again, an appropriate bias is applied to the modulator section to lower the absorption and facilitate the alignment.

4) The characterization of the device is performed for different values of the applied bias on the modulator section, while the transmitted signal is recorded by an MCT detector. This method assures an improved signal-to-noise ratio at the detector as most of the stray light is spatially filtered before reaching it. The biasing of the passive section is itself kept constant between all measurements for consistency.

5) Once the measurement is finished, the chip is translated laterally to the next "S" shaped layout. This ensures fast and repeatable measurements, since input and output ports are now already pre-aligned with respect to the injection and collection lenses.

The comparison of the measured transmission versus the modulator bias for different length values allows the direct extraction of the absorption change $\Delta\alpha_{eff}(V)$ curve. To this end, 6 different lengths of the central active modulator section have been implemented on the chips. The 25, 50, 75 and 120 µm long sections should allow a fine characterization of the losses for a bias close to the resonance (-3 V to +1V for QWASS 01 design, as shown in Figure 4.11b). The longer sections (300 and 450 µm) are intended to be used for a fine characterization of the rest of the curve, far from resonance, as a stronger absolute transmission difference is expected for those two longer components, ensuring a more precise measurement. Then the absolute absorption losses $\alpha_{eff}(V)$ can be extracted through a simple system of equations, as the passive sections are biased equally during all the measurements, thus introducing the same linear absorption.

4.2.2 On chip interferometry for phase measurement

The measurement of the phase shift induced by the modulator section can be performed through interferometry, to convert a phase difference into a change in field intensity, directly measurable by a detector. This function can be performed by mean of an external Mach-Zehnder setup employing discrete optical components, or by its photonic integrated version. This latter version is the one that we are interested in developing, and that will be described in the following. Obvious advantages of such integrated version of the Mach-Zehnder are simpler alignment, improved mechanical stability, reduced footprint, etc... In our case, it requires only the alignment of the chip with a much simpler measurement setup. A general schematic representation of such an integrated Mach-Zehnder interferometer and the corresponding practical implementation is presented in Figure 4.12.

As its name suggests, its operating principle is based on interferometry: a laser beam of intensity I_0 is injected on one side of the *Mach-Zehnder* (MZ), before being split equally in two different branches. This splitting function can for instance be realized using a symmetrical 1×2 MMI, as discussed in the previous chapter 3. During its propagation across the upper branch of length L_{up}, half of the beam will experience a phase shift equal to $\frac{2\pi}{\lambda} n_{eff}^{up} L_{up}$, and a power attenuation of $exp(-\alpha_{eff}^{up} L_{up})$. Similar expressions of the phase shift and attenuation can be written for the beam propagating in the lower branch of the MZ using the notations

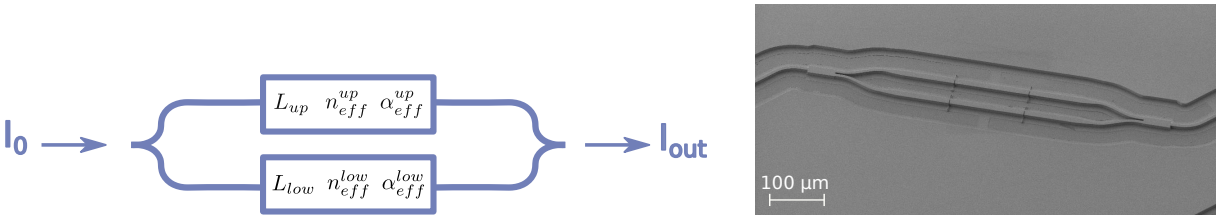

(a) (b)

Figure 4.12: a) Schematic representation of an integrated Mach-Zehnder interferometer. b) SEM picture of a processed Mach-Zehnder interferometer during this thesis.

of Figure 4.12a. It is therefore possible to show that the intensity at the output, in the most general case described in Figure 4.12, can be written as :

$$I_{out} = \frac{I_0}{4}\left|exp\left(-\frac{\alpha_{eff}^{up}}{2}L_{up} - j\frac{2\pi}{\lambda}n_{eff}^{up}L_{up}\right) + exp\left(-\frac{\alpha_{eff}^{low}}{2}L_{low} - j\frac{2\pi}{\lambda}n_{eff}^{low}L_{low}\right)\right|^2 \tag{4.16}$$

There are two different implementations of MZ found in the literature that can be used to characterize the phase shift induced by a modulator in the branches : the symmetrical or the asymmetrical MZ.

The symmetrical MZ has its upper and lower branches of the same length ($L_{up} = L_{low} = L$), it is therefore possible to simplify Equation 4.16 by regrouping some terms to obtain :

$$I_{out} = \frac{I_0}{4}exp\left(-\alpha_{eff}^{up}L\right)\left|1 + exp\left(-\frac{\Delta\alpha_{eff}}{2}L - j\frac{2\pi}{\lambda}\Delta n_{eff}L\right)\right|^2 \tag{4.17}$$

where $\Delta\alpha_{eff} = \alpha_{eff}^{low} - \alpha_{eff}^{up}$ and $\Delta n_{eff} = n_{eff}^{low} - n_{eff}^{up}$. Whenever used with balanced losses, such that $\Delta\alpha_{eff} \approx 0$, this expression further reduces to :

$$I_{out} \propto exp\left(-\alpha_{eff}^{up}L\right)cos^2\left(\frac{\pi}{\lambda}\Delta n_{eff}L\right) \tag{4.18}$$

Therefore, when the optical losses are balanced, it is possible to estimate the induced phase change between the two branches, and thus Δn_{eff}, for a given applied bias. Since the designed modulator presents a near symmetrical Lorentzian-shape modulation of the effective index, one can use this transfer function to its advantage to retrieve the effective index difference between two different biases, carefully chosen to have the same absorption through the modulator section. This, of course, requires a preliminary measure of the modulator absorption versus bias characteristic, in order to locate the position of the Lorentzian peak (and its extension), and to modulate the symmetrical MZ in a push-pull mode around this DC bias (we apply $V_{DC} + V_{pp}/2$ on the upper branch, and $V_{DC} - V_{pp}/2$ on the lower). An example of a characteristic curve is presented in Figure 4.13, simulated in the case of a device integrating the QWASS 02 active region embedded into an 8 µm wide waveguide. This measure allows to easily determine the bias difference that produces a π phase shift between both branches. Therefore, it is of great use to determine the V_π of the modulator associated to a given length. If different modulator

lengths in the symmetrical MZ configuration are implemented, one can measure different $V_\pi L_\pi$, and thus paves the curve $\Delta n_{eff}(V)$. Alternatively, having previously obtained the $\alpha_{eff}(V)$, one can extract the $\Delta n_{eff}(V)$ curve from the measurements obtained in push-pull mode using the expression Equation 4.18. The obtained continuous curve with that latter method, should match the discrete ones (one point per modulator length) obtained by the above method.

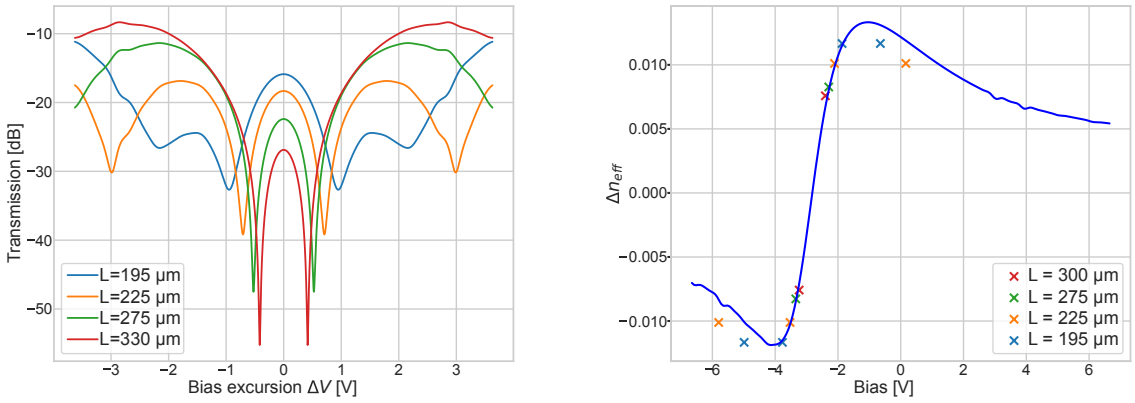

(a) (b)

Figure 4.13: a) Simulated transmission curves of symmetrical MZ at λ= 9.1 µm, for a modulation in push-pull mode around a DC-bias of -2.8 V. The QWASS_02 modulator design of waveguide width 8 µm and different length is used in that simulation. b) The retrieved effective index change from the transmission curve would correspond to the crosses. They well match the theoretical curves (in continuous lines) for the first resonance.

To illustrate this, we use the QWASS 02 design as an example, whose simulated transmission curves and performances are shown Figure 4.13. The characterization procedure using the aforementioned method would follow these steps:

(i) The linear absorption of the modulator is previously measured (with the "S" layouts) with respect to the bias, which allows locating the bias V_{DC} that ensures the peak of absorption.

(ii) An anti-symmetrical bias $V_{DC} + \Delta V$ on the upper branch and $V_{DC} - \Delta V$ on the lower branch is applied to the device (push-pull mode). The transmission of the symmetrical MZ is then measured.

(iii) Under the assumption that the phase shift induced by a bias $\pm V$ bias is symmetric with respect to V_{DC}, the position of the peaks $\pm\Delta V_{peak}$ in the transmission curves then gives the effective index change $\Delta n_{eff}(V_{DC} \pm \Delta V_{peak}) = \pm\frac{\lambda}{2L}$ provided that the length of the modulator section is exactly known (which is the case from the design).

In general, the assumption of a symmetric phase shift with respect to a varying applied bias is correct close to the resonance (i.e. around V_{DC}). But the further one moves from it, the less the symmetry of the phase change and absorption with respect to V_{DC} is preserved. This also means that away from the resonance, the local minima of absorption are shifted away

from the actual π phase difference as the approximation $\Delta\alpha_{eff} \approx 0$ is no more verified. This is due to the nature of the optical transition in the quantum wells, whose shape is likely to be distorted under a strong applied electric field that modifies its oscillator strength, making it slightly asymmetrical with respect to the applied bias. The waveguide geometrical dispersion induced by the change of optical index can also have an impact, but is expected to be negligible in comparison to the induced optical index change of the inter-subband transition. Therefore, we expect this method to work only for high-confined optical modes, whose optical index at V_{DC} would be far from the cut-off.

Let us remember that the optical losses of our components are expected to be high, dominated by the inter-subband absorption in the quantum wells. Since the whole MZ structures, including its MMI and access waveguides, would be made of the same stack of active layers, those would have to be strongly biased in order to adequately decrease the optical losses and provide a sufficient dynamics to resolve the features of the transmission curve. As an indication, a bias of 3V is expected to decrease the propagation losses to approximately 5 dB/mm in the case of the QWASS 02 design, and around 10 dB/mm for the QWASS 01 design at a 4V bias. The components devoted for this characterization are made with modulating section lengths of 80, 110, 140, 195, 225, 275, and 330 µm.The device layouts are presented in Appendix C. The MMI used in the MZ layouts are designed following the procedure described in chapter 3, and 3 length variations are implemented on the mask. Dedicated layouts for the characterization of the MMI used in those designs are also implemented on the mask, and planned to be used in order to select the best MMI design providing the highest transmission and the lowest imbalance at the optimum DC bias.

The asymmetrical MZ , contrarily to its symmetrical counterpart, allows for the characterization of the whole $\Delta n_{eff}(V)$ curve. In this different version of the MZ configuration, the modulated section has the same length, and the asymmetry is introduced by a different length ΔL of the two passive sections, such as illustrated in Figure 4.14a.

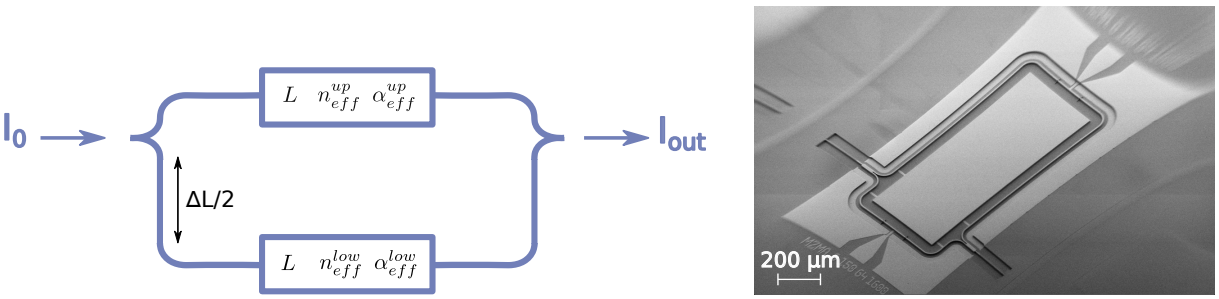

(a) (b)

Figure 4.14: a) Schematic representation of an integrated asymmetrical Mach-Zehnder interferometer. b) SEM picture of a processed asymmetrical Mach-Zehnder interferometer with its access electrodes.

In such a design, the output intensity would write as :

$$I_{out} \propto \left[1 + e^{-\alpha_0 \Delta L - \Delta\alpha L} + 2e^{-\frac{\alpha_0}{2}\Delta L - \frac{\Delta\alpha_{eff}}{2}L} cos\left(\frac{2\pi}{\lambda}(n_0 \Delta L + \Delta n_{eff} L)\right)\right] \tag{4.19}$$

where n_0 and α_0 are the values of the effective refractive index and the absorption in the passive sections of the MZ. This time the measurement of the transmission spectrum, with respect to the wavelength will show resonant peaks (where the transmission is minimal), with a free spectral range (FSR) given by :

$$\lambda_{res} = \frac{2n_0 \Delta L - \Delta n_{eff} L}{2m + 1} \quad \text{and} \quad FSR = \frac{\lambda_{res}^2}{n_g \Delta L} \tag{4.20}$$

where m is an integer, n_g is the group index in the passive waveguide sections (which can be obtained from computation). The FSR can also be directly measured on the transmission spectrum. A shift of the resonance wavelength $\Delta\lambda$ with an applied bias is linked to a phase shift by the proportionality relation :

$$\frac{\Delta\Phi}{2\pi} = \frac{\Delta\lambda}{FSR} \tag{4.21}$$

The underlying assumption is that the chromatic variation of the refractive index $\Delta n_{eff}(\lambda)$ and absorption $\Delta\alpha_{eff}(\lambda)$ be small on the wavelength measurement window. This is arguably the case with a tunable DFB-QCL (commercially available tunability are typically 2 to 3 cm^{-1} at 9.1 µm), whose tunable widow is about a percent of the inter-subband transition linewidth. An example of a simulated transmission spectrum as a function of the wavelength, and the extracted phase variation are reported in Figure 4.15, for the case of an asymmetric MZ.

Contrarily to the previous case of symmetric MZ, the whole $\Delta n_{eff}(V)$ curve can be effectively retrieved from transmission measurements. This measure necessitates a high resolution to resolve the features of the transmission spectrum, together with a fine-tuning of the QCL wavelength. Although experimentally challenging, this method is more versatile, and in principle more precise. It provides access to the whole phase curve, nevertheless it requires more expensive equipments that were not available at the time of the design and characterization of the components. Moreover, the characterization with symmetrical MZ would give more precise values of the phase shift at a few discrete bias difference. Indeed, the determination of the FSR is expected to be complex as it is close to the measurement wavelength accuracy with the actual best commercial wavelength meter (the FSR is only about 10 times the resolution). We also would like to point out that these measurements suppose to be able to measure a variation of transmission on the order of the percent for transmission already low (down to -15 dB through the entire device). It is needless to say that even with a high-power laser, this can be quite challenging in the LWIR domain.

We chose to have two designs implemented on the photolithography mask with $\Delta L = 1.6mm$ and $\Delta L = 2mm$, and with modulating section lengths of 50 and 150 µm, in order to be able to easily measure both modulator designs. Similarly to the symmetric MZ, we implemented 3 length variants of the MMI, which again can be individually characterized thanks to dedicated layouts on the chips (see Appendix C for the detailed layouts).

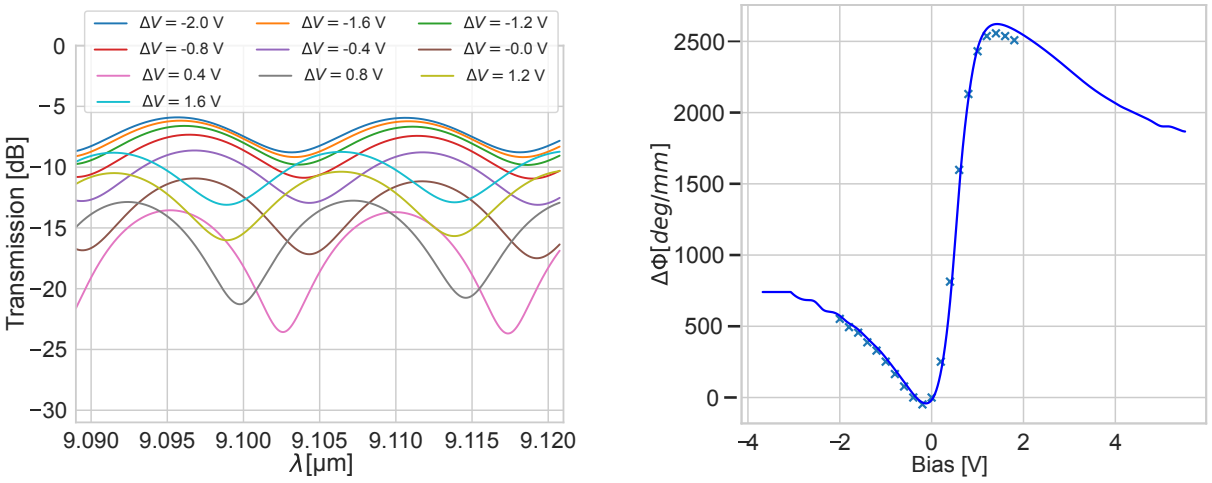

(a) (b)

Figure 4.15: a) Simulated transmission curves of an asymmetrical MZ with an applied bias of $0.58V$ on the upper branch and $0.58+\Delta V$ on the lower branch. A design close to the QWASS_01 modulator with a waveguide width of 8 µm, and modulating section lengths of 50 µm is used, and with a branch difference of length $\Delta L = 1.6mm$ in that simulation. b) The retrieved effective index variation obtained from the transmission curve is indicated by the crosses. They very well match the theoretical curves (the continuous blue line) over a large bias excursion. The FSR is equal to 0.155 µm from the spectrum at 1.6V (closest resonance to 9.1 µm)

4.2.3 Supplementary layouts

RF Coplanar waveguides. At the beginning of this chapter, we stressed that most of the components for characterization were mostly planned to work under DC bias and not under fast RF operation. This is due to the fact that for fabrication constraints, we planned to realize the devices onto a doped InP substrate, and many doped semiconductor layers in the active region are also present on the epi-structure, which would very likely limit the bandwidth of the access contacts, unless additional processing steps to decrease their parasitic capacitance are implemented (i.e. deposition of a thick polymer planarization layer to name one). As the fabrication of the modulator involves already a sufficiently long and complex processing, those additional steps were found to increase the complexity too much, especially considering that the optimized components processed for the flip-chip integration would have access RF coplanar waveguide on a dedicated sub-mount (see section 3), so it in principle should not experience such bandwidth limitations. Nevertheless, despite these limitations, we still decided to add an RF coplanar waveguide line to all the layouts devoted to static electro-optical characterization purposes, without further processing steps. This will provide some devices with simpler geometry onto which we could still perform electro-optical bandwidth measurements that will serve as a reference, and will be compared to the optimized flip-chip integrated ones, as it didn't imply more processing steps or added complexity. The RF coplanar waveguides implemented onto the epi-up devices have been designed following the analytical approach based on conformal mapping developed by Bedair and Wolff [208]. This model is adapted for the design of coplanar lines on insulating substrates, which is not the case there. Nevertheless, it provides a quick way

of designing the line itself. The underlying design process is developed in [208, 11] and we refer the interested reader to those references.

We designed the line to be a 50 Ω impedance line, even though the modulator itself would not have that impedance. A specifically designed impedance adaptation stage would be needed in order to transfer all the RF power to the modulator itself and avoid reflections, but since the limiting factor to the bandwidth would be expected to be the underlying doped layers, at this stage of the development we didn't design one. Moreover, this choice was also justified by the fact that all these epi-up layouts with on chip electrical access would principally be intended for static DC characterization purposes, while the epi-down layouts dedicated to high-frequency electro-optical characterizations have an optimized RF line on a dedicated sub-mount.

Straight waveguide layouts. As an alternative to the "S" shaped layouts for the characterization of the modulator absorption, we designed straight waveguides with an active section between two passive sections (biased as much as possible to lower their losses). Different variants of the layout have been implemented: one version with a total length of 500 µm integrating variables active modulating sections of 25, 50, 75, 120, 190, 200, 250, 300 and 450 µm, and another one with total length of 1000 µm embedding 600, 750 and 900 µm long active modulating sections. A schematic representation of the chips as well as an SEM image of one component is shown in Figure 4.16.

These straight waveguides layouts were planned to be employed for a similar purpose as the "S" bend components (i.e. for the characterization of the linear absorption $\alpha_{eff}(V)$ curve) in case the SNR at the output of the component would allow for a meaningful measurement, as the signal would most likely be buried in a much stronger signal from the uncoupled stray light. To that aim, it is planned to use a lock-in measurement technique, applying a low frequency and small amplitude RF signal on the central (modulating) section, which is polarized at different DC bias values V_{DC}, while suppressing the unwanted absorption of the passive sections by strongly DC biasing them (as discussed earlier in this chapter). The detected lock-in signal, would then be proportional to the local slope of the modulator transmission $\delta T(V_{DC}) = \frac{d\alpha_{eff}(V)L}{dV}\Big|_{V_{DC}} exp(-\alpha_{eff}(V_{DC})L)$, where T is the modulator section transmission and L the modulator section length. Knowing the length of the modulator, it is possible to extract the change of the linear absorption versus the applied bias V, $\Delta\alpha_{eff}(V)$ and, by comparing the measurements obtained for different active section lengths, to estimate the absolute value of the absorption. Furthermore, the lock-in technique allows for a better separation of the output signal from the noise, since the former has necessarily propagated through the active section (where the modulating RF signal is applied). With such characterization, we are thus sensitive to the coupled light only, and not to the uncoupled (unwanted) stray light, which is not modulated. The alignment of the chip with injection and collection lenses should therefore be facilitated by the simultaneous use of the straight geometry and the lock-in detection.

Symmetrical MZ with 90° hybrid. A further supplementary and more complex layout has been also implemented on the photolithography mask. It is composed of a symmetrical MZ

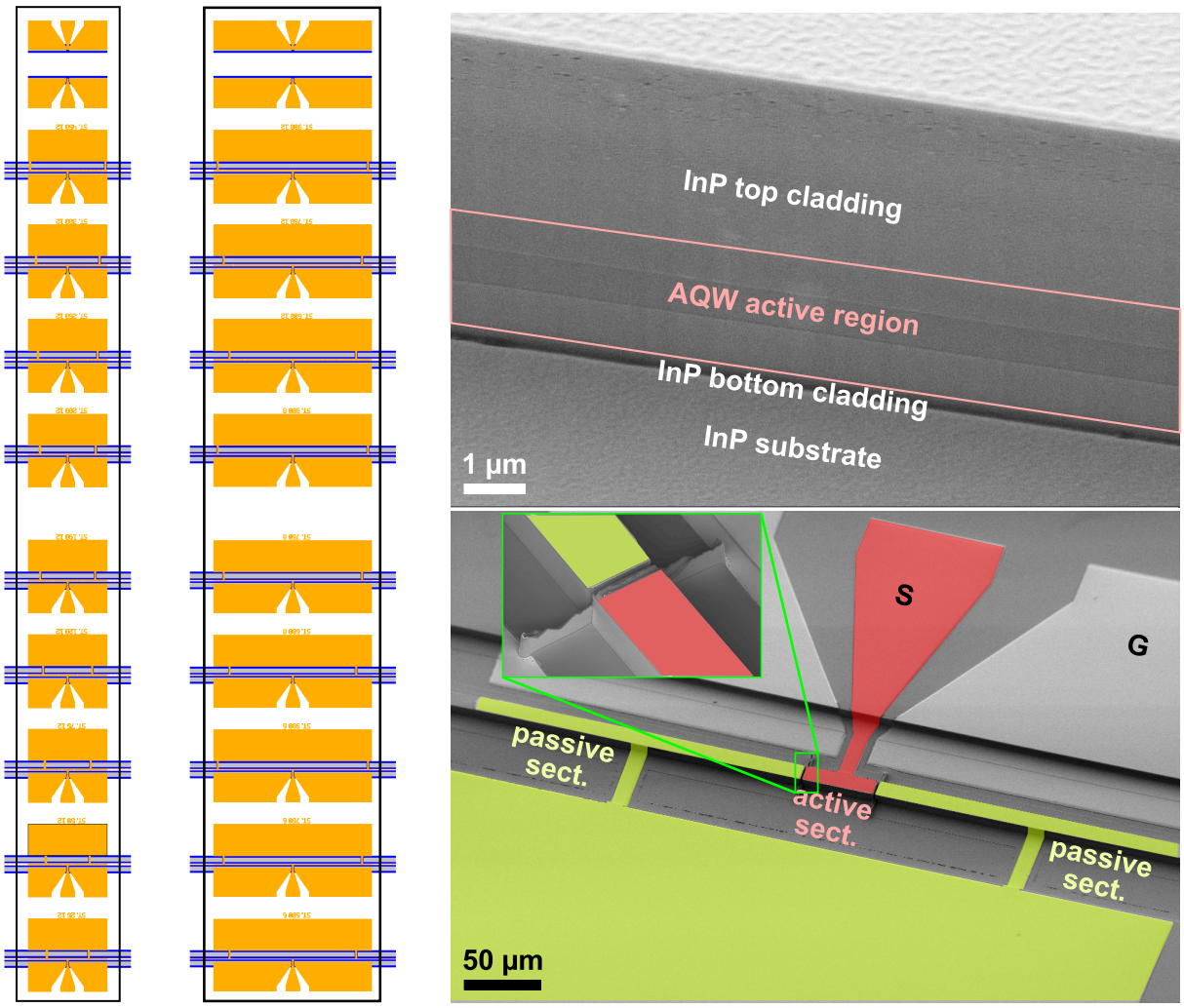

(a) (b)

Figure 4.16: a) Two 500 (left) and 1000 µm (right) long chips with different active (modulator) section lengths. The black box represents the chip dimension once cleaving is realized. b) SEM picture of a processed straight component during the thesis. A zoom on the vertical structure (4 µm thick InP top cladding, 2.5 µm thick InGaAs core embedding the asymmetrical coupled quantum wells) is shown in the top figure (the image has been taken before the passivation step). The finalized component with the three-section waveguide, the G-S-G coplanar line and passive pads for biasing are shown in the bottom picture. The (central) active and the passive sections are highlighted in red and green, respectively.

coupled to a 2×4 90° hybrid MMI. The working principle of this device has been described in chapter 2 (and will be further more in chapter 5). For the sake of completeness, here we only recall the basic idea behind the implementation of this particular layout. As can be seen in Figure 4.17, the two branches of the symmetrical MZ are feeding the two inputs of the 90° hybrid MMI. At the output of this MMI should 4 different interferograms be produced (one at each output), whose intensity will ideally evolve as :

$$I_j \propto I_{up} + I_{low} + 2\sqrt{I_{up}I_{low}}cos\left(\Delta\phi + \phi_j\right) \tag{4.22}$$

where I_{up} and I_{low} respectively are the optical intensity fed to the upper and to the lower MMI input, $\Delta\phi$ the phase shift difference induced between the MZ branches and ϕ_j the 90° hybrid MMI intrinsic phase at output j (which ideally takes the value +90, 0, -180, -90 for the four outputs respectively). Subtracting the output intensity values in phase opposition (measured on a camera or on different detectors) would give access to both the in phase and in quadrature components of the signal, making it possible to extract directly the phase difference introduced by the modulator integrated in the MZ. As discussed previously, here again the passive sections (here comprising the 90° hybrid MMI), can be biased in order to decrease their absorption to a minimum value, but also to tune the performance of the 90° hybrid MMI. Dedicated layouts having only the 90° hybrid MMI should be characterized first in order to select the optimal bias.

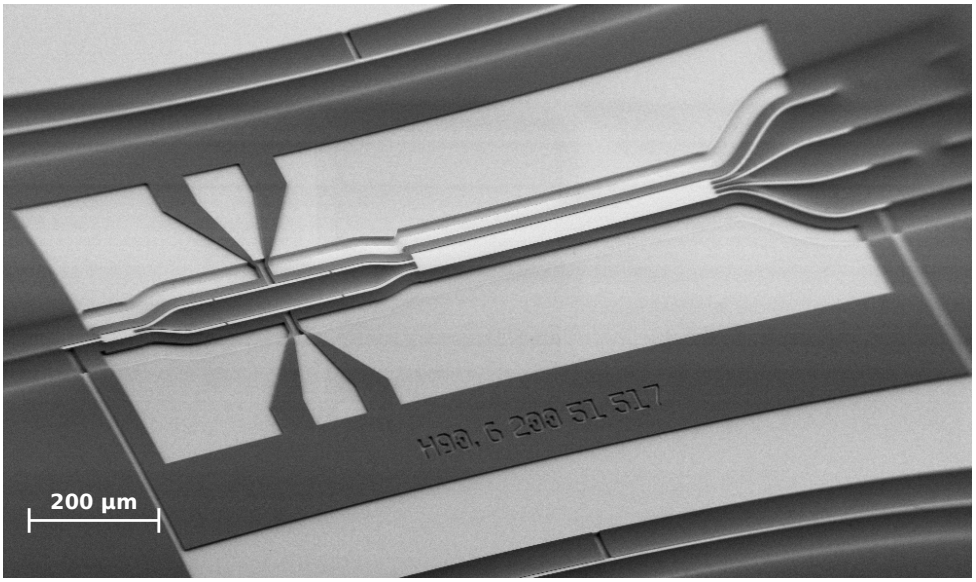

Figure 4.17: SEM picture of a device processed during this thesis. A symmetrical MZ is followed by a 90° hybrid MMI. This picture was taken prior to the contacts' metallization. The black area is the thick photoresist deposited and patterned before the lift-off step, ergo the blurring effect on the waveguide edges.

As we have reviewed the different designed layouts dedicated for various characterization purposes, we can now go further and detail the clean-room process that has been developed in order to fabricate all these different devices, before discussing their performances. For the more interested readers, a further detailed presentation of all the designed components and layouts

present on the photolithography mask is presented in Appendix C.

4.3 Fabrication

In order to illustrate the fabrication process of the devices, all of them being collectively and simultaneously processed on the same wafer, we will refer to the QWASS 01 layout for integration presented in Figure 4.10. For the processing of QWASS 02 wafers, minor changes in the layouts have been made, but those have no significant impact on what will be presented in the following.

The process flow is decomposed in 4 main steps that we will develop one by one in the next section :

- Active and passive waveguide sections separation.
- Ridge waveguide etching in a double trench geometry
- Waveguide passivation, electrical insulation and contacts opening.
- Contact metallizations

The process is performed on wafers integrating an InGaAs / ACQW waveguide core realized by MBE on a 2-inch S-doped InP substrate ($n=1\times10^{17}$ cm^{-3}), onto which an MOCVD InP top cladding is grown (see Table 4.1).

4.3.1 Active and passive waveguide separation

The first step of the fabrication process is the definition of the spacer which separates the active and passive waveguide sections. Due to the high aspect ratio of the spacer, (1 µm wide and 7 µm deep), this is one of the most challenging steps of the fabrication process. At first, a 1.2 µm thick SiN hard mask is deposited on the whole sample using PECVD. This SiN is then patterned by an RIE CHF_3-O_2 plasma dry etch using a thick SPR700-1.8 photoresist insulated through stepper projection photo-lithography. After removing the SPR700 1.8 photoresist, an ICP-RIE dry etching is used with a Cl_2 (10 sccm) CH_4 (8 sccm) H_2 (4 sccm) plasma at a pressure of 2 mTorr and RIE (ICP) electrical power of 100W (1200W). The samples, were placed on a carrier kept at 60°C without thermal paste. These steps are illustrated on Figure 4.18.

4.3.2 Ridge waveguide etching

After having etched the spacer between the active and passive waveguide sections, the same process is repeated to etch the ridge waveguides to a depth of 7µm, in a double trench geometry. Those steps are illustrated in Figure 4.19. The thin residual border visible around the previously etched spacer is resulting from the photoresist and SiN accumulation inside the spacer. It is mechanically removed at the final metallization step using an ultrasonic bath.

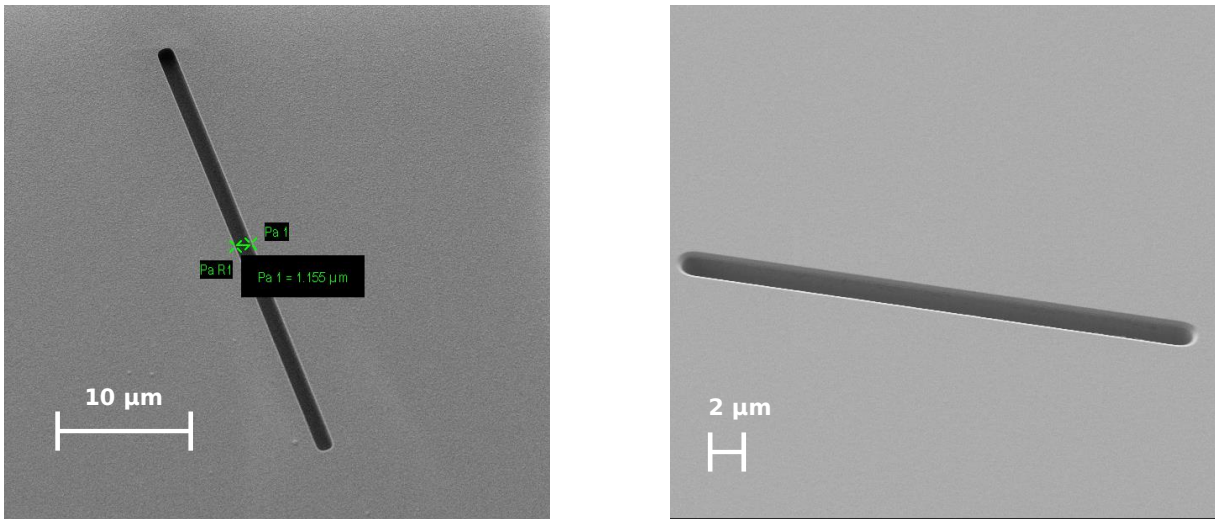

(a) (b)

Figure 4.18: a) SEM pictures of a) the spacer opening on the SiN hard mask after RIE and photoresist removal, and b) the spacer etched through the waveguide structure after ICP-RIE and SiN hard mask removal.

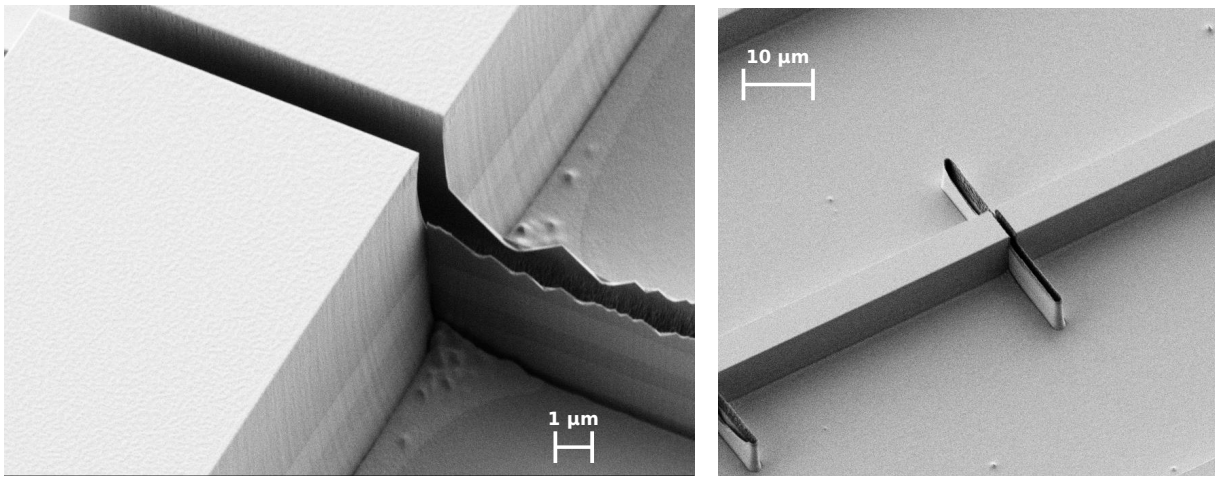

(a) (b)

Figure 4.19: a) SEM picture of the spacer after the ridge waveguide etching step and SiN mask removal. b) SEM picture of a QWASS_01 layout for integration after the ridge etching step.

4.3.3 Waveguide passivation and contacts opening

Once the waveguides have been defined, a thin 100 nm dielectric layer of HfO_2 is deposited on the whole sample using ALD technique. The deposition has been performed at a temperature of 250°C, but not plasma-enhanced since it was not available at the time of the process. This deposition technique as the advantage that the different precursor and reactants gases are injected in the chamber one at a time. The precursor gases will react with the sample surface until saturation, forming a homogeneous "activated" surface precursor. The reactants injected in the chamber will afterwards react with the "activated" surface precursor to form the desired material film until saturation is reached. Those self-limited steps are successively repeated until the desired film thickness is obtained. The great advantage of ALD is the enhanced homogeneity and conformal film layer deposition, which is independent of the sample topography. In our case, it is particularly interesting because it ensures a uniform covering across both the ridge waveguides, the bottom trenches and even the spacer sidewalls.

Once the dielectric layer is deposited, the electrical access to the waveguide top contact and the doped InP substrate are opened using a CHF_3 RIE dry etching plasma. A thick SPR220-4.5 photoresist film was used as a mask, in order to effectively cover the waveguides and trenches sidewalls. A two step stepper lithography with different focus levels and UV doses was then used, to ensure well-defined openings at both the bottom of the trenches and the top of the waveguides. Those steps are illustrated in Figure 4.20

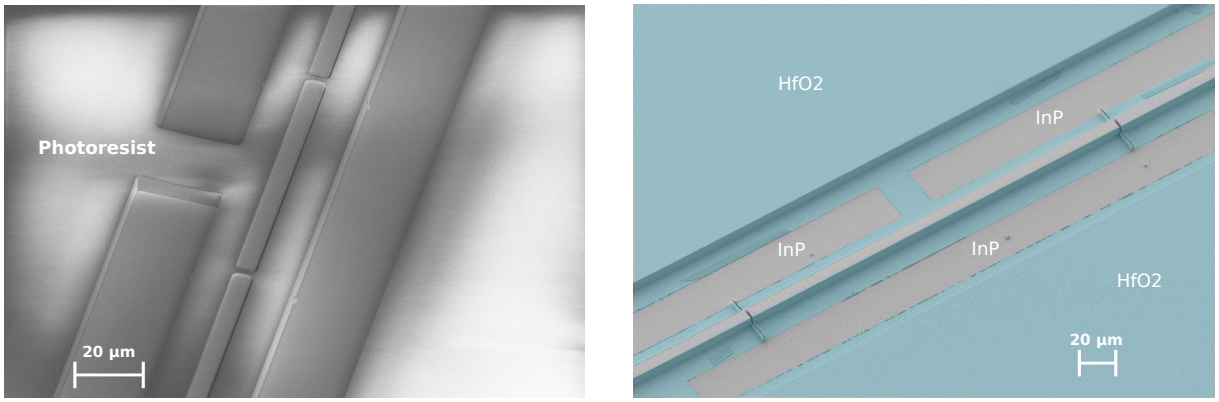

(a) (b)

Figure 4.20: SEM picture of a) the opened thick photoresist used for the electric contact opening through the HfO_2 film, and b) the resulting openings through the dielectric film (re-colourised) on a straight 3 sections waveguide device.

4.3.4 Metallizations

The metallic contacts deposition has been separated in three (very similar) steps, in order to compensate the height difference between the side and ridge contact layers, and thus match the requirement of having a planar metallization with an imposed gold thickness for the flip-chip eutectic bonding on the sub-mount (for more detail, see the component cross-sections on Figure 4.21). We start with the first layer of the metallization. A Ti/Pt/Au ohmic contact

(50/75/250 nm in thickness) is deposited on the sides of the components and at the bottom of the trenches. Then a second Ti/Pt/Au metallization (50/75/300 nm) is deposited on the top of the waveguides only, compensating for the 100 nm offset due to the HfO_2 layer laying under under the side metallizations. The third and last metallization step is the deposition of a 600 nm thick Au layer, which is needed to perform an efficient eutectic bonding during the next flip-chip process onto the host RF sub-mount. All these three steps use a lift-off technique with a thin LOR1A photoresist below a thick SPR220-4.5, which ensures well-defined electrical access and an easy lift-off, even in the case of tilted sputtered metallization layers. Indeed, the first two metallizations are done by sputtering at a 45° tilt angle of the sample, allowing for proper coverage on the sample top and sidewalls (with approximately a ratio 1/3 of the thickness on the sidewalls compared to the top of the wafer). The last metallization is done by evaporation, as only planar regions are metallized. Due to the non-negligible height difference across all the topology of the devices, for each metallization step, up to three UV insulations were performed, with different focus levels and insulating doses, to accurately define the patterns. In particular, one step for the top level (top waveguide and top sides of the trenches), one step for the bottom level (bottom of the trenches, 7 µm below) and one for the sidewall transitions where photoresist is locally thicker due to surface tension effects. Those steps are presented in Figure 4.21.

4.4 Electrical and optical characterizations of devices

The characterization of the multiple presented component layouts, planned to fully characterize both QWASS 01 and QWASS 02 designed waveguide structures, is an important step to validate both the design procedure, the models used for the performance prediction and the technological fabrication process. The components having been finalized at the very end of this work, only the QWASS 02 structure could be partially characterized. We will present preliminary characterizations, consisting in the (indirect) estimation of the electro-optical bandwidth of the components, and in the absorption and phase shift relations with respect to the applied electrical bias.

4.4.1 Electrical characterization

The electrical characterizations performed on the QWASS 02 device are devoted to firstly estimating its resistivity and current characteristic as a function of the applied electrical bias, and secondly its electro-optical bandwidth measured by means of a microwave rectification technique [209]. The results of these two measurements are presented in this paragraph.

I(V) characteristic of QWASS 02. The measure of the QWASS 02 I(V) characteristics has been performed on the straight layout structure (see Figure 4.16) when biasing only the central section. Those are shown in Figure 4.22, for different values of the active modulating section length L.

The QWASS 02 components seem to show very similar current densities. The slight asymmetry of the curves is related to the asymmetry of the band structure of the active region. Similarly, the resistance decreases exponentially with the applied bias, which reflects the decrease of the activation energy linked to the promotion of confined electrons in the quantum

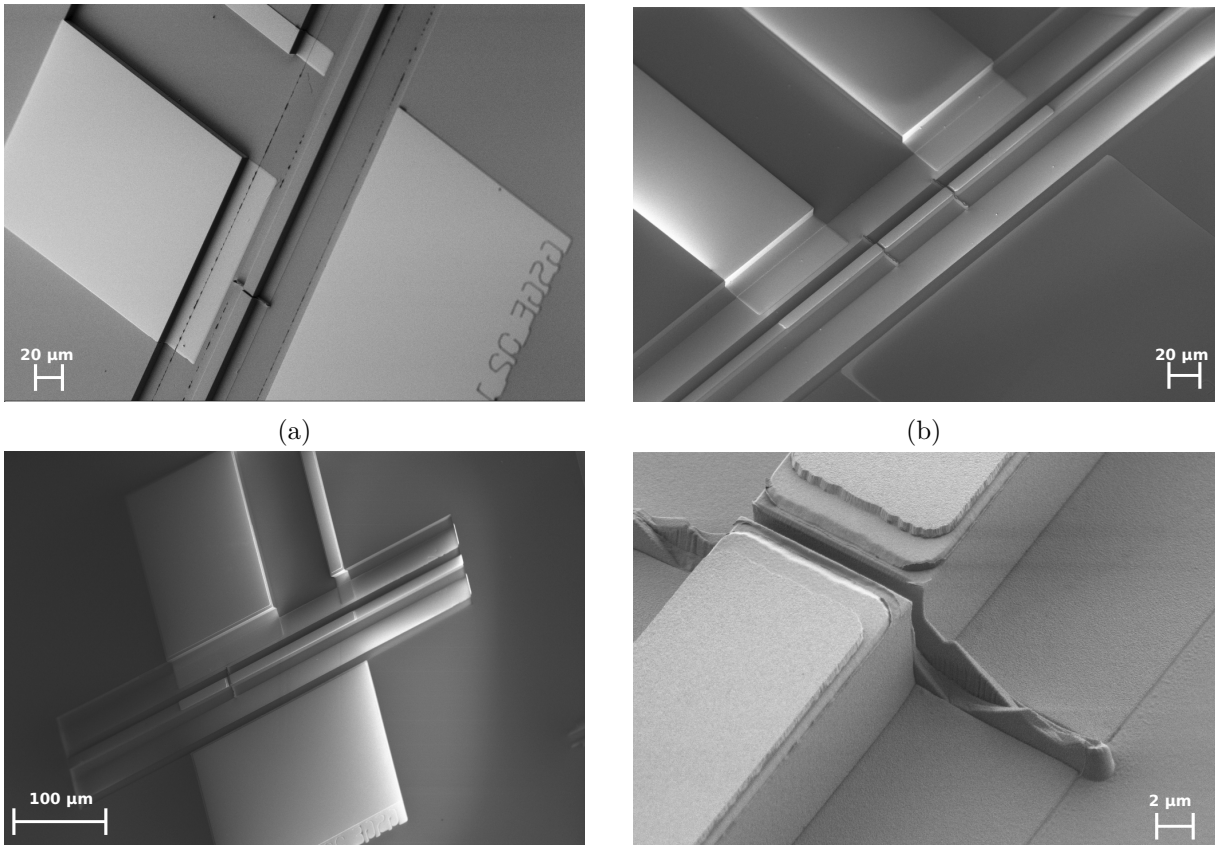

(a) (b)

(c) (d)

Figure 4.21: a) SEM pictures presenting different steps of the final metallization process on layouts devoted to flip-chip integration: a) first metallization step (sides metallization) are realized b) second metallization step (the top contact of the waveguide is added). c) Third metallization step (a supplementary gold layer is deposited on the top of the waveguides and on the lateral contact pads). d) Zoom of the two metallization layers near the spacer.

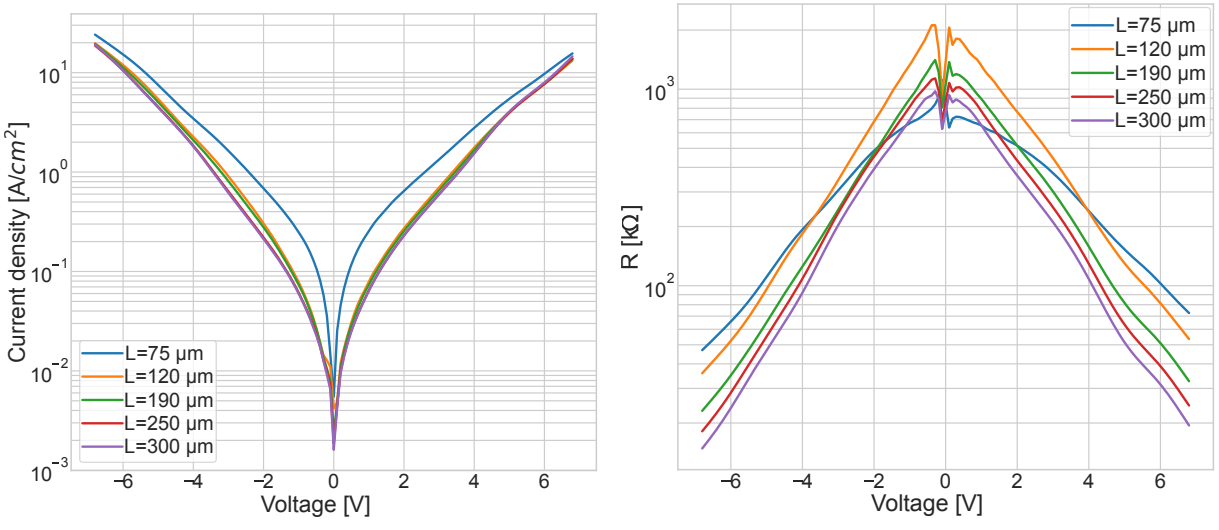

(a) (b)

Figure 4.22: a) Measured current densities of different components from the QWASS_02 straight waveguide configuration of width 8 µm. b) The corresponding component resistance.

wells to the continuum of free electronic states under bias. Only the shortest component measured here shows a slightly different behaviour, probably due to a damaged component. Those characteristics show the overall good quality of the fabrication, the current efficiently passing through the vertical active structure with negligible leaks. Moreover, the non-linear J(V) (or equivalently I(V)) characteristic of the components make it possible to use electrical rectification technique in order to estimate its electro-optical bandwidth [209].

Estimation of the electro-optical bandwidth through microwave rectification technique The non-linear current versus bias characteristic of the QWASS_02 (and QWASS_01) component can be written in the form of a Taylor expansion (we neglect the higher than second order contributions) :

$$I(V_0 + \delta V) = I(V_0) + \frac{\partial I}{\partial V}\delta V\Big|_{V_0} + \frac{1}{2}\frac{\partial^2 I}{\partial V^2}\Big|_{V_0} \delta V^2 \tag{4.23}$$

In this expression, V_0 is an applied DC bias onto which a small RF modulation signal δV is superimposed, $\delta V = V_m sin(2\pi f_m t)$. The time averaged current, from the above expression, then writes as :

$$\langle I(V_0)\rangle = I(V_0) + \frac{1}{4}\frac{\partial^2 I}{\partial V^2}\Big|_{V_0} V_m^2 \tag{4.24}$$

The measure of the second term of this current (the blue highlighted one), called the rectified current, is possible using a microwave rectification technique. To that aim, the measurement setup presented in Figure 4.23a, comprising a bias tee, an RF source (a synthesizer) and a DC source, can be employed. The frequency dependence of the rectified current is directly linked to the electro-optical frequency performance of the components. This indirect technique, which gives quite representative results with respect to a direct (optical) characterization, is relatively easy and fast to implement, and has the great advantage to avoid any challenging optical coupling of an external QCL source into the device, thus speeding up the device characterization.

The measured rectification current in the case of a QWASS 01 straight device with 200 µm long active section is presented on Figure 4.23b. The measurements were done around 0.4 V DC bias for a 5dBm RF injected power, no substantial change in the response was experienced for lower or higher values of those parameters (between 0 and 7 dBm). We observed a quickly decreasing response with increased frequency, with a rather low -3 dB cut-off frequency below 100 MHz, that is at least 10 times lower than the ones expected from the design. A measure of the on chip RF coplanar waveguide in open circuit configuration, which was implemented for de-embedding the contribution of the coplanar waveguide and retrieve the intrinsic frequency performance of the device, showed a parasitic capacitance on the order of 11 to 15 pF. This parasitic capacitance is attributed to the presence of the underlying doped semiconductor layers below the HfO_2 (which is only 100 nm thick), onto which are deposited the RF electrodes. In order to further verify this hypothesis, the coplanar waveguide of the same device was cut using a focused ion beam (FIB), down to the substrate (as visible on the bottom SEM picture of Figure 4.23a., leaving only a 20 µm long planar contact (plus the 50 µm long, at the bottom

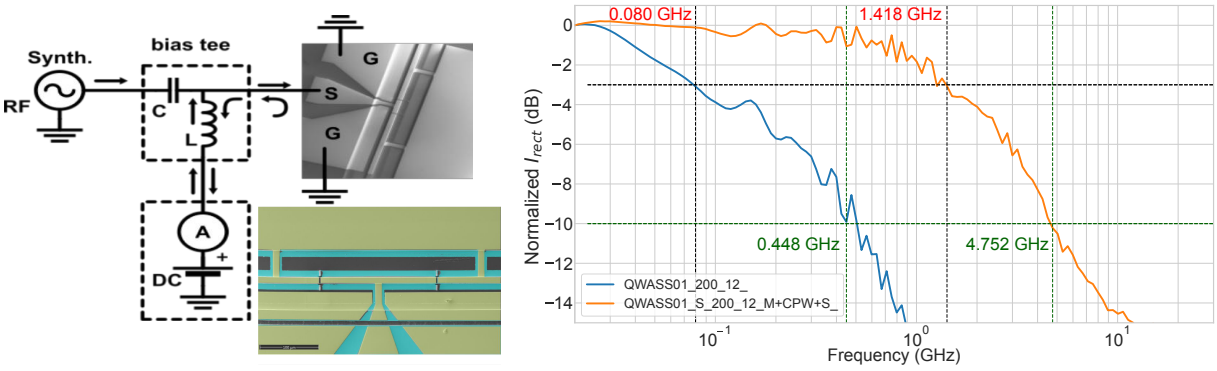

(a) (b)

Figure 4.23: a) microwave rectification measurement setup used for the characterization of QWASS 01 components in straight waveguide configuration. Bottom, a colorised SEM picture of a component whose coplanar waveguide has been cut using a Focus Ion Beam (FIB). b) Measured rectified current (normalised to its low frequency value) for a QWASS 01 device before (blue) and after (orange) the FIB cut of the RF coplanar waveguide

of the trench), which is just enough to place the RF probe on it. The result is a significant improvement of the -3dB cut-off frequency, which increased from 80 MHz up to 1.4 GHz (and up to 4.7 GHz if we consider the -10 dB cut-off), which represents a factor 18 nearly, confirming the limitation introduced by the poor RF coplanar waveguide design.

Again, it is worth mentioning, as previously explained, even though those devices are greatly limited in their high-speed operation by the coplanar RF electrode, they were mainly meant for DC characterization, and the limitations of the RF design were known. We stress again the fact that the components designed for flip-chip integration would have their RF coplanar waveguides realized on a dedicated RF sub-mount, on which they would be flip-chip bonded, and thus we expect to obtain significantly improved frequency bandwidth with them.

4.4.2 Optical characterization

To characterize the optical performance of the modulator, we used the optical setup shown in Figure 4.24, specifically designed and mounted in this work. An external-cavity quantum cascade laser (MirCat) is used as a tunable source and injected into the waveguide using an aspherical lens. The output of the waveguide is collimated and focused onto a LWIR camera (Dataray WinCamD-IR-BB) through a second aspherical lens. The component is placed on a dedicated support on a triaxial stage, and aligned while biasing the component to 5V to decrease the absorption associated with the passive sections, at a laser wavelength of 7.5 µm to further decrease the absorption of the component (which is designed to be maximum around 9.1 µm). That way, the alignment is facilitated. The measured component is a unique 500 µm long straight waveguide section (no passive section is present on that component). We followed the procedure presented in the paragraph subsubsection 4.2.1, unless we used the straight waveguide and measured only the transmission through that component due to considerable time constraints.

Prior to a measurement, a set of 10 images is recorded with an integrated shutter on the

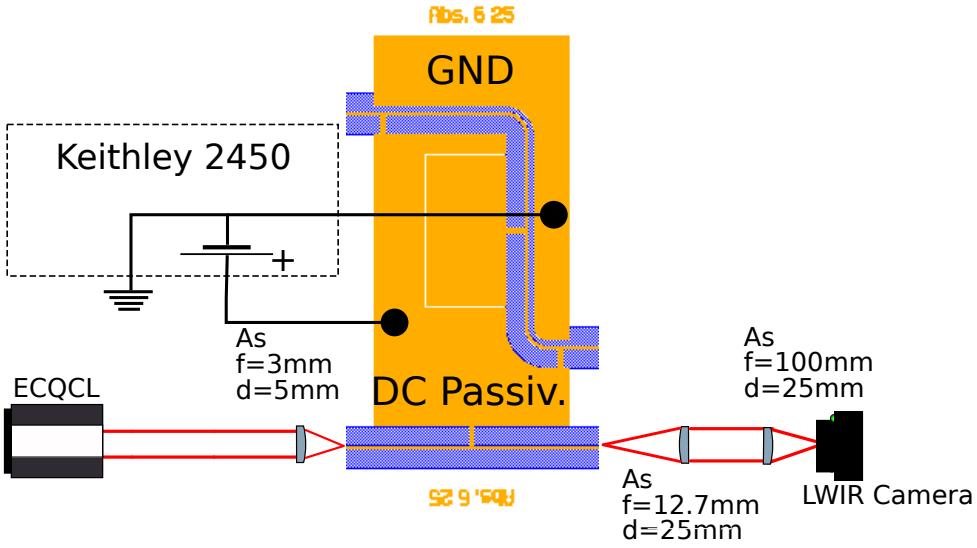

Figure 4.24: Optical characterization setup used for the measurement of the QWASS 02 absorption spectra. ECQCL : External Cavity Quantum Cascade Laser, AS : Aspherical lens.

camera. The resulting averaged image is used as a background reference correction in the next step. Then the shutter is removed and a second set of 10 images is recorded, averaged, and background corrected for different applied biases. The process is then repeated for several selected emission wavelength of the ECQCL. A re-alignment procedure is performed on the component between each measurement to compensate as much as possible for the chromaticity of the optical elements. The value of the pixels summed on a squared area around the waveguide output mode profile, is directly proportional to the modulator transmission. The squared area was taken sufficiently large to contain entirely the output (all the power is integrated). An example of a measured output field intensity recorded at the camera is shown in Figure 4.25a, while the retrieved (normalized) transmission is shown on Figure 4.25b .

To extract the absorption characteristic of the component, we fitted the measured data with a Lorentzian model :

$$L(V) = exp\left(\frac{A}{\pi}\frac{\gamma}{(V-V_0)^2+\gamma^2}\right) \tag{4.25}$$

where A is the Lorentzian amplitude, γ its linewidth and V_0 the bias at which the curve reaches its peak. Since the measured data are normalized transmission, and that at some point the signal reaches the noise floor of the camera, we actually fitted the experimental curves to the tails of the Lorentzian function, by using the following fitting function and a least-square algorithm:

$$F(V,A,V_0,\gamma,Tlim) = \begin{cases} 10log_{10}\left(\frac{L(V)}{max(L(V))}\right), & \text{if greater than Tlim } x \geq 1 \\ Tlim, & \text{otherwise} \end{cases} \tag{4.26}$$

where V is the measurement biases, (A, V_0, γ) are fitting parameters, $Tlim$ is the noise floor (that is manually adjusted for each measurement). An example of such a fitted function on measured data is shown in Figure 4.25b, the other fitted curves are shown in Appendix D. After this fitting procedure, a set of absorption curves versus the applied bias is obtained, for all

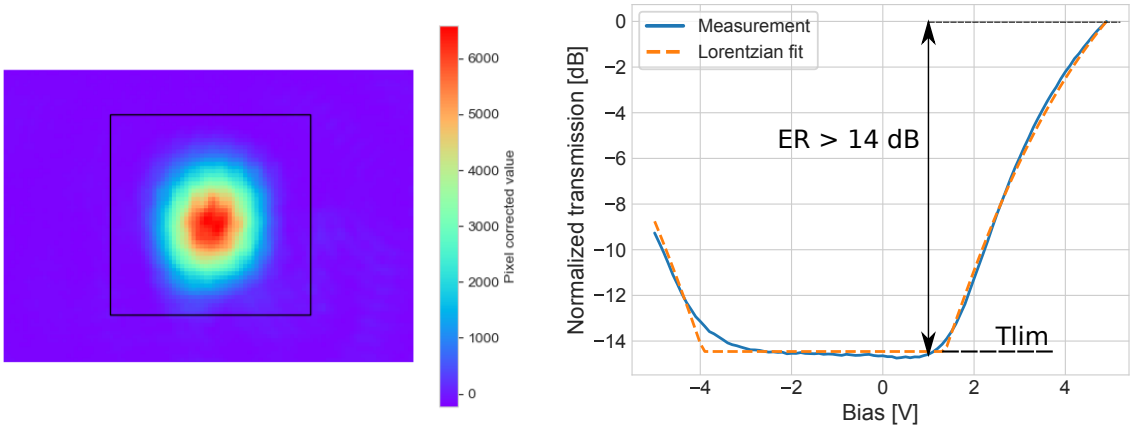

(a) (b)

Figure 4.25: a). Raw output images of the waveguide output (here for a wavelength equal to 9.1 µm). For all the acquired images, the output profile always lies inside the defined square area, as illustrated by the image. b). The extracted (normalized) transmission of the component, at λ= 9.1 µm through the 500 µm long waveguide. The fitted Lorentzian model is shown as the dashed orange line.

the scanned wavelengths ranging from 7.5 to 9.3 µm. Those are shown in Figure 4.26a. The transmission sharply diminishes to -8 dB/100 µm for λ from 7.5 to 9.3 µm, but not continuously. This sharp variation with respect to the wavelength underlines the sensitivity of the measurement and the low robustness of the measurement procedure. This is due to fitting extremely low values of the output transmission (that partly goes below the camera noise floor for certain values of the applied biase).

In Figure 4.26b, we can see that the component has a linear shift of its peak absorption position as a function of the applied bias, which we estimate as $\omega_{ISB} = 4.8V + 141.8$ where ω_{ISB} is the inter-subband transition energy expressed in meV Figure 4.26b. We believe the value of the Stark-shift to be relatively robust in its estimation, as the Lorentzian tails are well visible on most of the measured spectra, guaranteeing a relatively precise estimation of its peak position.

Phase shift estimation. In order to estimate the phase shift induced in the waveguide, we consider the evolution of the fitted transmission versus the photon energy at a given bias (which means that for each bias, we take the values of the Lorentzian lineshapes of Figure 4.26a that are on a vertical axis corresponding to the given bias, and repeat it for all biases). When drawn onto a plot, the transmission versus wavelength (or photon energy) at a given bias, follows a Lorentzian distribution with the wavelength $L(\omega)$, which verifies Kramers-Kronig relations :

$$L(\omega) = \epsilon_{BKG}(1 - \frac{\omega_p^2}{\omega^2 - \omega_0^2 - j\gamma}) \tag{4.27}$$

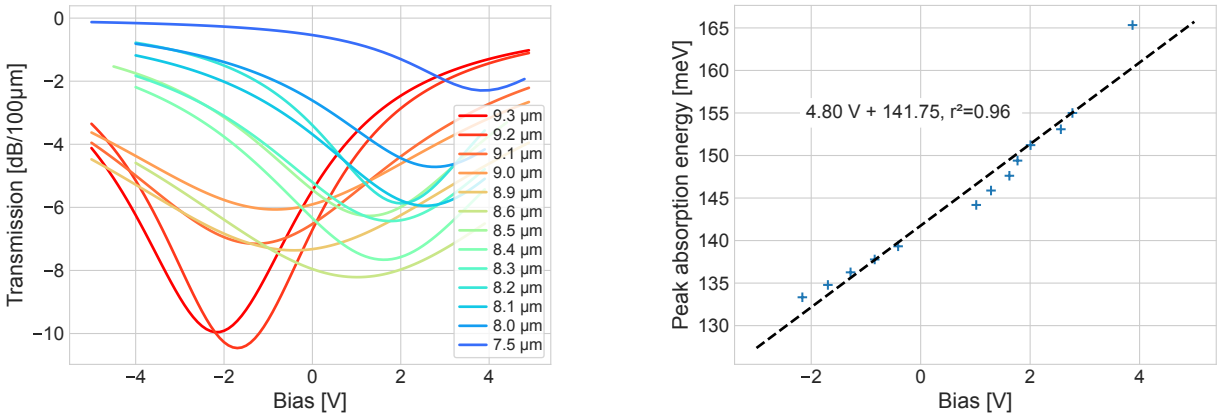

(a) (b)

Figure 4.26: a). Transmission curves obtained from the measured data after the Lorentzian fit procedure. b) Inter-subband Stark shift as a function of the applied bias, obtained from the fitted Lorentzian parameters.

where $\epsilon_{BKG} \approx 11.6$ for InGaAs at $\lambda = 9.1$ µm (the optical index model presented in [48] is used), ω_0 the resonant frequency of the Lorentzian, ω_p its plasma energy and γ its damping. We applied the Lorentzian model of Equation 4.27 to the complete set of extracted data from the transmission measurements, for all the different applied bias. An example is shown in Figure 4.27a, obtained for a bias value of 0.05 V. The initial guessed values fed to the fitting algorithm are extracted from the measured stark shift shown in Figure 4.26b for ω_0, to $w_p = 3meV$ and $\gamma = 0.1\omega_0$. The real part of this Lorentzian gives the real part of the optical effective index modulation, thus the phase modulation, while its imaginary part gives the absorption modulation. The resulting fitted characteristic is shown in Figure 4.27b for a wavelength of 9.1 µm. Here, we neglected the waveguide geometrical dispersion contribution [210].

On Figure 4.27a. we observe that the extracted values of the absorption from the previous fitted data (from Figure 4.26a) are distributed in the spectral domain following a Lorentzian shape. The resulting fitted values of the absorption and phase modulation are plotted in Figure 4.27b. These values are close to the theoretical ones with a resonant energy $\omega_0 = 166meV$, a damping factor of $\gamma = 33meV$ (which represents 20% of the resonant frequency ω_0) and a plasma frequency of $\omega_p = 2.6meV$ (here the definition of ω_p is normalized to $\epsilon_{BKG} = 11.6$, as seen from its expression given in Equation 4.27).

This concludes the characterization performed on the modulators. Further characterizations are needed in order to confirm these results. Although the results here presented are somehow still preliminary, from such devices we can expect to obtain absorption variation equal or greater than about 3dB per 100 µm propagation length (14dB for a device 500 µm long have been directly measured), with a corresponding estimated phase difference of 0.3 π corresponding to a $V_\pi L_\pi \approx 0.1V.cm$, which is comparable to the state of the art of electro-refraction modulator at telecoms wavelengths. Moreover, we want to clearly point out that the phase modulation has not been measured in this work due to time constraints, but only extracted through Kramers-Kronig relations on the transmission measurements (we fitted a Lorentzian model on

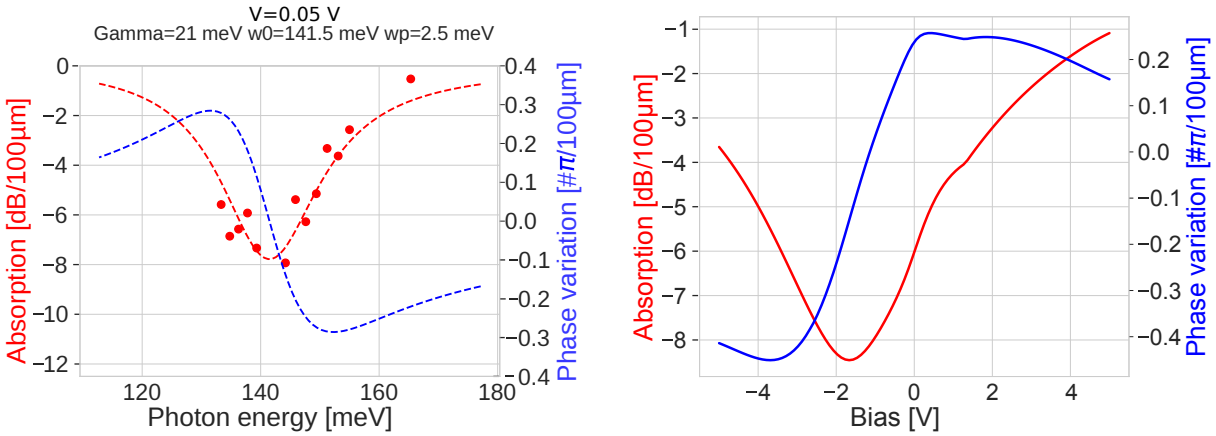

(a) (b)

Figure 4.27: a). Fitted Lorentzian absorption and phases curves on the measured data of QWASS 02 at a bias of 0.05 V, across all the scanned energy range (corresponding to the wavelengths between 7.5 and 9.3 µm). b) The resulting global extracted absorption and phase shift of the QWASS 02 modulator, in the (-5 V, +5 V) bias range. Data are normalized for an active modulator section length equal to L=100 µm.

the measurements). Nevertheless, this constitutes a clear demonstration of an electrically driven waveguide amplitude modulator in the LWIR spectral band, and the first waveguide amplitude modulator demonstration based on the inter-subband Stark shift. The complete performance heat-maps, representing the whole accessible phase space of the modulator is presented in Figure 4.28, with the measured and fitted absorption and phase modulation from Figure 4.27b, and optimal biases for phase modulation and performance are summarized in Table 4.3 below. One can see that the optimal biases are comparable with the designed values (with the exception of the bias -5V being on the lower bound of the measured and fitted data, suggesting that a lower bias would allow better performances in the limit of an applied field lower than 80kV/cm on the structure). The performance curve from Figure 4.27b are in good agreement with the simulated ones (Figure 4.9b) with a slightly larger linewidth and a small shift in bias of less than 2V. This is believed to come from a higher sensitivity of diagonal transitions in ACQW to an asymmetrical doping (the dopants are in the large well only), and to thickness variations between the two wells that are not correlated and that lead to an enlarged optical transition linewidth in comparison to an equivalent vertical transition in a single quantum well. The small shift in the position of the maximal absorption peak is itself believed to be linked to a slight change in the well and barrier dimensions from the designed ones that results in a shift of about 6% of the intersubband transition energy from the designed one. This is compatible with technological growth variation uncertainty.

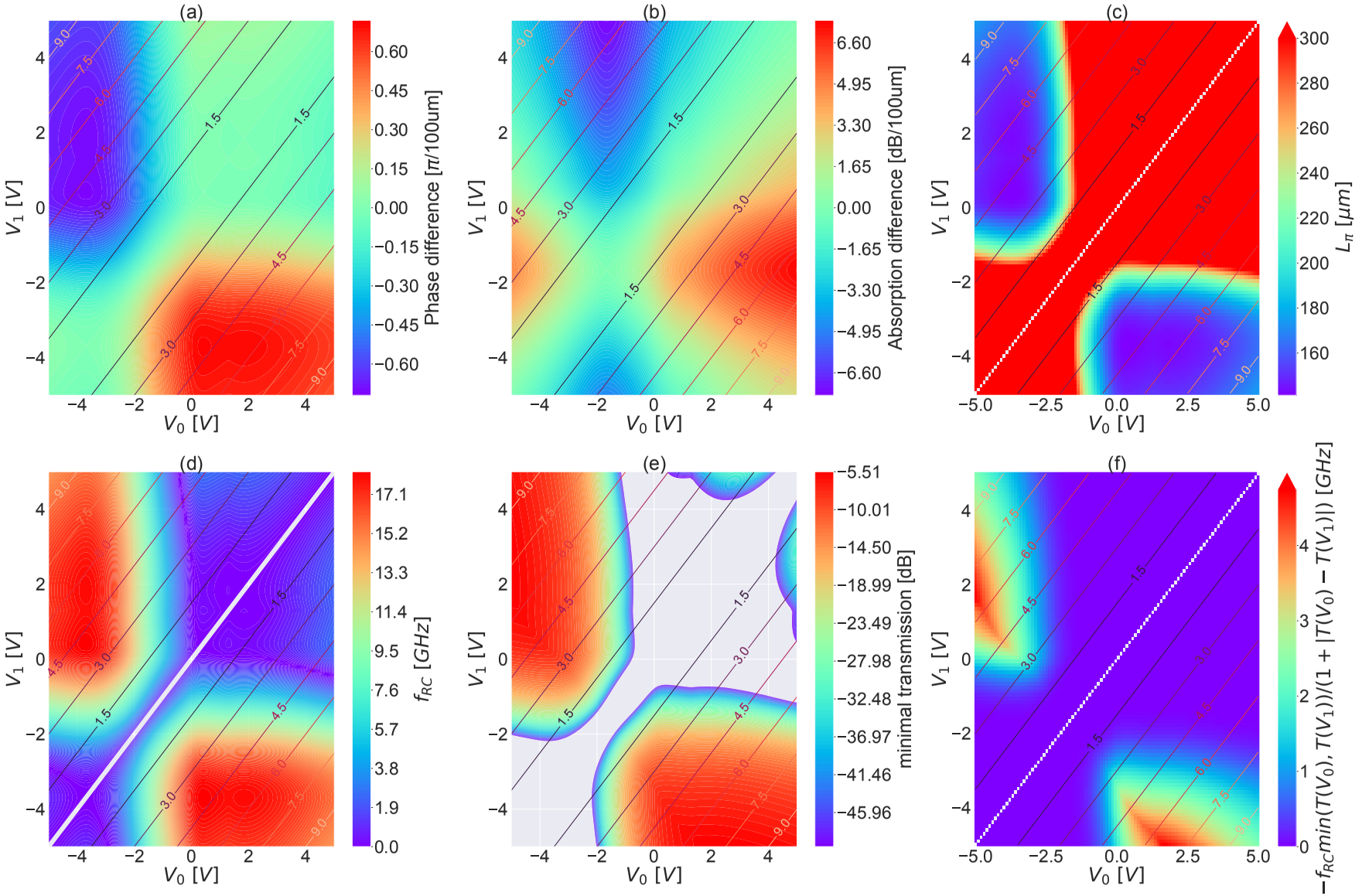

Figure 4.28: Performance heat-map of QWASS 02 as fitted on the measurements for a waveguide width of 8 µm. a) Phase modulation, b) Absorption modulation, c) L_π, d) f_{RC} for a length L_{pi}, e) minimal transmission for a length L_{pi}, f) FOM. Diagonal lines on the graphs are the value of the corresponding voltage excursion V_{pp}.

	Field <80kV/cm	V_{pp} <3V
Transmission [dB]	-5.5	-10
f_{RC} [GHz]	17	16
V_0, V_1 [V]	-5 and 1.7	-3.1 and -0.1
L_π [µm]	151	154

Table 4.3: Optimum biases for phase modulation and extrapolated performance with constraint of an applied electric field lower than -80kV/cm or a $V_{pp} < 3V$

5 Conclusion and perspectives

In this chapter, we have first presented the different physical effects that can be employed to achieve optical index modulation, with a focus on those that can be exploited on the mid-infrared range. The modulation of free carrier concentration in a waveguide core shows a great potential as its effect is more pronounced at longer wavelengths, this advantage is reduced by the fact that the typical volume in which those carrier densities are modulated do not scale with wavelength, which would necessitate particular waveguide geometries (such, for instance, inter-digitated PN junctions) to compensate for the lower optical field overlap, which complicates the fabrication and the subsequent integration with QCLs. The use of inter-subband Stark shift on the other hand, shows very strong modulation effect (as already reported in the literature), and is highly compatible with QCL as both stem from the same unipolar quantum technology, making their use particularly interesting for future monolithic integration. Our choice, therefore, was to focus on the use of Stark shift effect in ACQW into an optical waveguide, to realize a phase and amplitude integrated modulator.

In this chapter, we presented two active region designs, that show promising computed theoretical performances estimated by an home-made computational model. Those active regions were optimized in waveguide geometry to be flip-chip integrated by butt-joint flip-chip bonding together with a QCL and an optical amplifier on a dedicated RF sub-mount. The first (nominal) QWASS 01 design has been conceived to show high performances, that means a transmission greater than -8dB, a V_π of 3V for a L_π of 87 µm (thus an modulation efficiency of $V_\pi L_\pi$ of 0.03 V/cm) and a frequency cut-off around 30 GHz, which would be comparable to state-of-the-art modulators in the SWIR spectral band. The imposed fabrication constraints, namely using the same active region for the passive and active waveguides, led us to a more conservative design with a lightly doped active region, characterized by lower expected performances, but also with lower parasitic optical losses. This second alternative active region (indicated as QWASS 02) was designed to have a V_π of 5.3V for an L_π of 195 µm (thus $V_\pi L_\pi$ of 0.1 V/cm) and a reduced electro-optical bandwidth of 14 GHz, but optical loses much lower at zero bias, around -20 dB/mm in comparison to the -160 dB/mm of the QWASS 01 design.

A multiple dedicated on chip waveguide layouts have been presented. The idea behind was to have several configurations to be able to fully characterize the different electro-optical performances of the modulators. These are namely: symmetrical and asymmetrical Mach-Zehnder, planned for the characterization of the optical phase modulation ; straight and "S"-shaped waveguides for the estimation of the linear absorption and its modulation as a function

of the applied bias ; and some more exploratory alternatives, like Mach-Zehnder interferometers coupled with 90° hybrid MMI as an alternative layout for more advanced phase modulation characterizations. All of those have been fabricated during this thesis, for which a rather complex and time-consuming clean-room process has been developed.

Due to excessive absorption losses of the QWASS 01 structure (which were somehow relatively expected), optical characterization of the components has been possible only on devices integrating the QWASS 02 design yet. The results of such (still preliminary) characterizations showed very promising performances, close to the computed ones, with a maximal absorption of -8.5 dB/100 µm and a phase modulation of $0.7\pi/100\mu m$ between -4V and 1V, as extracted from a fit of the transmission with a Kramers-Kronig consistent model. Moreover, although the measured bandwidth showed limitations due to a parasitic capacitance associated to the RF coplanar waveguides, we were still able to measure a 1.4 GHz -3dB bandwidth on an epi-up component. Components dedicated to flip-chip integration should not have such limitations, and are expected to show much higher bandwidth. Despite that this is the first generation of devices, these performances already start to be comparable to state of the art performances in the telecom band around 1.55 µm.

As said before, these components are currently being assembled with a QCL and an optical amplifier on a dedicated RF sub-mount for high-speed operation. This integrated emitter would be the first demonstration of a fully integrated transceiver, in principle able to generate amplitude or phase modulated signals for free-space optical communication in the LWIR domain. This constitutes a very promising perspective for the development of future generations of mid-infrared integrated components.

In a longer-term perspective, the next generation of components would greatly benefit from the development of low-loss, passive waveguide structure based for instance on butt-joint regrowth of passive waveguides, or on the heterogeneous integration of components in a low-loss SiGe platform. This would permit to design complex optical functionalities benefiting from intrinsically low optical losses, which represented the main limiting factor in the devices developed during this thesis.

Finally, we would like to point out some difficulties we encountered in this work related to the design of the structure. The QWASS 01 design, which was particularly highly doped ($n_{2D} \approx 1e12\ cm^{-2}$) was not as resistive as expected, and didn't resist to relatively low voltage ($V \approx 3V$). We would suggest therefore to the designer wanting to pursue in the direction of this work to either use deeper energy levels (possibly with other barrier and/or well material to benefit from a higher band offset), or to use lower doping levels with possibly a higher number of periods.

Chapter 5

Coherent receiver for LWIR FSOC

Objectives

The development of the receiver for telecommunication link requires the association of a QCL acting as a local oscillator (LO), an optical amplifier and a detector. This chapter focuses on the development of all three elements to form a coherent photonic integrated receiver circuit. After presenting the different technologies of infrared detector and metrics to compare them, the chapter will focus on the development of a waveguide QCD in a coherent receiver. The general formalism of electronic transport in QCD will be recalled, and optimization of the device presented. Following the presentation of the fabrication of the device, its performances will be presented together with the performances of a 90 degree hybrid MMI for future implementation of an integrated I/Q coherent receiver.

Contents

1 LWIR detector and coherent detection

1.1 Figures of merits of infrared detectors

There exists a multitude of infrared detector technologies and geometries able to detect photons in the LWIR wavelengths. One can identify two kinds of infrared detectors :

- Thermal detectors which exploit a change of a physical property of a material when an impinging radiation heats it. The most common ones are pyroelectric cells and bolometers.
- Photonic detectors in which an impinging photon is absorbed by an electrical transition between two electronic states.

Thermal detectors, while very sensitive at room temperature, rely on physical mechanisms that are relatively slow compared to the other, their response hardly reaches tens of kilo-Hertz [211, 212] and are therefore not good candidates for telecommunication applications. They are, on the other hand, the most current detectors for imaging application and perhaps the most widely commercially available ones.

Photonic detectors can be very fast and easily reach tens of gigahertz frequency response as will be presented below. They are nevertheless very sensitive to their temperature of operation which limits their performances and has been an intensive subject of work in the last decade. Room temperature operation is a crucial aspect for an energy-efficient telecommunication link, as cooling a detector is costly in terms of energy consumption and also in terms of footprint.

Photonic detectors are the ones we will consider and present in this chapter. In order to compare them and identify the advantages and drawbacks of each one regarding our foreseen application, some FOM are useful. These FOM are based on definitions from references [213][19] and adapted for the characterization of photonic detectors used in direct detection (an impinging signal is directly collected on the photodetector or possibly pre-amplified) which is the simpler detection scheme, thus the one guiding our design for this first generation of a receiver.

Responsivity Probably the more meaningful one is the responsivity $\mathcal{R}$ given in [A.W^{-1}]. It is defined as the ratio between the photocurrent density $\mathcal{J}_{opt}$ in [A.m^{-2}] and the incident optical flux on the detector Φ in [W.m^{-2}]. This definition allows direct comparison of similar detector geometries under similar experimental conditions. This FOM depends upon the photon energy through the different efficiencies defined below.

EQE The *External Quantum Efficiency* (EQE) η_{ext} is a macroscopic characteristic of a photodetector defined as the ratio between the number of electrons produced at the output of the detector and the number of incident photons on the detector. It depends itself on two microscopic efficiencies :

- the absorption efficiency η_{abs}. It is the fraction of the incident photons in the detector active section that yield a photo electron. It depends on the optical geometry of the detector through the optical coupling and on the absorption mechanisms in the detector active section.

- the internal quantum efficiency η_i. It is the number of output electrons per photo-electrons generated. It is therefore an electrical transport term.

The overall EQE is then $\eta_{ext} = \eta_{abs}\eta_i$ and is linked to the responsivity by the following relation $\mathcal{R} = \eta_{ext}\frac{e}{h\nu}$ with e the elementary charge and $h\nu$ the incident photon energy.

NEP The *Noise Equivalent Power* (NEP) measures the optical power impinging on the detector that produces a signal equal to the noise of the detector. In a sense, it is the minimal power that the detector can unambiguously detect. For direct detection schemes, the NEP if often given in [W] and linked to the responsivity through the relation :

$$NEP = \frac{i_n}{\mathcal{R}} \tag{5.1}$$

where i_n is the current noise in [A]. It can also be given in [W.Hz$^{-0.5}$] especially for heterodyne detection scheme, in that case it is the ratio between the noise spectral density $\mathcal{S}_n$ and the responsivity $\mathcal{R}$.

Specific detectivity The specific detectivity $\mathcal{D}^*$ expressed in $Jones \equiv cm.W^{-1}.Hz^{-0.5}$. It is the inverse of the NEP normalized by the photodetector area and bandwidth measurement :

$$\mathcal{D}^* = \frac{\sqrt{A\Delta f}}{NEP} \tag{5.2}$$

In that expression, the photodetector area A is the optical area and not the electrical area. While it is often the case that the electrical and the optical area are the same, it is not the case in waveguide geometry. This FOM is strongly dependant to the measurement condition therefore several definitions are used [19]. Among them the dark detectivity $\mathcal{D}^*_{dark}$ is calculated with the noise curent i_n in the NEP measured without any illumination on the photodetector. The dark detectivity is a good metric as it only depend on the technology of the detector.

Electrical bandwidth In a telecommunication system, the electrical bandwidth of the photodetector is an important metric. Two different frequency cut-off can be used in order to compare the performance of a technology of photodetector. The first is the macroscopic frequency cut-off f_{3dB}. It is the frequency above which a given optical power modulation produces less than half the electrical power modulation it produces at very low frequencies. It is a macroscopic frequency bandwidth characterizing the transit time of photo-carriers from the active region of the detector to the external readout circuit, generally well described by a first order RC filter. It therefore characterizes the internal technology of the photodetector as well as it geometry and electrical environment in which it is integrated. This limit can come from any constituent of the detector (the readout circuit, the active structure, the interconnects etc...).

The second one is the intrinsic frequency cut-off f_{int} that is the microscopic intrinsic time limit of the physical mechanism at use. Also defined as the frequency above which the output signal power is half of its value at low frequencies, it is the ultimate limit of the macroscopic

f_{3dB} were it free of any parasitic cut-off. For example the intrinsic frequency cut-off of thermal detectors lies in the kilo-Hertz due to slow thermal diffusion processes while photonic detectors intrinsic frequency cut-off are often several tens of gigahertz and more.

1.2 State of the art of LWIR detectors

The diversified choice in commercially available LWIR photodetector covers a wide range of technological application, each with their performance requirements. In the telecommunication application it is important to have a detector with a high bandwidth (in the GHz range) and a low NEP. Moreover, the implementation in waveguide geometry and the integration with QCL has to be facilitated for the foreseen application, as well as ambient temperature operation. The following state of the art of available technologies justifies the choice of QCD as a photodetector to be integrated in the receiver.

HgCdTe based photodetectors are some of the more mature and widely available LWIR detector. They benefit from consequent developments since the 60's and it is, by far, their high responsivity that made their success. Wide detection wavelength tunability and quasi independent lattice parameter with composition, associated with the developments of new growth techniques also most likely contributed to their success [214, 215]. They have been developed in a multitude of forms taking advantages of different physical parameters of the alloys, photoconductors and photodiodes are the most common ones. Typical detectivity of uncooled HgCdTe detectors in the LWIR wavelength are up to 1×10^{9} Jones (whereas they reach up to 3×10^{12} Jones at 77K). The typical electrical bandwidth itself doesn't exceed 1GHz [211, 216]. Despite these promising performances, most of these detectors, and especially commercial ones, require cryogenic temperatures which are not compatible with telecommunication system requirements. Indeed, Auger recombination and tunnelling current have limited the rise in temperature operation of HgCdTe based detectors [217]. Moreover, cadmium and mercury are toxic materials whose use in electronic devices are restricted by the european RoHS directive. Nevertheless, recent work has been dedicated to push this platform into reaching room temperature operation with good performances, ref. [218] indicates the performance limit of HgCdTe based photodiodes and possible limiting factors in reaching them. An extensive comparative of all HgCdTe based detectors and particularly hot detectors is available in ref.[219].

Type II strained layer superlattice are a growing competitor to HgCdTe detectors due to their promise of lower Auger generation-recombination and lower fabrication cost compared to HgCdTe based detectors [220]. They are formed from alternating thin layers (a few monolayers) of InAs and GaSb (other materials combination such as InAsSb/GaSb or InAs/InAsSb "Ga-free" can be used, although GaSb has been preferred for its more convenient material growth [221, 219]). The alternating thin materials forms quantum wells in the valance and in the conduction band separated by a thin enough barrier to ensure coupling between wells, leading to the formation of minibands fig. 5.1a. Even though the theoretical performance improvement of *Type II Strained Layer superlattice* (T2SL) compared to HgCdTe photodiodes presented them

as a serious competitor, it has been shown that T2SL as an effective material, and even "Ga-free" or complementary barrier infrared T2SL, might not be able to reach HgCdTe photodiode performance and especially at high operation temperature [222]. Typical quantum efficiencies are about 50% to 60% in the LWIR wavelengths and detectivities up to 1×10^{12} Jones at 77K. Despite the limitation of T2SL, their association with the advantages of quantum cascade developed for QCL is likely to lead to a new generation of T2SL based photodiodes surpassing the forecast performances of HgCdTe detectors in high operation temperature in the mid infrared range [222, 223]. Recently Yan et al. have reported an interband cascade T2SL photodiode having a 260K maximum detectivity of 5×10^{8} Jones at a peak wavelength 10.4 µm. A little earlier Lei et al. demonstrated above 340K operation of such devices with peak detectivity reaching 1×10^{8} Jones at 300K at 7µm wavelength [224]. Nonetheless, detailed study of the frequency response of these detectors are still missing in the literature.

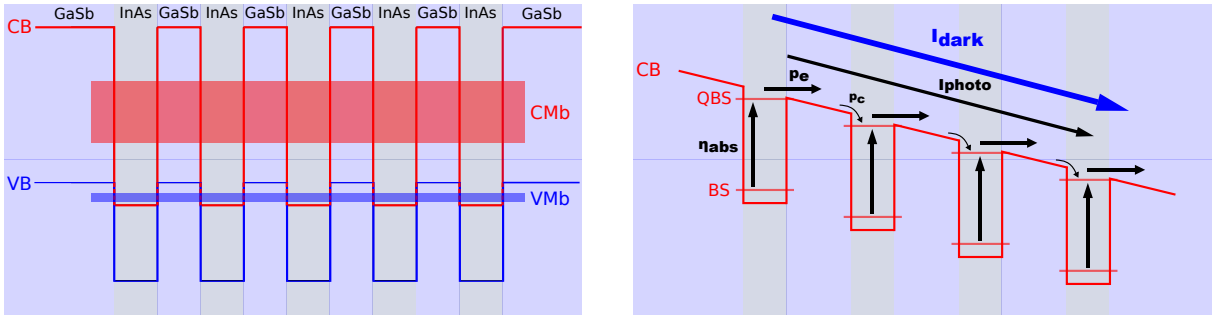

(a) (b)

Figure 5.1: (a) Typical band diagram of type II strained layer superlattice absorptive region. Optical absorption occurs between the valence miniband (VMb) and conduction miniband (CMb) formed by coupled quantum wells in the conduction band (CB) and valence band (VB). (b) QWIP typical band diagram. Larger barriers between adjacent quantum well lead to reduced coupling thus localized electron state in the conduction band in opposition to T2SL. Optical absorption occurs between a bound state (BS) in a well and a quasi bound state (QBS), photo-electrons are then extracted.

QWIP *Quantum Well Infrared Photodetector* are a photoconductor detector based on inter-subband absorption, demonstrated for the first time in the late 1980 years by Levine et al. [225]. Their structure is not unlike the structure of T2SL (fig. 5.1) as *Quantum Well Infrared Photodetector* (QWIP) are formed from alternating thin layers of III-V semiconductor materials (usually InAs/AlInAs, GaAs/AlGaAs or InSb/InAsSb) but with one major difference leading to completely different properties, the barrier separating each well is thick enough to ensure no coupling between the wells. Optical absorption occurs between the formed lower bound state in a well and the upper bound state. Careful positioning of the upper bound state close to the top of the well (ergo the "quasi bound state" denomination) allows the photo-excited electron to be efficiently extracted under bias creating a photo-current which is superimposed to a dark current fig. 5.1b. An intuitive way to see these components is to say that a photo-excited electron has a probability to be extracted from the quantum well p_e. Once extracted, it will propagate to the next quantum well, where it will have a probability p_c to be re-captured. The photocurrent

under uniform illumination on an N period (N quantum wells separated by a thick barrier) QWIP then writes as follows [213] :

$$I_{photo} \propto \eta_{abs} \frac{p_e}{N p_c} \tag{5.3}$$

Extensive discussion about the fundamental properties of QWIP is discussed in references [213, 19]. Contrarily to HgCdTe and T2SL photodiodes, QWIP are intersubband unipolar photodetectors : the photocurrent is only carried by electrons flowing in the conduction band and absorption occurs between two states within the conduction band ("holes" are essentially the non-mobile, unscreened donor impurities). While this results in sharp and strong optical transition compared to interband absorption, this also requires the use of carefully designed optical coupling to maximize the polarization parallel to the growth direction (see intersubband selection rule discussed in subsection 2.4). Another advantage of intersubband detector is that they are less sensitive to impurities and crystalline defaults leading to generation recombination, whose activation energy is around half the gap energy[1], well above the optical transition energy, which facilitates the fabrication of these devices. Typical performances of QWIP are detectivities above 10^{10} Jones at 100K in the LWIR but can reach room temperature operation with detectivity up to 10^7 Jones in the MWIR [221, 226]. They, in general, have a quantum efficiency below 10% due to the intersubband selection rule. Electrical bandwidth reaching tens of GHz have been reported thanks to fast LO-phonon assisted diffusion mechanism [19, 227]

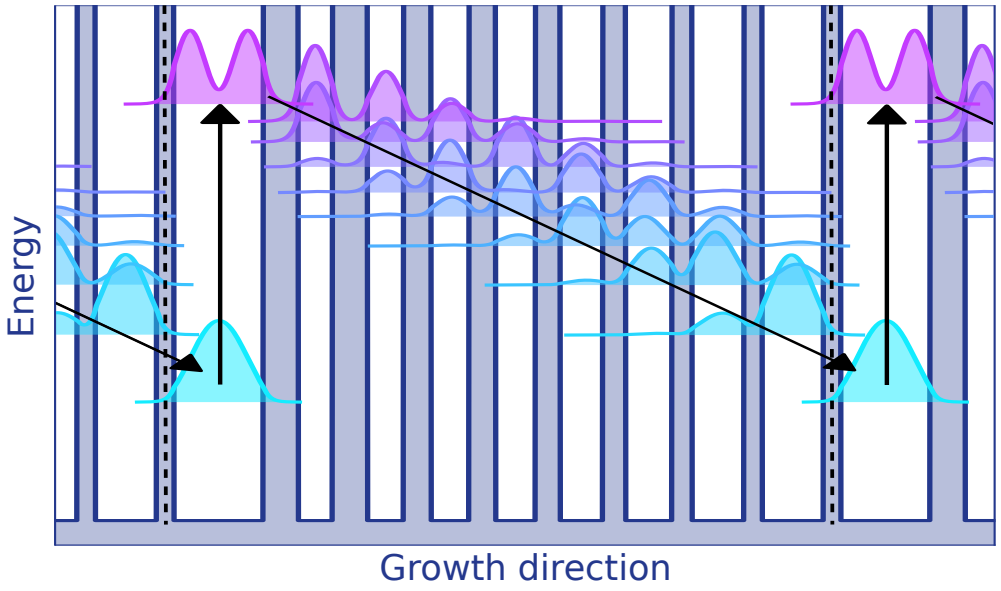

Figure 5.2: Band structure of an intersubband QCD. Optical absorption between the two levels of the large well is represented by the vertical arrow. The photo-excited electron is then extracted through the successive electronic levels of the cascade represented by the diagonal arrow, to the next optical well. The active region period is materialized by the two dotted lines.

[1]While this is often true, this strongly depends on the material used, it is not the case in InAs/InAsSb heterostructures

Intersubband QCD are as QWIP intersubband detectors and benefit from the same advantages and drawbacks. They can only detect photons whose polarization is parallel to the growth direction but benefit from fast transport mechanisms ensuring linearity and low saturability of the detector [228], and reduced sensitivity to impurities and crystalline defaults compared to interband detectors. QCD are born from the adjunction of a cascade, developed in the framework of QCL, to an absorbing quantum well, in order to efficiently extract the photo-electrons [229]. First report of a dedicated quantum well - cascade design for detection has been reported two years later in 2004 [230]. A typical band structure of QCD is presented in fig. 5.2. The asymmetry of the band structure allows detection without any applied bias. The similarity of band structure of QCL and QCD makes the heterogeneous integration of both on the same chip possible, greatly facilitating the fabrication process while limiting costs [155]. Room temperature QCD are reported with NEP of 80pW/√Hz and detectivity of 6.5×10^7 Jones [231]. Fast response with 3dB frequency cut-off above 25 GHz are reported, confirming the high potential of QCD for telecommunication applications [232]. A complete review of QCD is available in ref.[19].

New materials. Other detectors based on new materials such as graphene are being developed, but they are still in their early development. Nevertheless, their performance are worth mentioning as a potential future competitor to the above technologies. The review article ref.[233] presents a detail report of the developed technologies based on 2D materials covering the whole infrared spectrum. In the LWIR which is our particular interest, metal dichalcogenides seem to be better adapted materials than graphene, whose absorption coefficient is low. $PdSe_2$ photodetectors processed into field effect phototransistors have reached a detectivity of 10^9 Jones at room temperature from 1 to 10µm. Associated with MoS_2 into heterostructures, they even reached 10^{10} Jones, NEP of 0.1pW/√Hz, and response time in the 10 to 100µs range [234]. Polymer based photoconductors are also a recent trend in LWIR high-temperature detection, background limited detectivity greater than 10^9 Jones and NEP of 24 nW/√Hz has been demonstrated [235].

1.3 Coherent detection

In the first section we have exposed the main metrics allowing the comparison of different technologies of photodetectors. Telecommunication applications requiring smaller and smaller footprint, low-power consumption (which often work in pair), and high bandwidth, led us to the choice of intersubband QCD as a detector to be integrated in a future photonic chip together with a QCL. Indeed, the platform compatibility of QCD and QCL is of great advantage both for fabrication process compatibility, easier integrability and conjoint development with partners in charge of the QCL.

We have presented the performances of different technologies of infrared detectors has they would be in the case of direct detection, but as stated in chapter 1 and explained in chapter 2, direct detection is not the most efficient and robust implementation of a receiver for LWIR FSOC. Coherent detection allows the use of both phase and amplitude modulation to transmit

data at higher rates for a given modulation frequency (higher baud rate). Coherent receiver are based on the projection of the modulated signal received (Sx) onto a reference signal (LO) from a local oscillator laser. We can identify three regimes of coherent detection according to the frequency difference between Sx and LO. The Heterodyne detection regime is of particular interest for QCD based LWIR FSOC as it can considerably enhance the signal-to-noise ratio as we will see. A simplified schematic of the heterodyne detection principle is presented in Figure 5.3.

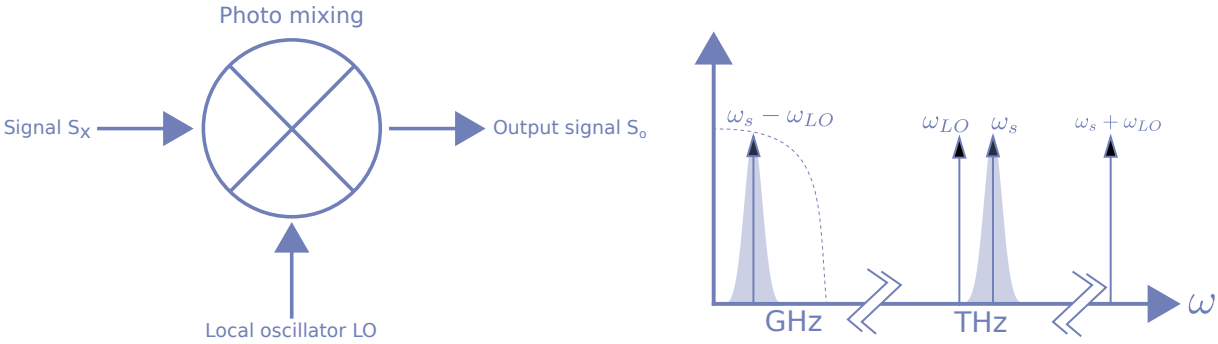

(a) (b)

Figure 5.3: a) Principle of heterodyne mixing. The signal S_x is mixed with the signal LO to produce a signal S_o. This mixing function can be done by a MMI for example. b) Spectrum of the produce mixed signal. In Heterodyne mixing, the frequency of the local oscillator (at ω_{LO}) is placed outside the bandwidth of the signal (at ω_s represented in shaded blue). The bandwidth of the quadratic detector, represented by the dotted line, filters out the high frequencies components (it averages them), leaving only the radio frequency signal generally in the GHz range.

We assume that the signal S_x is carried by an electric field E_s and LO by an electric field E_{LO} (the waveguide geometry ensures that both fields are linearly polarized provided that the waveguides are well-designed and fabricated). These fields are mixed in a photo-mixer (a MMI for example) to give an output signal S_o carried by an electric field E_o. In all generality, these fields write :

$$\begin{aligned} E_s(t) &= A_s(t)cos\left(\omega_s(t)t + \phi_s(t)\right) \\ E_{LO}(t) &= A_{LO}(t)cos(\omega_{LO}(t)t + \phi_{LO}(t)) \\ E_o(t) &= E_s(t) + E_{LO}(t) \end{aligned} \tag{5.4}$$

E_o is sent to a quadratic detector (sensitive to the optical intensity rather than the electrical field). In all generality, any detector presenting a non-linearity can be used but in practice photodiodes are the most commonly used as their quadratic dependence on the electrical field produces an undistorted heterodyne signal (provided that they are linear with respect to the impinging optical power). Time dependence of the above field amplitude, frequency, and phase can be caused by voluntary modulation or by noise variation. The conversion of E_o to an electrical signal I by the quadratic detector is then given by the following expression (we dropped the time fluctuation of phase, amplitude, and frequency for simplicity, but they have to be

considered, especially for modulated signal carrying information) :

$$I(t) \propto \frac{A_s^2}{2} + \frac{A_{LO}^2}{2} + A_s A_{LO} cos((\omega_s - \omega_{LO})t + \phi_s - \phi_{LO}) \tag{5.5}$$

In that last expression, the time-dependent terms at the optical frequencies ω_s and ω_{LO} have been averaged, since no considered detector is able to time resolve those fields. The term at frequency $\omega_s + \omega_{LO}$ is considered filtered out as its frequency is far greater than the frequency cut-off of the detector, therefore it is neglected. Filtering out the first two terms to leave only the last one, gives the heterodyne signal :

$$I_{het} \propto A_s(t) A_{LO}(t) cos((\omega_s(t) - \omega_{LO}(t))t + \phi_s(t) - \phi_{LO}(t)) \tag{5.6}$$

It is interesting to note that this heterodyne signal carries both the information on the instantaneous amplitude $A_s(t)$ and phase $\phi_s(t)$ of the signal. If the signal is an optically modulated signal carrying information, the heterodyne signal can be used to retrieve that information. Moreover, the power of the local oscillator (LO) can be chosen high enough to ensure a high signal-to-noise ratio, as we will see in the next part of this chapter. We will see that to take advantage of the heterodyne detection it is important to have a quadratic detector with the following characteristics

- a large bandwidth (in the GHz range) to time resolve the beating heterodyne signal
- high linearity and optical saturation power to ensure an undistorted signal
- a good EQE

All of those requirements can be met by QCD which is another reason for the choice of that kind of detector.

2 Design of waveguide QCD

After having presented the different infrared detector technologies available and justified the choice of QCD to be implemented in a telecommunication coherent receiver photonic circuit, we will develop in the following section the optimization of a waveguide QCD for that specific application. Firstly, the electronic transport formalism and the general trends it implies in the design of such structures, will be exposed following the work of Mathurin Lagrée [68]. Optical design and optimization will then be explained before the actual fabrication of the component. Finally the measured performances of the device will be exposed at the end of this section.

2.1 Elements of electronic transport

In chapter 2 we have seen how the band diagram of a heterostructure was simulated using a Schrödinger-Poisson auto-coherent solver, METIS, developed in the team. This code was applied in chapter 4 to the simulation of modulators in which only the dielectric function modelling of the

inter-subband transition was used, and the electrical transport was not explained in this chapter. As it is of great importance to understand the rules of QCD design, the following section will present the theoretical treatment of electrical transport in QCD as it is implemented in METIS, and its implications on the macroscopic quantities : dark-current, photo-response and signal to noise ratio. Direct application to the QCD structure named "QCD35b", designed in the MIR group of III-V Lab, will then be presented and compared to the measurements at the end of the chapter. As the electrical design of the band structure of this QCD was not part of this thesis work, we will only extract the performance simulated as is. Moreover, the more advanced rules of design presented in [68] were developed and stabilized after the design of that QCD. Therefore, the actual design of that one would most likely have been done differently and can likely be improved in a near future. QCD35b is composed of 15 periods of : **<u>96</u>**/37/**37**/37/**39**/ 29/**41**/28/**43**/26/**46**/24/**50**/21/**56**/19/**66**/18/(in bold are the InGaAs quantum wells, in plain text the AlInAs barriers and underlined the doped quantum well at $n_{2D} = 2e^{11}$ cm^{-2}.

2.1.1 Dark current and activation energy

In all detectors, a current will circulate through the electrical circuit under bias. This current can come from many origins inherent to the technology (intrinsic), but also from the fabrication process. Indeed, the fabrication most likely will induce crystalline defaults and/or impurities which will all be sources of SRH generation/recombination currents and necessitate careful passivation steps to ensure the device performance. The process induced currents sources often comes from impurity electronic states at mid gap in the semiconductor, which in the case of inter-subband devices require a much larger energy than the inter-subband transition. This makes these devices autopassivated and greatly simplify their fabrication process. Therefore, it is particularly interesting to minimize the intrinsic dark current, which will be superimposed to the photo-current under illumination, and add noise. This current can be calculated from the rates $\Gamma_{i\to j}$, calculated as explained in chapter 2. At a given position z_0 it is given by the net electron flux as [68] :

$$J_{dark} = q \sum_{\substack{i \\ z_i<z_0}} \sum_{\substack{j \\ z_j>z_0}} (\Gamma_{i\to j}\ n_i - \Gamma_{j\to i}\ n_j) \tag{5.7}$$

In that equation, z_i and n_i are respectively the barycentre and electron density of the wavefunction (or electronic state) i, and q the elementary charge. The simulated dark current density of QCD35b is presented in Figure 5.4.

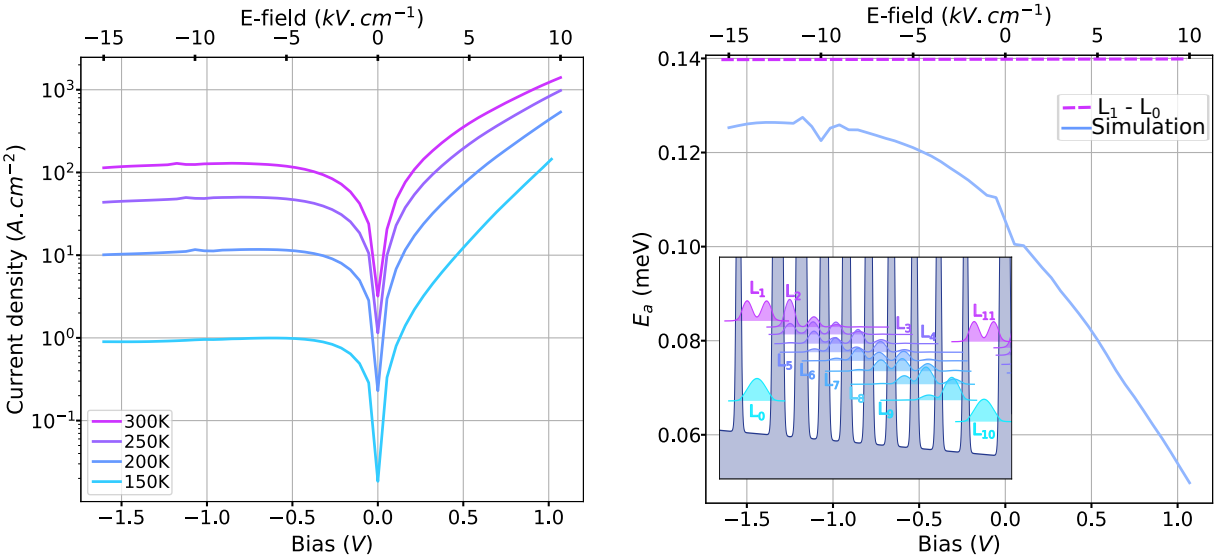

(a) (b)

Figure 5.4: (a) Simulated dark current densities for the 15 periods QCD35b versus applied bias or electrical field at different temperatures. (b) Simulated activation energy of QCD35b versus bias. The inset represents one period of that QCD at a -5 kV/cm electric field.

The dark current is a thermally activated current as seen in the simulated current densities Figure 5.4a. We evaluate the thermal activation energy E_a of that current at a fixed bias according to the Arrhenius law, the result is represented in Figure 5.4b :

$$J_{dark}(T) \propto exp\left(\frac{-E_a}{k_B T}\right) \tag{5.8}$$

This activation energy is lower than the commonly approximated energy difference between the Fermi energy level E_F (or the fundamental level L_0 if the Fermi level is below it) and the excited level in the optical quantum well (L_1 in Figure 5.4b insert). In the present structure as the Fermi level is 30 meV below L_0, this energy difference that we will call E_{approx}, is about 140 meV, which is 40% above the simulated activation energy at 0V. The simulated activation energy increases at negative biases to peak at -12kV/cm almost 30% greater than its value at 0V . This configuration tends to increase the energy difference between the levels in the cascade and depopulates them[2], the lower levels in the cascades are thus less and less acting as stepping stones and the activation energy increases. Furthermore, the coupling between L_1 and the upper levels of the cascade decreases as the bias becomes negative, until the activation energy reaches a maximum around 130 meV at about -12 kV/cm. Decreasing more the bias below -12kV/cm will then activate diagonal transitions (L_0/L_2, L_0/L_3, L_0/L_4 etc...) as the levels in the cascade become closer to the fundamental level L_0 and the structure becomes more asymmetrical. In opposition, increasing the bias toward positive biases will progressively "flatten" the cascade, creating a preferential path for the electrons and considerably decreasing the activation energy. With increasing positive biases, the activation energy will tend to the L_1 - L_{10} energy difference.

[2]This is valid for the design presented here and not a general trend

2.1.2 Photo-response, absorption and extraction probability

Having seen how the dark current is calculated by our simulation software METIS, we can now proceed with the photo-response under illumination of the detector. This photo-response comes from the calculation of two metrics :

- how likely is an impinging photon able to promote an electron to the excited state L_1 of an optically active quantum well, the **absorption spectrum** α.
- how likely will that photoelectron be extracted toward the fundamental level of the next optically active quantum well (or to the contact), the **extraction probability** p_e.

For the first metric, we have demonstrated in chapter 2 that the thickness of a quantum well being much smaller than the optical wavelength in the material, the absorption spectrum could be reduced to the expression below :

$$\alpha(\omega) \propto \mathfrak{Im}\left(\frac{-1}{\varepsilon^z_{QW}}\right) \tag{5.9}$$

In the above expression, ε^z_{QW} is the quantum well permittivity in the growth direction. It is calculated by the sum over all intersubband transitions (i to j) of lorentzian functions integrated over energies E:

$$\varepsilon_e = \varepsilon_{BKG} + \sum_{i,j \ i\neq j} \int_E \frac{\omega^2_{pij}\rho_{2D}(E)\left[f_{FD}(E_i)(1-f_{FD}(E_j)) - f_{FD}(E_j)(1-f_{FD}(E_i))\right]}{(\omega_{ij} + E(1-m_i/m_j))^2 - \omega^2 - j\Gamma\omega} dE \tag{5.10}$$

This ε^z_{QW} as well as the effective length L_{eff} on which it applies can then be fed to the analytic optical mode solver to simulate the real absorption of a given structure, in our case a waveguide, and obtain the absorption efficiency η_{abs} of the detector, which includes the geometrical overlap of the optical electric field and so-called depolarization shift, implicitly calculated when solving the Maxwell's equations. Detailed calculation of L_{eff} can be found in [236] and discussion of the above equation in chapter 2.

Once the absorption efficiency is calculated, only the extraction probability has to be calculated to simulate the photo-response of the QCD. This calculation takes advantage of the Markovian matrix formalism as explained in detail in [68]. For a QCD period of N confined levels (L_0 to L_{N-1}, $N = 10$ in our QCD) and at each instant n, an electron thermalized in the subband j has a probability p_{ij} to transit to the level i by the instant $n+1$, independently to the absolute step value n (the process has no memory). Under the following assumptions :

(i) we then consider that an electron in the fundamental state (L_0 for the period 0) will stay in that state until a photon promotes it to the excited level (L_1 for the period 0)

(ii) an electron will necessarily leave any other level but the fundamental between each step

(iii) an electron reaching the fundamental level in the next period (L_{11} for period 1) is extracted

the extraction process can be modelled by the Markov matrix P. The extraction probability is then the limit when n approaches infinity of the last element of the propagated vector p_n, with p_0 the initial "position" of the photoelectron in the first excited state (L_1 in period 0) :

$$p_e = p_\infty[N] \text{ with } p_\infty = \lim_{n\to+\infty} P^n \, p_0 \tag{5.11}$$

in which :

$$P = \begin{pmatrix} 1 & p_{01} & p_{02} & \cdots & p_{0(N-1)} & 0 \\ 0 & 0 & p_{12} & \cdots & p_{1(N-1)} & 0 \\ 0 & p_{22} & 0 & \cdots & p_{2(N-1)} & 0 \\ 0 & \vdots & \vdots & \vdots & \cdots & 0 \\ 0 & p_{(N-1)1} & p_{(N-1)2} & \cdots & 0 & 0 \\ 0 & p_{N1} & p_{N2} & \cdots & p_{N(N-1)} & 1 \end{pmatrix} \quad \text{and } p_0 = \begin{pmatrix} 0 \\ 1 \\ 0 \\ \vdots \\ 0 \end{pmatrix} \tag{5.12}$$

The photo-response of the QCD can then be calculated from the absorption efficiency and extraction probability as each of the N period of the QCD are in series [19] :

$$\mathcal{R}(\omega) = \eta_{abs}(\omega)\frac{p_e}{N}\frac{e}{\hbar\omega} \tag{5.13}$$

From Equation 5.13 one can think that the higher the number of period in the QCD, the lower the photo-response. As it is true for a very high number of period, it is less the case when reasonable number of period are used, as the absorption efficiency η_{abs} tends to be proportional the number of period. Indeed, in a structure where the electric field varies at scales much greater than the period length, adding a period will add the same absorption quantity until the total thickness of the absorbing region of the QCD becomes comparable to the in media optical wavelength. In the next section we will discuss the optimization of η_{abs} conjointly to the detector performances in more details.

2.2 Performance optimum of waveguide QCD

We have in the last section explained how the electronic properties of our QCD are calculated due to the band structure. However, we have not discussed the impact on the performance of the different degrees of freedom we have when designing it in a waveguide geometry. Let us consider a ridge waveguide of width W, length L and cross-section represented in Figure 5.5. The vertical structure of that waveguide is composed of a gold layer, 4 µm of InP n:1e17 upper cladding and 2.5 µm of InGaAs n:6e17 core on an InP n:1e17 substrate. In the middle of the core we put N periods of the QCD presented in Figure 5.4b insert. Vertical dimensions of the waveguide structure are chosen to match the optical mode of the QCL chosen, and the fundamental optical mode of the waveguide, to limit the coupling losses between the two as explained in chapter 2. Those dimensions are therefore not a degree of freedom in our design. Based on these assumptions we will explain in this section the optimization process of waveguide QCD for telecommunication applications.

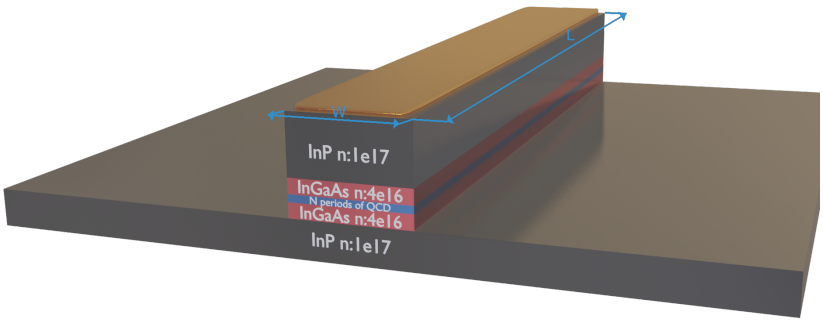

Figure 5.5: Waveguide geometry of our QCD. It is composed of a 2.5 µm thick InGaAs core embedding the N periods of the QCD in it centre, a 4 µm thick InP upper cladding and a thin layer of gold.

2.2.1 Signal to noise ratio

When designing a detector, one wants to maximize the signal-to-noise ratio of it for a given application. Geometrical parameters such as the length of the waveguide, the number of period of QCD embedded in the waveguide, and their doping can have a considerable impact on the final performances. Indeed, the optical power injected into the waveguide decreases exponentially with its propagation length as it is absorbed, so that after some distance there will be very little power left to be absorbed. On the other hand, any section of the waveguide of given length will add more electrical noise to the measurement, as well as reduce the component frequency cut-off. Choosing the right length is therefore detrimental to the performances of the final component. The signal-to-noise ratio dependence on these parameters can be intuitively linked to the noise and absorption dependence on these.

External quantum efficiency :

Under the assumption that the perturbation on the repartition of the optical electrical field induced by the introduction of one period of QCD in the core of the waveguide is negligible, because its dimension are much lower than the wavelength in the media (i.e. we assume that adding a period will not strongly impact the real part of the effective dielectric constant of the optical mode but only its imaginary part, ergo its losses), it is then reasonable to approximate the absorption efficiency by the following equation :

$$\eta_{abs} = \frac{\alpha n N}{\alpha n N + \beta} \tag{5.14}$$

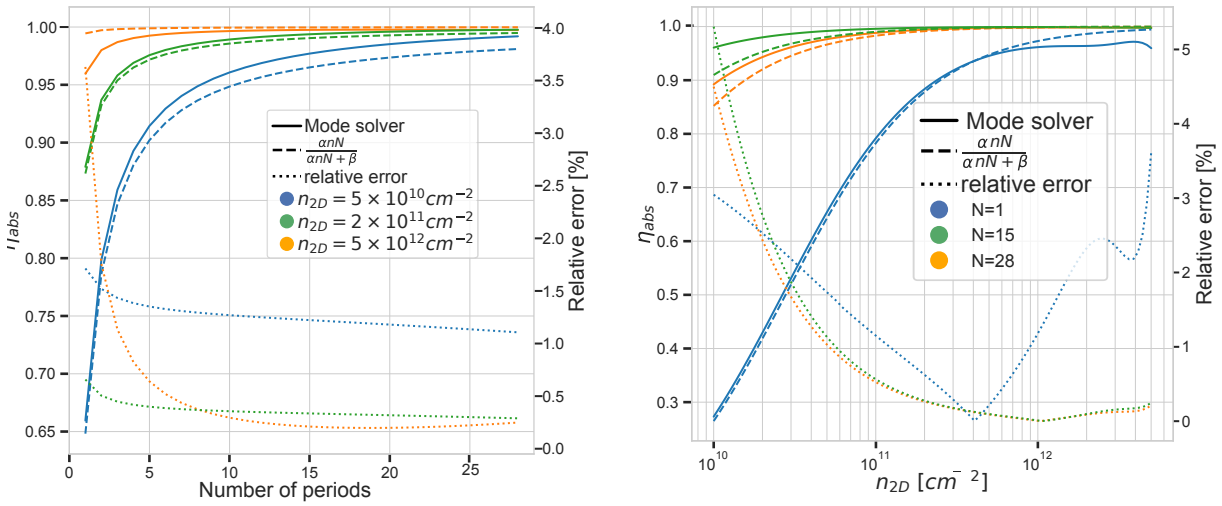

(a) (b)

Figure 5.6: (a) Comparison of the rigorous simulated absorption efficiency of the QCD35b for low, intermediate and high doping versus the number of period, with the approximate expression Equation 5.14. The same simulation versus the optical well doping for low, intermediate and high number of periods N

The absorption due to the inter-subband transition is considered to be the same for all the active quantum well of the N periods (we assume the same overlap with the optical electric field), α, and proportional to the doping of those well n (αn is given in m^{-1}). Other absorption mechanisms in the waveguide are also present and regrouped in the β term. They are considered to be independent of the number of period N as mostly coming from absorption in the gold top contact and to some extent in the thick semiconductor layers. These approximations are in good accordance with the numerically simulated performances using the planar mode solver introduced in chapter 2, as is reported in Figure 5.6. The relative error made using the approximate formula Equation 5.14 is always below 5%. In most practical applications requiring an intermediate number of period and doping (generally 5 to 10 periods and doping below 1×10^{12} cm^{-2}), this approximation will be of good use. Throughout its propagation, the optical mode power will exponentially decrease and produce less and less photoelectron by unit length. The EQE can then be cast in the form (we assume a unitary optical coupling coefficient) :

$$\eta_{ext} = \eta_{abs} \frac{p_e}{N} \left(1 - exp\left(-(\alpha n N + \beta) L\right)\right) \tag{5.15}$$

Signal to noise ratio :

We can use the result of Equation 5.15 to obtain an analytical expression of the signal-to-noise ratio in direct detection schemes, firstly in the case of direct detection. For QCD the noise S_J can be written accurately as [19] :

$$S_J = \frac{2e}{N} |J^+ + J^- + J_{opt}| \tag{5.16}$$

In that expression, J^+ and J^- are respectively the dark generation and recombination micro-current densities and J_{opt} the optical current density. The goal in designing a component is to minimize the dark generation and recombination micro-current densities. At a zero bias, both J^+ and J^- are equals and when a bias V_p is applied on one period, they only differ by an exponential term $exp(V_p/k_BT)$. An approximate expression of the dark micro-current densities is given by the following expression at zero bias [68] :

$$J^+ = J^- \equiv J_{dark} \equiv J_0 \; e^{\frac{n}{k_B T \rho_{2D}}} e^{-\frac{\omega_{ISB}}{k_B T}} \tag{5.17}$$

Where J_0 is considered independent of the doping and temperature, ρ_{2D} is the two-dimensional density of states, and n the active well doping ergo the electron density in one QCD period. In chapter 2 we have seen that the actual absorption peak is actually blue shifted in comparison to the inter-subband transition energy by the value of the plasma energy ($\tilde{\omega_{ISB}} = \sqrt{\omega_{ISB}^2 + \omega_p^2}$). For an initially judiciously chosen inter-subband transition energy, when looking at the influence of the doping on the dark noise, one has to take into account that shift and lower the designed transition energy when increasing the doping, which are both detrimental to the dark current noise. Therefore, we replace the ω_{ISB} in the above expression by the difference between the targeted photon energy and the plasma energy ω_p so that the current noise S_J is approximated by :

$$\tilde{J}_{dark}(\omega) = J_0 \; e^{\frac{n}{k_B T \rho_{2D}}} e^{-\frac{\sqrt{(\omega^2 - \omega_p^2)}}{k_B T}} \tag{5.18}$$

$$S_J = \frac{4e}{N} J_0 L W \; e^{\frac{n}{k_B T \rho_{2D}}} e^{-\frac{\sqrt{(\omega^2 - \omega_p^2)}}{k_B T}} \tag{5.19}$$

Following the above expressions 5.19 and 5.15, the SNR ratio of the waveguide can be approximated by :

$$SNR = \frac{\eta_{ext} e}{h\nu S_J} = \frac{\eta_{abs} p_e e}{2h\nu\sqrt{e J_0 N L W}} \left(1 - e^{-\frac{\alpha n N L}{\eta_{abs}}}\right) e^{\frac{n}{2k_B T \rho_{2D}}} e^{-\frac{\sqrt{(\omega^2 - \omega_p^2)}}{2k_B T}} \tag{5.20}$$

Interestingly, it is possible to express this SNR only with the fraction of the absorbed power A, which is the term in parentheses in the above expression. This leads to an expression of the SNR which is independent to the waveguide length L :

$$SNR = \sqrt{\frac{\alpha p_e^2}{4e J_0 W}} \frac{-A}{\sqrt{\log(1-A)}} \sqrt{\eta_{abs} n e} \, e^{\frac{n}{2k_B T \rho_{2D}}} e^{-\frac{\sqrt{(\omega^2 - \omega_p^2)}}{2k_B T}} \tag{5.21}$$

The optimization of the waveguide QCD for direct detection then consists in first in optimizing the doping and number of period (given an energy transition) to maximize the term in blue, then choosing the length L that allows an absorption of 71% of the power that maximizes the term in red. If the doping found produces a large plasma shift, tweaking the inter-subband transition by the value of the plasma shift can be a start for a second iteration of the above optimization process until a satisfying design is found.

When it comes to heterodyne detection, the above development doesn't hold. A new noise contribution appears, which depends on the local oscillator power P_{LO}. As the photocurrent in heterodyne detection is given by Equation 5.5, the signal-to-noise ratio when dominated by the shot noise can be written as (we neglect the local oscillator noise) :

$$SNR = \frac{2\eta_{abs}\frac{p_e}{N}\frac{e}{\hbar\omega}\sqrt{P_s P_{LO}}}{\sqrt{\frac{4e}{N}\tilde{J}_{dark}WL + 2e\eta_{abs}\frac{p_e}{N}\frac{e}{\hbar\omega}(P_s + P_{LO})}} \tag{5.22}$$

If the local oscillator can be chosen such as its optical power is much greater than the signal to be detected ($P_{LO} >> P_s$), then the signal-to-noise ratio can be as high as $\sqrt{2\eta_{abs}\frac{p_e}{N\hbar\omega}P_s}$ (expressed in $Hz^{-0.5}$). The local oscillator power necessary to transition to the heterodyne noise limited regime is given by the limit :

$$P_{LO} > \frac{2\tilde{J}_{dark}WL}{\eta_{abs}p_e}\frac{\hbar\omega}{e} \tag{5.23}$$

There seems to be no clear optimum length in the design of a waveguide QCD for heterodyne detection, the shortest component appears to be the best to minimize the necessary local oscillator power to be in an heterodyne limited regime of noise. As this power is rarely limiting with QCL the design of a waveguide optimized for direct detection is convenient for heterodyne detection too, provided that the necessary optical oscillator power is available. The local oscillator power necessary to reach that regime is plotted in Figure 5.7b in the case of the QCD35b structure embedded in a 8 µm wide waveguide, and whose length is chosen to absorb 71% of the optical power.

As the number of period increases, the absorption efficiency increases and the length necessary to absorb 71% of the optical power decreases, this results in a decrease of the LO power necessary to reach the heterodyne noise regime with the number of period. Similar behaviour is noticed with the doping of the active wells in Figure 5.7.

2.3 Fabrication

The optimization of the QCD35b structure has been presented in the last part as well as it's expected optical performances. In this part, we present the fabrication process of this structure in waveguide configuration. Multiple combination of length (50, 100, 150, 200, 500 µm) and width (8, 10, 12, 15, 20 µm) of waveguide have been fabricated as well as cylindrical and rectangular shaped mesas of different dimensions for dark current characterization. The whole fabrication process is done on molecular beam epitaxy grown structure on InP n:1e17 cm^{17} two inches substrates. A second growth step using metalorganic chemical vapour deposition defines the top InP cladding. The complete growth sheet is presented in Appendix A. The fabrication process is very similar to the processing of the modulators presented in chapter 4. Therefore, we will not develop it in more details.

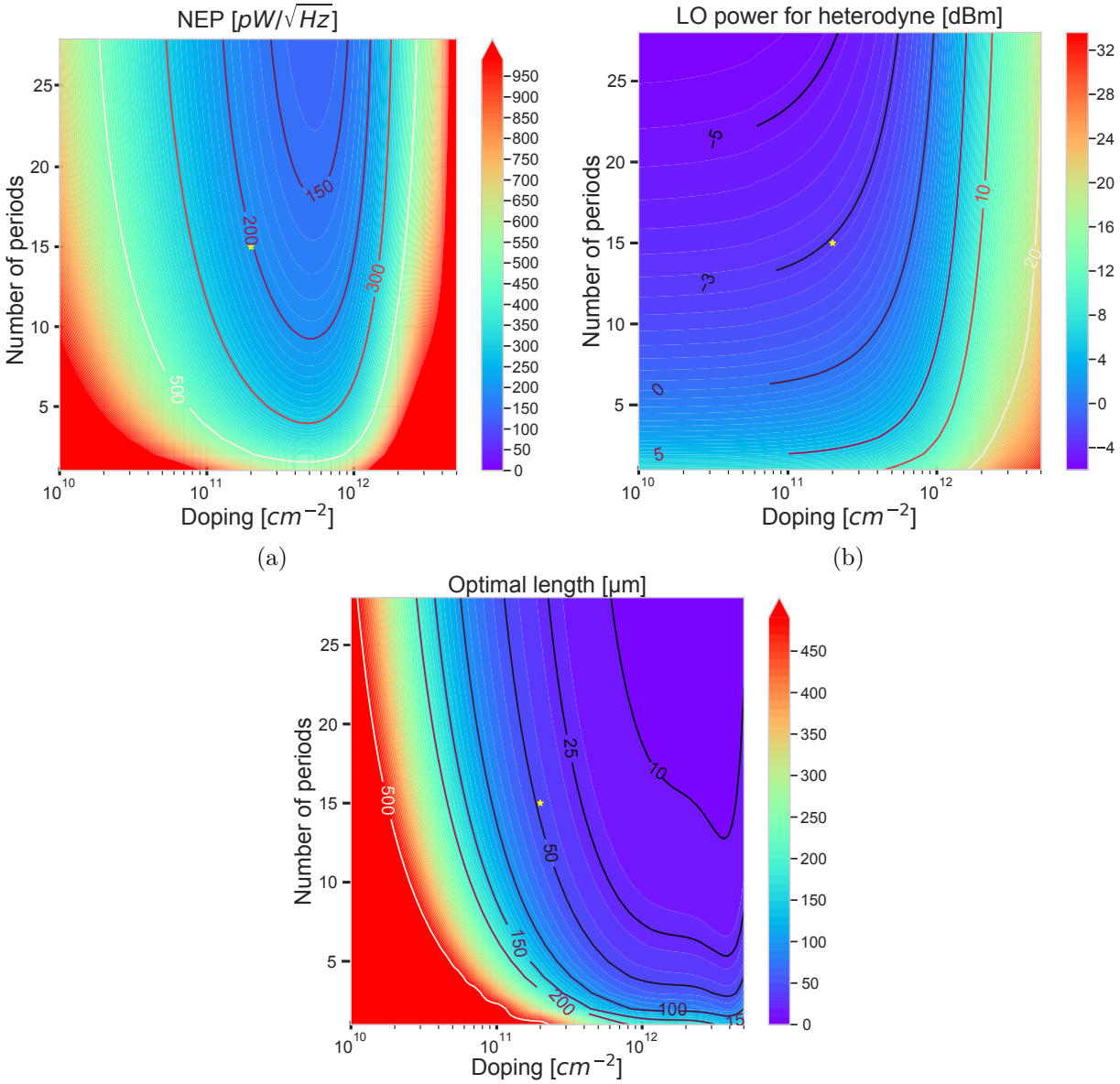

(a) (b) (c)

Figure 5.7: (a) NEP in direct detection of a waveguide optimized for direct detection with the QCD35b band structure. The extraction probability is 0.54 and the width 8 µm. b) Corresponding LO power necessary to reach the heterodyne limited noise regime of detection. The yellow star is the QCD35b 15 periods actual design. c) Optimal length to absorb 71% of the injected optical power.

2.3.1 Ridge etching

The first step is the definition of the ridge waveguide geometry. The ICP-RIE etching technique is used for that step with the following conditions : 90 W RIE power, 800 W ICP power, 9 SCCM Cl_2, 19 SCCM H_2, 2 SCCM Ar at a chamber pressure of 1.5 mTorr [237]. The chuck was cooled down to 60°C due to specific constraints on our equipment. To allow the sample to be heated by the plasma, no vacuum grease is used between the chuck and the sample allowing the temperature of the sample to build up, ensuring a good desorption of the produced $InCl_x$ compounds (as explained in chapter 4). A thick 1.2 µm silicon nitride hard mask deposited by PECVD and opened by fluorinated RIE as described in chapter 4 is used to define the etched ridges. Under those etching conditions, a selectivity SiN to InGaAs/InP of 1 to 8 has been found for the QCD structure. The SiN hard mask is then removed using the same fluorinated RIE recipe. An SEM picture of this step is presented Figure 5.8.

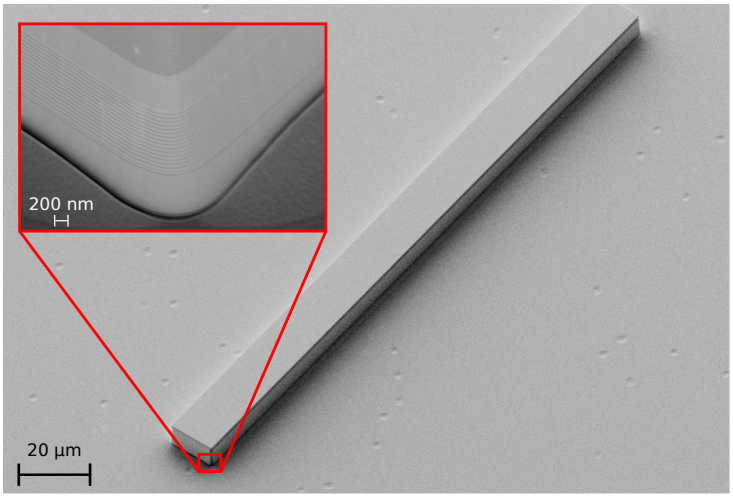

Figure 5.8: SEM picture of the etched ridge QCD waveguide. The inset presents a zoom on the waveguide core, where the QCD periods are clearly visible. Some crystalline defaults are visible as "holes" in the etched substrate.

2.3.2 Passivation and contact opening

Once the ridge waveguide has been etched, a thin 120 nm thick hafnium dioxide (HfO_2) is deposited on the whole sample to passivate the waveguide and electrically separate the metallized contacts to come. This deposition is done using the ALD technique (in thermal deposition mode at 250°C) for its high thickness uniformity on high topology samples. This HfO_2 film is then etched using the same fluorinated RIE recipe used to remove the SiN hard mask in the previous step. A thick photoresist (SPR 220 4.5) is used for that step in order to well cover all the surfaces and especially the waveguide edges. The result of that processing step in shown in Figure 5.9.

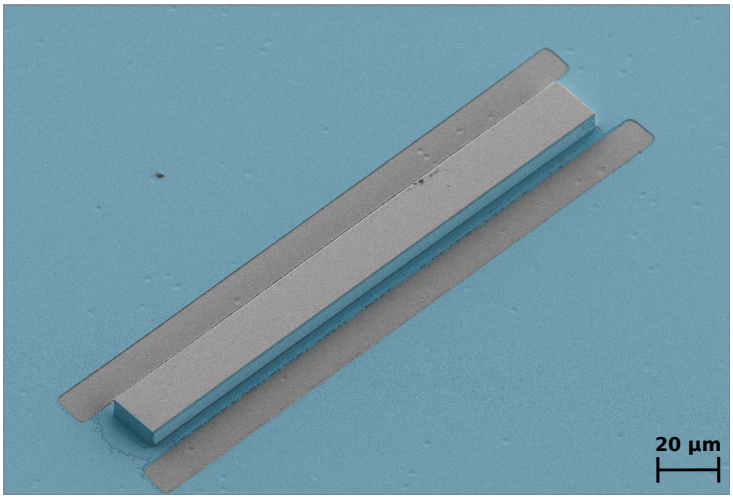

Figure 5.9: SEM picture of locally opened contacts in the HfO_2 thin film. The dielectric is coloured in light blue.

2.3.3 Metallization

The electrical Ti/Pt/Au 50/75/350nm ohmic contact is then deposited using the sputtering technique with a 45° angle tilt between the sample and the sputtered beam. This allows a good deposition uniformity on all the surface and particularly the vertical edges of the waveguide. The resulting metallized coplanar access contact is shown in Figure 5.10. The resulting component is formed of two ridge waveguides that are then cleaved along the central axis to produce two QCD waveguides with a cleaved facet after a thinning step. The thin dielectric on a doped substrate leads there to a strong parasitic capacitance which will greatly reduce the electrical bandwidth of the component similarly to the modulator. Nevertheless, the process used was already developed and further developments to limit this capacitance using for example a planarization with a thick polymer such as BCB, would have led to significant delay. Ultimately, the future generation will be processed on semi-insulating iron-doped InP, which would likely solve that issue.

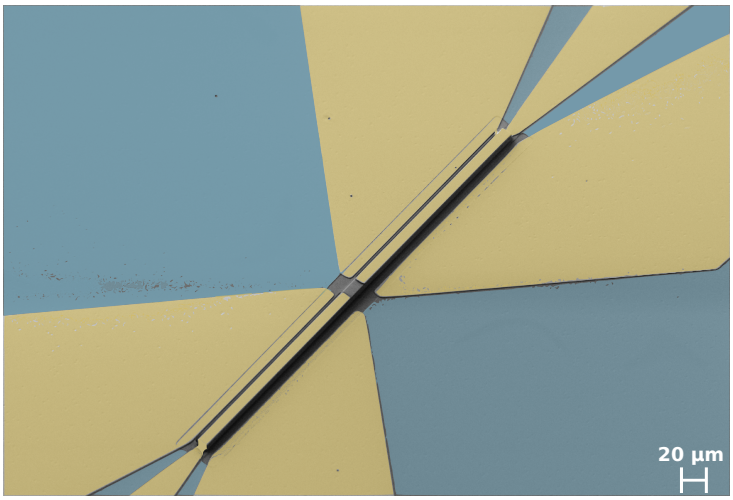

Figure 5.10: SEM picture of the finalized component before thinning and cleaving.

2.4 DC characterization

2.4.1 Dark current and activation energy

The activation energy of test structure of different dimensions is a good indicator of the growth and fabrication quality. To that end, a dedicated sample from the same wafer as the processed waveguides is used. It is composed of multiple circular and square mesa of different dimensions, which are reported in Table 5.1. Surface current densities are measured in a cryostat with a cold screen to ensure dark condition. Activation energy is then extracted from a linear regression of the data following Equation 5.8. The results are presented in Figure 5.11 and compared to the simulated activation energy[3]. It appears that even though the general trend of the activation energy with respect to the bias is similar to the simulated one, in that it peaks at a reverse bias (around -0.4 V) and decreases for stronger reverse bias or direct bias, the absolute value of that activation energy peak is almost 25 % below the simulated one and the peak appears at a bias which is 70 % below the simulated one. This difference is not understood yet, and can come from multiple origins that would have to be investigated.

The first one is the parameters used to model the quantum well interfaces (discussed in chapter 2). Those parameters have been extracted from MBE grown test samples and have been seen to correctly match the measured QCD performances from other geometries (see [68, 11]), thus should correctly match our component that have been grown during the same epitaxial campaign. But our waveguide QCD has seen a successive MOCVD growth of the 4 µm thick top cladding that could have modified, somehow, these parameters. Moreover, this regrowth has been seen to create crystalline defaults (such as cross-hatch) in the structure that were visible under optical microscopy, these are the consequences of constraint relaxation during the growth and corroborates the possibility of a modified band structure, that again would have to be investigated.

The second one is the possible presence of a shunt resistance in the component due to fabrication process induced defaults that would short-circuit some QCD period. On Figure 5.8 it is clearly visible that the 15 QCD periods are well above the substrate, therefore a shunt resistance, if process induced, would likely create a peripheral current contribution and an activation energy therefore depending on the perimeter of the test mesas. It doesn't seem to be the case as presented in Figure 5.11d) and neither is the case for an eventual surface contribution to the activation energy, as presented in Figure 5.11c), except maybe at strong direct bias, which is believed to actually be a measurement artefact due to mesa self heating.

The third one is a possibly badly determined component temperature. Indeed, the setup used at the time of that measurement had shown poor thermal contact between the component and the cold finger of the cryostat, and is still under investigation to improve the quality of this measurement. Nevertheless, this poor thermal contact should only impact the amplitude of the measured activation energy but not the bias at which it peaks unless self heating is confirmed.

The test structures for activation energy characterization have presented different results than simulated and the origin of that difference has yet to be determined. Nevertheless, the

[3]The measures have been done by Salvatore Pes and Nour Nawfal

	C2E	C3S	C4S	S2S	S3S	S4S
Area $[mm^2]$	0.04	0.09	0.24	0.04	0.09	0.25
Perimeter $[mm]$	0.71	1.06	1.75	0.8	1.2	2

Table 5.1: Mesa dimensions for the activation energy characterization

measured activation energy and the current density scalability to the component area are not expected to induce too degraded performance of the device. The photo-response and noise equivalent power in direct detection regime is the next investigated performance presented in the following section.

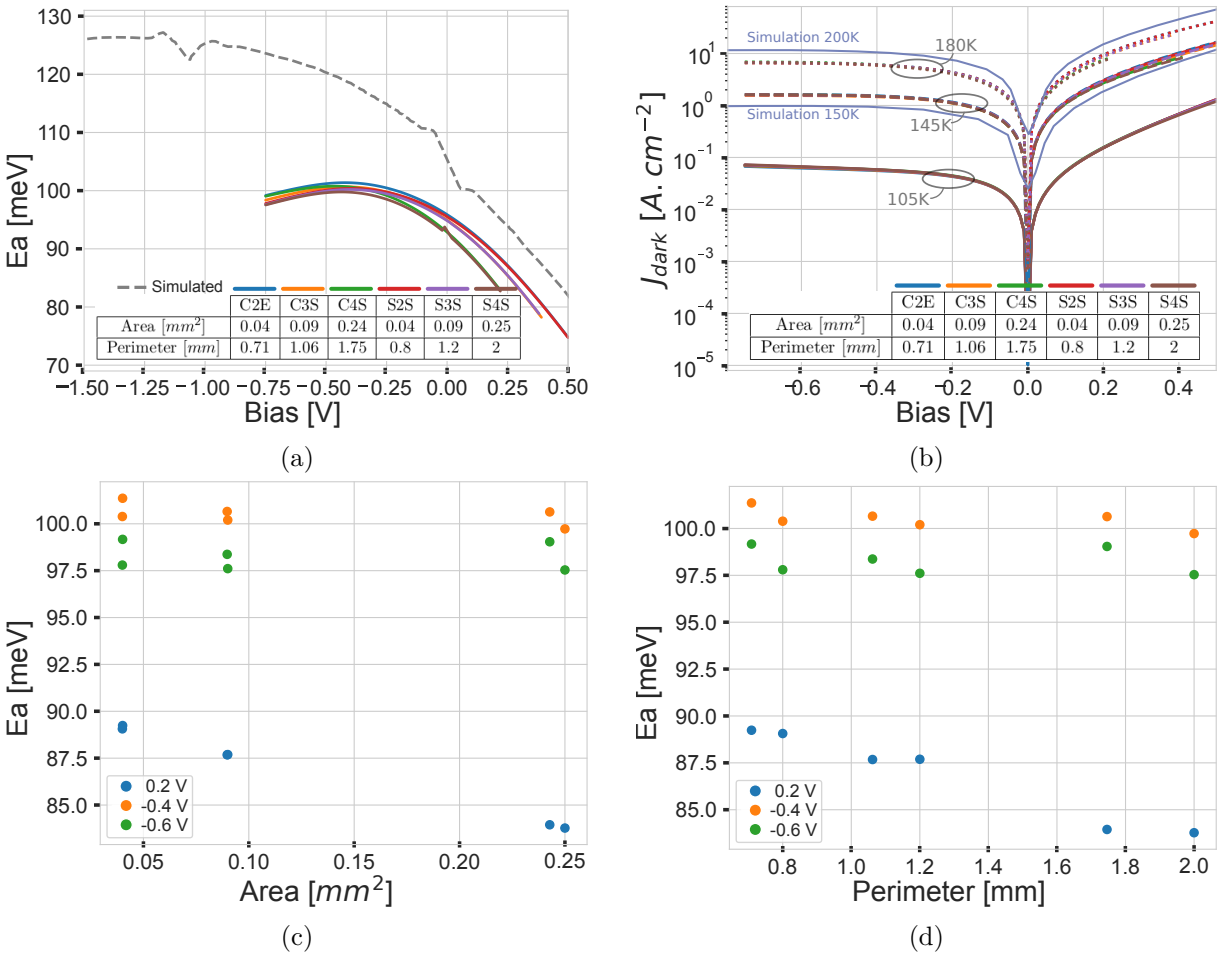

(a) (b) (c) (d)

Figure 5.11: a) Extracted activation energy from dark current densities between 105K and 180K. "C" labelled curves are circular mesas, "S labelled are square mesas. b) Dark current densities measured on different mesas at 105K (continuous lines), 145K (dashed lines) and 180K (dotted lines). c) Activation energy dependence with the mesa area, d) with the mesa perimeter.

2.4.2 Photoresponse of waveguide QCD

The measurement of the waveguide QCD photoresponse comes from the comparison between the current under dark condition with the current under illumination. A good knowledge of

the incident power injected into the waveguide is crucial to the good estimation of the device performance. To that end, an external cavity quantum cascade laser is used (MirCat™ from Daylight Solution) and focused into the waveguide QCD using an aspherical lens (Thorlabs C093TME-F) Figure 5.12a. The spectral power is measured close to the focal plane using a calibrated thermopile (Thorlabs S401C). To estimate the coupling efficiency between the beam spot and the waveguide fundamental mode, the spot at the focal plane is imaged onto a LWIR camera (WinCamD-IR-BB microbolometer camera from DataRay) and a 53.4 times magnification doublet of aspherical lenses. The beam spot diameter is thus estimated at 10.7 µm at $1/e^2$ Figure 5.12b. From a simulated optical mode distribution of the waveguide, it is then possible to estimate the coupling efficiency between the beam spot and the waveguide using the overlap integral of the electric fields Equation 5.24.

$$\eta = \frac{|\iint E_m^* \cdot E_{in} dxdy|^2}{\iint |E_m|^2 dxdy \iint |E_{in}|^2 dxdy} \tag{5.24}$$

In that equation, E_m is the simulated electric field of the fundamental TM mode of the waveguide and E_{in} the incident field. Whereas E_m is simulated using a vectorial mode solver, E_{in} is approximated by a gaussian beam at the focal plane of diameter 10.7 µm given by Equation 5.25, where r is the distance from the center of the gaussian in the (x,y) plane.

$$E(r, z = 0) = E_0 e^{-\left(\frac{r}{w_0}\right)^2} \tag{5.25}$$

From the overlap integral between the simulated TM00 mode and the gaussian beam at focus, and assuming a perfect alignment, we estimate a coupling efficiency $\eta_{20} = 0.46$ ($\eta_8 = 0.40$) into the 20 µm wide QCD waveguide (respectively 8 µm wide) at a 9.1 µm wavelength. A further facet reflectivity of 27% is considered from Fresnel reflection calculation. As the optical mode is well confined and almost doesn't change with the wavelength in the measured range, we further estimate a dependence of the coupling efficiency $\eta(\lambda) = \eta(\lambda_0)\frac{\lambda_0 f(\lambda_0)}{\lambda f(\lambda)}$ as the beam spot diameter roughly evolves as $1/\lambda f$ with f the focal length of the lens.

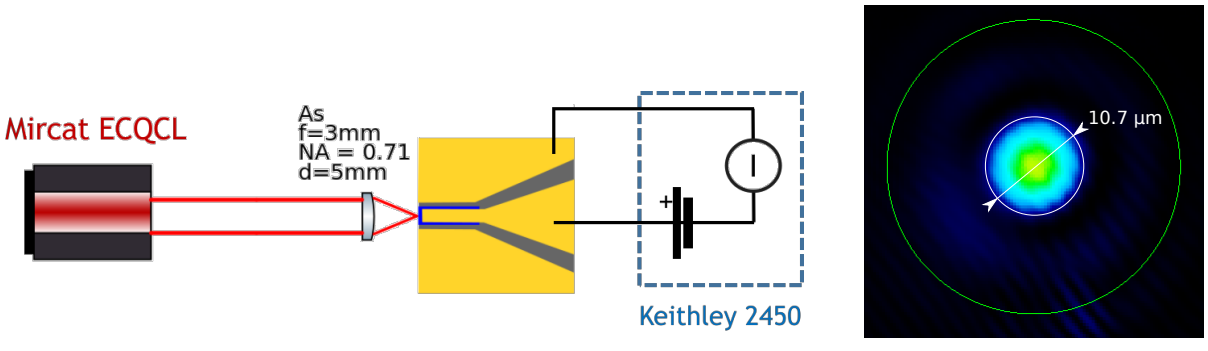

(a) (b)

Figure 5.12: (a) Measurement setup for waveguide QCD photoresponse characterization. (b) LWIR picture of the focal spot using a x53.4 magnification on a LWIR camera.

The photoresponse of the detector is then calculated from the current under illumination I_{ph}

and under dark condition I_{dark} measured on the same setup as :

$$\mathcal{R}(\lambda) = \frac{I_{ph}(\lambda) - I_{dark}(\lambda)}{\mathcal{P}(\lambda)\eta(\lambda)}$$

where $\mathcal{P}(\lambda)$ is the laser power measured at the focal spot and η the total coupling efficiency (approximately 0.336 at 9.1 µm). Responsivity of the 8 µm wide waveguide detectors are shown on Figure 5.13a. Fabry-Perot oscillation pattern are clearly visible on the measured spectral responsivity due to the gold covered back facet, and the cleaved uncoated input facet forming a cavity. Room temperature responsivities as high as 140 mA/W are demonstrated at a wavelength of 9.5 µm and above 100 mA/W at the targeted 9.1 µm wavelength. These are lower bound estimation of the real component performances due to the approximation of perfect alignment in the coupling efficiency calculation, and the consideration that all coupled power is effectively absorbed.

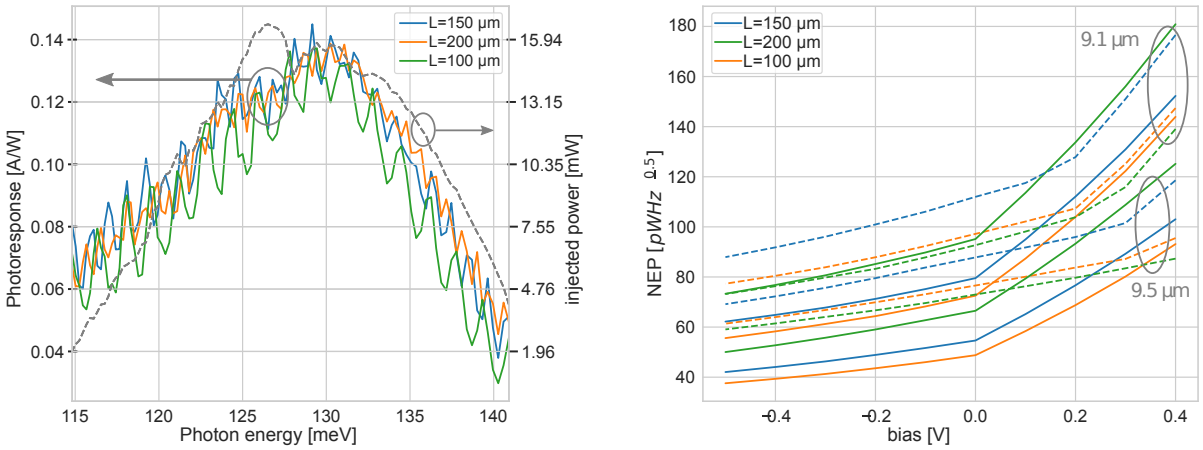

(a) (b)

Figure 5.13: (a) Spectral responsivity of the 8 µm wide waveguide of different length at -0.5V. (b) NEP of the same waveguides at peak responsivity and targeted wavelength. The plain lines are the NEP in dark limited noise (calculated from dark current measurement), and the dotted lines, the optical noise limited NEP (calculated from the current under illumination).

From the photo-current measurement used in the calculation of the photo-response it is possible to calculate the detector NEP using the noise expression Equation 5.16 and approximating the current of the detector as the current in an ideal diode as presented in details in [19]. The NEP (in the dark limited regime) is then given by :

$$NEP = \frac{A\sqrt{\frac{2e}{NA}|I_{dark}| + \frac{4k_BT}{r_d}}}{\mathcal{R}} \tag{5.26}$$

where A is the device electrical area and r_d its dark differential resistance. Similar expression under illumination is also possible to include the optical noise. In that case, the differential resistance and current have to be taken under illumination. The dark limited and optical noise limited NEP of the 8 µm wide QCD is shown in Figure 5.13b. The dark limited NEP of that

device goes down to 40 pW/Hz$^{0.5}$ in reversed bias at the peak responsivity, and the shortest component seems to minimize it. Nevertheless, the difference is small between the 100 µm and the 150 µm long waveguides, suggesting an optimal length close to 100 µm. Under illumination the optical noise takes the advantage and dominates the noise, the 150 µm long waveguide has the highest NEP while the 100 µm long presents a NEP under illumination close to the 200 µm long. This again suggests an optimal length close to 100 µm. These performances are very similar to the ones reported in [238], our apparent slightly better performances are essentially explained by a smaller component, thus a higher resistance in our favour, the overall structure being quite similar.

3 Toward integrated coherent receiver, passive hybrid 90 degree performances

In the above sections, we have discussed the design and performances of a QCD in waveguide geometry. This component is aimed to be integrated in a coherent receiver for telecommunication. To that end, a fast and reliable detection of the phase of a modulated signal is essential. A passive hybrid 90 degree is commonly used in coherent silicon photonics receiver, and we also have seen that the heterodyne detection scheme preserves the phase of the detected signal (Equation 5.6). In this section, we present the design of a passive hybrid 90 degree component based on MMI for that application, as they inherently exhibit quadrature phase behaviour and broadband functionality.

3.1 Design and robustness of 90° hybrid MMI

Based on the analytical development from Soldano [146] recalled in chapter 3 we have designed 90° hybrid MMIs and explored their robustness to variations in the fabrication process. These components are designed for deep ridge geometry on InP n:1e17 cm^{-3} substrate. The waveguide core is made of a 2.5 µm thick undoped InGaAs layer and a top cladding of 4 µm undoped InP. The deep ridge configuration allows a high index contrast, thus shorter components, lowering both the free carrier absorption in the doped substrate (required for the ICP etching in our process) and the potential impact of optical index uncertainty. The design presented here is based on general interference 4×4 MMI used as a 2×4. While this configuration produces longer component compared to the use of paired interference MMI, quadrature phase relation at the output are directly verified by symmetry, in opposition to the paired interference design which requires the addition of a phase shifter and a 2×2 MMI, or a tapered MMI as demonstrated in [239, 240], which makes the design more complex and potentially longer than the first option. The ideal phase relation of the hybrid 90° 4x4 MMI is presented in Figure 5.14.

As exposed in chapter 3, the design of MMI is parametrized by the position and width of the input waveguides ("a" and "w_a" in Figure 5.14) as well as the width and length of the multi-mode section ("W" and "L" in Figure 5.14). In our case, the width of the input waveguides is chosen to be 8 µm in order to match the width of the other receiver component's optical mode (QCL, amplifier and detector) and maximize their coupling into the device. The need of tapered input

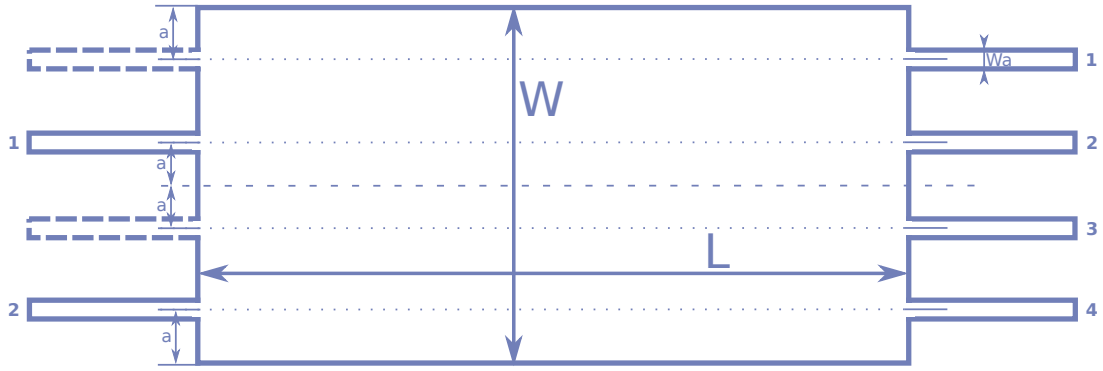

(a)

Input \ Output	1	2	3	4
1	$\frac{3\pi}{4}$	0	0	$\frac{-\pi}{4}$
2	0	$\frac{-\pi}{4}$	$\frac{3\pi}{4}$	0

(b)

Figure 5.14: (a) MMI 90° hybrid layout and dimensions denomination (adapted from [145]). The inputs 1 and 2 are the used ones. (b) Phase relation between the outputs for both inputs.

waveguide is therefore not needed and simplifies the design of the MMI for that first generation of components. Tapered input waveguide might be added in the future generation to enhance the performance of a well-chosen design. Further consideration on the total device transmission in the case of equally spaced inputs, fixed a ratio input width over multimode section width of 0.133, thus a 60 µm wide multimode section. Small variation around the equidistant input position (ergo small variation of "a") are then explored to minimize both the imbalance of the 90° hybrid MMI and phase error from the quadrature. To that end, imbalances are quantified in the prospect of the balanced photodiode usage, usually evaluated by the in-phase (I) and in quadrature (Q) *Common Mode Rejection Ratio* (CMRR) from input "i" expressed in edB [241].

$$CMRR_{iI} = 20\log_{10}\left(\frac{|P_{i1} - P_{i4}|}{P_{i1} + P_{i4}}\right) \quad \text{and} \quad CMRR_{iQ} = 20\log_{10}\left(\frac{|P_{i2} - P_{i3}|}{P_{i2} + P_{i3}}\right) \tag{5.27}$$

Where P_{ij} is the power transmitted from input i to output j. Usual requirements for telecom application in C band ($\lambda \approx 1.55$ µ) are CMRR below -20 edB and phase error below $\pm 5°$. These performances are our goal in designing this device. To that end, we analytically pre-designed the MMI following the same procedure used for the other types of devices presented in chapter 3. This procedure gave an optimal device length of 1720 µm for equidistant input/output, with a ratio input width/multimode section width of 0.133. A further numerical optimization was carried out using a commercially available mode solver, varying the position of the input waveguides from the equidistant ones (used in the pre-design). The resulting optimal design is given in Figure 5.15 continuous lines with a=6.08 µm (see Figure 5.14), W=60 µm and input waveguide 8 µm wide. In dashed (dotted) lines are presented the performance of the same design with input waveguide slightly shifted with respect to the optimal design, to estimate the

robustness of the component. This shift of the optimal "a" parameter is of +300 nm (-300 nm) that we chose as twice the estimated technologically experienced fabrication tolerances (due to alignment, focus and protoresist development variation).

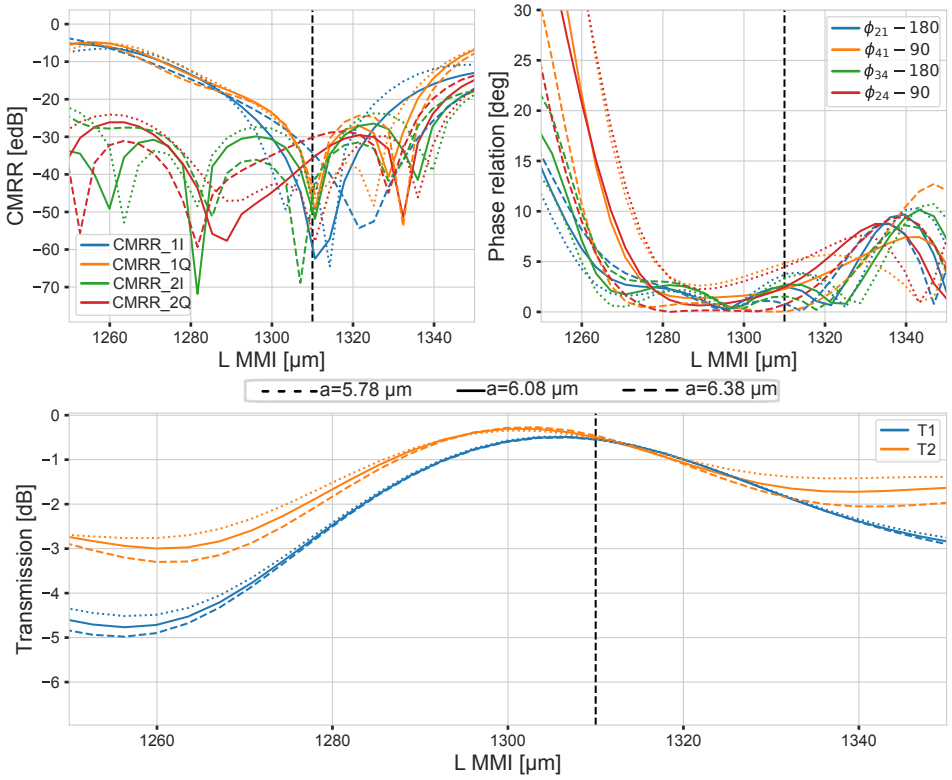

Figure 5.15: Upper left : Common mode rejection ratio of the designed hybrid 90° MMI in function of the length of the multimode section. Upper right : Phase error from quadrature, ϕ_{ij} refers to the introduced phase difference between output i and j. Bottom : Total transmission from input 1 or 2. In continuous line is the optimal design, in dashed and dotted lines are the optimal design with input positioned at plus or minus 300 nm regarding the optimal ones.

The optimal design presented in Figure 5.15 is chosen for its robustness to fabrication variation. Indeed, at the designed wavelength (9.1 µm) the CMRR are all below -20 edB for a multimode section of length between 1290 and 1325 µm, phase error below 5° for length between 1280 and 1315 µm, and insertion loss below -1 dB for length between 1295 and 1320 µm, for the optimal design and its two variations. The retained optimal design length is chosen to be 1310 µm. This guaranties phase errors close or below the 5° limit, CMRR below -20 edB and good throughput. Considering the analytical approximation of MMI sensitivity to small variation [147, 144] recalled here :

$$\frac{|\delta L|}{L} = \frac{|\delta \lambda|}{\lambda} = 2\frac{|\delta W|}{W} \tag{5.28}$$

the "bandwidth" in length is equivalent to an optical bandwidth of approximately ±200 nm around the 9.1 µm design wavelength, or a fabrication tolerance in width of about 700 nm. The fabrication tolerance are below the effective process variation that we estimate to be lower than

100 nm in the worst case scenario. Small variation of length are implemented in the mask to cope with potential fabrication variation. Lengths ranging from 1270 to 1350 µm by step of 20 µm are implemented on mask following the same procedure presented in chapter 3.

3.2 Optical performances of hybrid 90° MMI

The hybrid 90° MMI have been fabricated with the other MMIs and their fabrication process presented in chapter 3. Their optical characterization makes use of the same setup and method as the 2x2 MMIs only with 4 outputs. The setup used for that characterization is recalled in Figure 5.16.

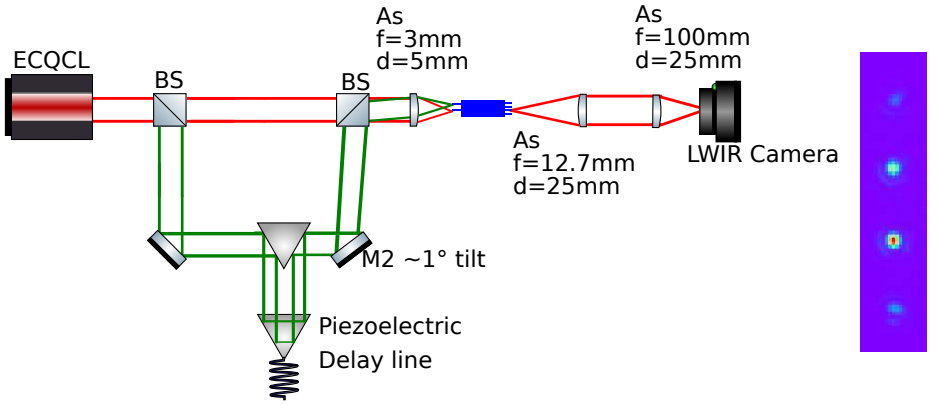

Figure 5.16: Optical setup for the characterization of the 90° hybrid MMI. ECQCL : External Cavity QCL, BS : Beam splitter, As : Aspherical lens, M : Mirror. On the right side is an example of a typically imaged far field of the output of a 90° hybrid MMI.

An external cavity quantum cascade laser is injected into one arm of the MMI. A delayed beam in injected into the other arm using a slightly tilted mirror. A piezoelectric delay line is used to scan the interference fringes imaged on a LWIR camera. For each measurement, a set of 10 images are taken with an integrated shutter on the camera and averaged to define a background image. That background is then subtracted from another set of 10 averaged images taken without the shutter. This procedure is repeated for all the delay and wavelength step necessary for the measurement, and then repeated at least three times to estimate the measurement uncertainty (re-aligning the device each time). The CMRR can be directly calculated from the raw background subtracted images. To that end, the power at one output is directly estimated by the pixel sum on a 10×10 pixels square around the output waveguide imaged (the result has been verified to be independent of the size or shape of the summed pixels around the waveguide) and used to calculate the CMRR as in Equation 5.27.

The phase relation between the output follows a similar procedure except that for each wavelength a scan of the delay line is performed for every wavelength step with the averaged imaged taken for each delay step. For each wavelength, the output power is measured by the sum of the pixels on the 10×10 square two. The measured power with respect to the delay are then cleared from high frequency noise in the frequency domain (we suppress the frequencies 2 times above the scanned wavelength frequency). At this time the interferograms are renormalized

between -1 and 1 in order to increase the fitting procedure robustness afterwards. The delay is then corrected, assuming a linear variation of half a scanned wavelength of the delay between two consecutive extremums of the user chosen best interferogram (in practice, the interferogram from the highest throughput output). Phase initial guess are retrieved from the Fourier transform of the interferograms using the corrected delay and then used as starting point to the global fit of sine function on all interferograms (the frequency if fitted globally, and each phase independently on each interferogram). This procedure is also repeated on three sets of measurements for all wavelengths in order to estimate the measurement uncertainty. Resulting measured CMRR and phase relation error of the best measured component (the one of length 1330 µm) are presented in Figure 5.17.

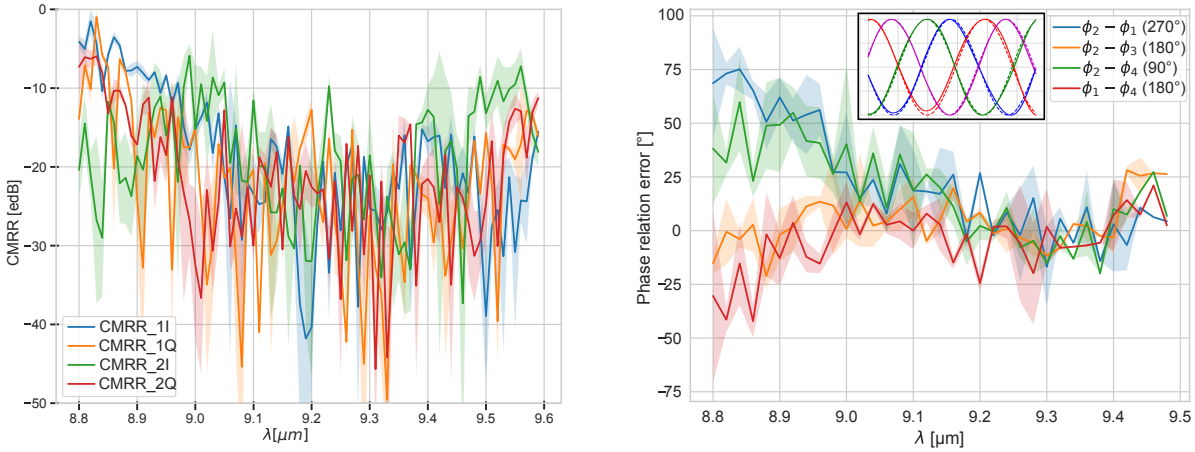

(a) (b)

Figure 5.17: (a) Measured CMRR of the 90° hybrid MMI of length 1330 µm. (b) Measured phase error from quadrature of the same component. The inset present the typical interferograms of the 4 outputs after renormalization and noise suppression at λ= 9.37 µm.

The CMRR for the in-phase (I) and quadrature (Q) outputs are below -10 edB from 9.1 µm to 9.4 µm, and probably below -20 edB, but the dynamic range of the camera and the measurement noise which is dominated by mode hopping of the QCL due to facet reflectivity, are limiting the precision of the measurement to an estimation of -20 to -25 edB. Phases errors are much more impacted by the laser mode hopping, and the measurement precision hasn't reached the degree limit. Nethertheless, the component shows phase errors below ±20° on the same band. This error falls below 12° on the 9.3 to 9.4 µm range. We believe the actual performances of our 90° hybrid MMI to be actually better as the measurement uncertainty in the actual setup appears to be relatively large (typically more than ±5°), and mostly due to laser mode hopping due to optical feedback in the laser cavity. To lower the measurement uncertainty, a short wavelength laser (in the visible) could be used for the delay line correction, and an optical isolator introduced after the ECQCL to stabilize the laser in a first iteration. Another possibility would be to use asymmetrical Mach-Zehnder of a short and known free spectral range (possibly integrated during the fabrication of the component) and scan the transmission spectrum of all outputs. The wavelength shift of the minimal transmission peaks between outputs are in that

case directly linked to the phase shift introduced by the component and the free spectral range of the Mach-Zehnder (which can be measured too). This method, while potentially more precise, would necessitate a precise wavelength meter coupled to the QCL, which was not available at the time of this thesis.

4 Conclusion and future integration prospect

In this chapter, we have demonstrated a waveguide QCD with noise equivalent power in direct detection down to 40 pW/Hz$^{0.5}$ at a 9.5 µm wavelength and below 60 pW/Hz$^{0.5}$ at a 9.1 µm wavelength. In the prospect of integrating it with other components to form a fully integrated coherent I/Q receiver, we also developed and demonstrated a passive 90° hybrid based on MMI, having performances allowing coherent detection over a bandwidth of 100 nm around 9.3 µm. These components are yet discrete ones and their integration as such with a QCL and potentially an optical amplifier could be challenging as such. A way to potentially reduce the integration complexity could be the use of QCLD material, a specifically engineered band structure material in-between the QCD and the QCL band structure, that is able to perform both laser and detector functions at opposite biases. Some demonstration of such components have already been published and implemented into spectrometer [155, 242].

To that end, a carefully designed QCLD material could be locally etched to define the future location of the passive components. The passive component structure could then be locally regrown using low absorptive undoped material or even iron doped InP [243]. The next fabrication steps would be very similar to the ones for the waveguide QCD fabrication and result in a monolithically integrated coherent I/Q receiver. This process is summarized in the Figure 5.18 below.

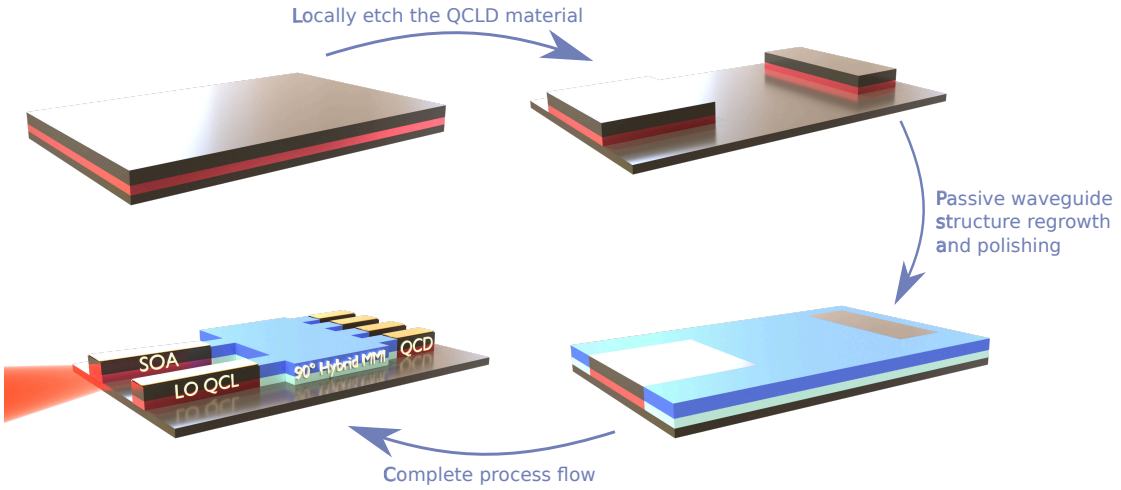

Figure 5.18: A possible simplified process flow to obtain a fully monolithically integrated coherent I/Q receiver with butt joint regrowth of low loss passive waveguide on a QCLD material. In black are doped InP substrate and top cladding, in red is the InGaAs waveguide core embedding the QCLD material, in light and dark blue are respectively undoped InGaAs passive waveguide core, and undoped (or iron doped) InP passive waveguide top cladding. SOA : Semiconductor Optical Amplifier, LO : Local Oscillator.

Conclusion and perspectives

In this manuscript, we have focused on the development of multiple building blocks with the goal to make the first coherent transceiver for FSOC in the LWIR wavelength window. In particular, we have developed passive beam combiners based on MMI for a coherent receiver, two versions of an external phase and amplitude modulator in waveguide geometry for the coherent emitter, and a QCD for the heterodyne detection.

In chapter 2 we have introduced the theoretical background of laser based optical communications, optical waveguide, and material optical properties that are used throughout the thesis. A focus has been given to the optical characterization of InP with different n doping concentration, HfO_2 and Al_2O_3 deposited by ALD at different temperature. Those characterizations were used to justify the use of HfO_2 as a passivating dielectric in the fabricated components.

The chapter 3 was used to further dive into the optical waveguides technologies. After a quick overview of the waveguide technological platform and waveguide geometries, we justified the choice of InGaAS on InP deep ridge waveguide structure for the components developed in this word. The theoretical framework of MMI was presented and used to design wideband and robust to fabrication variation, beam splitter and combiner, to be used as a coherent beam combiner in the future integrated heterodyne receiver. In particular, we presented the design of a 2×2 MMI and its optical characterization. That component showed splitting ratio close to the theoretical 50% with phase relations close to 180° on a wideband from 9 to 9.5 µm, showing their great potential as an integrated beam combiner for the coherent heterodyne receiver.

The focus has been given in chapter 4, to the most challenging component for LWIR FSOC : the external modulator. At first, we presented the different physical effects that can be used in the LWIR for optical modulation. The great potential of both carrier density modulation and inter-subband stark effect, in particular, has been underlined and our focus in this present work, given to the inter-subband Stak effect. Two designs of ACQW structures have been presented. The first one having high performances but also high optical losses when unbiased, was deemed as a high potential solution. But its characterization in this first generation was also seen as difficult due to the necessity to add passive waveguide sections to be able to cleave it with good facet quality, which in turn would induce high optical losses. Therefore, a second design with lower performances, higher driving voltage but lower optical losses when unbiased was presented. The high potential component theoretical performances are a transmission in operation greater than -8dB (-160 dB/mm at 0V), a V_π of 3V for a L_π of 87 µm (thus a $V_\pi L\pi$ of

0.03 V/cm) and frequency cut-off 30 GHz. The alternative component theoretical performances are a transmission in operation greater than -5dB (around -20 dB/mm at 0V), a V_π of 5.3V for a L_π of 195 µm (thus a $V_\pi L\pi$ of 0.1 V/cm) and frequency cut-off 14 GHz. Many characterization techniques and associated on chip layout have been presented, that were envisioned for the optical characterization of the designed modulators. Only the second design characterization was partly possible in the time-frame of this work, which showed component performances close to the designed ones, and a cut-off frequency up to 1.4 GHz, limited by the on-chip coplanar electrical access.

Finally, in the last chapter, chapter 5, we focused on the coherent receiver, and in particular on the QCD for heterodyne coherent detection. The theoretical background behind the design of a QCD have been presented and the simulated performances of the component fabricated (but not designed) in this work have been presented. Its measured performances showed great responsivity up to 140 mA/W at a 9.5 µm wavelength with noise equivalent power in direct detection down to 40 pW/Hz$^{0.5}$ at a 9.5 µm wavelength and below 60 pW/Hz$^{0.5}$ at a 9.1 µm wavelength. Following the theoretical development of chapter 3 we presented a designed 90° hybrid MMI for coherent detection with balanced QCD. CMRR for the in-phase (I) and quadrature (Q) outputs have been measured below -10 edB from 9.1 µm to 9.4 µm and phase relation error (from the quadrature relations) below 20° on the same band, and even below 12° from 9.3 to 9.4 µm.

Throughout this thesis, a wide diversity of active and passive optical components have been designed and fabricated. Only a fraction of them could be characterized in the time frame of this work. Nevertheless, in a near future the focus should be given to improving the characterization setup robustness and thoroughly measuring the components.

For the characterization of passive components, an optical isolator, or better, achromatic optics and a coherent white source such as a super-continuum source, could be used to improve the measurement accuracy of the already measured components, and measure the other ones accurately. The already measured components could be used as a starting point for further improvement to next generation devices, by adding tapered transition for instance.

Concerning the active components, the designed ones could be reproduced and processed with passive waveguide regrowth in order to greatly facilitate their optical characterization. Lots of characterizations could also be performed on the existing ones, fabricated during this thesis, as most of them could not be in this work. This could have an enormous impact on improving the reliability of the QWASS_02 design measured performance and, for the QWASS_01, give its supposedly improved performances even though it would be more challenging to measure. In the meanwhile the components fabricated to be integrated, will be in a very near future, integrated with a QCL and an optical amplifier in a coherent emitter, which should give a better input on their in-situ performances.

Bibliography

[1] Optical telegraph - Wikipedia — en.wikipedia.org. https:\kern-\h@ngcolonwd\kern\h@ngcolonwd//en.wikipedia.org/wiki/Optical_telegraph (cited on page 2).

[2] Telegraph - Electrical Signals, Morse Code, Communication — britannica.com. https:\kern-\h@ngcolonwd\kern\h@ngcolonwd//www.britannica.com/technology/telegraph/Development-of-the-telegraph-industry (cited on page 2).

[3] D Robertson. The great telephone mystery. *IEE Rev.*, 52(2):44–48, 2006 (cited on page 2).

[4] Anton A Huurdeman. *The worldwide history of telecommunications*. John Wiley & Sons, 2003 (cited on page 3).

[5] The european table of frequency allocations and applications in the frequency range 8.3 khz to 3000 ghz (eca table). 2021. URL: https://efis.cept.org/reports/ReportDownloader?reportid=1 (visited on 11/14/2023) (cited on page 4).

[6] Mohammad Ali Khalighi and Murat Uysal. Survey on free space optical communication: a communication theory perspective. *IEEE communications surveys and tutorials*, 16(4):2231–2258, 2014 (cited on pages 4, 5).

[7] Wallace D. Williams, Michael Collins, Don M. Boroson, James R. Lesh, Abi Biswas, Richard Orr, et al. Rf and optical communications: a comparison of high data rate returns from deep space in the 2020 timeframe, 2007 (cited on page 4).

[8] Hany Elgala, Raed Mesleh, and Harald Haas. Indoor optical wireless communication: potential and state-of-the-art. *IEEE Communications magazine*, 49(9):56–62, 2011 (cited on page 5).

[9] Debbie Kedar and Shlomi Arnon. Urban optical wireless communication networks: the main challenges and possible solutions. *IEEE Communications Magazine*, 42(5):S2–S7, 2004 (cited on page 5).

[10] Yannik Horst, Bertold Ian Bitachon, Laurenz Kulmer, Jannik Brun, Tobias Blatter, Jean-Marc Conan, et al. Tbit/s line-rate satellite feeder links enabled by coherent modulation and full-adaptive optics. *Light Sci. Appl.*, 12(1):153, 2023 (cited on page 5).

[11] Grégory Quinchard. *Détecteur infrarouge hétérodyne à cascade quantique*. PhD thesis, 2021 (cited on pages 5, 30, 105, 142).

[12] Alexandre Delga and Luc Leviandier. Free-space optical communications with quantum cascade lasers. *Quantum sensing and nano electronics and photonics XVI*, volume 10926, pages 140–155. SPIE, 2019 (cited on pages 5–10).

[13] Paul Corrigan, Rainer Martini, Edward A Whittaker, and Clyde Bethea. Quantum cascade lasers and the kruse model in free space optical communication. *Optics Express*, 17(6):4355–4359, 2009 (cited on pages 5, 9).

[14] Ronald L Fante. Electromagnetic beam propagation in turbulent media: an update. *Proceedings of the IEEE*, 68(11):1424–1443, 1980 (cited on page 6).

[15] Larry C Andrews and Ronald L Phillips. *Laser beam propagation through random media*. Press Monographs. SPIE Press, Bellingham, WA, 2nd edition, 2005 (cited on pages 6, 7).

[16] Robert M Manning. Beam wave propagation within the second rytov perturbation approximation. *Radiophys. Quantum Electron.*, 39(4):287–295, 1996 (cited on page 6).

[17] Wilbur P Brown. Second moment of a wave propagating in a random medium. *J. Opt. Soc. Am.*, 61(8):1051, 1971 (cited on page 6).

[18] Scott Bloom, Eric Korevaar, John Schuster, and Heinz Willebrand. Understanding the performance of free-space optics. *Journal of optical Networking*, 2(6):178–200, 2003 (cited on page 8).

[19] Alexandre Delga. Quantum cascade detectors: a review, *Mid-infrared Optoelectronics*, pages 337–377. Elsevier, 2020 (cited on pages 10, 123, 124, 127, 128, 134, 136, 145).

[20] Clément Gilles. *Optique intégrée pour sources largement accordables moyen-infrarouge*. Theses, Université Paris Saclay (COmUE), 2017 (cited on pages 10, 48–50, 56, 71, 82, 83, 97).

[21] Ahmed Osman. *Germanium mid-infrared photonic integrated circuits*. PhD thesis, 2021 (cited on page 10).

[22] Seungyong Jung, Daniele Palaferri, Kevin Zhang, Feng Xie, Yae Okuno, Christopher Pinzone, et al. Homogeneous photonic integration of mid-infrared quantum cascade lasers with low-loss passive waveguides on an inp platform. *Optica*, 6(8):1023–1030, 2019 (cited on page 10).

[23] Norbert Grote and Herbert Venghaus, editors. *Fibre Optic Communication*. SPringer series in optical sciences. Springer, Berlin, Germany, 2012th edition, 2012 (cited on pages 13, 17, 19, 78, 79).

[24] Théo Verolet. *Hybrid semiconductor lasers for advanced coherent formats in datacenter interconnects*. Theses, Université Paris-Saclay, 2020 (cited on page 15).

[25] Zhe Yang, Lin X. Cai, Aaron Gulliver, Liang He, and Jianping Pan. Beyond powers of two: hexagonal modulation and non-binary coding for wireless communication systems. *arXiv: Signal Processing*, 2017 (cited on page 15).

[26] Shuangyi Yan, Xuan Weng, Yuliang Gao, Chao Lu, Alan Pak Tao Lau, Yu Ji, et al. Generation of square or hexagonal 16-QAM signals using a dual-drive IQ modulator driven by binary signals. *Opt. Express*, 20(27):29023–29034, 2012 (cited on page 16).

[27] C R Doerr, L Zhang, P J Winzer, and A H Gnauck. 28-gbaud InP square or hexagonal 16-QAM modulator. *Optical Fiber Communication Conference/National Fiber Optic Engineers Conference 2011*, Los Angeles, California. OSA, 2011 (cited on page 16).

[28] Claude Elwood Shannon. A mathematical theory of communication. *The Bell system technical journal*, 27(3):379–423, 1948 (cited on page 17).

[29] Kazuro Kikuchi and Satoshi Tsukamoto. Evaluation of sensitivity of the digital coherent receiver. *J. Lightwave Technol.*, 26(13):1817–1822, 2008 (cited on page 17).

[30] G T Djordjevic, D N Milic, and I D Radojkovic. Performance of free-space optical systems in the presence of receiver imperfections. *IOP Conf. Ser. Mater. Sci. Eng.*, 1032(1):012002, 2021 (cited on page 17).

[31] Andrea Goldsmith. *Wireless communications*. Cambridge university press, 2005 (cited on pages 17, 19).

[32] John G Proakis. *Digital communications*. McGraw-Hill, Higher Education, 2008 (cited on pages 17, 19).

[33] Isaac A Ezenugu and Dike Happiness Ugochi. Performance analysis of m-ary amplitude shift keying digital modulation scheme (cited on page 19).

[34] Peter Y Yu and Manuel Cardona. *Fundamentals of semiconductors*. Graduate texts in physics. Springer, Berlin, Germany, 4th edition, 2010 (cited on pages 20, 39, 48, 75).

[35] Lukas Novotny and Bert Hecht. *Principles of nano-optics*. Cambridge University Press, Cambridge, England, 2nd edition, 2012 (cited on page 20).

[36] R de L. Kronig. On the theory of dispersion of x-rays. *J. Opt. Soc. Am.*, 12(6):547, 1926 (cited on page 22).

[37] H Damany and E Uzan. Calcul des coefficients de fresnel d'un cristal uniaxe absorbant et application à la détermination des constantes optiques. *Opt. Acta (Lond.)*, 17(2):131–142, 1970 (cited on page 22).

[38] Ashim Kumar Bain. *Crystal optics: Properties and applications*. Wiley-VCH Verlag, Weinheim, Germany, 2019 (cited on page 22).

[39] Robert W Boyd. *Nonlinear optics*. Academic Press, San Diego, CA, 4th edition, 2020 (cited on page 22).

[40] Dietrich Marcuse. *Light transmission optics*. 1972 (cited on pages 23, 55).

[41] T D Visser, B Demeulenaere, J Haes, D Lenstra, R Baets, and H Blok. Confinement and modal gain in dielectric waveguides. *J. Lightwave Technol.*, 14(5):885–887, 1996 (cited on pages 28, 90).

[42] T D Visser, H Blok, B Demeulenaere, and D Lenstra. Confinement factors and gain in optical amplifiers. *IEEE J. Quantum Electron.*, 33(10):1763–1766, 1997 (cited on page 28).

[43] Jan Haes, Bart Demeulenaere, Roel Baets, D Lenstra, TD Visser, and H Blok. Difference between te and tm modal gain in amplifying waveguides: analysis and assessment of two perturbation approaches. *Optical and Quantum Electronics*, 29:263–273, 1997 (cited on page 28).

[44] Edward D Palik. *Handbook of optical constants of solids*, volume 3. Academic press, 1998 (cited on pages 29, 48, 86).

[45] Mikhail N. Polyanskiy. Refractive index database. URL: https://refractiveindex.info (visited on 08/22/2023) (cited on page 29).

[46] E Pelletier, F Flory, and Y Hu. Optical characterization of thin films by guided waves. *Appl. Opt.*, 28(14):2918–2924, 1989 (cited on page 29).

[47] H. Fujiwara. *Spectroscopic Ellipsometry: Principles and Applications*. Wiley, 2007 (cited on page 29).

[48] G Quinchard, T Poletti, R Zakhama, J Pereira, A Larrue, G Badano, et al. Revisiting the Fabry-Perot reflectivity method for mid-infrared optical index measurement: case study of InGaAs, AlInAs, and InP. *Appl. Opt.*, 61(14):4079–4086, 2022 (cited on pages 30, 32–34, 86, 117).

[49] S Mark Spearing, Christine H Tsau, and Martin A Schmidt. Gold thermocompression wafer bonding, 2004 (cited on page 30).

[50] D J Lockwood, Guolin Yu, and N L Rowell. Optical phonon frequencies and damping in AlAs, GaP, GaAs, InP, InAs and InSb studied by oblique incidence infrared spectroscopy. *Solid State Commun.*, 136(7):404–409, 2005 (cited on pages 31, 32).

[51] Sadao Adachi. Optical dispersion relations for gap, gaas, gasb, inp, inas, insb, al x ga1- x as, and in1- x ga x as y p1- y. *Journal of Applied Physics*, 66(12):6030–6040, 1989 (cited on pages 32–34).

[52] Wengang Bi and Aizhen Li. The dispersion of the refractive index of iii-v semiconductors. *Journal of applied physics*, 71(6):2826–2829, 1992 (cited on pages 33, 34, 86).

[53] GD Pettit and WJ Turner. Refractive index of inp. *Journal of Applied Physics*, 36(6):2081–2081, 1965 (cited on pages 33, 34).

[54] DA Anderson, N Apsley, P Davies, and PL Giles. Compensation in heavily doped n-type inp and gaas. *Journal of applied physics*, 58(8):3059–3067, 1985 (cited on pages 34, 86).

[55] Jan Kischkat, Sven Peters, Bernd Gruska, Mykhaylo Semtsiv, Mikaela Chashnikova, Matthias Klinkmüller, et al. Mid-infrared optical properties of thin films of aluminum oxide, titanium dioxide, silicon dioxide, aluminum nitride, and silicon nitride. *Appl. Opt.*, 51(28):6789–6798, 2012 (cited on pages 35, 39).

[56] T.J. Bright, J.I. Watjen, Z.M. Zhang, C. Muratore, and A.A. Voevodin. Optical properties of hfo2 thin films deposited by magnetron sputtering: from the visible to the far-infrared. *Thin Solid Films*, 520(22):6793–6802, 2012 (cited on pages 35, 39).

[57] D Bormann. An infrared dielectric function model for amorphous solids. *Journal of applied physics*, 71(1):1–6, 1992 (cited on page 36).

[58] A D Rakic, A B Djurisic, J M Elazar, and M L Majewski. Optical properties of metallic films for vertical-cavity optoelectronic devices. *Appl. Opt.*, 37(22):5271–5283, 1998 (cited on page 36).

[59] J Orosco and C F M Coimbra. Optical response of thin amorphous films to infrared radiation. *Phys. Rev. B.*, 97(9), 2018 (cited on page 36).

[60] J Orosco and C F M Coimbra. On a causal dispersion model for the optical properties of metals. *Appl. Opt.*, 57(19):5333, 2018 (cited on page 36).

[61] Mauro David, Ismael C. Doganlar, Daniele Nazzari, Elena Arigliani, Dominik Wacht, Masiar Sistani, et al. Surface protection and activation of mid-ir plasmonic waveguides for spectroscopy of liquids, 2023. eprint: arXiv:2305.16522 (cited on page 37).

[62] T. Ouisse. *Electron Transport in Nanostructures and Mesoscopic Devices: An Introduction*. ISTE. Wiley, 2013 (cited on page 39).

[63] Felix Bloch. Über die quantenmechanik der elektronen in kristallgittern. *Eur. Phys. J. A*, 52(7-8):555–600, 1929 (cited on page 40).

[64] Emmanuel Rosencher and Borge Vinter. *Optoelectronics*. Cambridge University Press, Cambridge, England, 2002 (cited on page 40).

[65] Takeya Unuma, Masahiro Yoshita, Takeshi Noda, Hiroyuki Sakaki, and Hidefumi Akiyama. Intersubband absorption linewidth in gaas quantum wells due to scattering by interface roughness, phonons, alloy disorder, and impurities. *Journal of applied physics*, 93(3):1586–1597, 2003 (cited on page 41).

[66] R_ Ferreira and Gerald Bastard. Evaluation of some scattering times for electrons in unbiased and biased single-and multiple-quantum-well structures. *Physical Review B*, 40(2):1074, 1989 (cited on page 41).

[67] Romain Léon Terazzi. *Transport in quantum cascade lasers*. PhD thesis, ETH Zurich, 2012 (cited on page 41).

[68] Mathurin Lagrée. *Transport électronique en régime de couplage fort lumière-matière pour les dispositifs quantiques moyen-infrarouge*. Theses, Université Paris-Saclay, 2022 (cited on pages 41–44, 86, 130, 131, 133, 137, 142).

[69] Virginie Trinité, Ezzeddine Ouerghemmi, Vincent Guériaux, Mathieu Carras, Alexandru Nedelcu, Eric Costard, et al. Modelling of electronic transport in quantum well infrared photodetectors. *Infrared Physics & Technology*, 54(3):204–208, 2011 (cited on pages 41, 86).

[70] Eicke R Weber, Robert K Willardson, HC Liu, and Federico Capasso. *Intersubband transitions in quantum wells: physics and device applications*. Academic press, 1999 (cited on page 43).

[71] Gerd Mueller. *Intersubband Transitions in Quantum Wells: Physics and Device Applications II*. Academic Press, 1999 (cited on page 43).

[72] G Pegolotti, A Vasanelli, Y Todorov, and C Sirtori. Quantum model of coupled intersubband plasmons. *Phys. Rev. B Condens. Matter Mater. Phys.*, 90(3), 2014 (cited on page 43).

[73] H Willenberg, G H Döhler, and J Faist. Intersubband gain in a bloch oscillator and quantum cascade laser. *Phys. Rev. B Condens. Matter*, 67(8), 2003 (cited on page 43).

[74] Emmanuel Rosencher and Borge Vinter. *Optoelectronics*. Cambridge University Press, 2002 (cited on page 43).

[75] NSM Archive - Physical Properties of Semiconductors — ioffe.ru. http:\kern-\h@ngcolonwd\kern\h@ngcolonwd//www.ioffe.ru/SVA/NSM/Semicond/ (cited on page 43).

[76] M Załużny and C Nalewajko. On the absorption of infrared radiation by electrons in step quantum wells. *Acta Physica Polonica A*, 87(2):449–452, 1995 (cited on page 44).

[77] Esperanza Luna, Alvaro Guzmán, Achim Trampert, and Gabriel Alvarez. Critical role of two-dimensional island-mediated growth on the formation of semiconductor heterointerfaces. *Phys. Rev. Lett.*, 109(12):126101, 2012 (cited on page 44).

[78] Esperanza Luna, Alvaro Guzmán, Achim Trampert, and Gabriel Alvarez. Critical role of two-dimensional island-mediated growth on the formation of semiconductor heterointerfaces. *Phys. Rev. Lett.*, 109(12):126101, 2012 (cited on page 44).

[79] Richard A Soref, Stephen J Emelett, and Walter R Buchwald. Silicon waveguided components for the long-wave infrared region. *Journal of Optics A: Pure and Applied Optics*, 8(10):840, 2006 (cited on page 48).

[80] Richard Soref. Mid-infrared photonics in silicon and germanium. *Nature photonics*, 4(8):495–497, 2010 (cited on page 48).

[81] Dingding Ren, Chao Dong, and David Burghoff. Integrated nonlinear photonics in the longwave-infrared: a roadmap. *MRS Communications*:1–15, 2023 (cited on pages 48, 49).

[82] Shuo Cui, Radwan Chahal, Catherine Boussard-Pledel, Virginie Nazabal, Jean-Louis Doualan, Johann Troles, et al. From selenium-to tellurium-based glass optical fibers for infrared spectroscopies. *Molecules*, 18(5):5373–5388, 2013 (cited on page 48).

[83] Song Gao and Xiaoyi Bao. Chalcogenide taper and its nonlinear effects and sensing applications. *iScience*, 23(1):100802, 2020 (cited on page 48).

[84] Kevin Zhang, Gerhard Böhm, and Mikhail A Belkin. Mid-infrared microring resonators and optical waveguides on an inp platform. *Applied Physics Letters*, 120(6), 2022 (cited on page 49).

[85] Ruijun Wang, Philipp Täschler, Zhixin Wang, Emilio Gini, Mattias Beck, and Jérôme Faist. Monolithic integration of mid-infrared quantum cascade lasers and frequency combs with passive waveguides. *ACS Photonics*, 9(2):426–431, 2022 (cited on page 49).

[86] Nicolas Hô, Mark C Phillips, Hong Qiao, Paul J Allen, Kannan Krishnaswami, Brian J Riley, et al. Single-mode low-loss chalcogenide glass waveguides for the mid-infrared. *Optics letters*, 31(12):1860–1862, 2006 (cited on page 49).

[87] Hongtao Lin, Lan Li, Yi Zou, Sylvain Danto, J David Musgraves, Kathleen Richardson, et al. Demonstration of high-q mid-infrared chalcogenide glass-on-silicon resonators. *Optics letters*, 38(9):1470–1472, 2013 (cited on page 49).

[88] Helen L Butcher, David G MacLachlan, David Lee, Robert R Thomson, and Damien Weidmann. Demonstration and characterization of ultrafast laser-inscribed mid-infrared waveguides in chalcogenide glass ig2. *Optics Express*, 26(8):10930–10943, 2018 (cited on page 49).

[89] Helen L Butcher, David G MacLachlan, David Lee, Robert R Thomson, and Damien Weidmann. Demonstration and characterization of ultrafast laser-inscribed mid-infrared waveguides in chalcogenide glass ig2. *Optics Express*, 26(8):10930–10943, 2018 (cited on page 49).

[90] Mickael Brun, Pierre Labeye, Gilles Grand, Jean-Michel Hartmann, Fahem Boulila, Mathieu Carras, et al. Low loss sige graded index waveguides for mid-ir applications. *Optics express*, 22(1):508–518, 2014 (cited on page 49).

[91] Mickael Brun, Pierre Labeye, Gilles Grand, Jean-Michel Hartmann, Fahem Boulila, Mathieu Carras, et al. Low loss sige graded index waveguides for mid-ir applications. *Optics express*, 22(1):508–518, 2014 (cited on page 49).

[92] K Gallacher, RW Millar, U Griškevičiūte, L Baldassarre, M Sorel, M Ortolani, et al. Low loss ge-on-si waveguides operating in the 8–14 μm atmospheric transmission window. *Optics express*, 26(20):25667–25675, 2018 (cited on page 49).

[93] Hsien-Yu Liao, Seungyong Jung, Swapnajit Chakravarty, Ray T Chen, and Mikhail A Belkin. Low-loss ge-on-gaas platform for mid-infrared photonics. *2017 Conference on Lasers and Electro-Optics (CLEO)*, pages 1–2. IEEE, 2017 (cited on page 49).

[94] K S Chiang. Performance of the effective-index method for the analysis of dielectric waveguides. *Opt. Lett.*, 16(10):714–716, 1991 (cited on page 49).

[95] A Kumar, D F Clark, and B Culshaw. Explanation of errors inherent in the effective-index method for analyzing rectangular-core waveguides. *Opt. Lett.*, 13(12):1129–1131, 1988 (cited on page 49).

[96] OV Ivanova, Remco Stoffer, Lasse Kauppinen, and Manfred Hammer. Variational effective index method for 3d vectorial scattering problems in photonics: te polarization. *Progress In Electromagnetics Research Symposium PIERS 2009, Moscow, Proceedings*, pages 1038–1042. Citeseer, 2009 (cited on page 49).

[97] Trevor Mark Benson and PC Kendall. Variational techniques including effective and weighted index methods. *Progress In Electromagnetics Research*, 10:1–40, 1995 (cited on page 49).

[98] E A J Marcatili. Dielectric rectangular waveguide and directional coupler for integrated optics. *Bell Syst. Tech. J.*, 48(7):2071–2102, 1969 (cited on page 49).

[99] Wouter J Westerveld, Suzanne M Leinders, Koen W A van Dongen, H Paul Urbach, and Mirvais Yousefi. Extension of marcatili's analytical approach for rectangular silicon optical waveguides. *J. Lightwave Technol.*, 30(14):2388–2401, 2012 (cited on page 49).

[100] T M Benson and P C Kendall. Variational techniques including effective and weighted index methods. *Electromagn. Waves (Camb.)*, 10:1–40, 1995 (cited on page 49).

[101] Helen L Butcher, David G MacLachlan, David Lee, Robert R Thomson, and Damien Weidmann. Ultrafast laser-inscribed mid-infrared evanescent field directional couplers in GeAsSe chalcogenide glass. *OSA Contin.*, 1(1):221, 2018 (cited on page 49).

[102] C-C Chang, J D Kirch, P Buelow, C Boyle, T F Kuech, D Lindberg III, et al. Buried-heterostructure mid-infrared quantum cascade lasers fabricated by non-selective regrowth and chemical polishing. *Electron. Lett.*, 51(14):1098–1100, 2015 (cited on page 49).

[103] Kamal Ghoumid, Richard Ferriere, Badr-Eddine Benkelfat, Brahim Guizal, and Tijani Gharbi. Optical performance of bragg gratings fabricated in ti: linbo _3 waveguides by focused ion beam milling. *Journal of lightwave technology*, 28(23):3488–3493, 2010 (cited on page 50).

[104] Marc Reig Escalé, David Pohl, Anton Sergeyev, and Rachel Grange. Extreme electro-optic tuning of bragg mirrors integrated in lithium niobate nanowaveguides. *Opt. Lett.*, 43(7):1515, 2018 (cited on page 50).

[105] L Pierno, M Dispenza, A Secchi, A Fiorello, and V Foglietti. A lithium niobate electro-optic tunable bragg filter fabricated by electron beam lithography. *Journal of Optics A: Pure and Applied Optics*, 10(6):064017, 2008 (cited on page 50).

[106] Xavier Pommarede. *Circuits photoniques intégrés III-V/Si pour les applications en télécommunications optiques*. Theses, Université Paris Saclay (COmUE), 2017 (cited on pages 50, 58).

[107] Qianfan Xu, Vilson R Almeida, Roberto R Panepucci, and Michal Lipson. Experimental demonstration of guiding and confining light in nanometer-size low-refractive-index material. *Opt. Lett.*, 29(14):1626–1628, 2004 (cited on page 50).

[108] Sebastian Koeber, Robert Palmer, Matthias Lauermann, Wolfgang Heni, Delwin L Elder, Dietmar Korn, et al. Femtojoule electro-optic modulation using a silicon–organic hybrid device. *Light Sci. Appl.*, 4(2):e255–e255, 2015 (cited on page 51).

[109] C Haffner, W Heni, Y Fedoryshyn, J Niegemann, A Melikyan, D L Elder, et al. All-plasmonic Mach–Zehnder modulator enabling optical high-speed communication at the microscale. *Nat. Photonics*, 9(8):525–528, 2015 (cited on page 51).

[110] Borislav Hinkov, Florian Pilat, Laurin Lux, Patricia L Souza, Mauro David, Andreas Schwaighofer, et al. A mid-infrared lab-on-a-chip for dynamic reaction monitoring. *Nat. Commun.*, 13(1):4753, 2022 (cited on page 51).

[111] Mauro David, Davide Disnan, Elena Arigliani, Anna Lardschneider, Georg Marschick, Hanh T Hoang, et al. Advanced mid-infrared plasmonic waveguides for on-chip integrated photonics. *Photonics Res.*, 11(10):1694, 2023 (cited on page 51).

[112] Zheng Wang, Xiaochuan Xu, Donglei Fan, Yaguo Wang, Harish Subbaraman, and Ray T Chen. Geometrical tuning art for entirely subwavelength grating waveguide based integrated photonics circuits. *Sci. Rep.*, 6(1), 2016 (cited on page 51).

[113] Marc Ibrahim, Jens H Schmid, Alireza Aleali, Pavel Cheben, Jean Lapointe, Siegfried Janz, et al. Athermal silicon waveguides with bridged subwavelength gratings for TE and TM polarizations. *Opt. Express*, 20(16):18356–18361, 2012 (cited on page 51).

[114] Weixin Liu, Yiming Ma, Yuhua Chang, Bowei Dong, Jingxuan Wei, Zhihao Ren, et al. Suspended silicon waveguide platform with subwavelength grating metamaterial cladding for long-wave infrared sensing applications. *Nanophotonics*, 10(7):1861–1870, 2021 (cited on page 51).

[115] J Soler Penadés, A Sánchez-Postigo, M Nedeljkovic, A Ortega-Moñux, J G Wangüemert-Pérez, Y Xu, et al. Suspended silicon waveguides for long-wave infrared wavelengths. *Opt. Lett.*, 43(4):795, 2018 (cited on page 51).

[116] Dong Zhang, Yuefeng Wang, Qiang Fu, Weiwei Chen, Pengjun Wang, Shixun Dai, et al. Ultra-high-enhancement-factor integrated long-wave infrared gas sensor based on the tapered sub-wavelength grating slot waveguide. *Results in Physics*, 48:106442, 2023 (cited on page 51).

[117] Attila Mekis, JC Chen, I Kurland, Shanhui Fan, Pierre R Villeneuve, and JD Joannopoulos. High transmission through sharp bends in photonic crystal waveguides. *Physical review letters*, 77(18):3787, 1996 (cited on page 51).

[118] C Jamois, RB Wehrspohn, LC Andreani, C Hermann, Ol Hess, and U Gösele. Silicon-based two-dimensional photonic crystal waveguides. *Photonics and Nanostructures-Fundamentals and Applications*, 1(1):1–13, 2003 (cited on page 51).

[119] H Kurt and D S Citrin. Biochemical sensing application of photonic crystal based devices in the far-infrared regime. *CLEO/Europe. 2005 Conference on Lasers and Electro-Optics Europe, 2005*, Munich, Germany. IEEE, 2006 (cited on page 51).

[120] Richard A Soref, Zexuan Qiang, and Weidong Zhou. Far infrared photonic crystals operating in the reststrahl region. *Opt. Express*, 15(17):10637–10648, 2007 (cited on page 51).

[121] Toshiaki Suhara. Integrated optics, *Comprehensive Microsystems*, pages 165–199. Elsevier, 2008 (cited on page 52).

[122] Gyeongho Son, Seungjun Han, Jongwoo Park, Kyungmok Kwon, and Kyoungsik Yu. High-efficiency broadband light coupling between optical fibers and photonic integrated circuits. *Nanophotonics*, 7(12):1845–1864, 2018 (cited on page 52).

[123] Bahaa EA Saleh and Malvin Carl Teich. *Fundamentals of photonics*. john Wiley & sons, 2019 (cited on pages 52, 53).

[124] Amnon Yariv and Michiharu Nakamura. Periodic structures for integrated optics. *IEEE journal of quantum electronics*, 13(4):233–253, 1977 (cited on page 53).

[125] A R Nelson. Coupling optical waveguides by tapers. *Appl. Opt.*, 14(12):3012–3015, 1975 (cited on page 54).

[126] A Milton and W Burns. Mode coupling in optical waveguide horns. *IEEE J. Quantum Electron.*, 13(10):828–835, 1977 (cited on page 54).

[127] B Luyssaert, P Bienstman, P Vandersteegen, P Dumon, and R Baets. Efficient nonadiabatic planar waveguide tapers. *J. Lightwave Technol.*, 23(8):2462–2468, 2005 (cited on page 54).

[128] S Hadi Badri and M M Gilarlue. Ultrashort waveguide tapers based on luneburg lens. *J. Opt.*, 21(12):125802, 2019 (cited on page 54).

[129] Paul-Henri Tichit, Shah Nawaz Burokur, and André de Lustrac. Waveguide taper engineering using coordinate transformation technology. *Opt. Express*, 18(2):767–772, 2010 (cited on page 54).

[130] WK Burns, AF Milton, and AB Lee. Optical waveguide parabolic coupling horns. *Applied Physics Letters*, 30(1):28–30, 1977 (cited on page 54).

[131] Yunfei Fu, Tong Ye, Weijie Tang, and Tao Chu. Efficient adiabatic silicon-on-insulator waveguide taper. *Photonics Res.*, 2(3):A41, 2014 (cited on pages 54, 55).

[132] P K Tien. Light waves in thin films and integrated optics. *Appl. Opt.*, 10(11):2395–2413, 1971 (cited on pages 55, 56).

[133] F P Payne and J P R Lacey. A theoretical analysis of scattering loss from planar optical waveguides. *Opt. Quantum Electron.*, 26(10):977–986, 1994 (cited on pages 55, 56).

[134] Frédéric Grillot, L Vivien, E Cassan, and S Laval. Influence of waveguide geometry on scattering loss effects in submicron strip silicon-on-insulator waveguides. *IET optoelectronics*, 2(1):1–5, 2008 (cited on page 56).

[135] E Jaberansary, T M B Masaud, M M Milosevic, M Nedeljkovic, G Z Mashanovich, and H M H Chong. Scattering loss estimation using 2-D fourier analysis and modeling of sidewall roughness on optical waveguides. *IEEE Photonics J.*, 5(3):6601010–6601010, 2013 (cited on page 56).

[136] Wim Bogaerts, Peter Bienstman, and Roel Baets. Scattering at sidewall roughness in photonic crystal slabs. *Opt. Lett.*, 28(9):689–691, 2003 (cited on page 56).

[137] M Heiblum and J Harris. Analysis of curved optical waveguides by conformal transformation. *IEEE J. Quantum Electron.*, 11(2):75–83, 1975 (cited on page 57).

[138] Raffaella Costa, A Melloni, M Martinelli, and P Monguzzi. A new bend design criterium: the matched bend. *Integrated Photonics Research*, Vancouver, Canada. OSA, 2002 (cited on page 57).

[139] M K Smit, E C M Pennings, and H Blok. A normalized approach to the design of low-loss optical waveguide bends. *J. Lightwave Technol.*, 11(11):1737–1742, 1993 (cited on page 57).

[140] Meisam Bahadori, Mahdi Nikdast, Qixiang Cheng, and Keren Bergman. Universal design of waveguide bends in silicon-on-insulator photonics platform. *J. Lightwave Technol.*, 37(13):3044–3054, 2019 (cited on page 57).

[141] D. Marcuse. *Light Transmission Optics*. Bell Laboratories series. Van Nostrand Reinhold, 1982 (cited on page 57).

[142] F Ladouceur and E Labeye. A new general approach to optical waveguide path design. *J. Lightwave Technol.*, 13(3):481–492, 1995 (cited on pages 58, 59).

[143] William Henry Fox Talbot. Facts relating to optical science. *Philosophical Magazine*, 9:401 (cited on page 61).

[144] P A Besse, M Bachmann, H Melchior, L B Soldano, and M K Smit. Optical bandwidth and fabrication tolerances of multimode interference couplers. *J. Lightwave Technol.*, 12(6):1004–1009, 1994 (cited on pages 62–64, 148).

[145] M Bachmann, P A Besse, and H Melchior. General self-imaging properties in N × N multimode interference couplers including phase relations. *Appl. Opt.*, 33(18):3905–3911, 1994 (cited on pages 62, 63, 147).

[146] Lucas Beda Soldano. *Multimode interference couplers: Design and applications*. Delft University Press, Clifton, NJ, 1994 (cited on pages 62, 146).

[147] L B Soldano and E C M Pennings. Optical multi-mode interference devices based on self-imaging: principles and applications. *J. Lightwave Technol.*, 13(4):615–627, 1995 (cited on pages 62, 148).

[148] T M Benson and P C Kendall. Variational techniques including effective and weighted index methods. *Electromagn. Waves (Camb.)*, 10:1–40, 1995 (cited on page 62).

[149] K S Chiang. Performance of the effective-index method for the analysis of dielectric waveguides. *Opt. Lett.*, 16(10):714–716, 1991 (cited on page 62).

[150] R Ulrich. Light-propagation and imaging in planar optical waveguides. *Nouv. Rev. Opt.*, 6(5):253–262, 1975 (cited on page 62).

[151] E C M Pennings, R van Roijen, M J N van Stralen, P J de Waard, R G M P Koumans, and B H Verbeck. Reflection properties of multimode interference devices. *IEEE Photonics Technol. Lett.*, 6(6):715–718, 1994 (cited on page 64).

[152] M T Hill, X J M Leijtens, G D Khoe, and M K Smit. Optimizing imbalance and loss in 2 x 2 3-db multimode interference couplers via access waveguide width. *J. Lightwave Technol.*, 21(10):2305–2313, 2003 (cited on pages 65, 66).

[153] Vladyslav Vakarin, Joan Manel Ramírez, Jacopo Frigerio, Andrea Ballabio, Xavier Le Roux, Qiankun Liu, et al. Ultra-wideband ge-rich silicon germanium integrated Mach–Zehnder interferometer for mid-infrared spectroscopy. *Opt. Lett.*, 42(17):3482, 2017 (cited on page 71).

[154] Mauro David, Davide Disnan, Elena Arigliani, Anna Lardschneider, Georg Marschick, Hanh T Hoang, et al. Advanced mid-infrared plasmonic waveguides for on-chip integrated photonics, 2023 (cited on page 71).

[155] Borislav Hinkov, Florian Pilat, Laurin Lux, Patricia L Souza, Mauro David, Andreas Schwaighofer, et al. A mid-infrared lab-on-a-chip for dynamic reaction monitoring. *Nat. Commun.*, 13(1):4753, 2022 (cited on pages 71, 128, 151).

[156] Jifeng Liu, Mark Beals, Andrew Pomerene, Sarah Bernardis, Rong Sun, Jing Cheng, et al. Waveguide-integrated, ultralow-energy gesi electro-absorption modulators. *Nature photonics*, 2(7):433–437, 2008 (cited on page 74).

[157] Dazeng Feng, Shirong Liao, Hong Liang, Joan Fong, Bhavin Bijlani, Roshanak Shafiiha, et al. High speed gesi electro-absorption modulator at 1550 nm wavelength on soi waveguide. *Optics express*, 20(20):22224–22232, 2012 (cited on page 74).

[158] Yu-Hsuan Kuo, Yong Kyu Lee, Yangsi Ge, Shen Ren, Jonathan E Roth, Theodore I Kamins, et al. Strong quantum-confined stark effect in germanium quantum-well structures on silicon. *Nature*, 437(7063):1334–1336, 2005 (cited on page 74).

[159] Jacopo Frigerio, Vladyslav Vakarin, Papichaya Chaisakul, Marcello Ferretto, Daniel Chrastina, Xavier Le Roux, et al. Giant electro-optic effect in ge/sige coupled quantum wells. *Scientific reports*, 5(1):15398, 2015 (cited on page 74).

[160] Michael Bass. *Handbook of Optics. Vol 2, Devices, Measurements, and Properties*. McGraw-Hill, 1995 (cited on page 74).

[161] Susumu Namba. Electro-optical effect of zincblende. *JOSA*, 51(1):76–79, 1961 (cited on page 74).

[162] Gerhard Hagn. *Electro-optic effects and their application in Indium Phosphide waveguide devices for fibre optic access networks*. PhD thesis, ETH Zurich, 2001 (cited on page 75).

[163] A Cingolani, M Ferrara, M Lugarà, and F Levy. Pockels effect in gallium selenide. *Solid State Communications*, 29(9):677–679, 1979 (cited on page 75).

[164] Ch Bosshard, R Spreiter, L Degiorgi, and P Günter. Infrared and raman spectroscopy of the organic crystal DAST: polarization dependence and contribution of molecular vibrations to the linear electro-optic effect. *Phys. Rev. B Condens. Matter*, 66(20), 2002 (cited on page 75).

[165] Skylar Deckoff-Jones, Yixiu Wang, Hongtao Lin, Wenzhuo Wu, and Juejun Hu. 2d-material-enabled multifunctional mid-IR optoelectronics. Sailing He and Laurent Vivien, editors, *Smart Photonic and Optoelectronic Integrated Circuits XXII*, San Francisco, United States. SPIE, 2020 (cited on page 75).

[166] Brian R Bennett, Richard A Soref, and Jesus A Del Alamo. Carrier-induced change in refractive index of inp, gaas and ingaasp. *IEEE Journal of Quantum Electronics*, 26(1):113–122, 1990 (cited on page 75).

[167] H Y Fan. Chapter 9 effects of free carriers on the optical properties, *Semiconductors and Semimetals*, Semiconductors and semimetals, pages 405–419. Elsevier, 1967 (cited on page 76).

[168] Alexis Abraham. *Développement de modulateurs optiques sur silicium à faible consommation énergétique pour les prochaines générations d'interconnexions optiques*. PhD thesis, 2016 (cited on pages 76, 78, 80).

[169] P F Yuh and K L Wang. Large stark effects for transitions from local states to global states in quantum well structures. *IEEE J. Quantum Electron.*, 25(7):1671–1676, 1989 (cited on page 76).

[170] R P G Karunasiri, Y J Mii, and K L Wang. Tunable infrared modulator and switch using stark shift in step quantum wells. *IEEE Electron Device Lett.*, 11(5):227–229, 1990 (cited on page 76).

[171] E Dupont, D Delacourt, V Berger, N Vodjdani, and M Papuchon. Phase and amplitude modulation based on intersubband transitions in electron transfer double quantum wells. *Appl. Phys. Lett.*, 62(16):1907–1909, 1993 (cited on page 76).

[172] E B Dupont, D Delacourt, and M Papuchon. Mid-infrared phase modulation via stark effect on intersubband transitions in GaAs/GaAlAs quantum wells. *IEEE J. Quantum Electron.*, 29(8):2313–2318, 1993 (cited on page 76).

[173] N Vodjdani, B Vinter, V Berger, E Böckenhoff, and E Costard. Tunneling assisted modulation of the intersubband absorption in double quantum wells. *Appl. Phys. Lett.*, 59(5):555–557, 1991 (cited on page 76).

[174] Carlo Sirtori, Federico Capasso, Deborah L Sivco, AL Hutchinson, and Alfred Y Cho. Resonant stark tuning of second-order susceptibility in coupled quantum wells. *Applied physics letters*, 60(2):151–153, 1992 (cited on page 76).

[175] J Teissier, S Laurent, C Manquest, C Sirtori, A Bousseksou, JR Coudevylle, et al. Electrical modulation of the complex refractive index in mid-infrared quantum cascade lasers. *Optics Express*, 20(2):1172–1183, 2012 (cited on pages 77, 82).

[176] Matthew J Dicken, Koray Aydin, Imogen M Pryce, Luke A Sweatlock, Elizabeth M Boyd, Sameer Walavalkar, et al. Frequency tunable near-infrared metamaterials based on vo 2 phase transition. *Optics express*, 17(20):18330–18339, 2009 (cited on page 77).

[177] Douglas H Werner, Do-Hoon Kwon, Iam-Choon Khoo, Alexander V Kildishev, and Vladimir M Shalaev. Liquid crystal clad near-infrared metamaterials with tunable negative-zero-positive refractive indices. *Optics Express*, 15(6):3342–3347, 2007 (cited on page 77).

[178] Xuefang Hu, Xiangyue Zhao, Yinwei Gu, Shuping Jin, Hussain Shafqat, Yiping Cui, et al. A plasmon modulator by dynamically controlling the spatial distribution of carrier density in graphene. *Optics Communications*, 513:128093, 2022 (cited on page 77).

[179] David AB Miller. Energy consumption in optical modulators for interconnects. *Optics express*, 20(102):A293–A308, 2012 (cited on page 79).

[180] Ke Liu, Chen Ran Ye, Sikandar Khan, and Volker J Sorger. Review and perspective on ultrafast wavelength-size electro-optic modulators. *Laser & Photonics Reviews*, 9(2):172–194, 2015 (cited on page 80).

[181] Tianqi Xu, Yuan Dong, Qize Zhong, Shaonan Zheng, Yang Qiu, Xingyan Zhao, et al. Mid-infrared integrated electro-optic modulators: a review. *Nanophotonics*, (0), 2023 (cited on pages 80, 81).

[182] Xi Xiao, Hao Xu, Xianyao Li, Zhiyong Li, Tao Chu, Yude Yu, et al. High-speed, low-loss silicon Mach-Zehnder modulators with doping optimization. *Opt. Express*, 21(4):4116–4125, 2013 (cited on page 80).

[183] Tatsurou Hiraki, Takuma Aihara, Koichi Hasebe, Koji Takeda, Takuro Fujii, Takaaki Kakitsuka, et al. Heterogeneously integrated III–V/Si MOS capacitor Mach–Zehnder modulator. *Nat. Photonics*, 11(8):482–485, 2017 (cited on page 80).

[184] Wei-Che Hsu, Bokun Zhou, and Alan X Wang. MOS capacitor-driven silicon modulators: a mini review and comparative analysis of modulation efficiency and optical loss. *IEEE J. Sel. Top. Quantum Electron.*, 28(3):1–11, 2022 (cited on page 80).

[185] Hanzhi Tang, Qiang Li, Chong Pei Ho, Junichi Fujikata, Masataka Noguchi, Shigeki Takahashi, et al. Modulation bandwidth improvement of III-V/Si hybrid MOS optical modulator by reducing parasitic capacitance. *Opt. Express*, 30(13):22848–22859, 2022 (cited on page 80).

[186] Gengxin Chen, Kaixuan Chen, Ranfeng Gan, Ziliang Ruan, Zong Wang, Pucheng Huang, et al. High performance thin-film lithium niobate modulator on a silicon substrate using periodic capacitively loaded traveling-wave electrode. *APL Photonics*, 7(2), 2022 (cited on page 80).

[187] C Hoessbacher, A Josten, B Baeuerle, Y Fedoryshyn, H Hettrich, Y Salamin, et al. Plasmonic modulator with >170 GHz bandwidth demonstrated at 100 GBd NRZ. *Opt. Express*, 25(3):1762, 2017 (cited on page 80).

[188] A Barzaghi, V Falcone, S Calcaterra, D Marris-Morini, M Virgilio, and J Frigerio. Modelling of an intersubband quantum confined stark effect in ge quantum wells for mid-infrared photonics. *Optics Express*, 30(26):46710–46721, 2022 (cited on page 81).

[189] Miguel Montesinos-Ballester, Lucas Deniel, Natnicha Koompai, Thi Hao Nhi Nguyen, Jacopo Frigerio, Andrea Ballabio, et al. Mid-infrared integrated electro-optic modulator operating up to 225 mhz between 6.4 and 10.7 μm wavelength. *ACS photonics*, 9(1):249–255, 2022 (cited on page 81).

[190] Thi Hao Nhi Nguyen, Natnicha Koompai, Victor Turpaud, Miguel Montesinos-Ballester, Jonathan Peltier, Jacopo Frigerio, et al. 1 ghz electro-optical silicon-germanium modulator in the 5-9 μm wavelength range. *Optics Express*, 30(26):47093–47102, 2022 (cited on page 81).

[191] Stefano Pirotta, Ngoc-Linh Tran, Arnaud Jollivet, Giorgio Biasiol, Paul Crozat, Jean-Michel Manceau, et al. Fast amplitude modulation up to 1.5 GHz of mid-IR free-space beams at room-temperature. *Nat. Commun.*, 12(1):799, 2021 (cited on page 81).

[192] Hamza Dely, Thomas Bonazzi, Olivier Spitz, Etienne Rodriguez, Djamal Gacemi, Yanko Todorov, et al. 10 gbit/s free space data transmission at 9 µm wavelength with unipolar quantum optoelectronics. *Laser Photon. Rev.*, 16(2):2100414, 2022 (cited on page 81).

[193] Hamza Dely, Baptiste Chomet, Thomas Bonazzi, Djamal Gacemi, Angela Vasanelli, Axel Evirgen, et al. Heterodyne coherent detection of phase modulation in a mid-infrared unipolar device. *Opt. Express*, 31(19):30876–30883, 2023 (cited on page 81).

[194] Hyeongju Chung, Inyong Hwang, Jaeyeon Yu, Gerhard Boehm, Mikhail A Belkin, and Jongwon Lee. Electrical phase modulation based on mid-infrared intersubband polaritonic metasurfaces. *Adv. Sci. (Weinh.)*, 10(16):e2207520, 2023 (cited on page 81).

[195] Meint Smit, Xaveer Leijtens, Huub Ambrosius, Erwin Bente, Jos Van der Tol, Barry Smalbrugge, et al. An introduction to inp-based generic integration technology. *Semiconductor Science and Technology*, 29(8):083001, 2014 (cited on page 81).

[196] M Takenaka, Y Kim, J Han, J Kang, Y Ikku, Y Cheng, et al. CMOS photonics technologies based on heterogeneous integration of SiGe/Ge and III-V on si. *2015 IEEE International Electron Devices Meeting (IEDM)*, Washington, DC, USA. IEEE, 2015 (cited on page 81).

[197] Paramjeet Kaur, Andreas Boes, Guanghui Ren, Thach G Nguyen, Gunther Roelkens, and Arnan Mitchell. Hybrid and heterogeneous photonic integration. *APL Photonics*, 6(6), 2021 (cited on page 81).

[198] JM Ramirez, Q Liu, V Vakarin, J Frigerio, A Ballabio, X Le Roux, et al. Graded sige waveguides with broadband low-loss propagation in the mid infrared. *Optics express*, 26(2):870–877, 2018 (cited on page 81).

[199] Donato Pasquariello and Klas Hjort. Plasma-assisted inp-to-si low temperature wafer bonding. *IEEE Journal of Selected Topics in Quantum Electronics*, 8(1):118–131, 2002 (cited on page 82).

[200] Gunther Roelkens, Joris Van Campenhout, Joost Brouckaert, Dries Van Thourhout, Roel Baets, P Rojo Romeo, et al. Iii-v/si photonics by die-to-wafer bonding. *Materials Today*, 10(7-8):36–43, 2007 (cited on page 82).

[201] Tin Komljenovic, Duanni Huang, Paolo Pintus, Minh A Tran, Michael L Davenport, and John E Bowers. Photonic integrated circuits using heterogeneous integration on silicon. *Proceedings of the IEEE*, 106(12):2246–2257, 2018 (cited on page 82).

[202] O Kayser, R Westphalen, B Opitz, and P Balk. Control of selective area growth of inp. *Journal of crystal growth*, 112(1):111–122, 1991 (cited on page 82).

[203] RG Walker. Simple and accurate loss measurement technique for semiconductor optical waveguides. *Electronics letters*, 13(21):581–583, 1985 (cited on page 97).

[204] Alfredo De Rossi, Valentin Ortiz, Michel Calligaro, Loic Lanco, Sara Ducci, Vincent Berger, et al. Measuring propagation loss in a multimode semiconductor waveguide. *Journal of applied physics*, 97(7), 2005 (cited on page 97).

[205] Roberta Ramponi, Roberto Osellame, and Marco Marangoni. Two straightforward methods for the measurement of optical losses in planar waveguides. *Review of scientific instruments*, 73(3):1117–1120, 2002 (cited on page 97).

[206] IP Kaminow and LW Stulz. Loss in cleaved ti-diffused linbo3 waveguides. *Applied Physics Letters*, 33(1):62–64, 1978 (cited on page 97).

[207] Joan Manel Ramírez, Vladyslav Vakarin, Papichaya Chaisakul, Jacopo Frigerio, Andrea Ballabio, Clement Gilles, et al. Ge-rich sige waveguides for mid-infrared photonics. *Silicon Photonics XII*, volume 10108, pages 199–204. SPIE, 2017 (cited on page 97).

[208] Said S Bedair and Ingo Wolff. Fast, accurate and simple approximate analytic formulas for calculating the parameters of supported coplanar waveguides for (m) mic's. *IEEE Transactions on Microwave Theory and Techniques*, 40(1):41–48, 1992 (cited on pages 104, 105).

[209] HC Liu, Jianmeng Li, M Buchanan, and ZR Wasilewski. High-frequency quantum-well infrared photodetectors measured by microwave-rectification technique. *IEEE journal of quantum electronics*, 32(6):1024–1028, 1996 (cited on pages 111, 113).

[210] Magnus Haakestad and Johannes Skaar. Causality and Kramers-Kronig relations for waveguides. *Opt. Express*, 13(24):9922–9934, 2005 (cited on page 117).

[211] Antoni Rogalski. *Infrared and terahertz detectors, third edition*. CRC Press, 2019 (cited on pages 123, 125).

[212] Chen Chen, Cheng Li, Seunghwan Min, Qiushi Guo, Zhenyang Xia, Dong Liu, et al. Ultrafast silicon nanomembrane microbolometer for long-wavelength infrared light detection. *Nano Lett.*, 21(19):8385–8392, 2021 (cited on page 123).

[213] Harald Schneider and Hui Chun Liu. *Quantum well infrared photodetectors*. Springer Series in Optical Sciences. Springer, Berlin, Germany, 2007th edition, 2006 (cited on pages 123, 127).

[214] W D Lawson, S Nielsen, E H Putley, and A S Young. Preparation and properties of HgTe and mixed crystals of HgTe-CdTe. *J. Phys. Chem. Solids*, 9(3-4):325–329, 1959 (cited on page 125).

[215] Antony Rogalski. Hgcdte infrared detector material: history, status and outlook. *Reports on Progress in Physics*, 68(10):2267, 2005 (cited on page 125).

[216] J Piotrowski and A Rogalski. Uncooled long wavelength infrared photon detectors. *Infrared Phys. Technol.*, 46(1-2):115–131, 2004 (cited on page 125).

[217] A. Rogalski. 7 - hgcdte photodetectors. Eric Tournié and Laurent Cerutti, editors, *Mid-infrared Optoelectronics*, Woodhead Publishing Series in Electronic and Optical Materials, pages 235–335. Woodhead Publishing, 2020 (cited on page 125).

[218] M Kopytko and A Rogalski. New insights into the ultimate performance of HgCdTe photodiodes. *Sens. Actuators A Phys.*, 339(113511):113511, 2022 (cited on page 125).

[219] Ghenadii Korotcenkov, editor. *Handbook of II-VI semiconductor-based sensors and radiation detectors*. Springer International Publishing, Cham, Switzerland, 1st edition, 2023 (cited on page 125).

[220] Dominic Kwan, Manoj Kesaria, Ezekiel Anyebe Anyebe, and Diana Huffaker. Recent trends in 8–14 μm type-II superlattice infrared detectors. *Infrared Phys. Technol.*, 116(103756):103756, 2021 (cited on page 125).

[221] Chandler Downs and Thomas E. Vandervelde. Progress in infrared photodetectors since 2000. *Sensors*, 13(4):5054–5098, 2013 (cited on pages 125, 127).

[222] A Rogalski, P Martyniuk, and M Kopytko. Type-II superlattice photodetectors versus HgCdTe photodiodes. *Prog. Quantum Electron.*, 68(100228):100228, 2019 (cited on page 126).

[223] Dhafer O Alshahrani, Manoj Kesaria, Ezekiel A Anyebe, V Srivastava, and Diana L Huffaker. Emerging type-II superlattices of InAs/InAsSb and InAs/GaSb for mid-wavelength infrared photodetectors. *Adv. Photonics Res.*, 3(2):2100094, 2022 (cited on page 126).

[224] Lin Lei, Lu Li, Hao Ye, Hossein Lotfi, Rui Q Yang, Matthew B Johnson, et al. Long wavelength interband cascade infrared photodetectors operating at high temperatures. *J. Appl. Phys.*, 120(19):193102, 2016 (cited on page 126).

[225] B F Levine, K K Choi, C G Bethea, J Walker, and R J Malik. New 10 μm infrared detector using intersubband absorption in resonant tunneling GaAlAs superlattices. *Appl. Phys. Lett.*, 50(16):1092–1094, 1987 (cited on page 126).

[226] Etienne Rodriguez, Alireza Mottaghizadeh, Djamal Gacemi, Daniele Palaferri, Zahra Asghari, Mathieu Jeannin, et al. Room-temperature, wide-band, quantum well infrared photodetector for microwave optical links at 4.9 μm wavelength. *ACS Photonics*, 5(9):3689–3694, 2018 (cited on page 127).

[227] Michael Hakl, Quyang Lin, Sylvie Lepillet, Maximilien Billet, Jean-François Lampin, Stefano Pirotta, et al. Ultrafast quantum-well photodetectors operating at 10 μm with a flat frequency response up to 70 ghz at room temperature. *ACS photonics*, 8(2):464–471, 2021 (cited on page 127).

[228] Alicja Dabrowska, Mauro David, Stephan Freitag, Aaron Maxwell Andrews, Gottfried Strasser, Borislav Hinkov, et al. Broadband laser-based mid-infrared spectroscopy employing a quantum cascade detector for milk protein analysis. *Sens. Actuators B Chem.*, 350(130873):130873, 2022 (cited on page 128).

[229] Daniel Hofstetter, Mattias Beck, and Jérôme Faist. Quantum-cascade-laser structures as photodetectors. *Appl. Phys. Lett.*, 81(15):2683–2685, 2002 (cited on page 128).

[230] L Gendron, M Carras, A Huynh, V Ortiz, C Koeniguer, and V Berger. Quantum cascade photodetector. *Appl. Phys. Lett.*, 85(14):2824–2826, 2004 (cited on page 128).

[231] G Marschick, M David, E Arigliani, N Opačak, B Schwarz, M Giparakis, et al. High-responsivity operation of quantum cascade detectors at 9 µm. *Opt. Express*, 30(22):40188–40195, 2022 (cited on page 128).

[232] G Quinchard, C Mismer, M Hakl, J Pereira, Q Lin, S Lepillet, et al. High speed, antenna-enhanced 10.3μm quantum cascade detector. *Appl. Phys. Lett.*, 120(9):091108, 2022 (cited on page 128).

[233] Xinwei Guan, Xuechao Yu, Dharmaraj Periyanagounder, Mercy Rose Benzigar, Jing-Kai Huang, Chun-Ho Lin, et al. Recent progress in short- to long-wave infrared photodetection using 2D materials and heterostructures. *Adv. Opt. Mater.*, 9(4):2001708, 2021 (cited on page 128).

[234] Mingsheng Long, Yang Wang, Peng Wang, Xiaohao Zhou, Hui Xia, Chen Luo, et al. Palladium diselenide long-wavelength infrared photodetector with high sensitivity and stability. *ACS Nano*, 13(2):2511–2519, 2019 (cited on page 128).

[235] Jarrett H Vella, Lifeng Huang, Naresh Eedugurala, Kevin S Mayer, Tse Nga Ng, and Jason D Azoulay. Broadband infrared photodetection using a narrow bandgap conjugated polymer. *Sci. Adv.*, 7(24):eabg2418, 2021 (cited on page 128).

[236] S J Allen Jr, D C Tsui, and B Vinter. On the absorption of infrared radiation by electrons in semiconductor inversion layers. *Solid State Commun.*, 88(11-12):939–942, 1993 (cited on page 133).

[237] John S Parker, Erik J Norberg, Robert S Guzzon, Steven C Nicholes, and Larry A Coldren. High verticality InP/InGaAsP etching in Cl2/H2/Ar inductively coupled plasma for photonic integrated circuits. *J. Vac. Sci. Technol. B Nanotechnol. Microelectron.*, 29(1):011016, 2011 (cited on page 140).

[238] G Marschick, M David, E Arigliani, N Opačak, B Schwarz, M Giparakis, et al. High-responsivity operation of quantum cascade detectors at 9 µm. *Opt. Express*, 30(22):40188–40195, 2022 (cited on page 146).

[239] Seok-Hwan Jeong and Ken Morito. Optical 90 degree hybrid with broad operating bandwidth of 94 nm. *Opt. Lett.*, 34(22):3505–3507, 2009 (cited on page 146).

[240] Seok-Hwan Jeong and Ken Morito. Compact optical 90 degrees hybrid employing a tapered 2x4 MMI coupler serially connected by a 2x2 MMI coupler. *Opt. Express*, 18(5):4275–4288, 2010 (cited on page 146).

[241] Yves Painchaud, Michel Poulin, Michel Morin, and Michel Tetu. Performance of balanced detection in a coherent receiver. *Opt. Express*, 17(5):3659–3672, 2009 (cited on page 147).

[242] Borislav Hinkov, Mauro David, Gottfried Strasser, Benedikt Schwarz, and Bernhard Lendl. On-chip liquid sensing using mid-ir plasmonics. *Frontiers in Photonics*, 4:1213434 (cited on page 151).

[243] Jjm Hans Binsma, M. van Geemert, Frank Heinrichsdorff, Teus van Dongen, Ronald Broeke, Eajm Erwin Bente, et al. Movpe waveguide regrowth in ingaas/inp with extremely low butt-joint loss, 2001 (cited on page 151).

Appendix A

QCD35b growth sheet

Layer	**Material**	**Thickness** [Å]	**Doping (Si)** [cm^{-3}]	
Top cladding MOCVD	GaInAs	1000	Max	
	InP	100	7,00E+18	
	InP	27000	1,00E+17	
	InP	12000	2,00E+16	
	GaInAs	200	1,00E+17	
Contact	GaInAs	6533	4E+16	
	AlInAs	**18**		
	GaInAs	68		
	AlInAs	19		
	GaInAs	59		
	AlInAs	21		
	GaInAs	53		
	AlInAs	24		
Cascade	GaInAs	49		
	AlInAs	26		
	GaInAs	45		
	AlInAs	28		
	GaInAs	42		
	AlInAs	29		
	GaInAs	39		
	AlInAs	37		
Optical well	GaInAs	96	2,4E+17 (1/3)	
	AlInAs	18		
	GaInAs	66		
	AlInAs	19		
	GaInAs	56		
	AlInAs	21		
	GaInAs	50		
	AlInAs	24		
	GaInAs	46		
Cascade	AlInAs	26		**x14**
	GaInAs	43		
	AlInAs	28		
	GaInAs	41		
	AlInAs	29		
	GaInAs	39		
	AlInAs	37		
	GaInAs	37		
	AlInAs	37		
optical well	GaInAs	96	2E+17 (1/3)	
	AlInAs	30		
	GaInAs	80	1E+17	
	AlInAs	30		
Injector	GaInAs	86	1E+17	
	AlInAs	35		
	GaInAs	90	1E+17	
	AlInAs	35		
Contact	GaInAs	6733	4E+16	
Substrate	**InP**	**500** μm	**1E+17**	

Appendix B

Modulator growth sheets

1 QWASS01

Layer	Material	Thickness [Å]	Doping (Si) [cm^{-3}]	
Top Cladding MOCVD	GaInAs	1000	Max	
	InP	100	7,00E+18	
	InP	27000	1,00E+17	
	InP	12000	2,00E+16	
	GaInAs	200	1,00E+17	
Core WG	GaInAs	9250	6,00E+16	
ACQW	AlInAs	200		x19
	GaInAs	52	2,70E+18	
	AlInAs	14		
	GaInAs	26		
	AlInAs	200		
	GaInAs	52	2,00E+18	
	AlInAs	14		
	GaInAs	26		
	AlInAs	200		
	GaInAs	52	1,80E+18	
	AlInAs	14		
	GaInAs	26	1,80E+18	
	AlInAs	200		
Core WG	GaInAs	9450	6,00E+16	
Substrate	**InP**	**500 µm**	**1,00E+17**	

2 QWASS02

Layer	Material	Thickness [Å]	Doping (Si) [cm^{-3}]	
	GaInAs	1000	Max	
Top Cladding MOCVD	InP	100	7,00E+18	
	InP	27000	1,00E+17	
	InP	12000	2,00E+16	
	GaInAs	200	1,00E+17	
Core WG	GaInAs	8700	6,00E+16	
ACQW	AlInAs	200		x23
	GaInAs	52	9,00E+17	
	AlInAs	12		
	GaInAs	24		
	AlInAs	200		
	GaInAs	52	5,00E+17	
	AlInAs	12		
	GaInAs	24		
	AlInAs	200		
	GaInAs	52	6.20E+17	
	AlInAs	12		
	GaInAs	24	6.20E+17	
	AlInAs	200		
Core WG	GaInAs	8900	6,00E+16	
Substrate	**InP**	**500 µm**	**1,00E+17**	

Appendix C

Mask layouts

1 Absorption cell

This cell is composed of "S" shaped waveguides with a central modulator section of length L, and waveguides of width W. The offset between input and output waveguides is 600 µm. A Straight waveguide is added to some components to facilitate the first alignment. These components are planned for absorption vs bias characterization of the modulators.

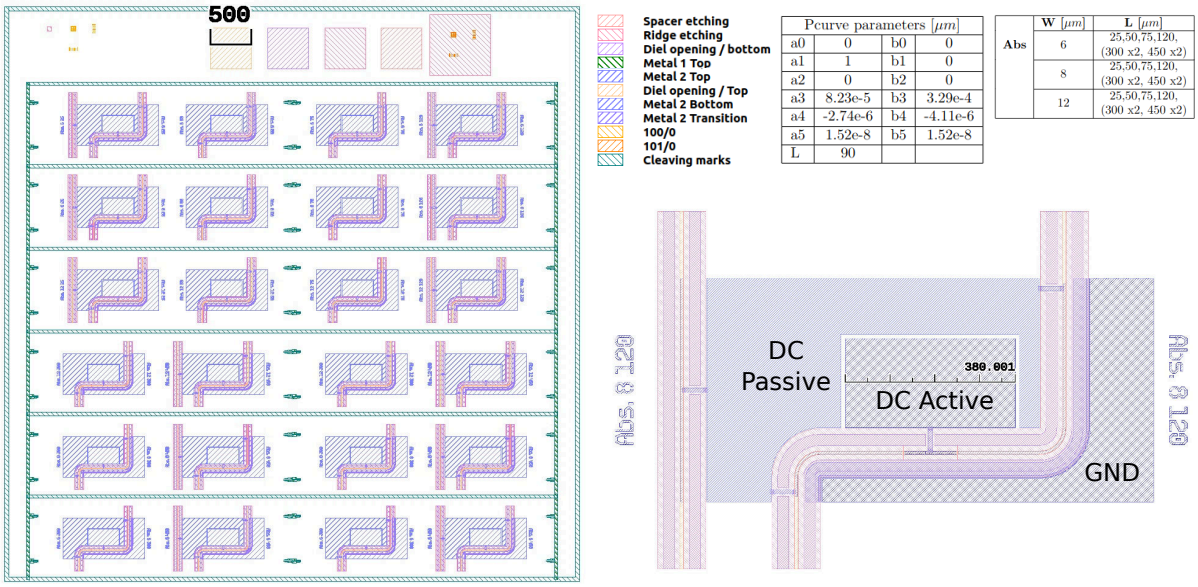

Pcurve parameters [µm]			
a0	0	b0	0
a1	1	b1	0
a2	0	b2	0
a3	8.23e-5	b3	3.29e-4
a4	-2.74e-6	b4	-4.11e-6
a5	1.52e-8	b5	1.52e-8
L	90		

	W [µm]	L [µm]
Abs	6	25,50,75,120, (300 x2, 450 x2)
	8	25,50,75,120, (300 x2, 450 x2)
	12	25,50,75,120, (300 x2, 450 x2)

2 Straight cell

This cell is composed of straight waveguides with coplanar RF waveguide. The modulator length is comprised between 25 and 450 µm for a chip 550 µm long, or 750 to 900 µm for a chip 1050 µm long. Layouts to characterize the three variations of 90° hybrid MMIs are also added, as well as RF coplanar electrodes in short and open circuit.

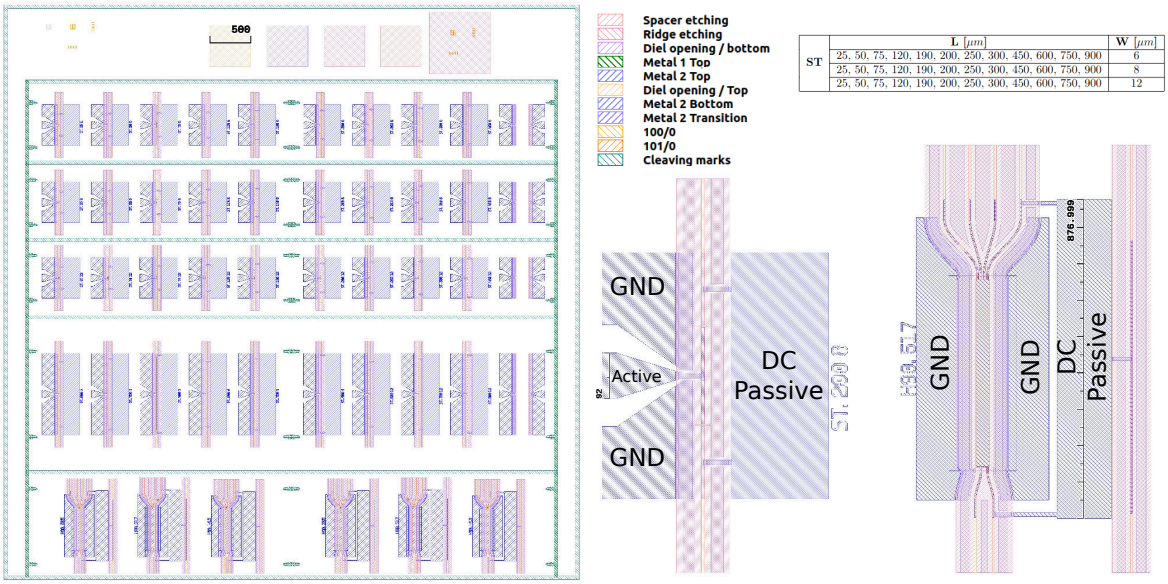

	L [μm]	W [μm]
ST	25, 50, 75, 120, 190, 200, 250, 300, 450, 600, 750, 900	6
	25, 50, 75, 120, 190, 200, 250, 300, 450, 600, 750, 900	8
	25, 50, 75, 120, 190, 200, 250, 300, 450, 600, 750, 900	12

3 Mach Zehnder cells

There are 3 versions of this cell, each one made of Mach-Zehnder with the same version of MMI (see the image for their dimensions). The length of the active section L ranges from 80 to 330 µm with modulator active section waveguide width W of 6, 8 or 12 µm (all passive sections are 6 µm wide). Three characterization layout for the MMI are added at the bottom with "S" bend parameters from the absorption cell layout. The pcurve parameters for the Mach-Zehnder are : (a_0 = 0, a_1 = 1, a_2 = 0, a_3 = 4.86e-4, a_4 = -1.11e-05, a_5 = 6.71e-08), (b_0 = 0, b_1 = 0, b_2 = 0, b_3 = 6.95e-4, b_4 = -1.58e-05, b_5 = 9.58e-08) and L=66 (dimensions in μm or assimilated). For the MMI characterization layout outputs, pcurve parameters (a_0 = 0, a_1 = 0, a_2 = 0, a_3 = 4.32e-4, a_4 = -6.17e-05, a_5 = 2.35e-08), (b_0 = 0, b_1 = 1, b_2 = 0, b_3 = 2.16e-4, b_4 = -3.09e-05, b_5 = 1.17e-08) and L=105 are used, dimensions in μm or assimilated.

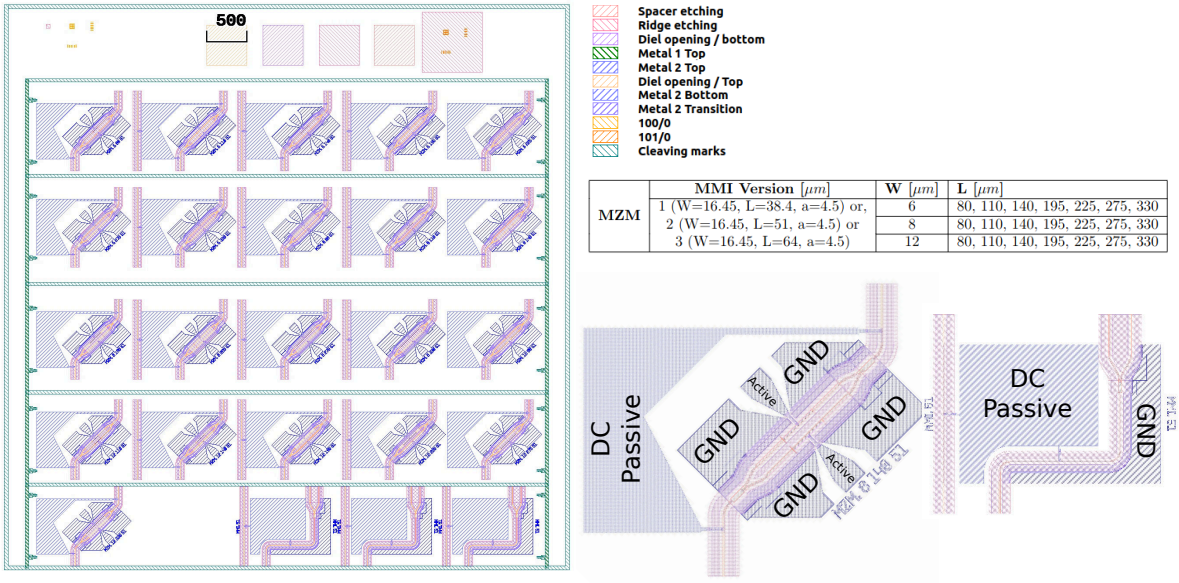

	MMI Version [μm]	W [μm]	L [μm]
MZM	1 (W=16.45, L=38.4, a=4.5) or,	6	80, 110, 140, 195, 225, 275, 330
	2 (W=16.45, L=51, a=4.5) or	8	80, 110, 140, 195, 225, 275, 330
	3 (W=16.45, L=64, a=4.5)	12	80, 110, 140, 195, 225, 275, 330

4 Asymmetrical Mach Zehnder cells

There are 3 versions of this cell, each one made of Mach-Zehnder with the same version of MMI (see the image for their dimensions). The length of the active section L is 50 or 150 µm with active modulator waveguide width W of 6, 8 or 12 µm (all passive sections are 6 µm wide) and *DeltaL* of 1600 or 2000 µm. The pcurve parameters for the Mach-Zehnder are : ($a_0 = 0$, $a_1 = 1$, $a_2 = 0$, a_3 = 8.23e-5, a_4 = -2.74e-06, a_5 = 1.52e-08), ($b_0 = 0$, $b_1 = 0$, $b_2 = 0$, b_3 = 3.29e-4, b_4 = -4.12e-06, b_5 = 1.52e-08) and L=90 (dimensions in μm or assimilated).

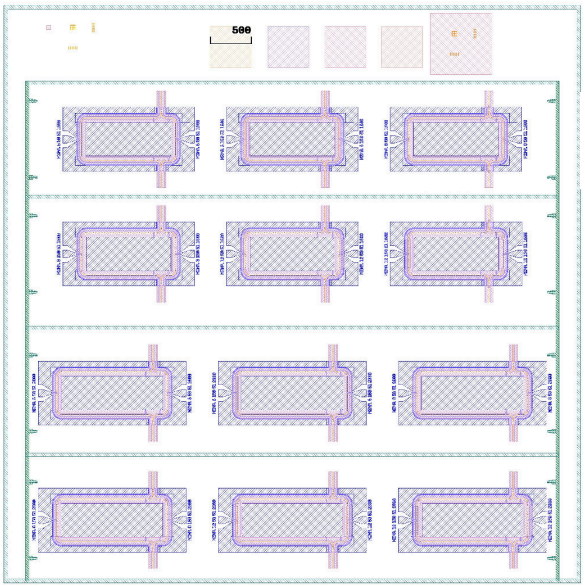

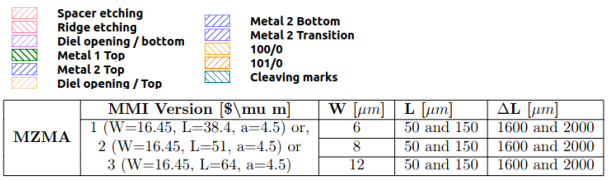

	MMI Version [$\mu m]	W [$\mu m]	L [$\mu m]	ΔL [$\mu m]
MZMA	1 (W=16.45, L=38.4, a=4.5) or,	6	50 and 150	1600 and 2000
	2 (W=16.45, L=51, a=4.5) or	8	50 and 150	1600 and 2000
	3 (W=16.45, L=64, a=4.5)	12	50 and 150	1600 and 2000

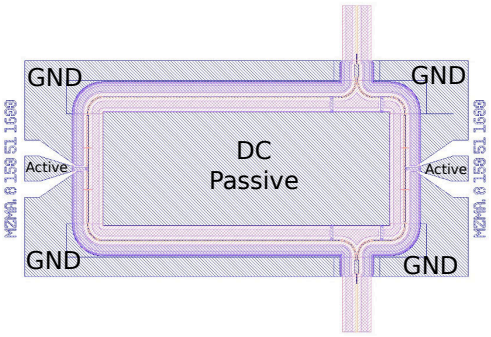

5 Mach Zehnder and H90 cell

There are 3 versions of this cell, each one made of Mach-Zehnder with the same version of MMI (see the image for their dimensions). The length of the active section L is 100 or 200 µm for active modulator waveguide width W of 6, 8 or 12 µm (all passive sections are 6 µm wide). Three versions of the 90° hybrid MMI are on the cell, their dimensions are in the image legend. The pcurve parameters for the Mach-Zehnder are the same as for the Mach-Zehnder cell. Pcurves parameters are for the 90° hybrid MMI inputs : ($a_0 = 0.0$, $a_1 = 1.0$, $a_2 = 0.0$, a_3 = 3.82e-4, a_4 = -8.42e-6, a_5 = 4.95e-8), ($b_0 = 0.0$, $b_1 = 0.0$, $b_2 = 0.0$, b_3 = 4.83e-4, b_4 = -1.07e-5, b_5 = 6.27e-8) and L = 68 ; for the inner outputs : ($a_0 = 0.0$, $a_1 = 1.0$, $a_2 = 0.0$, a_3 = 1.79e-4, a_4 = -2.15e-6, a_5 = 6.88e-9), ($b_0 = 0.0$, $b_1 = 0.0$, $b_2 = 0.0$, b_3 = 1.56e-4, b_4 = -1.87e-6, b_5 = 5.98e-9) and L = 125 ; for the outer outputs : ($a_0 = 0.0$, $a_1 = 1.0$, $a_2 = 0.0$, a_3 = 7.29e-5, a_4 = –7.81e-7, a_5 = 2.23e-9), ($b_0 = 0.0$, $b_1 = 0.0$, $b_2 = 0.0$, b_3 = 3.32e-4, b_4 = -3.56e-6, b_5 = 1.02e-8) and L = 140.

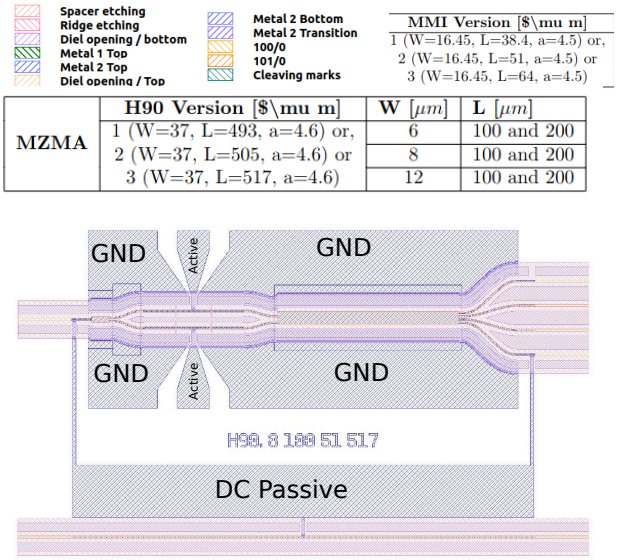

6 Modulator for integration GS

There are three different designed layouts for the integration on a dedicated submount with RF electrodes. The first one is a simple layout, single section waveguide of 300, 250 or 200 µm with a G-S electrode on submount.

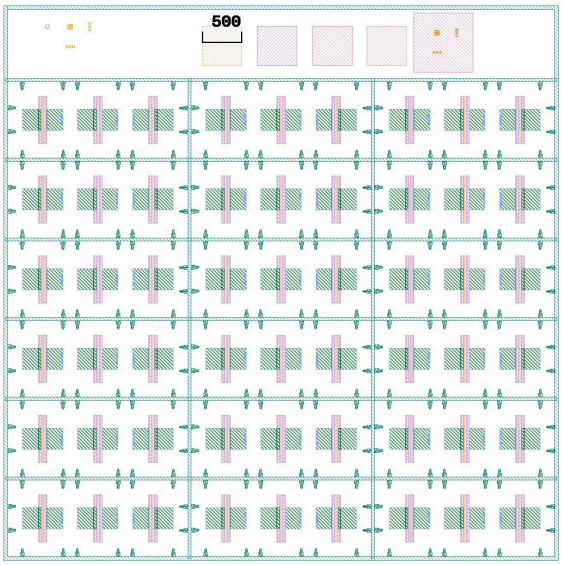

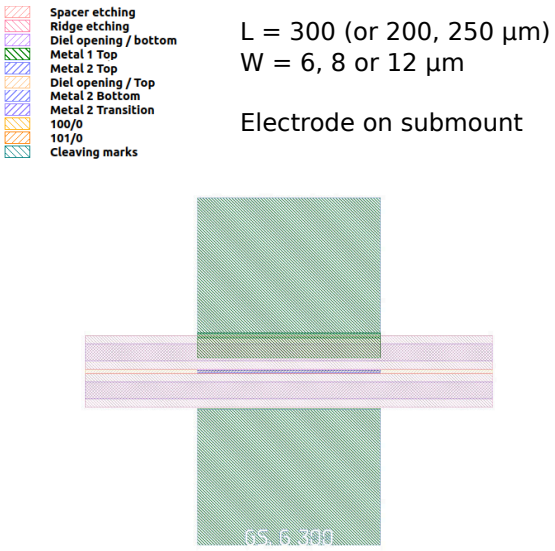

The second is a single section waveguide of 300, 200 or 250 µm with a GSG electrode on submount.

The third is a three section waveguide with an active section of 70, 85 or 100 µm and total length of 300 µm for QWASS_01 structure with GSG electrode and DC passive bias electrode on submount. For the QWASS_02 structure it is composed of a two sections waveguide with active section of 170, 190 or 210 µm and total length of 300 µm with a GSG electrode on submount

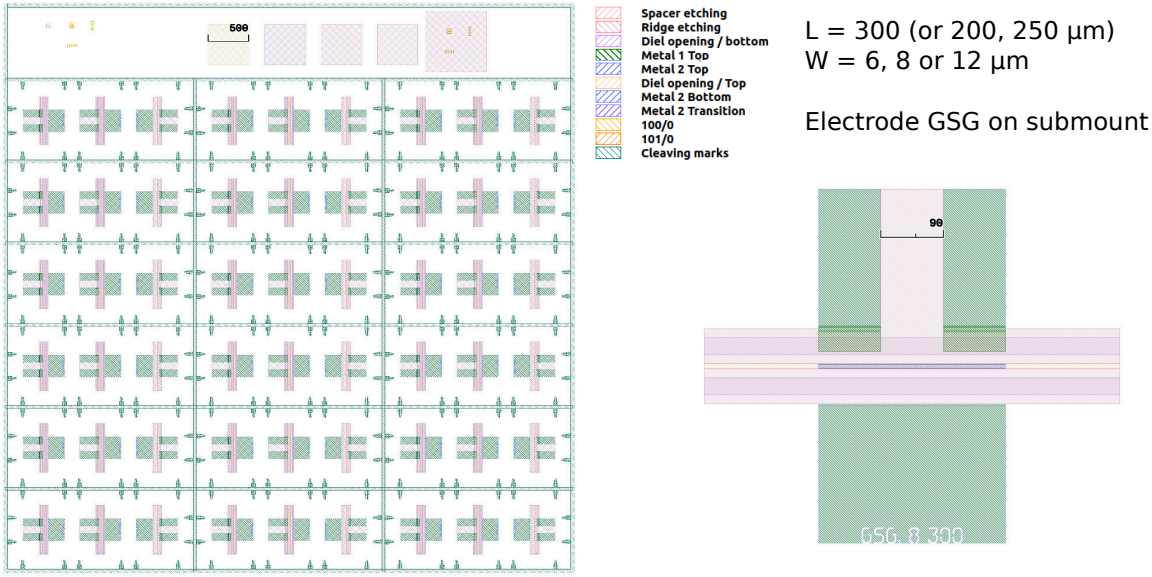

and a DC passive electrode (with passive waveguide metallised or not).

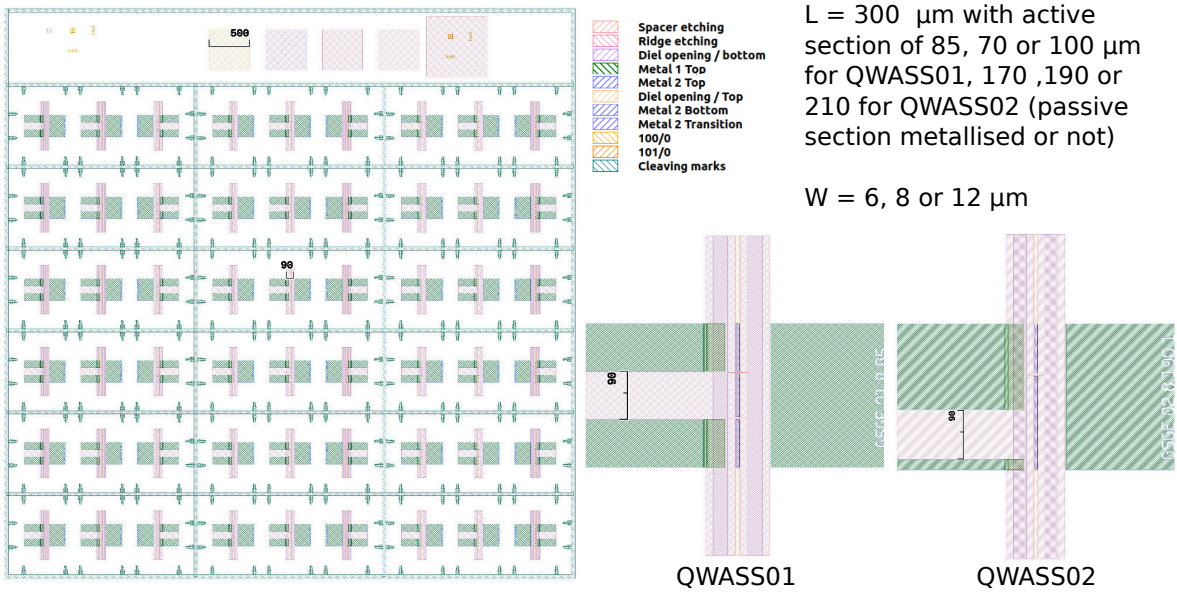

7 Whole sample implantation :

For QWASS_01 and QWASS_02 processed samples, the following cell implantation is used (the 2 sections QWASS_02 being in place of the QWASS_01 three sections for the corresponding sample) :

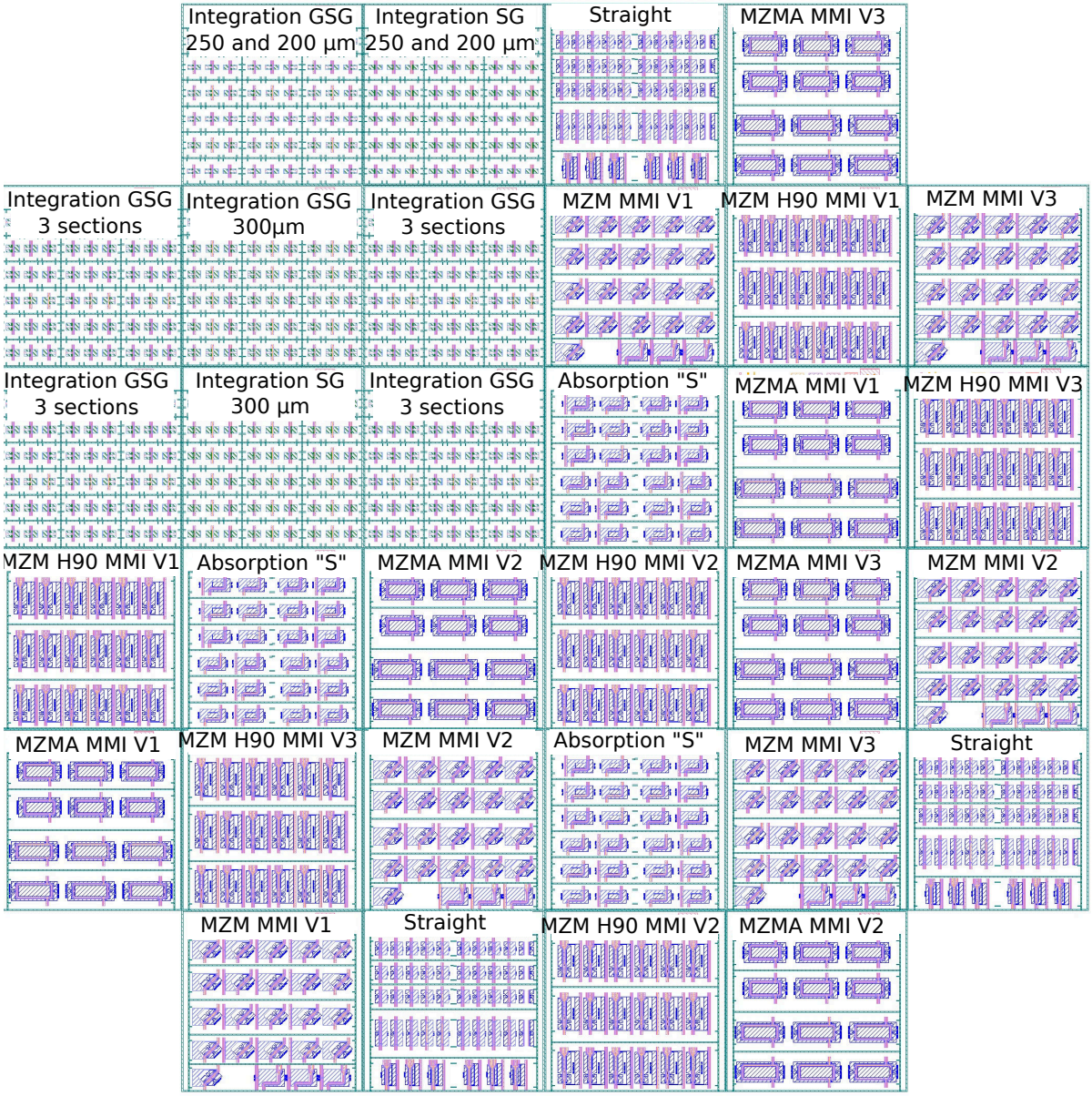

8 Passive MMI layout and implantation :

Similarly, for the processing of passive MMI structures, those being made using contact lithography, one single mask is used to define the etched waveguides (and alternatively, one for the marks and labels). Its implantation if presented here : The following components are implemented on this one :

- General interference 2×2 MMIs with waveguides of 6, 8 or 12 µm
- Restricted interference 2×2 MMIs with waveguides of 6, 8 or 12 µm (width)
- Symmetrical 1×2 MMIs with waveguides of 6, 8 or 12 µm
- 2×4 90° hybrid MMIs with waveguides of 6, 8 or 12 µm

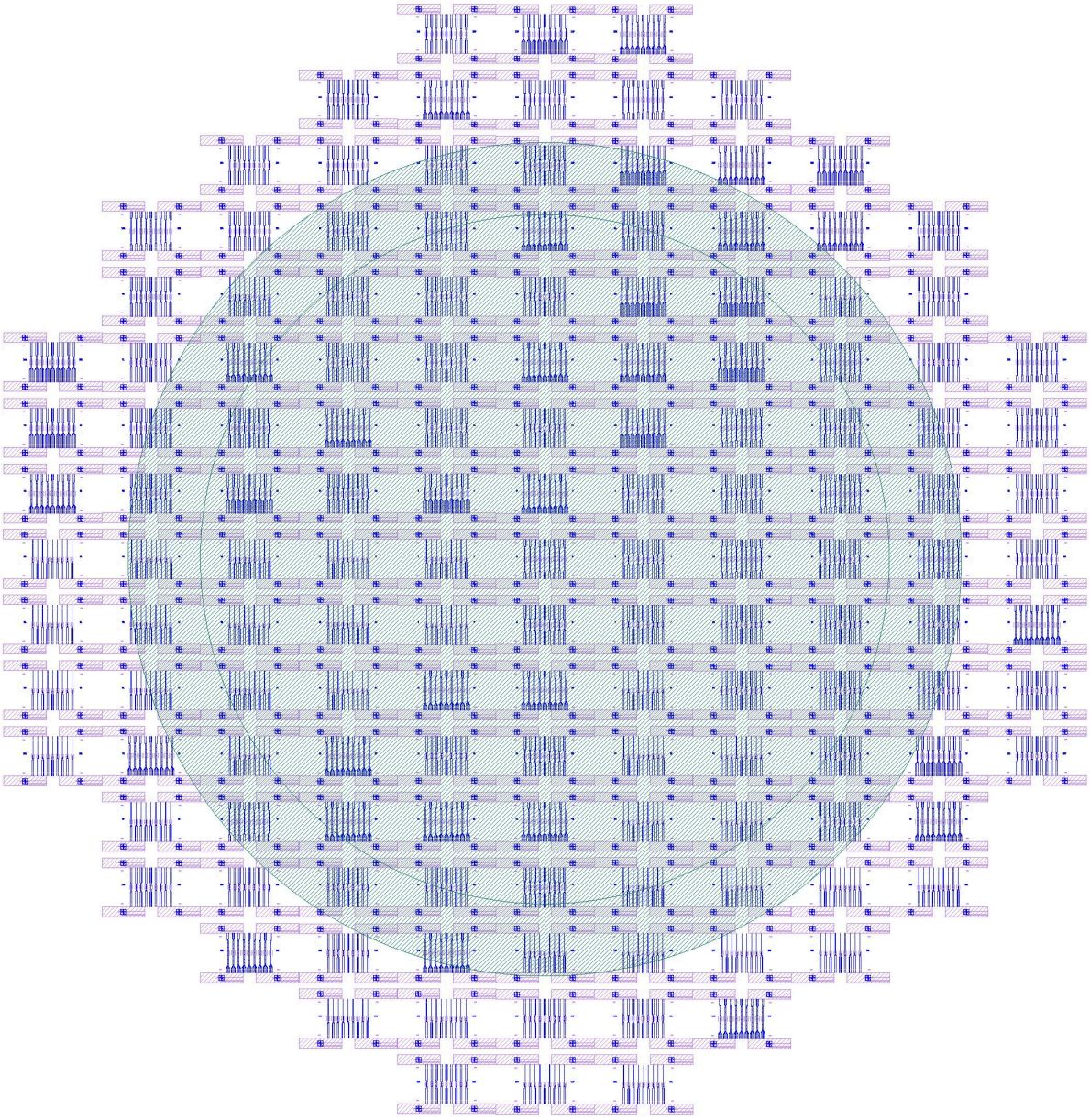

each of those designs are reproduced 9 times with 8 different length variations by step $\delta L/2$. See chapter 3 for its definition. Their optimal dimensions are :

- L = 67.68, 125.7 or 218.9 µm, W= 18.75, 25.8, 34.3 µm, a = 4.8, 6.5 or 8.56, δL = 12, 20 or 40 µm for waveguide width of respectively 6, 8 and 12 µm. Those dimensions are those of 1×2 MMIs.
- L = 94.6, 194 or 43.6 µm, W = 19.2, 27.8 or 467.7 µm, a = 3.9, 5.2 or 7.7, δL = 12, 20 or 40 µm for waveguide width of respectively 6, 8 and 12 µm. Those dimensions are those of 2×2 restricted interferences MMIs.
- L = 334.1, 493.6 or 1283.7 µm, W = 20.9, 25.6 or 41.7 µm, a = 7.4, 8.3 or 12.8, δL = 12, 20 or 40 µm for waveguide width of respectively 6, 8 and 12 µm. Those dimensions are

those of 2×2 general interferences MMIs.

- W = 37, 60 or 62 µm, L = 494.5, 1310 or 1398 µm, a = 4.3, 6.1 or 7.7, δL = 12, 40 or 20 µm for waveguide width of respectively 6, 8 and 12 µm. Those dimensions are those of 2×4 MMIs.

Each design and its variations are repeated along a spiral distribution on the whole sample.

Appendix D

Modulator absorption fitted data

The fitted lorentzian functions discussed in chapter 4 are presented here. The extracted data at the given bias is presented by the red dots, the fitted lorentzian functions by the red (fitted absorption) and blue (phase) dashed curves.

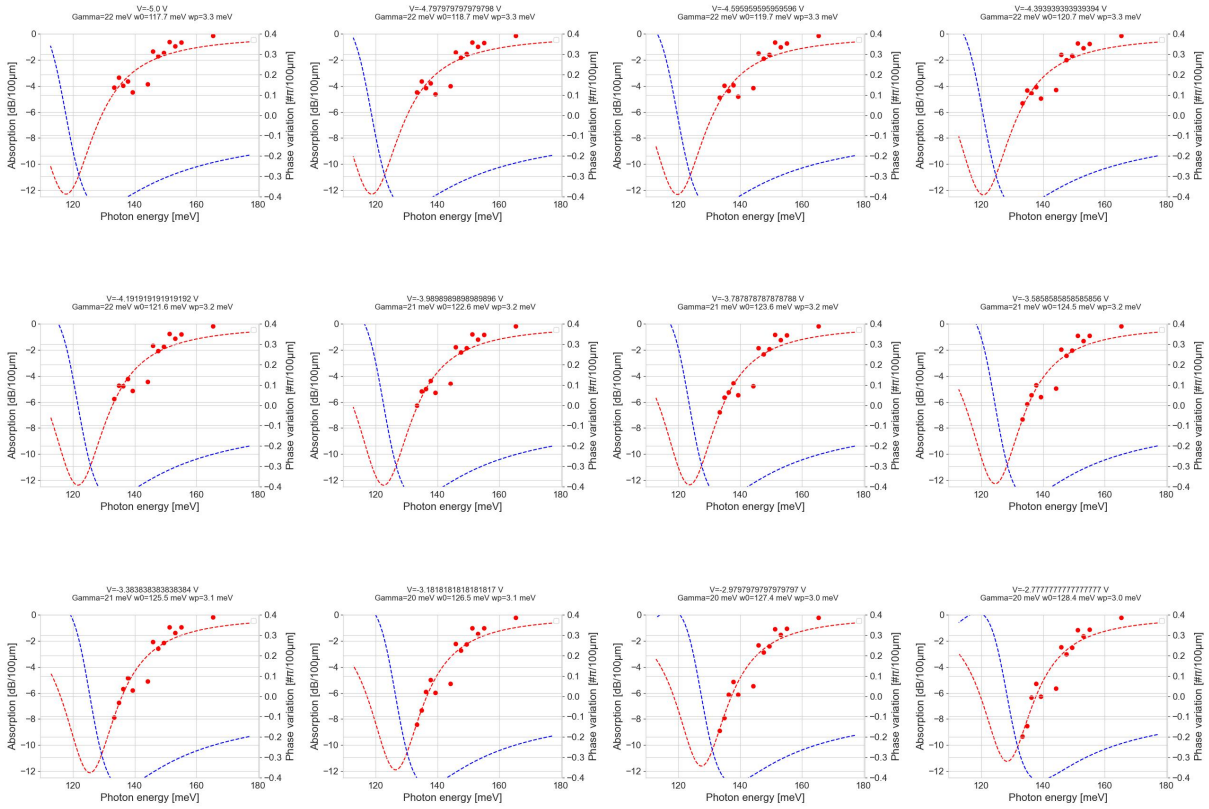

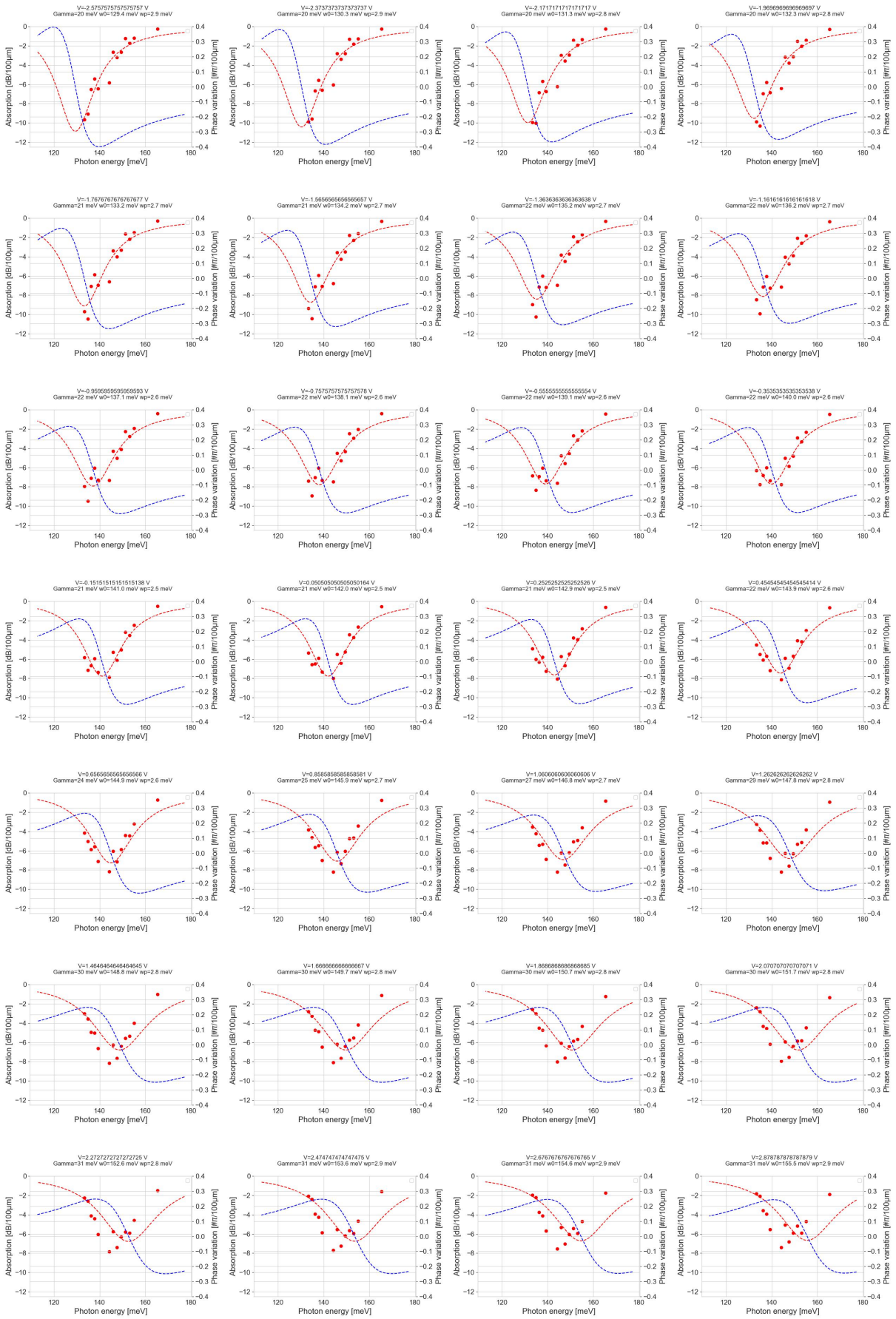
V=-2.5757575757575757 V
Gamma=20 meV w0=129.4 meV wp=2.9 meV
V=-2.3737373737373737 V
Gamma=20 meV w0=130.3 meV wp=2.9 meV
V=-2.1717171717171717 V
Gamma=20 meV w0=131.3 meV wp=2.8 meV
V=-1.9696969696969697 V
Gamma=20 meV w0=132.3 meV wp=2.8 meV
V=-1.7676767676767677 V
Gamma=21 meV w0=133.2 meV wp=2.7 meV
V=-1.5656565656565657 V
Gamma=21 meV w0=134.2 meV wp=2.7 meV
V=-1.3636363636363638 V
Gamma=22 meV w0=135.2 meV wp=2.7 meV
V=-1.1616161616161618 V
Gamma=22 meV w0=136.2 meV wp=2.7 meV
V=-0.9595959595959593 V
Gamma=22 meV w0=137.1 meV wp=2.6 meV
V=-0.7575757575757578 V
Gamma=22 meV w0=138.1 meV wp=2.6 meV
V=-0.5555555555555554 V
Gamma=22 meV w0=139.1 meV wp=2.6 meV
V=-0.3535353535353538 V
Gamma=22 meV w0=140.0 meV wp=2.6 meV
V=-0.15151515151515138 V
Gamma=21 meV w0=141.0 meV wp=2.5 meV
V=0.05050505050505164 V
Gamma=21 meV w0=142.0 meV wp=2.5 meV
V=0.2525252525252526 V
Gamma=21 meV w0=142.9 meV wp=2.5 meV
V=0.4545454545454414 V
Gamma=22 meV w0=143.9 meV wp=2.6 meV
V=0.6565656565656566 V
Gamma=24 meV w0=144.9 meV wp=2.6 meV
V=0.8585858585858581 V
Gamma=25 meV w0=145.9 meV wp=2.7 meV
V=1.0606060606060606 V
Gamma=27 meV w0=146.8 meV wp=2.7 meV
V=1.2626262626262626 V
Gamma=29 meV w0=147.8 meV wp=2.8 meV
V=1.4646464646464645 V
Gamma=30 meV w0=148.8 meV wp=2.8 meV
V=1.6666666666666667 V
Gamma=30 meV w0=149.7 meV wp=2.8 meV
V=1.8686868686868685 V
Gamma=30 meV w0=150.7 meV wp=2.8 meV
V=2.070707070707071 V
Gamma=30 meV w0=151.7 meV wp=2.8 meV
V=2.272727272727725 V
Gamma=31 meV w0=152.6 meV wp=2.8 meV
V=2.474747474747475 V
Gamma=31 meV w0=153.6 meV wp=2.9 meV
V=2.6767676767676765 V
Gamma=31 meV w0=154.6 meV wp=2.9 meV
V=2.8787878787878787 V
Gamma=31 meV w0=155.5 meV wp=2.9 meV
Absorption [dB/100µm]
Phase variation [#rr/100µm]
Photon energy [meV]

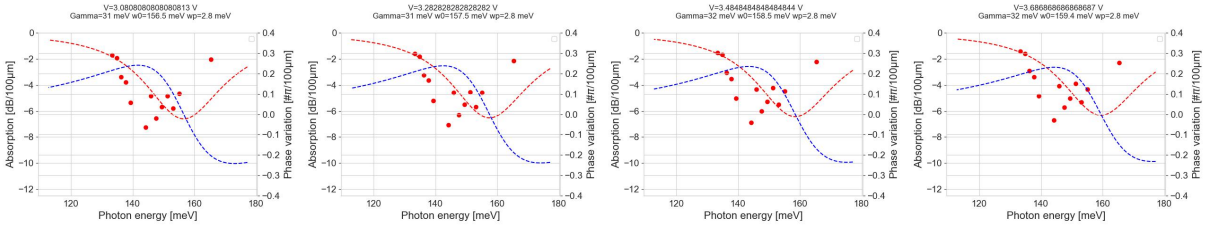
V=3.0808080808080813 V
Gamma=31 meV w0=156.5 meV wp=2.8 meV
V=3.282828282828282 V
Gamma=31 meV w0=157.5 meV wp=2.8 meV
V=3.4848484848484844 V
Gamma=32 meV w0=158.5 meV wp=2.8 meV
V=3.686868686868687 V
Gamma=32 meV w0=159.4 meV wp=2.8 meV
Absorption [dB/100µm]
Phase variation [#π/100µm]
Photon energy [meV]

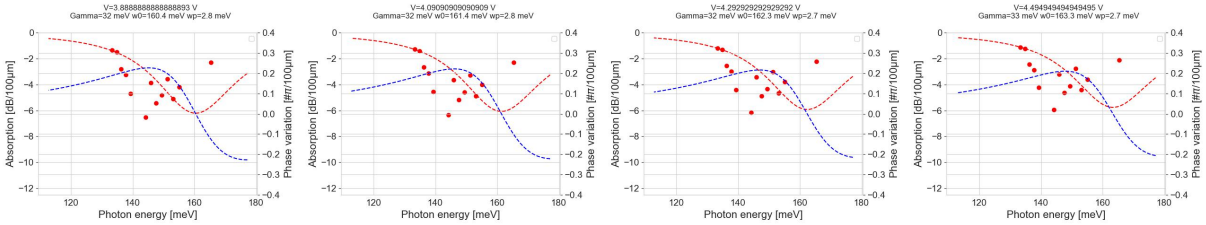
V=3.8888888888888893 V
Gamma=32 meV w0=160.4 meV wp=2.8 meV
V=4.09090909090909 V
Gamma=32 meV w0=161.4 meV wp=2.8 meV
V=4.292929292929292 V
Gamma=32 meV w0=162.3 meV wp=2.7 meV
V=4.494949494949495 V
Gamma=33 meV w0=163.3 meV wp=2.7 meV
Absorption [dB/100µm]
Phase variation [#π/100µm]
Photon energy [meV]

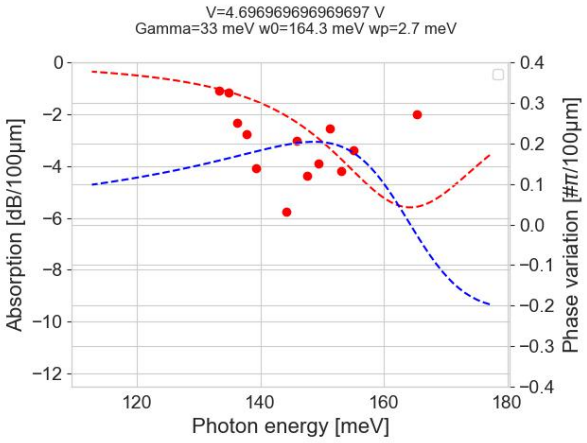
V=4.696969696969697 V
Gamma=33 meV w0=164.3 meV wp=2.7 meV
Absorption [dB/100µm]
Phase variation [#π/100µm]
Photon energy [meV]

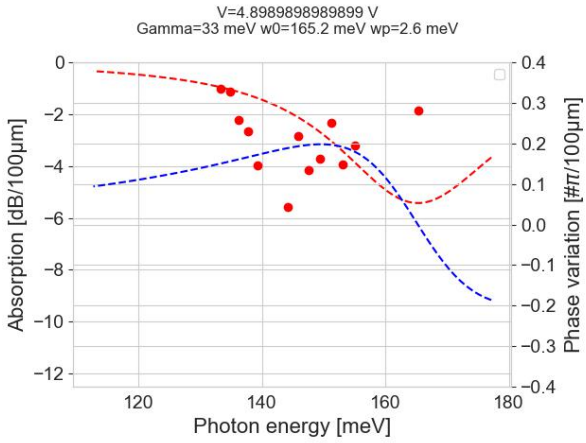
V=4.8989898989899 V
Gamma=33 meV w0=165.2 meV wp=2.6 meV
Absorption [dB/100µm]
Phase variation [#π/100µm]
Photon energy [meV]

Appendix E

Résumé des chapitres

1 Chapitre 1 : Introduction générale

Dans ce premier chapitre, nous situons le contexte et les motivations du travail effectué et présenté dans cette thèse. Une première partie se concentre sur l'état actuel des télécommunications et les éléments historiques ayant mené à son actuel constitution. En effet, l'actuel réseau de télécommunication est majoritairement constitué de télécommunications optiques sur le réseau fibré pour sa partie câblée, et des télécommunications radiofréquences pour sa partie espace libre. Actuellement, dans un contexte de croissance conséquente des débits échangés, des solutions alternatives ont besoin d'être développées pour subvenir aux besoins à venir en termes de communication haut débit. En particulier, les télécommunications en espace libre sont vues comme une solution crédible pour répondre à ce besoin, et dans une seconde partie, leurs avantages et les challenges liés à leur développement sont exposés. Elles ont l'intérêt de nécessiter des infrastructures moins couteuses que leur alternative câblée ou fibrée, et procurent une meilleure sécurité et efficacité énergétique que leur alternative radiofréquence. Néanmoins, la sensibilité d'un lien de télécommunication optique en espace libre, vis-à-vis des perturbations atmosphériques, posent un conséquent challenge à leur développement. Dans ce contexte, plusieurs études ont démontré la moindre sensibilité des longueurs d'ondes de l'infrarouge lointain, en comparaison des longueurs d'ondes des télécommunications fibrées (infrarouge proche), à ces perturbations. Toutefois, les composants optiques pour l'infrarouge lointain qui nous intéressent, ne bénéficient pas de la maturité technologique de ceux de l'infrarouge proche, très largement développés pour les télécommunications fibrées. C'est pourquoi dans ce travail de thèse, nous nous concentrons sur le développement des briques de bases nécessaires pour constituer un système de télécommunication en espace-libre aux longueurs de l'infrarouge lointain. Les briques développées et présentées dans les chapitres suivants sont tous des composants en géométrie de guide d'onde pour leur intégrabilité en circuits photoniques.

2 Chapitre 2 : Éléments théoriques de télécommunication et semi-conducteurs

Dans la première partie de ce chapitre, nous présentons les éléments théoriques de la modulation optique d'un faisceau de lumière monochromatique (laser) pour transmettre de l'information. Plusieurs types de modulations en phase et en amplitude sont présentés, et plusieurs formats de modulation cohérente d'ordre élevé sont discutés. La capacité d'un canal présentant un bruit blanc gaussien est présentée. Nous rappelons ainsi en particulier qu'il est tout aussi important d'avoir une bande passante élevée et un bon rapport signal/bruit. Le taux d'erreur binaire de différents formats de modulation à travers ce canal est présenté, et l'importance d'un diagramme de constellation bien construit est rappelée, en lien avec le taux d'erreur binaire.

Dans la seconde partie de ce chapitre, nous présentons toute la théorie utilisée pour concevoir les composants optiques actifs et passifs présentés dans les chapitres suivants. En particulier, nous présentons l'importance de la bonne connaissance des indices optiques des matériaux utilisés, et les différentes méthodes de mesures de ces derniers. Nous présentons deux méthodes employées pour caractériser les propriétés optiques de semi-conducteurs et de diélectriques, ainsi que les indices optiques obtenus par ces méthodes et les limites des méthodes de caractérisations employées.

Dans la suite du chapitre, nous présentons les aspects théoriques et l'incidence du confinement électronique sur les propriétés optiques d'un matériau constitué de puits quantiques. Les incertitudes sur la fabrication et la modélisation des puits quantiques, en particulier la modélisation des interfaces des puits quantiques, est discutée, ainsi que la méthode de calibration employée pour garantir un bon accord entre performances simulées et réalisées.

3 Chapitre 3 : Optique guidée et composants passifs

Ce chapitre est dédié à l'optique guidée. Dans une première partie, nous présentons les différentes géométries de guide d'onde employées, leurs avantages et inconvénients. Différentes plateformes technologiques pour l'infrarouge lointain et leurs performances associées sont également comparées. Les différentes sources de perte optique sont discutées dans la suite de cette partie, ainsi que les moyens de les modéliser et de les limiter. Nous présentons les pertes de couplage entre les guides de différentes sections, ou les moyens d'injecter un faisceau laser dans un guide d'onde. Les pertes optiques liées à la rugosité d'interface des guides sont aussi présentées et leur impact justifié comme étant négligeable pour le travail présenté dans la suite du manuscrit. Enfin, les pertes radiatives dans des guides courbés et les moyens employés pour y pallier sont présentés à la fin de cette partie. En particulier, nous avons présenté la méthode de conception des sections de guide courbées, qui nous a permis de trouver un compromis entre les pertes optiques par radiation et les pertes par absorption dans le matériau très absorbant constituant nos guides d'ondes. Le choix de guides d'ondes "deep ridge" est finalement justifié et successivement employé dans ce travail, pour la compatibilité en termes d'intégration avec des QCLs déjà développés par un partenaire.

Dans la seconde partie de ce chapitre, nous présentons les aspects théoriques des interféromètres multimodes (MMI), des composants photoniques passifs employés pour leur robustesse et leur largeur de bande optique. Ces éléments sont ensuite utilisés pour la conception de recombineurs de faisceaux, dans l'optique de leur utilisation comme photo-mixeur pour une détection hétérodyne cohérente avec des photodiodes balancées. Ceux-ci ont été réalisés, et leurs performances optiques mesurées et rapportées dans cette partie. Nous avons démontré la capacité de notre composant à séparer la puissance injectée dans une de ses entrées en deux parts égales avec une incertitude inférieure à 8% sur une bande allant de 9 à 9.4 µm. Les relations de phases entre les sorties sont proches du théorique 180° (±10°) sur la même bande. À notre connaissance, les performances présentées ici due MMI 2×2 comme recombineur de faisceaux, sont à la pointe de la technologie dans la bande spectrale de l'infrarouge lointain. Mais, très peu de retours sur les performances de ces composants sont rapportés dans la littérature, pour le fonctionnement dans l'infrarouge lointain.

4 Chapitre 4 : Modulateur de phase et d'amplitude intégré pour les télécommunications espace libre dans l'infra-rouge lointain

Dans ce chapitre, nous présentons d'abord les différents effets physiques qui peuvent être utilisés pour réaliser une modulation d'indice optique, en mettant l'accent sur celles exploitables dans l'infrarouge lointain. La modulation de la concentration en porteurs libres dans le cœur d'un guide d'ondes montre un grand potentiel. En effet, sa force est plus prononcée aux longueurs d'onde plus grandes. Cet avantage est néanmoins tempéré par le fait que le volume typique dans lequel ces densités de porteurs sont modulées, ne change pas avec la longueur d'onde, ce qui nécessite des géométries de guides d'ondes particulières pour compenser le recouvrement plus faible avec le champ optique, compliquant la fabrication et l'intégration ultérieure avec les QCLs.

L'utilisation de l'effet Stark inter-sous-bande, d'autre part, montre un très fort effet de modulation (comme déjà rapporté dans la littérature) et est hautement compatible avec les QCLs, car les deux sont fondés sur la même technologie de composants. Cela rend sont utilisation particulièrement intéressante pour une future intégration monolithique. Notre choix a donc été de nous concentrer sur l'utilisation de l'effet Stark dans des puits quantiques asymétriques couplés, insérés dans un guide d'onde optique, pour réaliser un modulateur de phase et d'amplitude.

Dans la suite de ce chapitre, nous présentons deux conceptions de régions actives, qui montrent des performances simulées prometteuses. Ces régions actives ont été optimisées en géométrie de guide d'ondes pour être intégrés à des puces, epi-down, avec un QCL et un amplificateur optique, sur une embase RF dédiée. Le premier design (nominal), QWASS 01, a été conçu pour montrer des performances élevées, c'est-à-dire une transmission supérieur à -8dB, un $V\pi$ de 3V pour un $L\pi$ de 87 µm (donc une efficacité de modulation de $V\pi L\pi$ de 0,03 V/cm) et une fréquence de coupure autour de 30 GHz, ce qui serait comparable à l'état de l'art modulateurs dans la bande spectrale SWIR. Les contraintes de fabrication imposées, notamment l'utilisation de la même région active pour les guides d'ondes passifs et actifs, nous a conduit à un second

design plus conservateur, avec une région active peu dopée, caractérisé par des performances attendues plus faibles, mais également avec diminution des pertes optiques parasites. Cette seconde région active alternative (nomée QWASS 02) a été conçu pour avoir un $V\pi$ de 5,3 V pour un $L\pi$ de 195 µm (donc un $V\pi L\pi$ de 0,1 V/cm) et une bande passante électro-optique de 14 GHz, mais des perte optique beaucoup plus faible à polarisation nulle, environ -20 dB/mm par rapport aux -160 dB/mm du QWASS 01. Plusieurs configurations de guides d'ondes dédiées aux caractérisations sur puce ont été présentées. Il s'agit de Mach-Zehnder symétriques et asymétriques, prévus pour caractériser la modulation de phase optique ; de guides droits et en "S" pour estimer l'absorption linéaire et sa modulation en fonction de la polarisation appliqué ; et de quelques alternatives plus exploratoires, comme les interféromètres Mach-Zehnder couplé à un MMI hybride 90° pour une caractérisation de la modulation de phase plus avancé. Tout ces composants ont été fabriqués durant cette thèse, pour laquelle un processus de fabrication complexe et fastidieux en salle blanche a été développé. En raison des pertes d'absorption excessives de la structure QWASS 01, la caractérisation optique des composants n'a été possible que sur des composants QWASS 02. Les résultats de ces caractérisations (encore préliminaires) ont montré des performances très prometteuses, proches de celles calculées, avec une absorption maximale de -8,5 dB/100 µm et une modulation de phase de $0{,}7\pi/100$ µm entre -4V et 1V, telle qu'extraite à partir d'un fit de la transmission avec un modèle vérifiant les relations de Kramers-Kronig. De plus, même si le la bande passante mesurée a montré des limitations dues à une capacité parasite associée aux guides d'ondes RF coplanaires, nous avons quand même pu mesurer une bande passante de 1,4 GHz à -3 dB sur un composant épi-up. Les composants dédiés à l'intégration de flip-chips ne devraient pas avoir de telles limitations, et devraient afficher une bande passante beaucoup plus élevée.

5 Chapitre 5 : Récepteur cohérent pour les télécommunications espace libre dans l'infra-rouge lointain

Dans la première partie de ce chapitre, nous présentons les différentes technologies de détecteurs pour l'infrarouge lointain. Après avoir comparé, sur la base des figures de mérites exposées au début du chapitre, ces différentes technologies, notre choix d'utiliser des détecteurs à cascade quantique est justifié. Il s'ensuit une présentation des éléments théoriques permettant de modéliser et de simuler les performances de tels composants, employés pour présenter les performances théoriques du composant QCD réalisé dans ce travail. Par la fabrication du composant en question est présentée et ses performances mesurées.

Nous présentons les performances d'un détecteur à cascade quantique (QCD) en géométrie de guide d'ondes ayant une NEP en détection directe jusqu'à 40 pW/$Hz^{0.5}$ à une longueur d'onde de 9,5 µm et inférieure à 60 pW/$Hz^{0.5}$ à une longueur d'onde de 9,1 µm.

Dans la perspective de l'intégrer avec d'autres composants pour former un récepteur cohérent I/Q, nous avons également développé et démontré un hybride 90° basé sur des MMIs, dont les performances permettent une détection cohérente sur une largeur de bande de plus de 100 nm autour de 9,3 µm. Ses CMRR sont mesurées inférieurs à -10edB sur une bande allant de 9.1 à

9.4 µm et les erreurs sur les relations de phase sont inférieures à ± 20° sur la même bande, voir ± 10° sur la bande 9.3 - 9.4. Il est important de souligner içi que l'incertitude sur ses performances est largement dominée par l'incertitude introduite par le banc de mesure lui-même, et ne traduit pas les performances du composant en lui-même attendues comme étant bien meilleures.

RÉSUMÉ

Les communications optiques en espace libre sont devenues un domaine d'intérêt croissant au cours des dernières années, dans lequel les dispositifs optoélectroniques fonctionnant dans la gamme des longueurs d'onde de l'infrarouge lointain (LWIR) pourraient être de sérieux concurrents des longueurs d'onde traditionnelles des télécommunications pour les liaisons atmosphériques. En effet, les grandes longueurs d'onde sont moins affectées par les perturbations atmosphériques. Toutefois, le déploiement des communications en espace libre dans le LWIR est limité par la disponibilité des éléments de base passifs et actifs tels que les modulateurs d'amplitude et de phase rapide et les recombineurs de faisceaux.

Dans ce travail, nous présentons le développement d'un modulateur externe en géométrie guide d'onde, basé sur l'effet Stark inter-sous-bande, fonctionnant à $\lambda = 9$ µm. Cet effet est particulièrement intéressant pour la modulation en raison de sa réponse intrinsèquement rapide, son accordabilité élevée et linéaire en longueur d'onde avec une tension appliquée, et sa faible consommation d'énergie. Nous avons intégré des puits quantiques asymétriques couplés dans un guide d'ondes InGaAs sur InP afin de maximiser l'interaction optique tout en minimisant la capacité électrique du composant. Le résultat est un modulateur polyvalent capable d'effectuer une modulation d'amplitude ou de phase par un choix judicieux de la polarisation et de l'intensité de la modulation RF appliquées. Dans l'optique d'une future intégration monolithique, nous avons conçu et fabriqué des recombineurs de faisceaux passifs en guide d'ondes basés sur des interféromètres multimodes (MMI) ainsi que des détecteurs à cascade quantique (QCD) pour la détection cohérente. Nous présentons leurs performances, et en particulier celles d'un séparateur MMI 2x2 3dB et d'un MMI hybride 90 degrés 2x4, qui sont des éléments essentiels pour les émetteurs-récepteurs intégrés pour communications cohérentes.

MOTS CLÉS

Optique intégrée, guide d'onde, modulation optique, télécommunications en espace libre, infrarouge lointain

ABSTRACT

Free-Space Optical (FSO) communications has become a field of growing interest over the past years in which optoelectronic devices operating in the Long Wave Infrared (LWIR) wavelength range could be serious competitors to traditional telecom wavelengths for atmospheric links as they are less impacted by atmospheric perturbations. However, the deployment of LWIR FSO communications is limited by the availability of basic passive and active building blocks such as high-speed modulators and beam combiners among others. In this work, we present an external integrated modulator based on inter-subband Stark effect operating at $\lambda = 9$ µm. This effect is of particular interest for modulation due to its intrinsically fast response, high wavelength tunability under applied bias and low RF power consumption. We embedded asymmetrical coupled quantum wells within a deep ridge InGaAs on InP core waveguide in order to increase the optical interaction and reduce the geometrical capacitance. The result is a versatile modulator able to perform either amplitude or phase modulation by an appropriate choice of applied DC bias and RF modulation. In addition, we designed and fabricated passive waveguide beam combiners based on Multi Mode Interferometer (MMI) and quantum cascade detectors (QCD). We present their performance and in particular 2x2 3dB MMIs splitter as well as 2x4 90 degree Hybrid MMIs which are critical building blocks for integrated transceivers based on complex modulation format and are planned to be integrated with a QCD.

KEYWORDS

Photonic integrated circuit, optical waveguide, optical modulator, free space optical communications, long wave infrared